# Analysis of Dimethyl Ether (DME) Injection Spray Characteristics in Comparison to Diesel and Theoretically Predicted Spray Characteristics

**D.J. Valentim**

A dissertation submitted to the Faculty of Engineering and the Built Environment, University of the Witwatersrand, Johannesburg, in fulfilment of the requirements for the degree of Master of Science in Engineering.

Johannesburg, October 2014

# Declaration

I declare that this dissertation is my own, unaided work, except where otherwise acknowledged. It is being submitted for the degree of Master of Science in Engineering in the University of the Witwatersrand, Johannesburg. It has not been submitted before for any degree or examination at any other university.

Signed this 16th day of October 2014

D.J. Valentim

# Acknowledgements

I would like to thank my parents for their support during this period, without their love and support I would not be where I am today. I would like to thank my uncle Luis for his guidance. I would like to thank Professor Daniele Cipolat for his guidance and support throughout this study. I would like to thank Frank Testa from DPA Diesel for his assistance with the fuel injection equipment, the countless pumps he exchanged made it possible to complete this study successfully. I would also like to thank Ralf from TW Diesel for providing me with refurbished pumps and injectors when they where damaged.

The financial assistance of the National Research Foundation (NRF) towards this research is hereby acknowledged. Opinions expressed and conclusions arrived at, are those of the author and are not necessarily to be attributed to the NRF.

# Abstract

The objectives of this research are to compare the spray characteristics of diesel and Dimethyl ether (DME), in order to investigate parameters which influence the spray characteristics such as penetration, cone angle, and spray velocity. A standard common rail system was used to inject high pressure fuel into a constant volume pressure chamber. Tests were conducted at 300 bar to 500 bar injection pressure, and atmospheric pressure to 17.7 bar chamber pressure using carbon dioxide as an ambient gas at room temperature. A Z-shaped schlieren system with a high power LED was used to form images for the high speed camera operating at 20 000fps. An experiment controller was constructed to simultaneously control the triggering of: the injector, the high speed camera, and the recording of pressure data. The diesel and DME spray penetration and tip velocity was found to increase with an increase in injection pressure, and the opposite result was seen with an increase in chamber pressure. DME consistently penetrated less than diesel throughout the tests conducted, the difference in penetration was larger at the lowest chamber pressures. The difference between DME and Diesel decreased at higher chamber pressures to 6 - 9%. The cone angle for DME was consistently larger than that of diesel for all the tests conducted. Both fuels showed a relatively linear increase in cone angle with an increase in chamber pressure, with the exception of the tests at atmospheric conditions. The DME had a tendency of flash boiling at these conditions resulting in a large cone angle. Experimental results were compared to theoretical predictions of penetration and cone angle. The experimental penetration for diesel and DME were reasonably predicted by some of the theoretical models at the higher chamber pressures. No correlation was found in terms of injection pressure for the diesel cone angle, whereas the DME showed a slight increase with an increase in injection pressure. While analysing the results a hesitation in the intial 0.2ms was observed, this was found to be due to the placement of the single-hole in the nozzle and the resultant pressure distribution around the injector needle. This hesitation was factored out when comparing penetration results to theoretical predictions.

# Contents

# List of Figures

# List of Tables

# List of Symbols

| **Symbol** | **Description** | **Unit** |
|---|---|---|
| $d_o$ | - Orifice diameter | [m] |
| $\rho_g$ | - Gas density | [kg/m$^3$] |
| $\rho_l$ | - Liquid density | [kg/m$^3$] |
| $\theta$ | - Cone Angle | [$^o$] |
| $\Delta P$ | - Pressure difference | [Pa] |
| $\mu$ | - Dynamic viscosity | [Pa.s] |
| $l_o$ | - Orifice length | [m] |
| $T_g$ | - Gas temperature | [$^o$K] |
| $v_{in}$ | - Initial fuel velocity | [m/s] |
| $\alpha_d$ | - Volume fraction of droplets in spray | [-] |
| $\tilde{\rho}_g$ | - $\rho_g/\rho_l$ | [-] |
| $C_d$ | - Coefficient of Discharge | [-] |
| $P_{Ambient}$ | - Ambient Pressure | [bar] |
| $P_{Injection}$ | - Injection Pressure | [bar] |
| S | - Spray penetration | [m] |

# Nomenclature

| | |
|---|---|
| CCD | - Charge Coupled Device |
| CFC | - Chlorofluorocarbon |
| CI | - Compression Ignition |
| $CO_2$ | - Carbon Dioxide |
| CR | - Common Rail |
| DAQ | - Data Acquisition |
| DCU | - Diesel Control Unit |
| DME | - Dimethyl Ether |
| ECU | - Electronic Control Unit |
| EGR | - Exhaust Gas Recirculation |
| fps | - Frames per second |
| ICCD | - Intensified Charged Coupled Device |
| LED | - Light Emitting Diode |
| $N_2$ | - Nitrogen Gas |
| Nd:YAG | - Neodymium-doped yttrium aluminum garnet, a crystal used in lasers |
| $NO_x$ | - Nitric Oxides |
| PDPA | - Phase Dopler Particle Analyser |
| TTL | - Transistor transistor logic |
| VCO | - Valve Covered Orifice |

# 1 Introduction

## 1.1 Background

Compression ignition (CI) engines are known to have improved thermal efficiency, improved fuel consumption, and lower carbon dioxide emissions when compared to spark ignition engines [1; 2]. It is for this reason that compression ignition engines are used in a number of applications such as transport, earth moving and power generation. One of the main concerns with CI engines is that they produce nitric oxides ($NO_X$) and particulate matter, which are harmful to the environment. Increasing emission standards in Europe have assisted in the development of, increasingly efficient, diesel fuelled CI engines. The way that modern diesel engines can achieve higher efficiencies is due to the development in the fuel injection systems. The higher injection pressures, precise control of the injection duration, and different spray strategies help reduce unburnt fuel which aid in reducing soot and harmful emissions. This emphasisis the importance of the spray characteristics as they influence various aspects of the CI engines performance. In order to further attempt to improve the emissions of these CI engines, research into alternative fuels has been conducted. Aspects which are the focus of much research are emissions, performance, and spray characteristics.

Previous studies at the University of the Witwatersrand have focused on the injector spray characteristics using both diesel and DME (Dimethyl Ether) in a common-rail fuel injection system. Tests were conducted at low ambient pressures and densities with the maximum ambient pressure of 18 bars. The main focus of the current research will be to analyse the injector spray characteristics, of DME and diesel, at higher ambient pressures and densities than done so by the previous students. Analysing the injector spray characteristics will allow the understanding of the behaviour of the fuel spray, and from this, conclusions can be drawn with respect to the plausibility of using DME as an alternative fuel in a CI engine.

## 1.2 Motivation

Energy demand is increasing at a staggering rate, and one of the most reliable methods of providing energy is from fossil fuels. It is known that emissions produced by burning these fuels are largely responsible for the production of greenhouse gases which are thought to be responsible for global warming as well as air pollution. It is for this reason that emission regulations are becoming increasingly stringent in order to push for the development of cleaner running engines and for the development of cleaner alternative fuels. Dimetheyl Ether (DME) is an alternative fuel which can be considered as a fuel for compression ignition engines. It is suitable to be used in a CI engine as it has similar properties to those of diesel, some are superior and some are inferior. DME has been found to have a similar thermal efficiency to that of diesel [3],[2], and lower harmful emissions are produced as DME is an oxygenated fuel. A reasonable amount of research has been conducted on DME with regards to emissions and engine performance. The investigation of spray characteristics is an on-going field of research [4]. It is necessary to understand the spray characteristics of a fuel as this has a direct impact on the performance of the engine. The spray will influence the burning of the fuel in the engine cylinder which is related to power, efficiency and emissions. It is thus important to analyse the spray characteristics of diesel and to investigate the influence of injection parameters as well as ambient parameters on the spray characteristics. It is then possible to identify the most influential parameters and determine their effects. The spray characteristics of DME are then compared to those of diesel, and this will allow for the evaluation of DME as a prospective alternative fuel. This analysis will then highlight the advantages of using DME in a CI engine.

Additionally, it is important to be able to predict the behaviour of the injection sprays, as this aids designers in the development of the engine in terms of fuel utilization in the combustion chamber, and timing of injections. Multistage injections are used in newer generation common-rail engines, therefore it is useful to know how long the spray takes to develop and when a good air to fuel ratio is achieved. Correlations have been developed to predict penetration lengths for diesel fuel, therefore it is necessary to examine these correlations and determine if they are suitable for the prediction of DME spray penetration.

# 2 Literature Survey

## 2.1 Fuel Injection Systems

### 2.1.1 Methods of fuel injection

Two methods of fuel injection, namely the Direct Injection or Open Combustion Chamber method and the Pre-combustion chamber method [5], are discussed as they are more relevant to the study.

Direct Injection: Fuel is injected directly into the combustion chamber. The injection nozzle is designed so as to sufficiently penetrate the compressed air charge. This requires a high injection pressure [6]. Usually Multiple-hole type nozzles are used to give the best spray characteristics into the compressed air charge, the piston head design also aids in creating turbulence in the chamber so as to guarantee the best combustion conditions possible[6]. Some piston head designs are shown in Figure 2.1a. Direct injection engines can be started up from cold more easily than pre-chamber engines, due to the fact that the heat loss is less in this type of engine[6]. There are various types of direct injection engines which have been designed; one example is the Mexican Hat Combustion Chamber which is shown in Figure 2.1b.

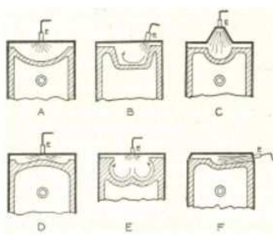


a)

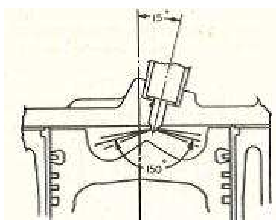


b)

Figure 2.1: a) Piston Head Variations [6] b) Direct Injection Combustion Chamber [6]

Pre-combustion chamber Injection: This type consists of a smaller combustion chamber (about 40% of the total combustion chamber volume) which is located above the cylinder in the cylinder head. This is connected to the main chamber via a throat, the injector sprays the fuel in the direction of this throat so as to achieve the best mixing possible. This mixture burns with insufficient air and this explosion sends the partially burnt fuel and un-burnt fuel into the main chamber where the combustion process is completed [5]. There are many types of pre-combustion chambers: Figure 2.2 shows the principle of a pre-combustion chamber.

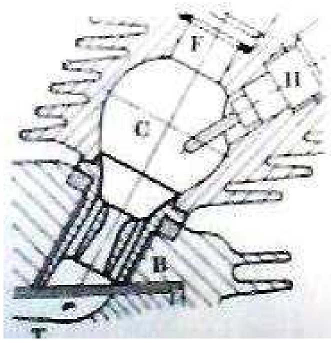


Figure 2.2: Pre-Combustion chamber [5]

### 2.1.2 Fuel Injection Systems

In the past there were many fuel systems in use to manage commercial diesel engines [7]. The principal types of systems were:

1. Air injection: compressed air was used to inject the fuel into the combustion chamber, where the pressure of the compressed air was much higher than the pressure in the cylinder. This method gave excellent atomization and the compressed air caused turbulence in the cylinder which enabled the fuel to mix very well [6]. This method worked well but at present it is not one of the main methods of providing injection and is rarely used as bulky and heavy air compressors are required[6].

2. Jerk Pump or Timed pump systems: high pressure fuel is pumped to the injector, causing the valve to open. The valve is usually set to open at a specific pressure which is set by the valve spring, and the injection is timed to occur at certain moments in the engine cycle [6]. The pump which is used to provide the high pressure to the injectors can be one of 3 basic types of pumps: A single unit multiple pumping element, which consists of plunger type pumping element for each cylinder of the engine. All these elements are usually housed in a single unit and are actuated by a single camshaft [6]. A single distributor type pump is also used where the pump receives fuel at a low pressure, and is then pumped to a

higher pressure by the pumping element. It is then distributed to the different cylinders by a built-in distributor at the correct cycle times [6]. There is also the combination of injector and pump, which is actuated by a push-rod and rocker-arm from the engine camshaft, where each cylinder has an individual unit [6].

3. Common Rail System (CR): In the common rail system fuel is not pumped to individual injectors by a single element pump or any other type of pump. The common rail system uses a high pressure pump which supplies pressurized fuel to an accumulator or rail [8], [9]. The schematic layout of a CR system is shown in Figure 2.3.

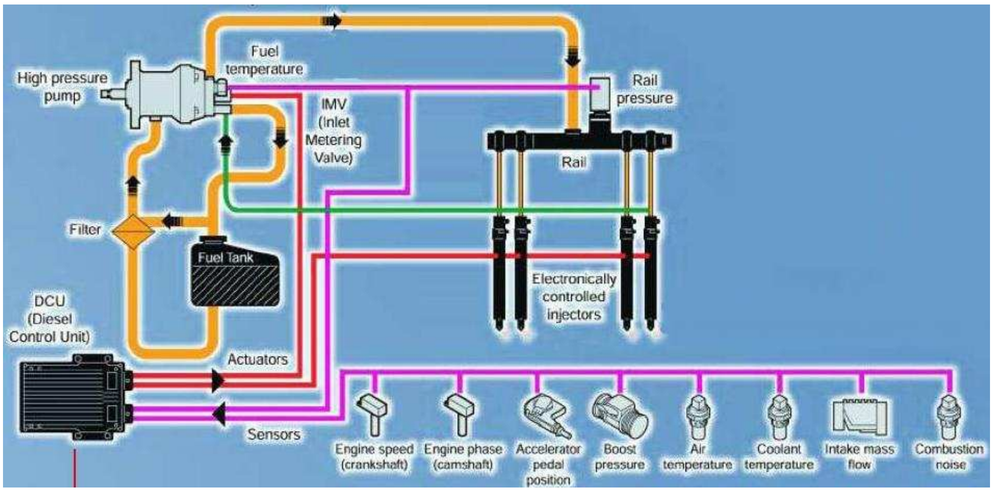


Figure 2.3: Schematic of a common rail fuel injection system [8]

The pressure to which the fuel is pressurized in the rail is controlled by the pump which is controlled by the engines electronic management system (or DCU-Diesel Control unit) [9]. The rail is a high pressure accumulator which prevents large pressure fluctuations due to injection. The rail has a pressure sensor which indicates the rail pressure to the electronic management system at any point [9]. This enables the engine controller to receive the pressure reading in the rail and calculates the flow and the injection advance [8]. A High pressure rail is shown in Figure 2.4. The rail pressure is maintained at its desired injection pressure value for that specific point in operation by a control valve [9]. If the pressure in the rail is lower than the required pressure then the control valve is closed and the pressure in the rail is allowed to increase. The opposite occurs if the actual rail pressure is higher than the required rail pressure where the control valve opens and allows the fuel to leak back into fuel system until the rail pressure reaches its desired value[9]. A feature of the accumulator or rail is that even after injection the pressure in the rail remains more or less constant [9]. Each injector is connected to the common rail by high pressure fuel lines. The injectors used in common rail systems are electro-hydraulic injectors, controlled by the electronic management system [9].

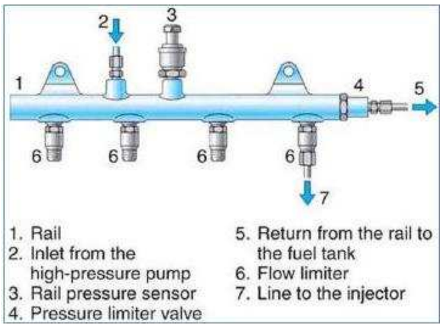


Figure 2.4: Common Rail, or Accumulator [9]

### 2.1.3 Electrohydraulic Injectors

The fuel injection in a common rail system is controlled by one of two main types of electronically controlled injectors (or electro-hydraulic injectors), namely the solenoid and piezoelectric actuated injectors[9]. Electro-hydraulic injectors use hydraulics (and spring force) to control the movement of the needle valve (open or closed) instead of relying on a spring force to determine the valve opening pressure. The pressurized fuel from the common rail enters the injector and passes through passages in the injector body. Pressurized fuel is held in a cavity above the nozzle (this pressure acts on the top of a control piston which holds the needle valve down in its seat [9]) as well as in the annular area under the needle valve [9].These two cavities are shown in Figure 2.5.

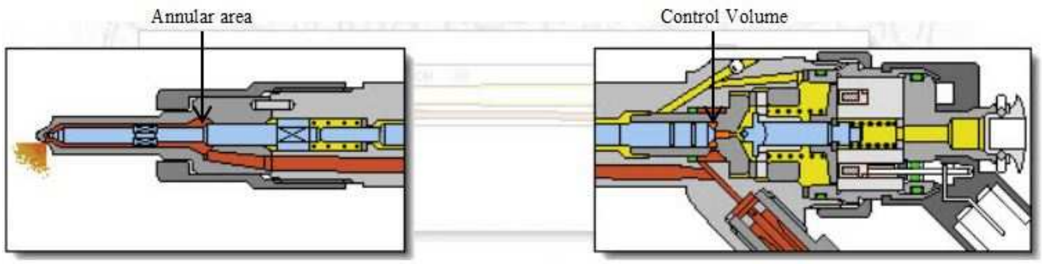


Figure 2.5: Section through a solenoid injector, indicating the control volume [10]

The pressure acting on the control piston is greater than the pressure acting on the annular valve area and this causes the valve to remain closed. In a solenoid actuated injector, the solenoid controls a small drain orifice in the cavity above the control volume. When injection is required a signal is sent to the solenoid and it is activated and the drain is opened thereby causing the pressure in this cavity to drop and allowing the valve to open and injection occurs. When the solenoid is deactivated the drain closes and injection ceases [10]. The Piezo-electrically actuated injector works in the same manner as a solenoid injector. Instead of using a solenoid coil, a stack of piezoelectric crystals are used to control the opening and closing of the small orifice drain. In solenoid injectors the speed is limited because of self-inductance in the coil, this is not a factor with piezo-electric injectors. Thus injector speeds for this type of injector can be considerably faster and multiple injections per firing cycle and combustion can be precisely controlled [10]. These actuation methods perform the injection timing and metering functions, they control how much fuel must be injected into the gas charge [11]. The period over which the injector is actuated determines the amount of fuel which is injected. The nozzle and the actuation mechanism are held together by the injector body. This casing makes it easy to place the injector in the cylinder head. Piezo-actuated and solenoid injectors are shown in Figure 2.6.

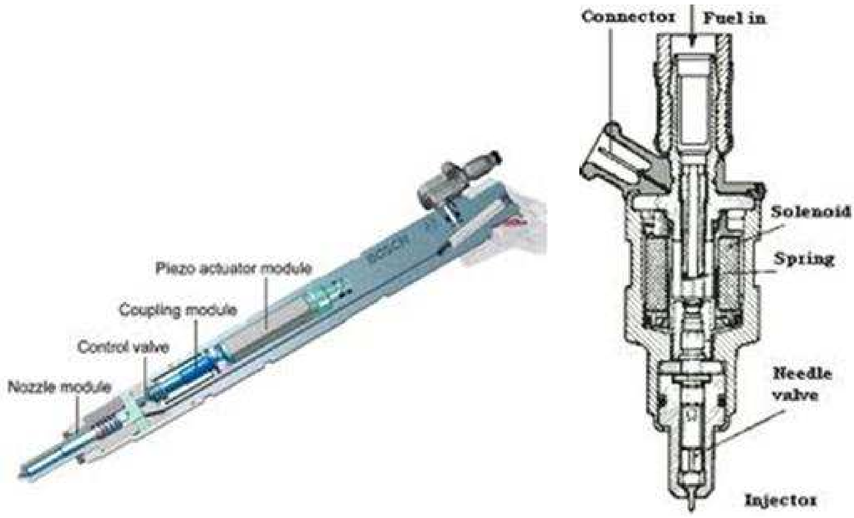


a) b)

Figure 2.6: Common-Rail Injectors (a) Piezoelectric Injector [12] (b) Solenoid Injector [6]

### 2.1.4 Injection Nozzles

There are several types of injection nozzles in use. These nozzles are used to achieve different types of sprays into the combustion chamber. Each of these nozzles have different spray characteristics and are chosen in certain engine types. The injection nozzle is selected based on the specific requirements of the engine being developed. A study conducted by N.A.C.A on fuel sprays under various injection and chamber pressures, using various types of injection nozzles, concluded that important characteristics to be considered were:

- Injection pressure: The penetration length of the spray was found to be directly proportional to the injection pressure. The penetration length of the spray increases with increasing injection pressure, after a certain limit is reached the penetration length of the spray does not increase any further and can even reduce the penetration length as the spray is finely atomized and the drops are then too light to penetrate the dense air [6].
- Density of the cylinder gas charge: The density of the compressed air charge affects the penetration length of the sprays, the pressure of the air has no direct effect on the penetration[6].
- Effect of fuel density: The penetration length increases with increasing fuel density, as it makes it more difficult to atomize the fuel and the spray angle becomes narrower thus increasing the penetration length [6].

There are two types of injection nozzles: the open type and the closed type. The open type nozzle does not have a valve to control the fuel injection through it; the fuel flow is controlled by the fuel pump [5]. The closed type nozzle needs a device of some form to actuate the valve so that fuel can flow through the injector; a mechanical, electronic or hydraulic control is needed for injection [6].

There are two basic types of the closed type injector nozzles, Sac type nozzles and Valve Covered Orifice (VCO) nozzles which are shown in Figure 2.7. As the name

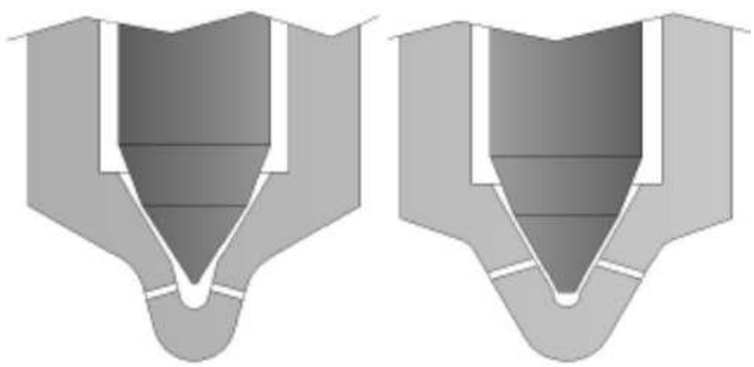

Figure 2.7: Section through a) Sac type nozzle, b) VCO nozzle [13]

suggests, the orifice holes in a VCO nozzle are covered by the needle when the injector is closed. This ensures that once the injector is closed, the holes are completely covered and the flow of fuel into the cylinder is abruptly stopped. If small amounts of fuel enter the engine after combustion has taken place, smoke and hydrocarbons will be present in the emissions[14]. VCO nozzles allow for more accurate timing of injections as well as metering of fuel [15]. The disadvantage of VCO nozzles is that if the pressure distribution around the needle is not equal, the spray emerging from each nozzle hole will not be the same, and it is more sensitive to needle misalignment than the sac type nozzle[14; 15]. Sac type nozzles are not effected as greatly as VCO nozzles by needle misalignment as the holes are not covered by the needle, so a pressure imbalance around the orifices is less likely to occur as the sac volume stabalises the pressure [14; 15]. Figure 2.8, shows the effect of needle misalignment on flow through the orifice holes in a VCO nozzle. The slight misalignment has a significant impact on the flow through the holes [16]. The effect of needle misalignment is related to the needle lift, the effect is therefore greater on the initial spray characteristics when the needle is lifting. The effects of misalignment are reduced as the needle reaches full lift[14; 16].

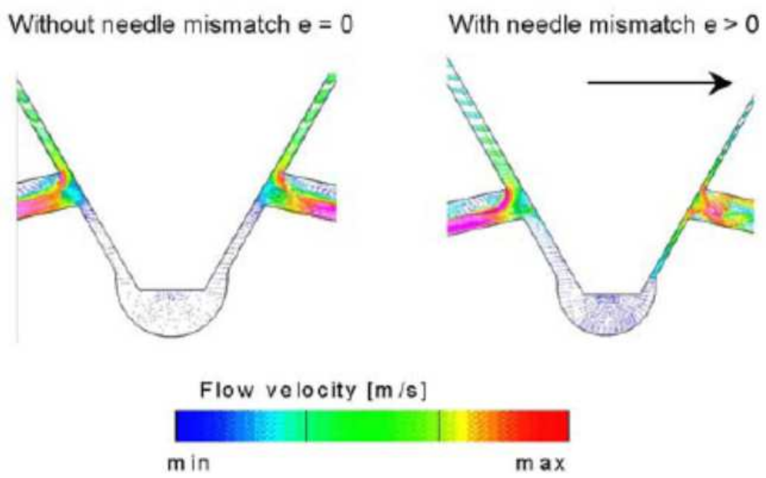


Figure 2.8: Effect of Needle Misalignment in a VCO nozzle [16]

### 2.1.5 Injector Parameters

Second generation common rail injectors are solenoid actuated injectors, controlled by the ECU. In order to actuate a solenoid it is required to be supplied with an inrush current for a fraction of the injection duration and a holding current for the remainder of the duration. [17]. The inrush current is provided by a large voltage of about 60V, resulting in a current exceeding the current rating of the solenoid coil. Thus it is applied to the injector for a short period, typically 100 to 200$\mu$s, therefore the coil does not burn out. The inrush current is required to establish a magnetic field in the solenoid as quickly as possible, thereby opening the injector as quickly as possible. Once a magnetic field is set up in the solenoid coil, the current required to maintain the coil in position is reduced, to the holding current [17]. The currents at these two stages of injector actuation vary with the injector used.

### 2.1.6 Alternative fuels

Fuel is a substance or material that is used to provide energy, and is transformed from its original state into energy, the most common method being to burn the fuel, as occurs in combustion engines. The fuels mainly used in combustion engines today are diesel and petrol, these are classified as fossil fuels. Fossil fuels are non-renewable as they take millions of years to form from dead plant material through biogenic and thermogenic processes. The demand for these fossil fuels has increased substantially over the recent years, and due to the fact that the oil reserves are non-renewable, the oil supplies are being depleted at a high rate without the possibility of them being replenished in the foreseeable future[18]. Another consequence of using fossil fuels is that when they are burnt they produce harmful gas emissions, which are widely thought to cause global warming. These emissions also pollute the air, and cause health problems for people in densely populated cities, as the air quality is greatly reduced causing pulmonary ailments.

Alternative fuels are fuels which are not derived from petroleum or crude oil [19]. Alternative fuels include: non-fossil natural gas, hydrogen, biofuels, and alcohols [19]. The interest in alternative fuels has increased over the past 20 years, with the aim of decreasing our reliance on fossil fuels as well as finding ways to reduce the harmful emissions produced by using fossil fuels. Alternative fuels such as hydrogen and DME can be used as they produce less harmful emissions which will be healthier for the environment. Alternative fuels can be derived or manufactured from natural renewable resources, making them attractive as they can then be produced in every country and the supply would then not be limited to the oil rich countries. The difficulties in using alternative fuels at the moment are infrastructural, technological and economic [20]. The infrastructure is not available, in terms of fuel delivery pumps for these fuels at all petrol stations, and the transport of these fuels from the manufacture plant to the fuel stations. Once a viable alternative fuel has been developed then the infrastructure required to support it can be steadily built to eventually replace fossil fuels. Economically, the cost of manufacturing alternative fuels is a factor. DME for example is expensive to produce but on a mass scale it can be produced at a lower price.

## 2.2 Dimethyl Ether

Dimethyl ether (DME) is a combustible gas which can easily be liquefied. DME is a colourless gas and has seen a growing interest in its use in the automotive industry as well as other areas such as power generation, heating and cooking [21]. It is a non-toxic gas and is environmentally friendly and does not pose any health issues [22]. The chemical structure of DME is shown in Figure 2.9 ($CH_3$-O-$CH_3$).

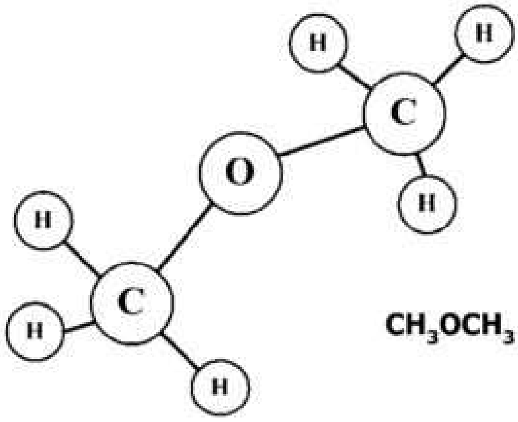


Figure 2.9: Dimethyl Ether Chemical Structure [22]

Dimethyl ether is considered as an alternative fuel for compression ignition engines due to the fact that it has a higher cetane number than diesel, which means it will combust easily in a compression ignition engine under the same conditions. It offers a similar thermal efficiency to a diesel fueled engine[3],[23]. The C-O bond energy in the DME is weak and this allows (initiates) a chain reaction to occur at lower temperatures which results in the physical delay being shorter than with conventional fuels[24]. DME is an oxygenated fuel, consisting of 35% oxygen by weight as seen in Table 2.1, and the chemical structure is free of carbon-carbon bonds which aids in the reduction in the amount of soot and particulate matter produced, as well as smokeless combustion ([3], [23], [24]). The oxygen component and the volatility of the DME fuel results in lower hydrocarbon and carbon monoxide emissions when compared to diesel [24]. The $NO_x$ emissions produced by a DME fuelled engine are higher than those produced by diesel fuelled engines at the same engine load, although these can be reduced by implementing Exhaust Gas Recirculation (EGR)[24].

The low boiling point of DME allows the fuel to evaporate more easily when injected into the engine cylinder in the liquid phase [22]. The injection pressure in a common rail system is high and this will aid in the vaporization of DME in the engine cylinder.

Table 2.1: Properties of Dimethyl Ether[22]

| Property (unit/condition) | Unit | DME | Diesel fuel |
|---|---|---|---|
| Chemical structure | | $CH_3$–O–$CH_3$ | – |
| Molar mass | g/mol | 46 | 170 |
| Carbon content | mass% | 52.2 | 86 |
| Hydrogen content | mass% | 13 | 14 |
| Oxygen content | mass% | 34.8 | 0 |
| Carbon-to-hydrogen ratio | | 0.337 | 0.516 |
| Critical temperature | K | 400 | 708 |
| Critical pressure | MPa | 5.37 | 3.00[a] |
| Critical density | $kg/m^3$ | 259 | – |
| Liquid density | $kg/m^3$ | 667 | 831 |
| Relative gas density (air = 1) | | 1.59 | – |
| Cetane number | | >55 | 40–50 |
| Auto-ignition temperature | K | 508 | 523 |
| Stoichiometric air/fuel mass ratio | | 9.0 | 14.6 |
| Boiling point at 1 atm | K | 248.1 | 450–643 |
| Enthalpy of vapourization | kJ/kg | 467.13 | 300 |
| Lower heating value | MJ/kg | 27.6 | 42.5 |
| Gaseous specific heat capacity | kJ/kg K | 2.99 | 1.7 |
| Ignition limits | vol% in air | 3.4/18.6 | 0.6/6.5 |
| Modulus of elasticity | $N/m^2$ | 6.37E+08 | 14.86E+08 |
| Kinematic viscosity of liquid | cSt | <.1 | 3 |
| Surface tension (at 298 K) | N/m | 0.012 | 0.027 |
| Vapour pressure (at 298 K) | kPa | 530 | ≪10 |

[a] Estimated on the basis of the equivalent chemical formula.

There are a number of advantages that DME has, but it is also necessary to consider the disadvantages in order to be able to evaluate the suitability of DME as an alternative fuel in its entirety. DME is a gas under atmospheric temperature and pressure. This makes it difficult to use in a common rail system as the high pressure pumping system and the fuel injectors require the fuel to be in the liquid phase, as the pump and fuel injectors are designed to operate with liquid fuel. DME becomes a liquid with increasing pressure, and decreasing temperature. Lowering the temperature of DME lowers the pressure required to maintain it in liquid form, as shown in Table A.1 in Appendix A which shows some of the thermodynamic properties of DME which were developed by Teng et al [25]. The compressibility of DME is higher than that of diesel, and it increases as liquid DME approaches its critical point (the point where it will turn from a liquid into a gas)[25].

The lower heating value of DME is lower than that of diesel. This means that for the same amount of fuel, DME produces less power. Teng et al [26] found that approximately 42% more DME and a longer injection duration would be required in order to produce the same power as diesel. DME has a low viscosity and this affects system wear as the pump may seize if no additional lubrication is added. The low lubricity of the fuel affects the pump more so than the injector, although the injector may show some leakages.

### 2.2.1 DME Production Method

DME can be manufactured from natural gas, coal, paper mill waste and agricultural by-products amongst others [21]. The fact that DME can be produced from such a variety of sources, especially waste sources, makes it that much more attractive as an alternative fuel as it will be more environmentally friendly. DME is primarily used as an aerosol propellant as it is odourless in small quantities, colourless and a suitable replacement to CFC's as it is environmentally friendly [27]. DME can be manufactured either by the dehydration of methanol or from synthesis gas which is produced from the gasification of coal [21], [27].

## 2.3 Spray Characteristics

The fuel is introduced into the cylinder through an injector, the fuel flows through the injector and through one or more orifices at a higher pressure than the cylinder gas charge. The pressures at which injectors usually operate are between 200 to 1700 bars. The jet leaves the nozzle with a velocity greater than 100m/s and this jet becomes turbulent and spreads out, which allows the fuel to mix with the compressed air. The spray begins to break up and the liquid starts to form droplets which have different sizes. As the spray develops further away from the nozzle, more air gets into the spray and the spray expands in width and the velocity decreases. As the process of air mixing with the fuel proceeds the fuel droplets begin to evaporate[11]. The fuel spray structure is shown in Figure 2.10, where $\theta$ is the spray cone angle and the definition of spray penetration is shown in the figure. The break up length is the length away from the nozzle where the fluid column exiting the nozzle has disintegrated within the cylinder[11]. The spray penetration into the combustion chamber has an important effect on the air utilization and fuel-air mixing rates. Depending on the engine design, the desired penetration length differs. For example, in engines where the cylinder walls are hot and the air present has a high degree of swirl, it is desired for the fuel spray to impinge on the walls, whereas in a multi-spray diesel combustion system over penetration is undesired as the walls are cold and there is a low degree of swirl and this lowers the mixing rate and increases the level of un-burnt fuel that the engine emits[11]. At the same time under penetration in such an engine is also undesired, therefore careful consideration is required regarding the desired penetration length [11].

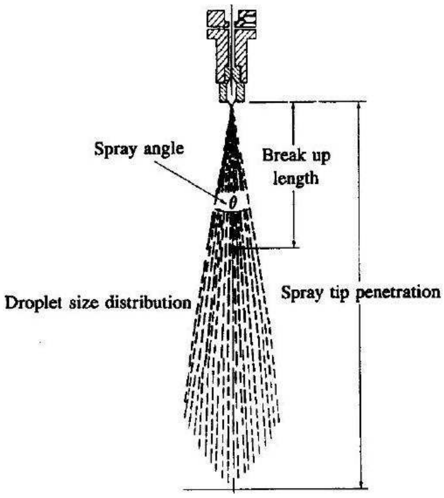


Figure 2.10: Schematic Representation of Fuel Spray Structure [11]

## 2.4 Atomization

For large fuel jet velocities, break up occurs, and the fuel jet spray diverges. At theses high velocities the fuel breaks up into droplets whose average diameters are smaller than the jet diameter, this is known as atomization[11]. The major element of the atomization mechanism is the aerodynamic interaction between the fuel and the air. The higher the jet velocity the larger the effect of the relative motion of the jet moving through the air, and this causes break up to occur. The distance from the nozzle in which break up occurs depends on the jet velocity, the higher the velocity the sooner breakup occurs[11]. The fuel jet usually forms a cone shaped spray at the end of the nozzle. The atomization of the fuel or the spray development of the fuel is affected by the fluid and gas density, and the fuel viscosity. The surface tension on the fluid droplets has a large effect on atomization[11].

The cone angle $\theta$ for jets in the atomization regime were found to follow the relationship shown in Equation 2.1 [11]:

$$tan\left(\frac{\theta}{2}\right) = \frac{1}{A}4\pi\left(\frac{\rho_g}{\rho_l}\right)^{0.5}\left(\frac{\sqrt{3}}{6}\right) \tag{2.1}$$

Where $\rho_l$ is the liquid density, $\rho_g$ is the gas density and A is a constant for a given nozzle geometry, usually taken as A=4.9.

Another formula for cone angle is given by Equation 2.2 [28][29]:

$$\theta = 0.05\left(\frac{d_o^2\rho_g\Delta p}{\mu^2}\right)^{0.25} \tag{2.2}$$

Where $\rho_g$ is the density of the compressed air charge in [kg/m$^3$], $\mu$ is the dynamic viscosity of air in [Pa.s], and $\Delta P$ is the effective pressure difference in [Pa]. Alternatively, Hiroyasu and Arai proposed a model for cone angles as shown below:

$$2\theta = 83.5 \left(\frac{l_0}{d_o}\right)^{-0.22} \left(\frac{d_o}{d_{sac}}\right)^{0.15} \left(\frac{\rho_g}{\rho_l}\right)^{0.26} \tag{2.3}$$

Where $d_o$ is the orifice diameter, $l_o$ is the length of the orifice, and $d_{sac}$ is the diameter of the sac and is very small for a VCO nozzle.

## 2.5 Theoretical Penetration Models

Various researchers have developed equations to predict the depth of penetration of a spray from an injector as a function of time. In the present work, equations proposed by four authors are considered. The approach used by each author is briefly summarized, and their relationships are then applied to the experimental conditions. The results are then compared with actual measured values.

Dent [30] proposed a model based on jet mixing where the penetration distance is predicted to be proportional to the square root of time. The model also takes into account the temperature and pressure of the gas in the combustion chamber. The equation proposed by Dent to predict the depth of penetration with time is given by Equation 2.4.

$$S = 3.07 \left(\frac{\Delta P}{\rho_g}\right)^{0.25} (td_o)^{0.5} \left(\frac{294}{T_g}\right)^{0.25} \tag{2.4}$$

Where $\Delta P$ is the pressure drop across the nozzle in [Pa], t is the time after the start of injection in [s], $d_o$ is the orifice diameter in [m], and $T_g$ is the gas temperature in [K]. This model does not take into account the properties of the fuel, this may provide an inaccurate prediction of the spray penetration.

Hiroyasu et al [31] considered the injection spray development to be made up of two stages separated by what has been defined as the jet break-up point. During the first stage the spray tip penetration is said to increase linearly with time. In the second stage, depth of penetration is proportional to the square root of time. Injection pressure has a greater effect on the initial motion of the jet, before break-up, whereas the density of the gas charge has more of an effect on the jet motion after jet break up [31]. The equations proposed by Hiroyasu et al to determine the depth of penetration for the two stages are as follows:

$$Pre-breakup(t < t_{break}) : S = 0.39 \left(\frac{2\Delta P}{\rho_l}\right)^{\frac{1}{2}} t \tag{2.5}$$

$$Post-breakup(t > t_{break}) : S = 2.95 \left(\frac{\Delta P}{\rho_g}\right)^{\frac{1}{4}} (d_o t)^{\frac{1}{2}} \tag{2.6}$$

where break-up time is given by Equation 2.7:

$$t_{break} = \frac{29\rho_l d_o}{(\rho_g \Delta P)^{\frac{1}{2}}} \tag{2.7}$$

$\Delta P$ is the pressure drop across the nozzle in [Pa]. This shows that the jet is faster before break-up and begins to lose momentum after break up.

Gosh and Hunt [32] consider the spray to have three zones: Zone 1, the velocity of the droplets are not affected by the velocity of the air stream as the droplets initial velocity is greater, Zone 2, the velocity of the droplets slows and is then similar to the velocity of the air, Zone 3, the velocity of the droplets decrease to a velocity less than their terminal velocity[33]. Sazhin et al [33] developed a model which is partly based on these three zones but the focus of the analysis was on the first and third zone. The effect on the droplet dynamics by the air is assumed as a small perturbation in the first zone, and two-phase flow is considered for the spray dynamics in the third zone [33].

This initial stage is where the jet is a stream of fluid before the actual spray atomizes. This flow can be described by one of three types of flow: Allen, Newton, and Stokes flow[33]. This stage is too short to be captured in the time intervals used in this study to make it significant. The second stage of spray development as proposed by Sazhin is described by the following relationship:

$$S = \frac{\sqrt{v_{in} d_o t}}{(1-\alpha_d)^{0.25} \tilde{\rho_g}^{0.25} \sqrt{tan\frac{\theta}{2}}} \times \left(1 - \frac{\sqrt{d_o}}{4\sqrt{v_{in}}(1-\alpha)^{0.25} \tilde{\rho_g}^{0.25} \sqrt{tan\frac{\theta}{2} t}}\right) \tag{2.8}$$

Where $v_{in}$ is initial droplet velocity in [m/s], $\alpha_d$ is the volume fraction of droplets in the spray, and $d_o$ is the orifice diameter in [m].

The bracketed term on the right hand side has a value very close to unity, due to the fact that after atomization has taken place, the volume fraction of droplets in the spray is considerably less than one. From the pressure drop across the nozzle, $v_{in}$ is given by Equation 2.9.

$$v_{in} = C_d \sqrt{\frac{2\Delta P}{\rho_l}} \tag{2.9}$$

By equating the right hand side term to one and substituting Equation 2.9 into Equation 2.8 a simplified equation for spray penetration is given by Equation 2.10.

$$S = 1.189 \left(\frac{1}{(1-\alpha_d)^{0.5}}\right)^{0.5} \left(\frac{C_d}{tan\frac{\theta}{2}}\right)^{0.5} \left(\frac{\Delta P}{\rho_g}\right)^{0.25} (d_o t)^{0.5} \tag{2.10}$$

The cone angle can be either predicted by available theoretical formulae or the measured cone angle can be used [34].

Wakuri et al [35] developed a spray penetration model based on momentum theory, where it is assumed that the relative velocity between the fuel droplets and the entrained air can be neglected. The momentum of the fuel spray induces the air into the fuel stream creating a mixture, and the surrounding air speeds up to the velocity of the fuel.

This model is given by Equation 2.11.

$$S = 1.189 C_d^{0.25} \left( \frac{\Delta P}{\rho_g} \right)^{0.25} \left( \frac{d_o t}{tan\frac{\theta}{2}} \right)^{0.5} \tag{2.11}$$

## 2.6 Previous Work

Testing of DME as an alternative fuel in terms of its spray characteristics as well as its emissions has been conducted in previous research by various authors. In order to proceed it is necessary to review the work done by others and compare what can be improved upon and what can be maintained.

Various authors have conducted research on various aspects of fuel injection analysis. In the current research the main focus is to compare dimethyl ether results to those of diesel fuel. Research done by authors purely on diesel testing will also be considered in this section in order to compare the results for diesel as well as to view the relationship obtained by other researchers between experimental and theoretical values. A number of relevant papers are summarised below:

### Dimethyl ether (DME) spray characteristics in a common-rail fuel injection system

Yu and Bae[3] investigated the spray characteristics of DME in a common-rail fuel injection system. The main focus of this work was on measuring the spray characteristics of DME and comparing them to those of diesel. The experimental facility used consisted of a constant volume test chamber with three optical ports in order to visualize the emanating spray. The chamber was pressurized with nitrogen gas. A normal common-rail system was used, the pressure in the accumulator was maintained by a back pressure regulator, the pressure in the rail was generated by an air-driven fuel pump. In order for the fuel to be compressed by the pump it is required to be in the liquid form, this was achieved by compressing the DME with nitrogen to 1.5MPa before it entered the fuel pump. Infineum R655 was used as a lubricity enhancer (500ppm) in order to prevent the injectors or the fuel pump from being damaged. A typical common-rail, sac-type injector with five holes of 0.168 mm diameter was used. A purpose built injector driver to fire the injectors was used and the authors found that the period in which the initial inrush current had to be applied, in order to trigger the injector and fully open the nozzle, should be $400\mu s$ to provide non-hesitant DME spray. Two types of images were recorded. Firstly macroscopic spray images were recorded using the Mie Scattering technique, and were captured by a charge couple device (CCD) camera using a strobe light system as the light source. Secondly, microscopic images were captured using an intensified charge coupled device camera and nano light illumination. The experimental parameters were 25, 40, and 55 MPa injection pressure with chamber pressures at atmospheric pressure and 3 MPa, all at $25^oC$ ambient temperature.

Cone angles for both diesel and DME were measured at $60d_o$, and the theoretical models used the instantaneous pressure difference ($\Delta P$) measured from the transient injection rate. The spray penetration results as well as the cone angle results for DME are shown in Figure 2.11, both are recorded at a chamber pressure of 3MPa. The authors found that the Dent model best predicted the spray penetration results. The effect of injection pressure on the cone angle of DME at higher chamber pressures was minimal.

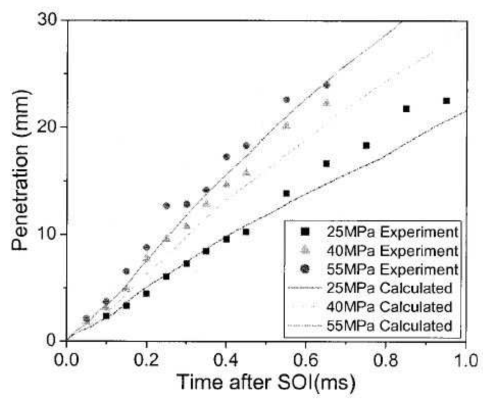


(a)

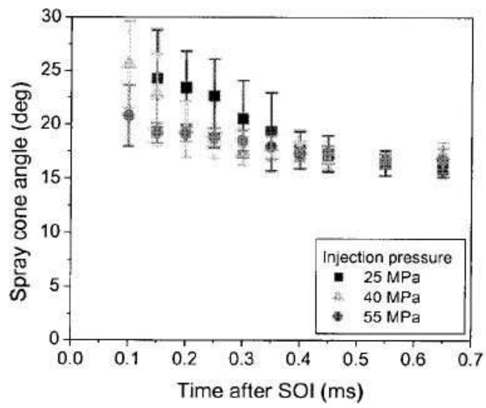


(b)

Figure 2.11: DME Results at a chamber pressure of 3MPa (a)Spray Penetration (b) Cone Angle[3]

Figure 2.12 shows the pressure history in the fuel line for both DME and diesel tests,where it was found that the DME pressure history for each injection showed a smaller amplitude as well as a longer oscillation period than that of diesel which was due to the compressibility of DME.

It was also found that as the chamber pressure increased, DME behaved similarly to

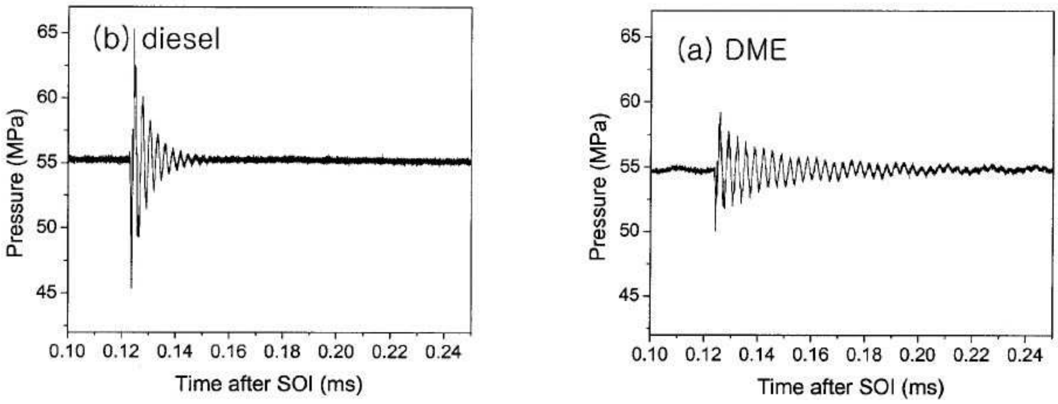


(a) (b)

Figure 2.12: Fuel Line Pressure History (a)DME fuel (b)Diesel fuel [3]

diesel. The DME spray edge and downstream portion of the spray shows DME in the vapour phase, which is good for combustion.

### Analysis of existing spray penetration models for dimethyl ether spray

Kim et al[34] investigated the use of existing spray penetration models to predict the penetration of DME sprays. The authors reviewed five models, namely: Wakuri et al[35], Hiroyasu et al[31], Dent[30], Sazhin et al[33], and the Schihl et al. Kim et al conducted spray tests in a high pressure chamber containing nitrogen like Yu et al[3],and used a common-rail injector together with a control unit in order to fire the injector. A surge tank replaced the common rail in order to maintain the DME at high pressure (up to 35MPa), and the fuel was pressurized by a compressed air driven pump. DME was pressurized by nitrogen to 1.6MPa in order to reduce the possibility of DME vaporizing in the fuel line. The spray angle and penetration were measured using a particle motion analysis system, which includes a spark light source and a CCD camera. The spray angle and penetration were measured by using the shadowgraphy technique and the edge of the spray was defined as 80% transmittance. The test parameters were: 0.6, 1, and 1.5MPa chamber pressure and 35MPa injection pressure. Orifice diameters of 0.2, 0.3, and 0.4mm were used to conduct tests. Figure 2.13 shows spray penetration results for an ambient pressure of 1.5MPa and two orifice diameters, namely, 0.2mm and 0.4mm. The depth of penetration was calculated using both the full (Equation (2.8)) and the simplified (Equation (2.10)) version of Sazhin et al's model and Kim et al [34] suggests that the simplified equation fits the results better. It was found that existing spray penetration models could be used to predict DME spray penetration, and recommended that, Wakuri et al as well as Sazhin et al's models be used for DME penetration prediction. These models require the spray cone angle in order to calculate

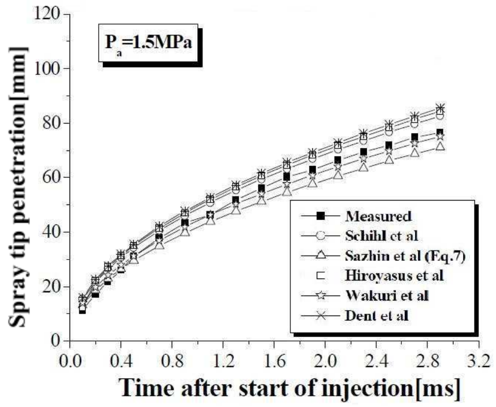


(a)

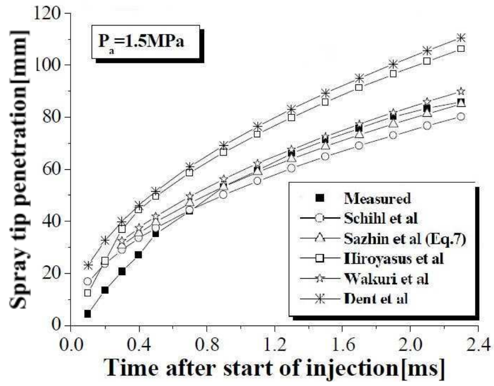


(b)

Figure 2.13: Spray Penetration results at 350 bar injection pressure for (a) 0.2mm diameter orifice (b) 0.4mm diameter orifice[34]

the predicted penetration and the authors suggested that measured cone angles at $30d_o$ for Wakuri et al's and $45d_o$ for Sazhin et al's model be used for the calculations.

**Macroscopic spray characteristics and breakup performance of dimethyl ether (DME) fuel at high fuel temperatures and ambient conditions**

Park et al[36] focused on DME fuel and analysed its macroscopic spray characteristics under high ambient conditions and fuel temperatures. Park et al obtained results through experiments and through a numerical simulation calculated using KIVA-3V code. Park et al varied the ambient gas temperature and pressure, as well as the fuel temperature in order to investigate the effects on the spray characteristics. A six-hole diesel injector was used (0.126mm diameter holes) and controlled by a TEMS, TDA-3200H injector driver. The spray visualization was achieved by using a Photron, Fastcam-APX Rs high speed camera with a 150W metal-halide lamp as a light source. The camera frame rate was set at 10,000fps. The DME was pressurized using nitrogen, it then passed through a parallel linked high pressure pump in order to provide the accumulator with pressurized DME. The injector and high speed camera were triggered in sync with one another by a digital delay/pulse generator. The testing parameters are given in Table 2.2. Some of the results obtained for spray penetration and for spray cone angle are shown in Figure 2.14.

The authors conclusions were: 1) DME has a shorter spray penetration and wider cone angle than diesel under atmospheric conditions, and under high ambient pressure the DME spray characteristics seem to be similar to those of diesel. The DME fuel temperature showed little impact on the spray characteristics. 2) An increase in ambient

Table 2.2: Park et al Experimental Conditions

| | |
|---|---|
| Test Fuels | DME, Diesel |
| Injection Pressure (MPa) | 60 |
| Ambient Pressure (MPa) | 0.1, 1.5, 3 |
| Injection Duration (ms) | 1 |
| Fuel Temperature (K) | 293, 330, and 370 |
| Ambient Temperature (K) | 293, 350, and 400 |

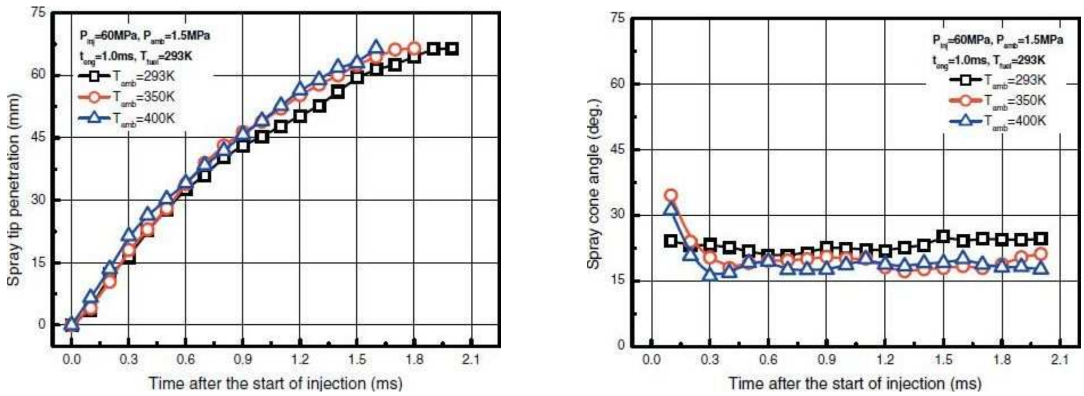


(a) (b)

Figure 2.14: DME Results at high ambient pressure and varying ambient temperatures (a)Spray Penetration (b)Cone Angle[36]

temperature increased the cone angle due to the flash boiling effect, although as the ambient pressure was increased the cone angle became narrower even at the higher temperature. 3) Atomization and evaporation occurred more actively with an increase in fuel and ambient temperatures.

**Study on the Dimethyl Ether Spray Characteristics According to the Diesel Blending Ratio and the Variations in the Ambient Pressure, Energizing Duration, and Fuel Temperature**

Park et al (2011)[37] conducted a study to investigate the effects of injection duration, chamber pressure, fuel temperature and diesel-DME blending ratio on the DME spray characteristics. A numerical simulation was also conducted in order to acquire spray results and these were compared with spray characteristic results obtained experimentally. The numerical results were calculated using KIVA computational fluid dynamics code. A standard common-rail system, consisting of a high pressure pump, the common-rail, and a solenoid injector with a hole-diameter of 0.3mm was used. The injections were triggered using a TEMS, TDA-3200H injector driver. A steam boiler was used to provide high temperature and pressure in order to raise the fuel temperature. A Photron Fastcam APX-RS high speed camera and a 150W metal-halide lamp light source were used to visualize the DME spray characteristics. The high speed camera frame rate was set at 10000 frames per second with a resolution of 256 x 603. Park et al used a digital delay/pulse generator in order to synchronise the high speed camera and the injection events. The experimental conditions are given in Table 2.3.

Table 2.3: Park et al Experimental Conditions

| | |
|---|---|
| Test Fuels | DME,DME5(DME5+Diesel95), DME15,and Diesel |
| Injection Pressure (MPa) | 70 |
| Ambient Pressure (MPa) | 1,and 3 |
| Injection Duration (ms) | 0.5, 1, and 1.5 |
| Fuel Temperature (K) | 290, 330, and 370 |
| Ambient Temperature (K) | 290 |

Spray tip penetration and cone angle results for DME are shown in Figure 2.15. The results for tip penetration seem to follow closely to one another for the three injection durations, which is what may be expected as the duration affects the total penetration length at the end of the injection. A short duration injection will have a shorter total penetration length than a long duration injection (depending on chamber conditions). The authors concluded that: 1) Compared to diesel, DME has a wider cone angle,

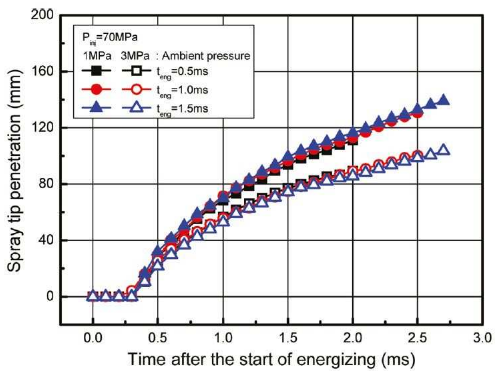


(a)

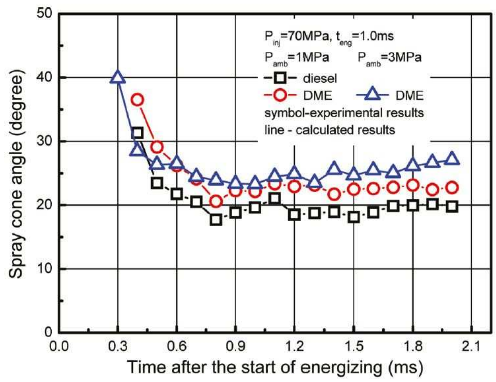


(b)

Figure 2.15: Experimental results for various ambient pressures (a)Spray Penetration for varying injection durations (b)Cone Angle[37]

the tip penetration proceeds slower, and has a small spray area. The higher chamber pressures impeded the sprays ability to penetrate the gas charge thereby weakening the ability of the ambient gas to entrain the spray. 2) The increase in injection duration increased the spay angles, penetration and spray area due to the fact that different quantities of fuel were being injected. These characteristics increased when DME fuel was blended with diesel, due to the fact that the blend has a higher density than neat DME. 3) Penetration and cone angle of DME spray decreased with an increase in fuel temperature, due to the evaporation of DME and the fact that the density of the fuel is now reduced at these higher temperatures.

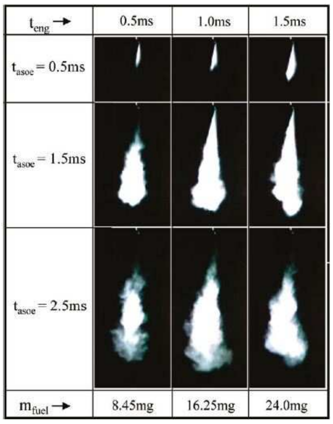


Figure 2.16: Effect of the energizing duration on the DME spray development process ($P_{inj}$ = 70 MPa and $P_{amb}$ = 1 MPa)[37]

**Experimental and analytical study on the spray characteristics of dimethyl ether (DME) and diesel fuels within a common-rail injection system in a diesel engine**

Suh and Lee (2008)[38] studied how the characteristics of dimethyl ether were affected by varying the injection parameters. It should be noted that again these results are compared to those of diesel. This is important as DME should provide more advantages in its spray characteristics, amongst other variables, than diesel if it is to be successful as an alternative fuel. The high pressure chamber was pressurized with nitrogen, to a maximum ambient pressure of 4MPa. The fuel was pressurized by means of two compressed air driven pumps, and the ambient temperature in the test chamber was controlled by means of a regulator. The DME was pressurized to 1MPa with nitrogen. An injector with a hole diameter of 0.3mm was utilized in order to conduct spray visualization tests. An ICCD camera, with a Nd:YAG laser as a light source, captured images of the spray. Microscopic spray characteristics or data were recorded by means of a PDPA droplet measuring system. Injection parameters are given in Table 2.4.

The spray tip penetration was defined as the maximum distance the spray reached from the nozzle tip, and a threshold level of 30 was selected in order to distinguish the spray from its surroundings in order to process the images. The authors also investigated the effect of injection pressure and duration on the injection rate. The

Table 2.4: Suh et al Experimental Conditions

| | |
|---|---|
| Test Fuels | DME,and Diesel |
| Injection Pressure (MPa) | 40, 50, 60 |
| Ambient Pressure (MPa) | 0.1, 1,and 2 |
| Injection Duration (ms) | 0.3-0.7 and 0.1ms intervals |
| Ambient Temperature (K) | 293, 393, 493 |

results are shown in Figure 2.17(a). The axial mean velocity of the spray is given in Figure 2.17(b). It was found that injection delay of DME was shorter than that of diesel and the peak injection rate of DME was smaller than that of diesel. The injection rate increased as the injection pressure increases and also peaked earlier. The

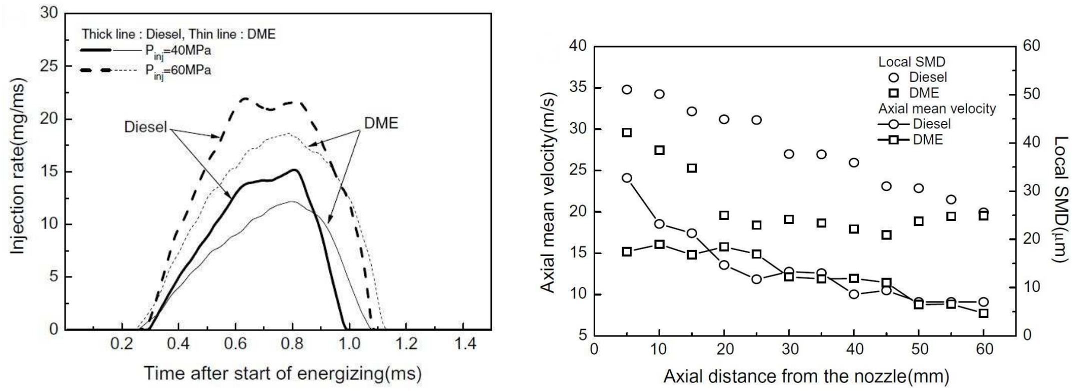


(a) (b)

Figure 2.17: Experimental results for (a) Injection Rate (b) Mean Axial Velocity[38]

results obtained for spray tip penetration are shown in Figure 2.18, where the effects of ambient pressure can be seen in Figure 2.18(a) and those of ambient temperature, in Figure 2.18(b). It was concluded that DME had a shorter and narrower spray than diesel at the equivalent injection conditions and that DME had a wider and slower spray at high ambient pressure. The diesel spray was found to be longer and wider at high ambient temperatures as DME showed a high evaporation rate. Suh et al found that the results for both experimental and predicted penetration seemed to follow closely, only being different in the initial stage of development. Diesel showed a higher velocity due to the fact that it has a larger momentum than DME because of its viscosity and density. DME was seen to have finer atomization characteristics when compared to diesel.

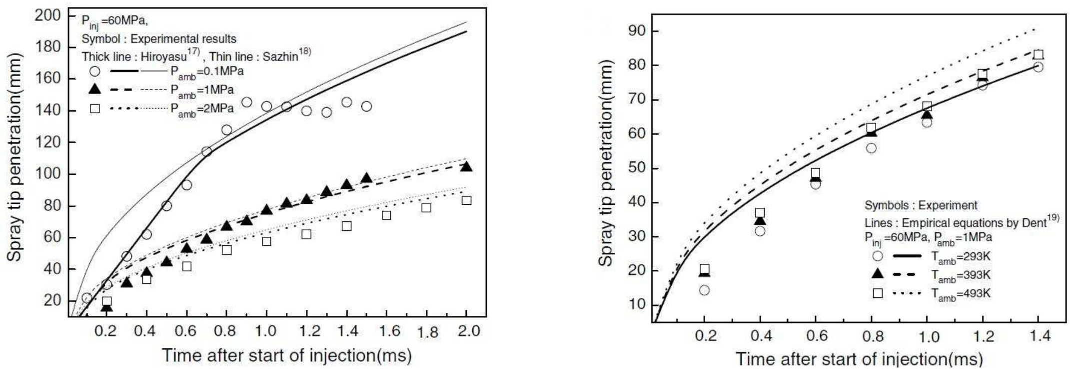


(a) (b)

Figure 2.18: Spray Penetration Results for (a)varying ambient pressure (b)varying ambient temperature[38]

**Time resolved measurements of the initial stages of fuel spray penetration**

The initial stages of spray penetration as determined experimentally (up to ≈0.5ms) are generally over predicted when compared to theoretical predictions. A study by Kostas et al(2009)[39] analysed spray penetration up to ≈0.5ms in greater detail and attempted to develop a correlation to predict the penetration for this initial stage. Kostas et al captured images of the initial stage of the spray penetration by means of an ultra-high speed camera. The frame rate of the camera was dependent on the chamber and injection pressures and the frame rates were set at: 500, 250, and 125 kfps, with an exposure of 1/8th of the frame rate. Kostas et al's experimental conditions are shown in Table 2.5. The authors found that the initial spray penetration was not

Table 2.5: Kostas et al Experimental Conditions

| | |
|---|---|
| Test Fuels | Diesel |
| Injection Pressure (MPa) | 50, 100 |
| Ambient Pressure (MPa) | 0.1, 1,and 5 |
| Injection Duration (ms) | 1 |
| Ambient Temperature ($^o$C) | 20+/-2 |
| Fuel Temperature ($^o$C) | 40+/-2 |
| Single hole injector (mm) | 0.2 |

linearly proportional to time but followed the relationship given by:

$$S(t) = At^{\frac{3}{2}} \tag{2.12}$$

A is a constant which is obtained from a least squares fit of the measured spray data [39]. It is suggested that this equation be used together with existing empirical models to predict spray penetration (Kostas et al). The equation is an empirical fit and is not based on any physical model but does comply with the initial conditions of S=0,U=0 at t=0, and fits the spray penetration for the initial stages of spray development.

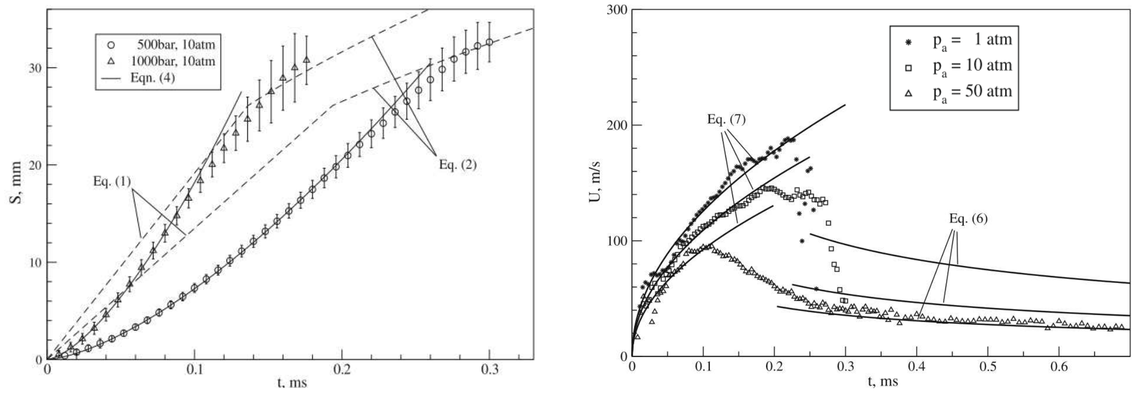


(a) (b)

Figure 2.19: Experimental and theoretical results for (a)initial spray penetration (b)Mean Axial Velocity[39]

In Figure 2.19(a) it can be seen that the experimental values follow the proposed equation quite closely for the initial stage of spray penetration (line denoted by eqn 4 in the image), the Eqn (2) lines represent Hiroyasu et al's model. Figure 2.19(b) shows how the differentiation of Equation 2.12 results in a curve for the tip velocity and how this line follows closely the experimental data. After the peak velocity, the conventional empirical model proposed by Hiroyasu et al predicts the spray velocity.

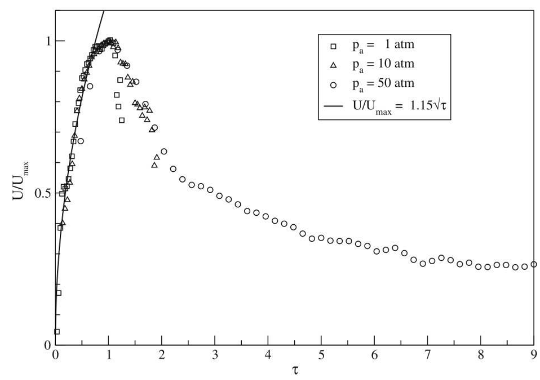


Figure 2.20: Spray tip velocity for $P_i = 1000$ bar. Plot is non-dimensionalised by Umax and tUmax[39]

Kostas' equation when scaled against maximum velocity and time, gives a good collapse of the data (the various tests, when non-dimensionalised fit the same curve) for the injections for each injection pressure as can be seen in Figure 2.20.

**Investigation on the fuel spray and emission reduction characteristics for dimethyl ether (DME) fuelled multi-cylinder diesel engine with common-rail injection system**

Youn et al[24] investigated the spray characteristics of DME as well as its emission reduction characteristics. Youn et al compares the DME spray characteristics with those of ultra low sulphur diesel. Tests for the spray visualization were performed with the parameters given in Table 2.6.

Table 2.6: Youn et al Experimental Conditions

| | |
|---|---|
| Test Fuels | ULSD, and DME |
| Injection Pressure (MPa) | 50 |
| Ambient Density (kg/$m^3$) | 11.5, 23, 34.5 |
| Injection Duration (ms) | 0.7 |

Figure 2.22 shows a comparison of spray images between diesel and DME at an injection pressure of 50MPa and various ambient densities at 0.9ms after the start of injection. It is clearly seen that the cone angles for the diesel and DME spray increase as the ambient density increases but the penetration decreases, furthermore the penetration of the DME is less than that of diesel at each density. Youn et al attribute these characteristics to factors such as injection pressure, ambient density and fuel properties, the lower fuel density of the DME means it has lower fluid momentum which explains why the diesel penetration progresses more rapidly than that of DME, and the rapid vaporisation of DME also contributes to this.

Figure 2.21(a) shows the relationship between diesel and DME spray penetration, while Figure 2.21(b) shows the change in cone angle for various ambient densities.

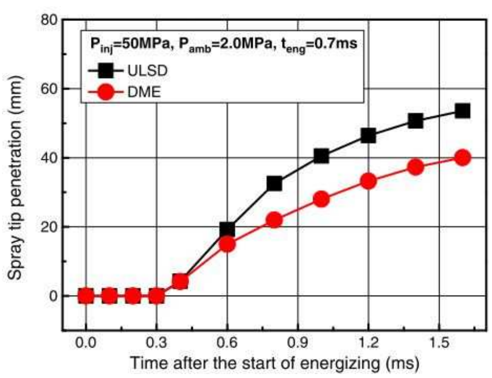


(a)

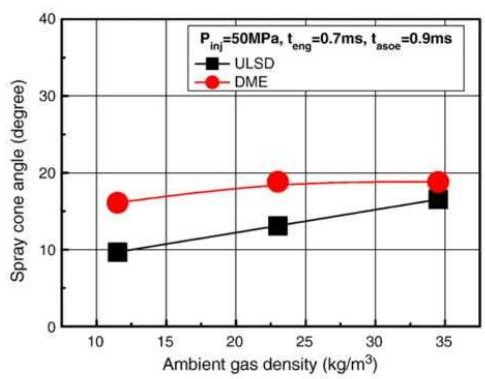


(b)

Figure 2.21: Experimental results for (a) Spray Penetration (b) Cone Angle[24]

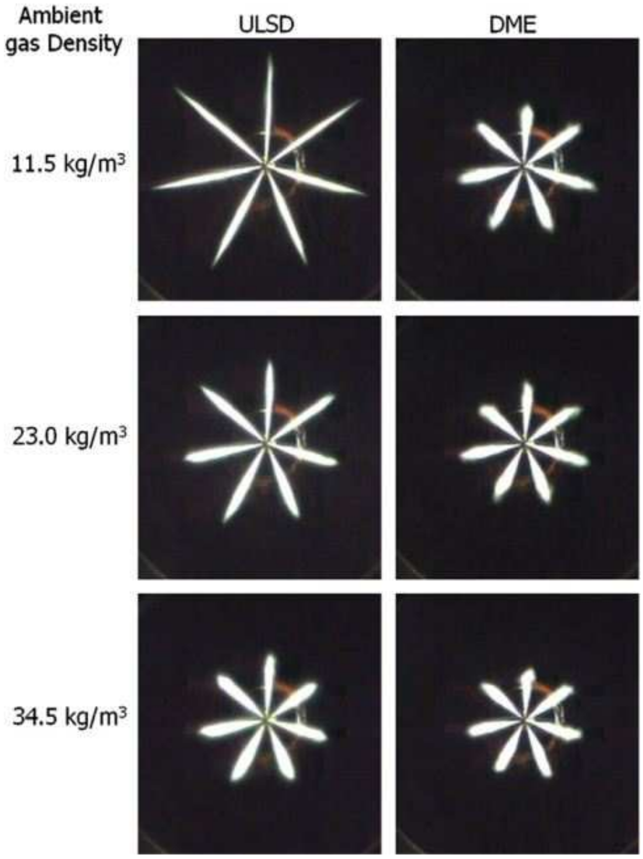


Figure 2.22: Youn et al Spray images for Diesel and DME at various ambient Densities[24]

In terms of the combustion characteristics Youn et al found that DME has a higher combustion pressure and a shorter ignition delay. The NOx emissions were found to be higher for DME at similar load conditions. But soot emissions, however, were found to be negligible due to the lack of carbon-carbon bonds.

# 3 Objectives

The main aims of this research are to conduct tests using dimethyl ether and diesel in a common rail system, and to investigate the potential of DME as an alternative fuel for a compression ignition engine in terms of spray characteristics. The objectives of the research are to:

- Develop an operating system in order to enable the researcher to easily conduct tests and record the necessary data, and compare the results.
- Investigate the effect of injection pressure on the spray penetration, spray cone angle and mean spray tip velocity.
- Investigate the effect of increasing chamber pressures (up to 25 bar) on the spray penetration, spray cone angle and mean spray tip velocity.
- Investigate the effect of chamber density compared to the effect of chamber pressure and determine which has the largest effect on spray characteristics.
- Investigate the behaviour of the fuel spray during the initial stages of penetration and attempt to develop a correlation to accurately predict this stage.
- Investigate the behaviour of DME within the accumulator rail, in terms of the pressure history, and test its suitability for a common rail system.
- Compare the experimentally obtained values for spray tip penetration, for diesel and DME, to established spray tip penetration models, in turn reviewing their ability to predict DME spray penetration.
- Analyse the results of the DME and its suitability as an alternative fuel.

# 4 Apparatus

A brief outline of the apparatus as it was found is given in Section 4.1, a risk analysis is conducted on the test rig in Section 4.2, and the modifications which were made to the test rig are outlined in Section 4.3.

## 4.1 Current State of Experimental Facility

The Test rig which is used to conduct DME and diesel tests can be split into three main sub-groups, namely: High Pressure chamber, Common Rail system, and High speed camera system

### 4.1.1 High Pressure Chamber

A cylindrical vessel is used as a constant volume chamber as shown in Figure 4.1. The chamber is fitted with a pressure gauge to monitor the ambient pressure within the chamber. The pressure within the chamber was regulated through a pressure regulator on the nitrogen cylinder supply. A ball valve was used to release the pressure from the chamber. The fuel injector is fastened in place at an angle such that the spray propagates through the centre of the viewing ports, in order to be able to view maximum possible penetration, as shown by the schematic in Figure 4.2. The pressure vessel is fitted with two diametrically opposite windows which are manufactured from NBK-7 Glass. The test chamber has a pressure limit of 2.5 MPa, which is the maximum pressure which the quartz glass is capable of withstanding without breaking. The test chamber contains an additional port perpendicular to the windows, to allow access into the chamber in order to clean the windows, and it is sealed by means of a 12mm steel plate.

Figure 4.1: Constant volume pressure chamber

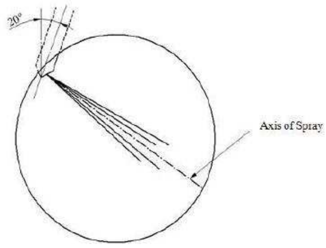


Figure 4.2: Schematic of injector spray positioning [40]

### 4.1.2 Common-Rail Injection System

The test rig utilizes a conventional common-rail system, shown in Figure 4.3, comprising of a five port rail (accumulator) which is fed by a high pressure fuel pump. An electronic injector is used and is supplied with high pressure fuel from the accumulator. The pump is driven by an AC three phase electric motor and the speed can be adjusted by varying the motor speed. The high pressure pump is rated at 1500bar. The injectors used in this project are Bosch six-hole injectors which are used in Mercedes Vito minibus. The inrush and holding currents for these injectors, as provided by TW Diesel, are 20 Amp inrush and 11.75 Amp holding current [41]. The Bosch injectors used were found to have a resistance of 0.5 ohms, this is what is known as a low resistance injector. The electronic injector is actuated using an analogue circuit developed by Mclean[41]. This circuit allows the operator to set the duration of the injection as well as the frequency of injections, the limits being 3.2ms - 6.4ms for the duration and 0.3Hz - 15.38Hz respectively. Five of the six holes were soldered closed so that a clear spray could be observed from one hole without the interference of spray from the other holes. The pressure within the common rail is regulated by a pressure regulator fitted at one end of the common rail. The pressure of the common rail is set by adjusting a potentiometer on a square wave generator, which changes the duty cycle of the square wave and thereby actuates the pressure regulator allowing pressure to build within the rail. The square wave actuates the pressure regulator in such a manner that more fuel will flow out of the overflow pipe if a low pressure is desired. The pressure within the rail is monitored by a pressure sensor built into the end of the rail, and is represented as a voltage on an LCD display. The pressure in the rail can then be determined by a lookup chart. The pressure history within the rail throughout testing is monitored and recorded by a piezoresistive pressure transducer fitted in the fuel line between the rail and the injector.


Figure 4.3: Common-Rail system driven by AC motor

A copper coil, shown in Figure 4.4, immersed in an ice bath is used to decrease the temperature of the DME, thereby maintaining it in liquid form. By lowering the DME temperature, the pressure required to maintain it in liquid form decreases and ensures the DME pressure is lower than the maximum inlet pressure of the common-rail pump.

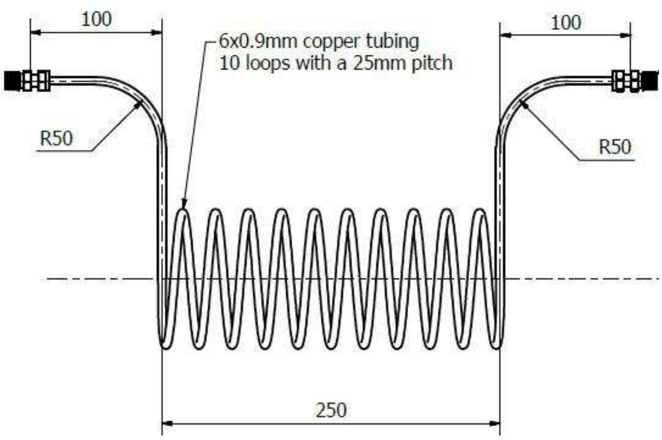


Figure 4.4: Copper cooling coil

### 4.1.3 High Speed Camera System

The imaging system used consists of a Photron Fastcam SA5 high speed camera, two parabolic mirrors, two condensing lenses, two knife edges, and a halogen globe for the light source. The imaging system layout can be seen in Figure 4.5. The mirrors, lenses and camera are arranged in a 'Z' formation which allows a parallel beam of light to pass through the test chamber. The high speed camera is triggered by a TTL signal,

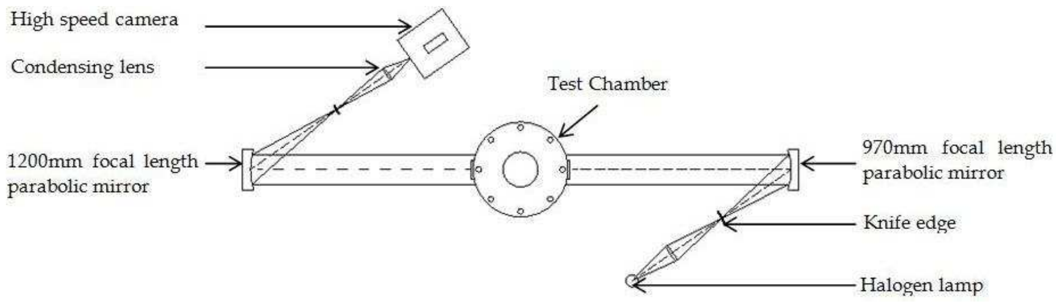


Figure 4.5: 'Z' Shape Schlieren Setup

generated by a programmable delay box. Previous researchers used this delay box to manually trigger the camera, and an attempt was made to incorporate a camera trigger circuit into the "'injector bot" design, this, however, was not implemented due to some difficulties before testing. The main issue was that the camera was not being triggered at the same time for each set of tests, thus a common reference point for all images allowing for a better analysis of the results, was not achieved.

## 4.2 Experimental Facility Risk Analysis

In this section the risks associated with operating the experimental facility were analysed. It was important to analyse the high risk areas and implement safeguards in order to reduce the risk of injury to the operator and the damage to the equipment. The two main areas of high risk were identified as the common rail system and the high pressure chamber. The risks associated and the safety measures which were implemented are detailed in the following subsections.

### 4.2.1 Common-Rail Injection System

The fuel pressure which is built up in common rail systems can exceed 1000bar, and therefore a large amount of energy is stored in the system. The pressure within the rail is not controlled by an ECU in this test rig, but by a purpose built circuit which generates a square wave to actuate the solenoid in the common rail. The controller has been limited to allow a maximum rail pressure of 700bar. One of the objectives of this project is to be able to set testing parameters through a software interface, the risk which may be brought about by doing this is that if the software crashes, the signals sent to the common rail solenoid cannot be predicted. Thus if the solenoid is held closed the pressure builds up within the rail and results in failure of the system. Depending on the location of the failure, this could result in injury. The pipes may burst and expose the researcher to high pressure fuel. It should be noted that the high pressure fuel will only maintain its pressure for one or two seconds, because once there is a void or a break in the high pressure system the pump will not produce the high pressure fuel. Therefore the danger would be as a result of the initial burst, either from the high velocity fuel or a piece of shrapnel from the equipment reaching the researcher.

In this research a high speed camera is used to capture images of the spray. If the common rail were to burst and continue to spray fuel into the room, there is a possibility it could come into contact with the camera, thus damaging the camera. In order to prevent the researcher from being injured or from any of the surrounding equipment being damaged, measures were put into place in order to reduce the likelihood of such an event. A pressure relief valve should be placed on the common rail in order to reduce the risk of a high pressure build-up. The pressure in the rail was measured by a common rail pressure sensor, which outputs a voltage signal which is proportional to the rail pressure. A voltage comparator was used to set a limit for the pressure within the common rail, if the limit were to be reached then power to the solenoid would be cut, thus reducing the rail pressure.

### 4.2.2 Pressure Chamber

The pressure chamber used to simulate the conditions found in an engine cylinder is the second area of concern regarding safety. The chamber consists of a thick steel chamber with two optical windows which are necessary to allow images of the spray to be captured, and one removable steel plate to allow the researcher to gain access into the chamber, and an injector which is mounted to the top section of the chamber. The scope of the project calls for the use of nitrogen to pressurize the chamber to a pressure of 25 bar to simulate density effects of air while eliminating the possibility of combustion.

The weakest points of the pressure vessel are the optical windows, as the steel plate is fastened with 8 machine screws and the thickness of the plate is greater than that of the glass. The glass poses the largest risk as, if one of the windows were to fail, they would cause catastrophic damage. The glass would shatter and due to the high energy within the chamber the glass fragments would be dispersed with high velocity. This would result in serious if not fatal injuries, and damage to the equipment. In order to prevent fatal injuries to the researcher in the case of the glass rupturing, shields were placed in between the researcher and the equipment. The shield would need to be clear in order to allow for the observation of the test rig as it is running, but thick enough to prevent any glass from penetrating it. A 10mm thick clear polycarbonate sheet was chosen and placed in a steel frame in order to serve as the shield. The shield would still allow the user to have limited access to certain parts of the rig, because in testing DME it may be difficult to run experiments without having safe access to the rig.

The pressure within the chamber was released from the bottom of the test chamber by a ball valve, introducing an obvious risk to the operator. An additional valve on the nitrogen bottle was introduced in order for the user to be able to relieve the pressure from the chamber while not being exposed to the risk of exploding glass. While the risk of the glass rupturing is low at lower pressures it does substantially increase as the pressure approaches 25bar. A three way valve is fitted at the outlet of the nitrogen bottle, allowing the operator to pressurise the test chamber from behind the safety shield and also allow the operator to vent the nitrogen from the pressure chamber into the ventilation system (in order to prevent asphyxiation). The three way valve is also in place so that if an accident were to occur, the operator could then rapidly cut the nitrogen supply to the chamber (this is important as the nitrogen supply will be open due to the minor leak in the test chamber).

Unfortunately it is not always possible to remain behind the screen while performing experiments and the operator may be required to get close to the test rig in order to bleed the system. It is important that the operator then wears a face shield and possibly a shield to protect the operator's body from any possible injury. The basic proposed layout of the test facility in order to incorporate the safety shield is shown in Figure 4.6. This layout allows the operator to safely conduct experiments from behind the protective shield while still being able to observe the test rig in case any problems may arise. All the controls to the test rig are placed behind the shield, therefore in an emergency everything can be switched off before entering the test area.

The stand on which the pressure chamber is seated was bolted to the ground and the pressure chamber was clamped to the stand. This was done so that in the event of the windows failing, the rapid expansion of the escaping nitrogen would not propel the test chamber across the room. The high speed camera is in the same vicinity as the test chamber and in order to protect it in the event that the glass fails, a thick perspex plate was clamped to the test chamber stand parallel to the optical path through the chamber.

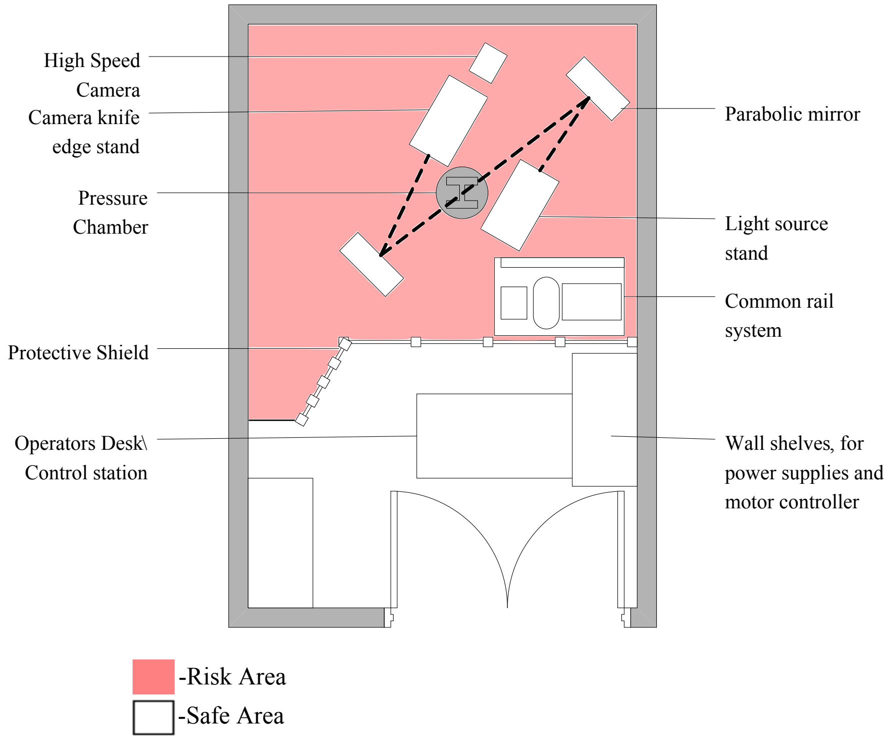


Figure 4.6: Test Facility Layout

## 4.3 Modifications to The Test Rig

### 4.3.1 DME Lubrication

DME has a low viscosity as mentioned in Section 2.2, as well as a low lubricity which causes problems with the high pressure pump. If not lubricated or run on diesel intermittently, it will seize. In order to reduce the possibility of the pump seizing and to reduce the time required to conduct DME experiments, the pump must receive lubrication. In order to do this, a method of lubricant delivery was designed.

The objective of this research is to analyse DME spray and it is important that any lubricant introduced into the DME, is small in quantity so as not to affect the DME properties.

DME is fed to the high pressure pump at a pressure of about 2 to 3 bar, the ideal place to introduce lubricant into the system is just before the high pressure pump so that any lubricant introduced will be mostly used by the pump (by lubricating the plungers of the pump). Since the fuel is at 2 bar it is necessary that the lubricant be at a slightly higher pressure than the DME, so that the lubricant will enter the fuel line. Another aspect is the metering of the lubricant and only a small amount would need to be introduced. To achieve this, a needle valve was used to allow small quantities of lubricant through when required. The solution developed to provide the high pressure pump with lubricant is shown in Figure 4.7.

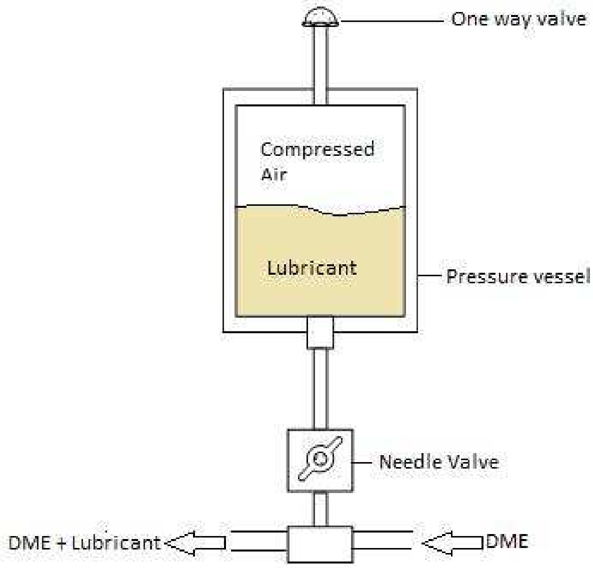


Figure 4.7: Schematic of DME lubrication system

The lubricant is held in a reservoir, which is pressurized using compressed air from the laboratory supply. The compressed air is introduced through a one way valve in order to prevent loss of pressure. There has to be sufficient oil in the reservoir to ensure that air is not pushed into the system. The needle valve is then used to regulate the lubricant supply and it is only opened slightly when the pump sounds like it is running dry (a grinding sound).

### 4.3.2 DME Cooling

The cooling coil used by previous students (as shown in section 4.1.2) was used to cool the DME before the inlet of the pump. The insulated container, in which the coil is placed, is filled with dry ice pellets which allow for a greater surface area in which heat can be transferred out of the DME. Initially a refrigeration system to cool the DME was considered, but the size of the system would be cumbersome. Dry ice was then considered, and since it has a temperature of -78.5 $^{o}C$ [42] it is cold enough to be able to substantially lower the temperature of DME, which has a freezing point of

-141$^oC$ [43] and therefore would not freeze when exposed to the dry ice. The lower the temperature of the DME, the less likely it is to vaporize in the fuel lines, thus the pressure needed to be supplied to the pump could be reduced.

### 4.3.3 Schlieren System

The Schlieren system was modified in order to allow for a higher frame rate. The 50W halogen lamp did not provide sufficient illumination at 10 000fps, the resulting images were dark and did not provide a reasonable contrast with the injection spray. Initially the idea of using a Xenon headlamp was considered as this would provide a large bright light source. This creates a high contrast between the injection spray and the background, which aids image processing. This idea was rejected on a cost basis.

A second option became available, which consisted of a high power LED light source, developed by a Masters student in the Flow research unit, Duncan Stevenson[44]. This light source simply required a DC voltage source of between 12 - 14V (as the appropriate circuitry had already been developed and can be found in Duncan Stevenson's masters report). This light source provided sufficient light at 12V for the images at 10 000fps. The fact that it could be set to be brighter at 14V was attractive, as a higher frame rate could be set to capture images of the initial spray characteristics. In which the spray penetration shows a different dependence on time to that predicted by the various penetration models. New parabolic mirrors were purchased with a focal length of 1200mm each, this ensured a better quality schlieren system and allowed clearer images to be captured.

## 4.4 Development of Test rig control software and hardware

One of the aims of this project was to develop hardware and software which would be able to control the common rail system. The controls would have to be simple and allow the user to run tests with relative ease compared to that experienced previously. The control of the test rig can be broken down into sub-systems which were developed: namely, Injector control circuit, Injector control software, Rail pressure control and software, and synchronization of tasks.

A National Instruments USB-6211 DAQ card is used to combine the physical tasks with the digital commands from the computer by the user. The USB-6211 DAQ card was used with code, which was developed in the Labview programming platform, to perform the required functions.

### 4.4.1 Injector Control Circuit

The injector circuit works on the same principle as that used by Mclean [41]. The current to the injector is switched on and off by a high power MosFet. In order to switch the mosfets at high speeds a mosfet driver was required. The switching of the mosfet is controlled by a National Instruments USB-6211 Data acquisition card, the specifications can be found on the National Instruments website. The DAQ was suitable for what was required by the Experiment Controller as it has high speed counters which are used to trigger the injector and the high speed camera. The mosfet switch is capable of a switching time of a few hundred nanoseconds. This has greater accuracy than is required to turn the injector on and off, as the mechanical response of the injector and the electrical response of the solenoid is in the order of microseconds. The schematic of the circuit is shown in Figure 4.8, the detailed development of the entire experiment controller can be found in Appendix B.

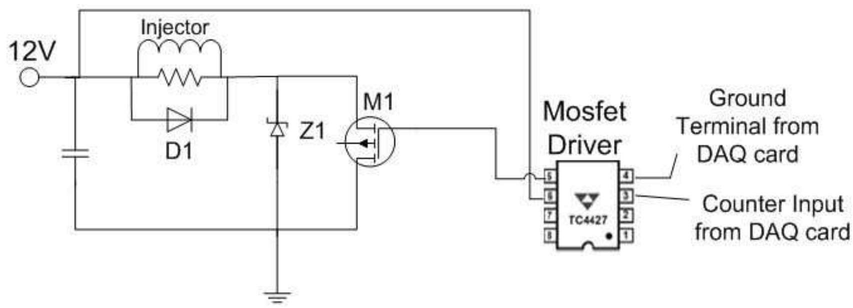


Figure 4.8: Injector Control Circuit Schematic

Power is supplied by a car battery, as it is able to provide the required amperage to actuate the solenoid in the injector within hundreds of microseconds. D1 is a diode placed across the injector in order to protect the mosfet from any voltage spikes created by the solenoid in the injector, and as an extra safeguard a Zener diode (Z1) is used to ground any reverse voltages produced by the solenoid when it suddenly closes. The injector parameters which will be controlled are: injection duration (in ms), injection spacing (in ms), and number of injections. The first two parameters have their limits. If injections are spaced too close together (in the order of hundreds of microseconds) the solenoid will burn out and similarly if the injection duration is made too long ($> 10$ms) then the solenoid will burn out, this may also damage the injector control circuitry.

### 4.4.2 Common-Rail Pressure Control

As mentioned in Section 4.1.2 the pressure in the common rail is regulated using a square wave, generated either by analog hardware or digitally through software(essentially pulse width modulation). Using the DAQ card, a square wave can be generated. The frequency and the duty cycle of the square wave is controlled through the user interface. By varying the duty cycle of the square wave the pressure in the common rail is changed. The frequency of the square wave is set at 1000Hz. The square wave essentially turns the pressure regulator solenoid on and off with a certain frequency, and in order to achieve this, a mosfet switch is used in conjunction with a mosfet driver. The circuit used to achieve this is identical to the circuit in Figure 4.8, the difference being that the injector solenoid is replaced by the pressure regulator and a 13V power supply. As mentioned in Section 4.2.1, a failure or crash of the software for any reason, can result in unpredictable behaviour of the common-rail solenoid (if the DAQ sends a constant 5V signal, the solenoid will close fully, resulting in the pressure rapidly increasing). A voltage comparator circuit is incorporated into the pressure control circuit design. The comparator compares the output voltage from the pressure transducer in the rail to a voltage set by the operator. If the voltage of the operator is equal to the transducer voltage then the power to the solenoid is cut, and the pressure would not be allowed to reach or surpass the maximum set pressure.

### 4.4.3 High Speed Camera

In order to achieve consistency between the spray images that will be obtained, it is essential that the user be able to trigger the camera remotely in conjunction with the triggering of the injector. This will allow the spray images to have a defined temporal evolution, and events can be related across separate data sets.

Since the time resolution with which the camera needs to be synchronised with the injection events is also in the range of microseconds, it seemed fitting that mosfet switches be used to allow a trigger signal to be sent to the camera. In order to protect the high speed camera from any possible erroneous inputs, the trigger signal is first sent to a delay box, and the delay generator then delivers a safe trigger signal to the camera. The time delay is set to the minimum ($50\mu s$) and the voltage to 2V. This voltage is the required input voltage, which is produced by the experiment controller, to trigger the delay box, in turn triggering the camera. The M1 mosfet is controlled by the same trigger signal which triggers the injection events as well as the pressure logger. The electrical circuit is shown in Figure 4.9. The second mosfet (M2) is used in order

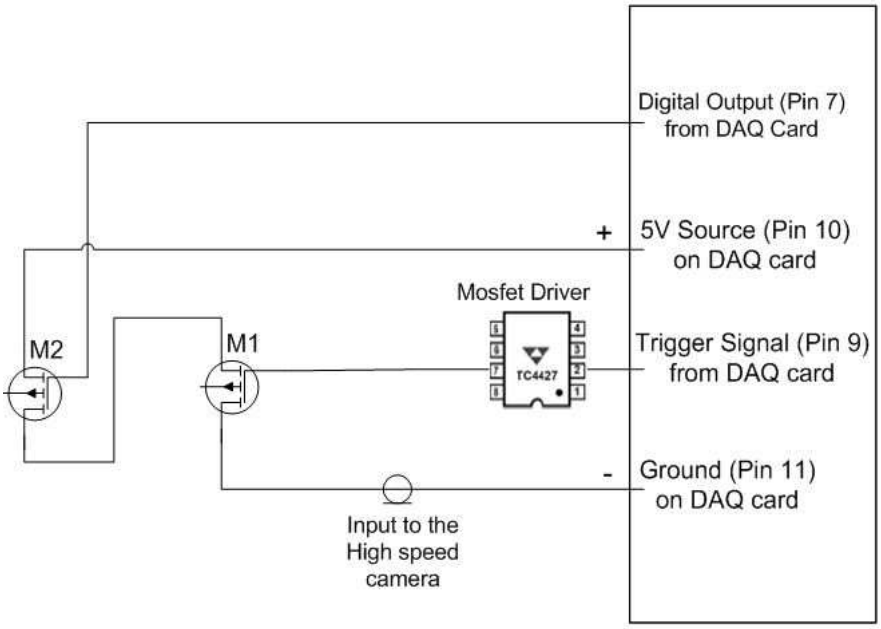


Figure 4.9: High Speed Camera Trigger Circuit Schematic

to allow the user the option to test the injector and data logging without triggering the camera. It creates a second break in the circuit, both switches need to be closed in order to trigger the camera. Mosfet M1 is the high speed switch, if the camera is to be triggered then M2 will already be closed and the high switching rate of M1 will trigger the camera. This ensures that everything is triggered simultaneously.

### 4.4.4 Fuel Pressure Data Logging

The pressure history in the fuel line is measured by an analog input on the DAQ card. The DAQ card is capable of 250KS/s (KiloSamples/second) sampling rate. For the purposes of this study the sampling rate is set at 100 kHz which will allow the user to capture the pressure history in great detail. The amount of samples to be recorded is dependent on the total injection event period.

### 4.4.5 Synchronization

As mentioned in Section 4.4.3, in order to have a consistent temporal account of the injection events, the signals triggering the camera, the injector, and the pressure data logger need to be synchronized. Using the DAQ card this is possible by setting one of the digital outputs (Pin 9) to high when it is required to trigger. The injector and the pressure logger are then set to start their events once this digital output is high (a feature of the hardware and software used), and this signal will then close the mosfet switch in the camera circuit and trigger the camera. In this way everything comes back to one output and, due to the accuracy of the DAQ card, the events will be consistently recorded.

Simply put, when the "trigger" button in the software is clicked, the output on the digital channel will go high and trigger all the peripheral components. Since the delay box introduces a small time delay, it is required to offset this delay by introducing a delay of the same magnitude for the injection event, as shown in Figure 4.10.

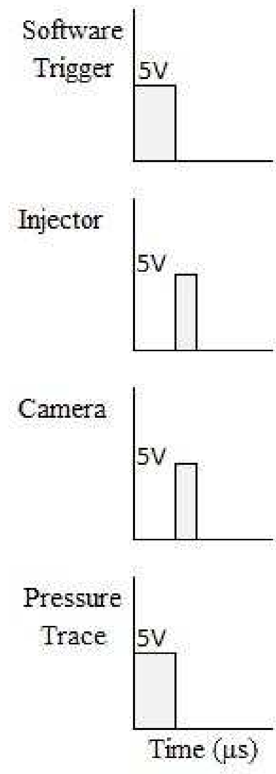


Figure 4.10: Signal Synchronization

Unfortunately due to limitations of the hardware a delay to the pressure trace logger could not be added, but if the delay is known it can easily be subtracted from the recorded data.

### 4.4.6 Experiment Controller Software

The user interface with which the operator can run experiments is shown in Figure 4.11. The respective functions which can be performed using the program are broken down as follows:

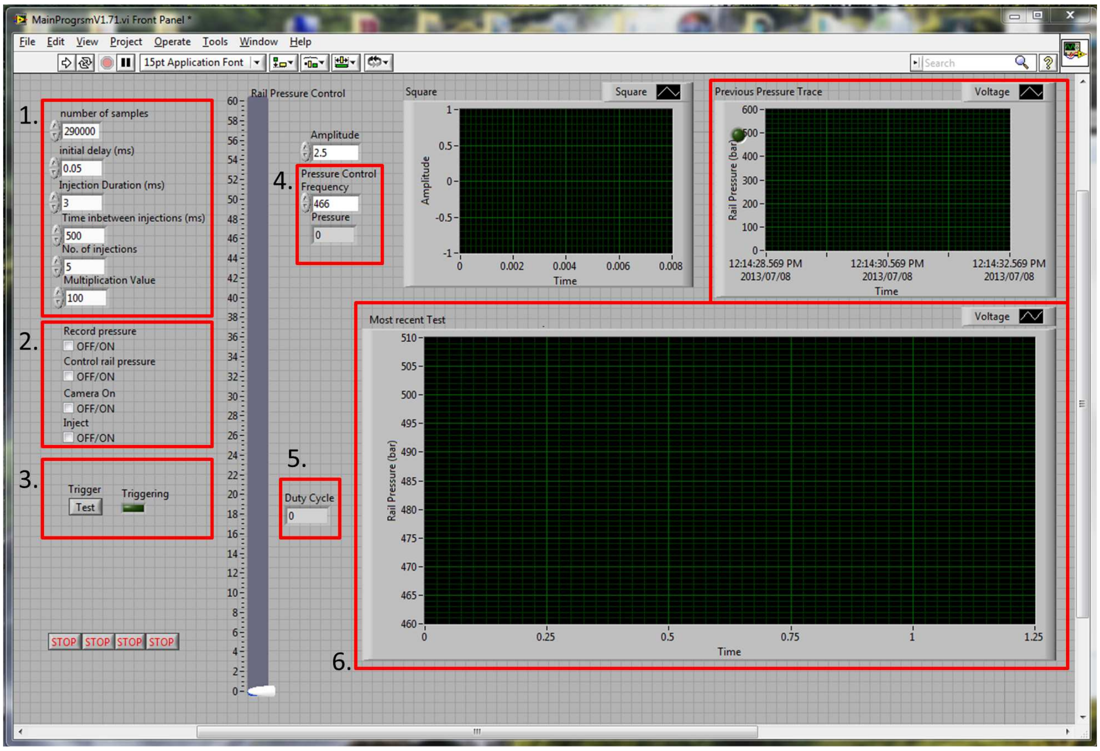


Figure 4.11: Experiment Controller User Interface

1. Injection Parameters - All the relevant injection parameters are set in these boxes such as: injection duration, injection spacing, number of injections, and delay box offset.

2. Function selection - These check boxes allow the user to record images and pressure traces together or they can be done separately if the function needs to be tested.

3. Trigger - This button is clicked once all the appropriate settings have been set and a test is to be conducted.

4. Common-rail pressure regulator frequency - The frequency of the square wave is set in this box.

5. Rail Pressure Adjust - The duty cycle is varied by adjusting the slider, which then in turn controls the rail pressure.

6. Pressure Trace Display - The graph will indicate the pressure trace of the test most recently conducted, after the pressure trace data is saved first, a separate graph also shows the pressure trace for the second last test conducted.

Figure 4.12 shows the connections the Experiment Controller required in order to control the test equipment. Table 4.1 gives the description for the components labeled in Figure 4.13. The specifications of the equipment used are given in Appendix H.

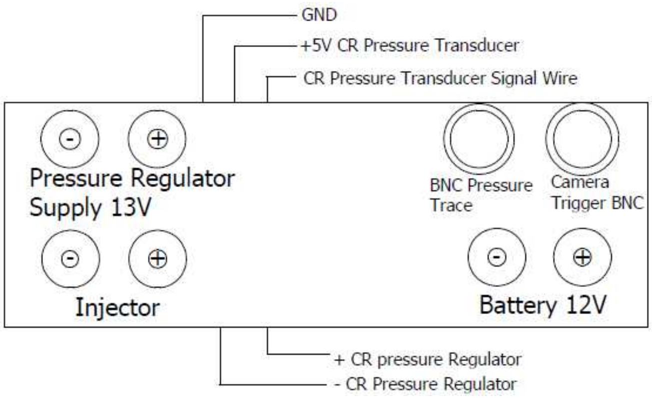


Figure 4.12: Experiment Controller Explanation

Table 4.1: Apparatus Schematic Key

| No. | Description | No. | Description |
|---|---|---|---|
| 1 | Photron SA5 High Speed Camera | 15 | Cooling coil in cooler box |
| 2 | Condensing lens | 16 | AC motor controller |
| 3 | Knife edge | 17 | DME bottle |
| 4 | Parabolic mirror (f=1200mm) | 18 | Nitrogen or $CO_2$ bottle |
| 5 | LED light source | 19 | Experiment controller |
| 6 | Dual DC power supply | 20 | High Pressure 3 way ball valve for ambient gas control |
| 7 | Low pressure pump switch board | 21 | Ambient pressure gauge |
| 8 | Low pressure diesel shuttle pump | 22 | Pressure chamber |
| 9 | Piezo pressure transducer | 23 | Injector |
| 10 | Kistler charge amplifier | 24 | Delay generator |
| 11 | Secondary overflow tank | 25 | AC motor |
| 12 | Radial high pressure pump | 26 | Bosch common rail pressure transducer |
| 13 | High pressure pump overflow | 27 | Bosch common rail (Accumulator) |
| 14 | Fuel 3 way valve | 28 | Bosch common rail pressure regulator |

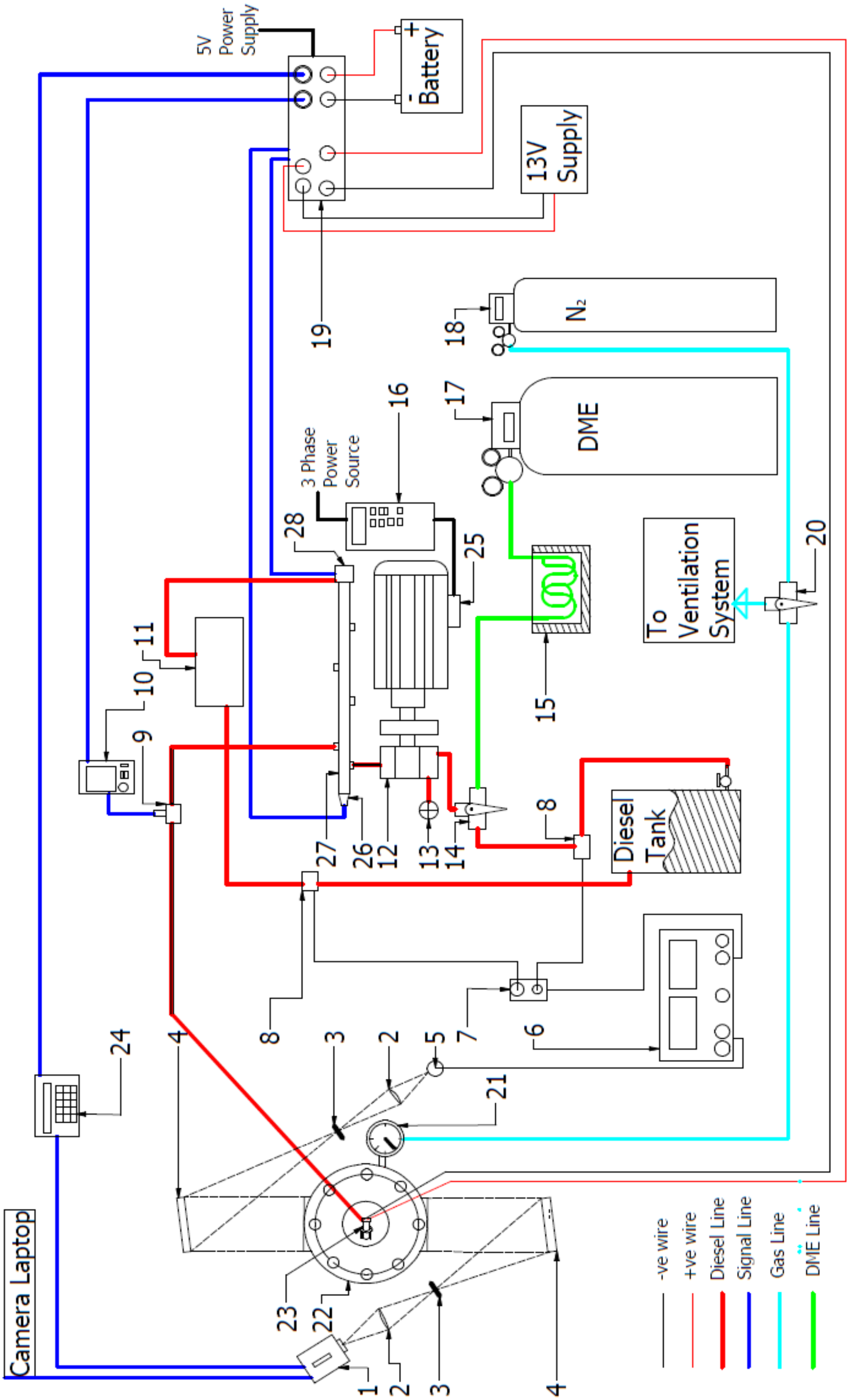


Figure 4.13: Apparatus Schematic

# 5 Methodology

The methodology followed to conduct the experiments required for this research is outlined in the following two subsections.

## 5.1 Experimental Planning

The main purpose of this study is to analyse the spray characteristics of DME and compare them to those of diesel. Parameters which are to be tested are fuel injection pressure, and chamber pressure. Tests are conducted with injection pressures starting at 200bar in 100bar increments to 600bar. The maximum injection pressure tested is 600 bar, as in previous research it was found that DME behaved erratically at higher pressures [3],[34]. Nitrogen is one of the gases used to pressurise the test chamber as it has similar properties to those of air, and it is an inert gas which will allow diesel and DME to be injected into a high ambient pressure without the risk of combustion. Tests will be conducted using nitrogen for ambient pressures, starting at atmospheric pressure and going up to 24 bar ambient pressure in 2 bar increments.

The limiting chamber pressure which can be tested is around 24 bar. In order to determine if ambient density has a greater effect than ambient pressure (implying that ambient pressure is only a means of achieving a high ambient density) on the spray characteristics, carbon dioxide gas is used as an ambient gas. Carbon dioxide has a higher molecular weight than nitrogen, so it is able to reproduce the same density conditions as nitrogen but at a lower pressure. It should be noted that tests will be conducted with diesel first, using both these gases. Once the tests have been completed, one of the objectives will be fulfilled (regarding diesel and the effect of ambient density on spray characteristics), but if the results show that there is no difference between the nitrogen tests and the carbon dioxide tests (at equivalent ambient density conditions) this will allow carbon dioxide to be used as an ambient gas. Using carbon dioxide as an ambient gas will allow the researcher to test up to an ambient pressure of 20 bar (which will be safer for the operator as it is reasonably under the limit) while simulating air (or nitrogen) pressures of around 30 bar due to $CO_2$'s higher molecular weight. If carbon dioxide can be used as an appropriate gas then the entire DME to diesel comparison will be conducted using $CO_2$ as it is much safer and will allow higher ambient densities to be tested than previously possible with nitrogen.

## 5.2 Procedure

The procedure which should be followed to perform the appropriate experiments is given below.

### 5.2.1 Start-up Procedure

1. Check that all the high pressure lines are connected properly and that the return lines are connected to the return drum as shown in Figure 4.13.
2. Connect the Kistler charge amplifier to the pressure sensor, and then connect the output of the amplifier to the pressure logger BNC port of the Experiment controller.
3. Turn on the Kistler charge amplifier and ensure that the range is set to either 1000bar or about 700 bar i.e. the output voltage will correspond to 100 bar/ Volt. The sensitivity should be set to -2.459 pC/bar.
4. Connect the camera trigger from the Experiment controller to the Time delay unit's input. Then connect the output of the time delay unit to the TTL trigger BNC cable on the high speed camera.
5. The time delay on the unit should be set to 50$\mu$s which is the lowest possible value (This has been (and can be) taken into account, for the injection trigger).
6. Ensure that the low pressure pumps, common rail regulator, schlieren LED light source, and the Experiment controller are connected correctly to the appropriate power sources as shown in Figure 4.13.
7. Connect the injector leads to the Experiment controller, making sure positive and negative are correctly matched.
8. Connect the thermocouple to the Fluke thermometer and ensure that the tip of the thermocouple is in the region of the injector tip.

9. The Experimental controller must be connected to the laptop loaded with the Experiment controller software via a USB cable. The software can then be run. The injection parameters are then set on this software (The laptop requires Labview to be loaded in order to run the software).

10. Connect the LAN cable from the high speed camera to the high speed camera's laptop.

11. The Photron Fastcam laptop must be turned on, the image capturing software should then be opened.

12. The frame rate should be set at 20000 frames per second.

13. Ensure there is enough diesel in the fuel tank and that there is sufficient DME in the DME bottle. The DME bottle has to be weighed in order to determine if there is still sufficient DME in the bottle as it will always maintain the same pressure.

14. Clean all the windows in the test chamber.

15. Ensure cover plate is tightened sufficiently (especially when testing at high chamber pressures).

16. Turn the three way valve on the nitrogen supply thereby changing the flow of nitrogen to the chamber.

### 5.2.2 Setting up the 'Z' shape Schlieren System

1. The optics should form a 'Z' shape; the mirrors need to be placed apart with the test section placed between the mirrors (the two parabolic mirrors should be at least two focal lengths apart, 2400mm).

2. The knife edge and lens stands need to be placed so that they form a 'Z' shape, and the angle between the stands and the mirror axis needs to be as small as is possible in order to reduce optical abberations or effects.

3. Once the light source stand and the camera side stand are in roughly the right positions, it is essential to ensure that the mirrors, the condensing lenses, and the light source's centres are all at the same height. This can be done crudely by filling up a length of clear tubing with water and placing one end near the centre of the chamber and the other at the centre of the lens, for instance. The other method which can be used to ensure the optics are at the same height is to use laser crosshairs, but when the laser is used it is important to ensure that the light source stand is level or the laser beam will not be of much use.

4. Switch on the LED power supply and slowly increase the voltage to 13V.
5. Place the first lens about 30mm (depending on the focal length of the lens) from the LED, and then attempt to find the focal point of the lens by moving it back and forth until a focused image of four squares of light is seen on a sheet of paper.
6. Place the first knife edge at the focal point of the lens.
7. Cut out the other three colours produced by the LED by using insulation tape and ensure that only white light is allowed to pass through the knife edge.
8. Place the stand so that the knife edge is on the focal point of the mirror (1200mm).
9. Ensure that the light passes through the test section by adjusting the angle of the mirror.
10. Place the second stand approximately 1150mm away from the second mirror.
11. Place the second knife edge at the second mirrors focal point (1200mm).
12. Place the second lens at its focal point from the second knife edge (approximately 300mm).
13. Place the camera behind the second lens, and remove knife edges. Then adjust camera position until a focused image is seen on the computer screen.
14. The amount of light can be adjusted by raising or lowering the LED voltage.
15. The sensitivity is raised or lowered by adjusting the gap between the second knife edges.
16. A grid on a transparent sheet should be placed on the windows and the image on the computer should show straight lines, if not, the angle between the mirrors and stands is not identical for both sides and steps 1-12 should be repeated until these angles are equal.
17. Place a threaded bold in the plane of the spray and repeat steps 1-14 in order to achieve a good image. If a piece of paper is moved from the test chamber towards the second parabolic mirror along the light path, the image should remain in focus and the same size the entire distance. If it does not then the position of the light source and the knife edge are incorrect, the knife edge is not at the first mirror's focal point.

### 5.2.3 Bleeding the Common-rail System

## Diesel

1. Loosen the high pressure fuel line from the injector and place the open end in a beaker.

2. Set the three-way valve to provide diesel to the high pressure pump (handle facing down).

3. Ensuring that the fuel tank is open, turn on the low pressure pump and allow the fuel to run until no air bubbles are seen in the fuel lines.

4. Ensure the pressure demand for the common rail is set to a minimum value (or zero pressure).

5. The high pressure pump should then be turned on for approximately 20 seconds and then turned off.

6. The high pressure line can then be connected to the injector and tightened.

7. Turn on the high pressure pump and the pressure in the rail should be increased gradually and the injector can then be fired in order to remove any air bubbles in the injector body.

## DME

1. Submerge the copper coil in the dry ice solution, and wait few minutes for the temperature to stabilise.

2. Loosen the high pressure fuel line from the injector and place the open end in a beaker.

3. Open the DME bottle, and then regulate the outlet pressure to 200-300kPa on the pressure regulator (on the coil side).

4. The three way valve must be set to allow DME flow to the HP pump.

5. Allow DME to flow into a beaker so all diesel in the system is removed.

6. Once diesel is purged from the system, place open end of high pressure line into a large bottle while holding onto the fuel line fastening nut, and observe until liquid DME emerges.

7. Once liquid DME is present in the fuel line, turn on the high pressure pump and observe the fuel stream emanating from the fuel line.

8. When the liquid emanating from the fuel line is continuous and no intermittent vapor is seen then quickly attach the fuel line to the injector and tighten the nut and a second person should stop the high pressure pump.

### 5.2.4 Running Experiment Controller Software

The user interface for the Experiment controller software is shown in Figure 5.1, and the process followed in order to conduct tests using this software is outlined as follows.

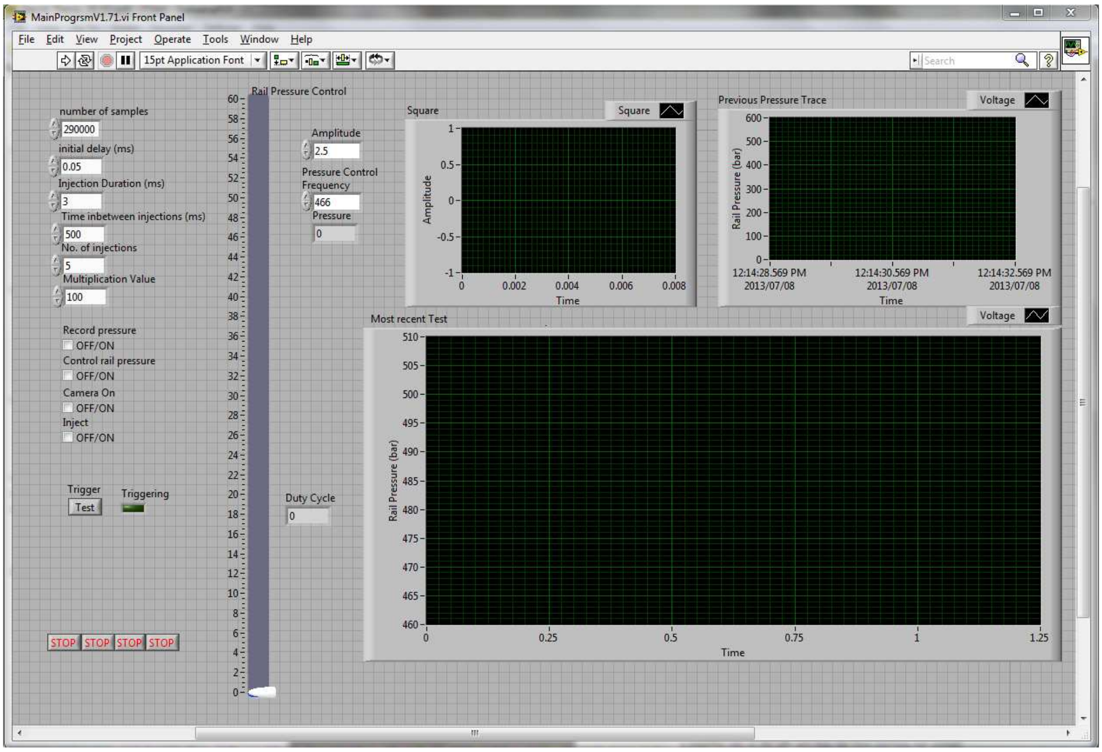


Figure 5.1: Experiment Controller User Interface

1. Set the number of samples to record for the pressure trace (taking into account a sampling rate of 100 kHz and then the total injection test period).

2. Set the initial delay on the injection events. (This takes into account the delay on the time delay unit).

3. Set the: Injection duration, intervals between successive injections, number of injections, and the multiplication value which is used to convert the charge amplifiers readings into bar (this value can be found on the charge amplifier display).
4. Once the AC motor is running, select the "Control rail pressure" box and then using the slider, adjust the pressure in the rail slowly until the desired pressure is seen on the Kistler charge meter.
5. Select the "Record Pressure Trace" Box and the "Arm camera" box, these can be selected independently depending if the user wants to solely record the pressure trace or only capture images.
6. Arm the time delay unit by pressing the "*" button, if images are to be captured.
7. Select the "Inject" box.
8. When ready to conduct the test click on the "Test" Button, and the test will run.
9. Save the pressure trace files as they are generated by the program.
10. After each test lower the rail pressure to zero, as the spray images take time to save and therefore reduce strain on the regulator.

### 5.2.5 Diesel Testing

1. Open the diesel tank.
2. Bleed the common rail system as outlined in section 5.2.3.
3. Zero the pressure transducer by pressing the "Meas" button on the charge amplifier.
4. Slowly pressurize the test chamber by increasing the pressure on the nitrogen cylinder pressure regulator until the desired chamber pressure is achieved.
5. Allow temperature in the chamber to reach room temperature.
6. Turn on the low pressure pump.
7. Set the AC motor to a frequency of 16 Hz and start the motor by pressing the forward button.
8. Follow the steps given in section 5.2.4.
9. Once the test has run, save the images on the high speed camera laptop.
10. Repeat steps 8 and 9 for the remaining injection pressures.

11. Repeat steps 3 to 10 for the tests conducted at the remaining chamber pressures, each time increasing the chamber pressure.
12. Close the nitrogen supply and slowly release the pressure inside the test chamber (by slowly turning the three way valve to close off the nitrogen supply and vent the chamber) before approaching the spray chamber.

### 5.2.6 DME Testing

It was decided that for the DME tests, the old rail pressure controller would be used as it allowed for faster control of the rail pressure. The DME tests are required to be run at a fast pace and for as short a period as possible and the manual rail pressure controller allows this to be achieved more easily.

1. Put on a face shield and proceed to bleed the system as mentioned above.
2. Ensure the camera is ready to record and accept a trigger signal.
3. Ensure steps 1, 2, 3, 5, 6, and 7 from section 5.2.4 are completed.
4. Slowly pressurise the test chamber, and allow 10 minutes to allow the temperature to reach steady state and to ensure that the windows are able to handle the required pressure.
5. Bleed the injection system as outlined in section 5.2.3 for DME and exit the test area as quick as possibly (limit the time spent in test area while chamber is pressurised).
6. Set the AC motor speed to 21Hz.
7. Run the AC motor by pressing the forward button on the motor controller.
8. Using the old manual pressure regulator control adjust the rail pressure to the desired pressure.
9. Click the " Test" button on the experiment control software.
10. Save the pressure trace file as it is generated.
11. Lower the rail pressure to zero and switch off the AC motor.
12. Repeat steps 1-3, and 6-11 for the different injection pressures.
13. Repeat steps 1-12 for the different chamber settings.

It is advised that a maximum of three consecutive tests should be conducted with DME (a single test being one rail pressure at one chamber pressure). The fuel injection system should then be run with diesel in order to lubricate the system. The lubrication system shown in Section 4.3.1 was not used as the DME tests conducted were quick and the system was turned off after each test. It is suggested that in future for longer tests that the lubrication system should be used. When running the diesel through the system the DME needs to be shut off to the pump on the three way valve, the fuel line to the injector should be disconnected and allow the DME to exit the fuel injection system. The system should then be bled with diesel and connected to a separate injector (a separate injector is used in order to mitigate the need to bleed the diesel from the injector when a DME test is to be run). The diesel can then be run for a couple of minutes to allow lubrication of the pump components. Thereafter the procedure outlined in section 5.2.6 can be followed.
When tests are conducted using carbon dioxide to pressurise the test chamber, the same procedures as outlined above can be followed with the exception being that carbon dioxide is used in place of nitrogen.

## 5.3 Precautions

Some of the precautions which should be taken in order to prevent injury and malfunction are listed in the following sections:

### 5.3.1 General Precautions

1. Once the chamber is pressurised, allow about 3 to 5 minutes for the temperature to reach steady state but most importantly to ensure that the windows are safe at that chamber pressure.
2. Minimise time spent in the chamber area while experiments are being run as high pressure exists in the system.
3. Ensure the injector is placed in such a way that the emanating spray is parallel to the windows.
4. Although obvious, ensure that the chamber is depressurized before attempting to open the access port to clean the windows, a lapse of concentration during the experiment can result in serious injury.
5. Check that the optics are set up appropriately as the images can be out of focus and have some aberrations.

6. Ensure that all the wires are connected properly as the Experiment controller will not work properly if any are not connected (camera trigger will not work if the 12V battery is not connected).
7. Do not bump the optics when working in the vicinity of the mirrors and lenses. It is important to set up the optics in a manner which reduces the possibility of bumping them.
8. Ensure that the common rail pressure is set to zero and the check box is unchecked before switching on the AC motor.
9. It is important to maintain a steady hand when adjusting the common rail pressure as large increments will cause a rapid pressurisation of the common rail.
10. Ensure that the pressure regulator on the nitrogen or $CO_2$ bottle is turned completely anticlockwise (0 bar) so as not to rapidly pressurise the test chamber when the bottle is opened, possibly cracking the windows.
11. The test chamber has a small leak and it is necessary to maintain the nitrogen supply open in order to compensate for this.
12. When venting the pressure chamber, ensure the extraction fans are turned on.
13. Ensure that the voltage supplied to the light source is consistent for all tests as this will later affect the processing program.

### 5.3.2 Diesel Testing

1. Ensure that the fuel being supplied to the common rail does not run out during the operation of the common rail system.

### 5.3.3 DME Testing

1. Ensure the coiling coil is adequately submerged in the dry ice.
2. Limit the DME pressure to the pump to about 300kPa maximum as the shaft seal will rupture.
3. When bleeding the system with DME ensure that thick leather gloves are worn when attempting to fasten the fuel line to the injector, as frost bite and cold burns can occur if exposed to the sub zero temperature of the DME spraying from the fuel line. Unfortunately there is no easier way of properly bleeding the system without following this procedure.

# 6 Data Processing

The data gathered during experimentation is in the form of high speed images and data files which contain the pressure history information.

## 6.1 Pressure Trace

The pressure traces are recorded by the Labview program where the files are saved in a .TDMS format (Labview format). This speeds up the saving process and the captured data can quickly be displayed in the experimental controller software. In order to process the pressure history graphs a MATLAB program was created to read the Labview data files and create usable graphs. The code used to perform this function is given in Appendix G.

## 6.2 High Speed Images - Measuring Spray Penetration and Cone Angle

The high speed camera images were processed using a Labview software package known as Vision Development Module. This software allowed the images to be manipulated and processed as required. The steps followed to process the images are represented in a flowchart in Figure 6.1. The background image is taken from the start of each injection event (when no spray is present in the view), and is created by the Labview program and contains certain details which the program uses to compare images to the background image (a standard gray scale image will not be suitable and results in an error in the program).The original image is then converted to gray scale, once this is done the background image is subtracted from the spray image, leaving behind only the spray. By subtracting the background, any fuel droplets on the window from previous tests are eliminated. This leaves only the spray mass, which is then rotated to the

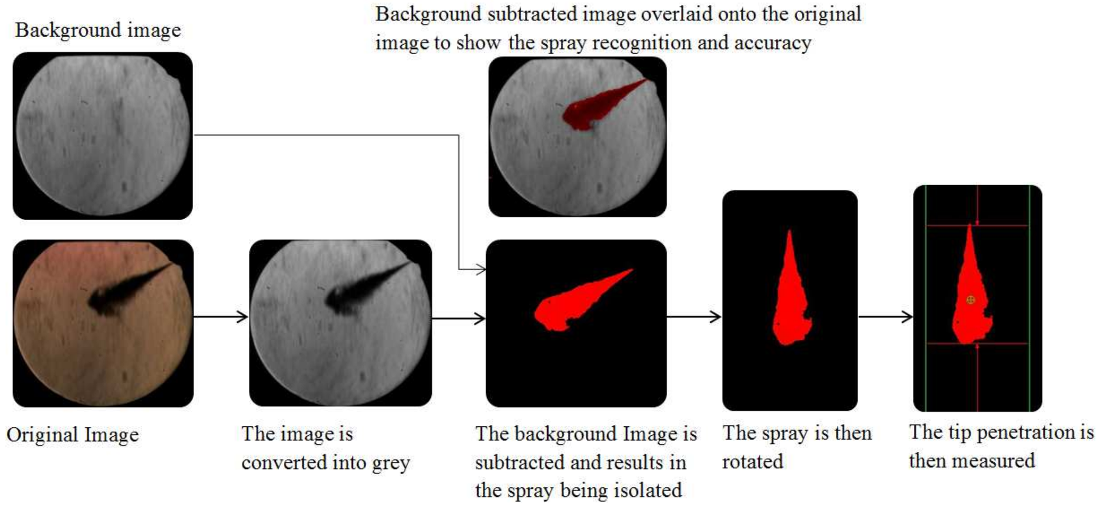


Figure 6.1: Spray Penetration Image Processing Flowchart

vertical position so that the software defines the two extreme points of the spray, which represents the penetration length. The image is originally calibrated before processing, by using the window diameter to relate pixel widths to mm.

The cone angle is extracted from the images using a slightly different method to the one used for spray penetration, as seen in Figure 6.2. The original image was rotated and converted to gray scale as above. A Labview function is then used to find the spray edges, thus allowing the angle between the lines to be measured. The image is cropped to only $60d_o$ from the injector tip (i.e. angle is only measured until $60d_o$)[3].

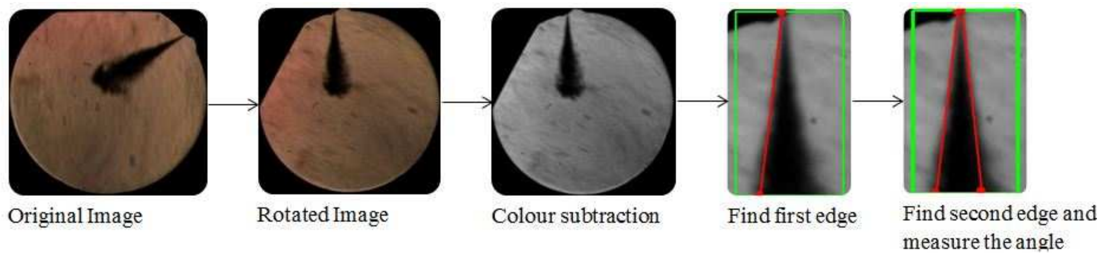


Figure 6.2: Cone Angle Image Processing Flowchart

## 6.3 Theoretical Models Sample Calculations

The experimental results are compared to theoretical predictions proposed by various authors. Equations developed by four authors namely Dent, Hiroyasu et al, Sazhin et al, and Wakuri et al are used to generate spray penetration curves. The difference between the predicted penetration and experimental penetration will be analysed for both Diesel and DME and the ability of the equations to predict penetration will be discussed. A sample calculation for each model is shown in this section.

Calculations are performed using the parameters from the data point given in Table 6.1.

Table 6.1: Sample Calculation Data

| | |
|---|---|
| Time after start of injection (ms) | 1 |
| Injection Pressure (MPa) | 50 |
| Ambient Pressure (MPa) | 1.77 |
| Injection Duration (ms) | 3 |
| Ambient Temperature (K) | 288 |
| Nozzle Diameter (mm) | 0.164 |
| Gas Density (kg/$m^3$) | 32.73 |
| Diesel Density (kg/$m^3$) | 832 |
| Diesel Cone Angle ($^o$) | 16.45 |

The first theoretical spray penetration model used is that proposed by Dent, given by Equation 2.4. Substituting the values into the expression yields:

$$S = 3.07 \left(\frac{\Delta P}{\rho_g}\right)^{0.25} (td_o)^{0.5} \left(\frac{294}{T_g}\right)^{0.25}$$

$$S = 3.07 \left(\frac{(500 - 17.77) \times 10^5}{32.73}\right)^{0.25} (0.001 \times 0.000164)^{0.5} \left(\frac{294}{288}\right)^{0.25}$$

$$S = 0.04354m = 43.54mm$$

The theoretical expression presented by Hiroyasu is more detailed and suggests that the spray penetration changes as the spray breaks up in the gas charge. The spray penetration is calculated using Equations 2.5, 2.6, and 2.7. The break up time is first calculated to see which equation should be used for this data point.

$$t_{break} = \frac{29\rho_f d_o}{(\rho_g \Delta P)^{\frac{1}{2}}}$$

$$t_{break} = \frac{29 \times 832 \times 0.000164}{(32.73 \times (500 - 17.77) \times 10^5)^{\frac{1}{2}}}$$

$$t_{break} = 0.0000996s = 99.6\mu s$$

The break up time is less than the time for the data point being used, therefore Equation 2.6 is used to calculate the penetration length.

$$S = 2.95\left(\frac{\Delta P}{\rho_g}\right)^{\frac{1}{4}}(d_o t)^{\frac{1}{2}}$$
$$S = 2.95\left(\frac{(500-17.77)\times 10^5}{32.73}\right)^{\frac{1}{4}}(0.000164\times 0.001)^{\frac{1}{2}}$$
$$S = 0.04163m = 41.63mm$$

The simplified form of Sazhin et al's equation is used to predict the penetration length (Equation 2.10). The $C_d$ value used for this equation is 0.8. The result is as follows:

$$S = 1.189\left(\frac{1}{(1-\alpha_d)^{0.5}}\right)^{0.5}\left(\frac{C_d}{tan\frac{\theta}{2}}\right)^{0.5}\left(\frac{\Delta P}{\rho_g}\right)^{0.25}(d_o t)^{0.5}$$
$$S = 1.189\left(\frac{1}{(1-10^{-4})^{0.5}}\right)^{0.5}\left(\frac{0.8}{tan\frac{16.45}{2}}\right)^{0.5}\left(\frac{(500-17.77)\times 10^5}{32.73}\right)^{0.25}(0.164\times 1\times 10^{-6})^{0.5}$$
$$S = 0.039475m = 39.48mm$$

Wakuri et al's equation is calculated as follows:

$$S = 1.189C_d^{0.25}\left(\frac{\Delta P}{\rho_g}\right)^{0.25}\left(\frac{d_o t}{tan\frac{\theta}{2}}\right)^{0.5}$$
$$S = 1.189\times 0.8^{0.25}\left(\frac{(500-17.77)\times 10^5}{32.73}\right)^{0.25}\left(\frac{0.000164\times 0.001}{tan\frac{16.45}{2}}\right)^{0.5}$$
$$S = 0.04173m = 41.73mm$$

The results of each penetration prediction are compared in Table 6.2.

Table 6.2: Sample Calculation Data

| Model | Penetration value (mm) |
|---|---|
| Experimental Penetration Value | 41.71 |
| Dent Model | 43.54 |
| Hiroyasu Model | 41.63 |
| Sazhin Model | 39.48 |
| Wakuri Model | 41.73 |

The Hiroyasu, Wakuri and Sazhin model predicted the penetration quite accurately whereas the Dent model over-predicted penetration by about 1.8mm(4.1%).

## 6.4 Uncertainty Analysis

The uncertainty in the measurement of the Spray Penetration and the Cone Angle is only a result of the program (the threshold setting). The image recognition software ensures that the spray penetration measurement process is as consistent as possible for all data sets. The threshold value was set at 37, as this was found to be the value which defined the spray accurately. Although it had to be set at about 43 for some images as the measurements were resulting in erroneous values. In order to verify that this slight change in threshold did not affect the results obtained, random data sets were chosen and the software was run with the threshold set at 30, 50 and 70. When plotting the data with three different threshold values, the curves were nearly identical with the maximum deviation being 2 mm, two examples can be seen in Figure 6.3. Figure 6.3 shows the results for the same injection, when measured using three different threshold values, the 30 and 50 thresholds do not show much deviation, the maximum in this case was less than 1mm, and the 70 threshold in this case did not deviate much but was the most inaccurate over all the samples processed. The deviations occur because when the threshold is higher, the perceived edge of the spray will be pushed back by a few pixels. Between a threshold of 30 and 50 it was noted that the deviation in penetration was minimal and any threshold set in this range would not produce results which are incorrect and have a large uncertainty. It should also be noted that when the images were being processed the perceived spray was overlaid onto the actual image and it was checked that the two agreed with one another.

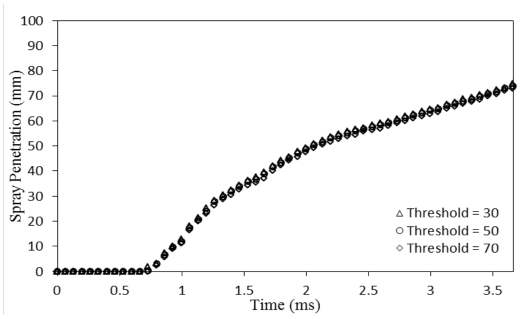


a)

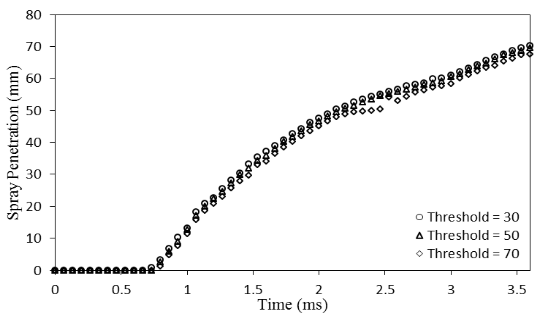


b)

Figure 6.3: Spray penetration processed using threshold values of 30, 50, and 70 at $P_{injection}$ = 400bar and a)$P_{chamber}$ = 22 bar , and b) $P_{chamber}$ = 22 bar

When considering the penetration prediction models, it can also be argued that some sort of uncertainty exists in these predicted values as the equations used consist of various measured parameters which in themselves have an uncertainty value. It is therefore reasonable to perform an uncertainty analysis on these equations and determine the sensitivity of the penetration calculated to any small variations in the measured parameters such as injection, ambient pressure and cone angle. The calculations can be seen in Appendix C and the values and uncertainties used for the calculations are given in Table 6.3. Some of the processed values are shown in Table 6.4. The values used in the uncertainty analysis are very conservative values in order to give an indication of the worst case scenario.

Table 6.3: Parameters used for uncertainty calculations

| Parameter | Value | Uncertainty |
|---|---|---|
| Pressure difference ΔP (bar) | 482.23 | 10 |
| Chamber Density (kg/m³) | 32.73 | 1.08 |
| Cone Angle (˚) | 16.45 | 2 |
| Discharge Coefficient Cd | 0.8 | 0.1 |
| Nozzle Diameter (m) | 0.000164 | - |

Table 6.4 shows the uncertainty values for the Dent, Sazhin et al, and Wakuri et al models in comparison to the measured value. The dent model had the lowest percentage uncertainty (1%) compared to 6.2% for Sazhin and Wakuri. The largest contributor to the uncertainty in the Sazhin and Wakuri models was found to be the cone angle. Dent does not include cone angle in his model, and the formulation using the remaining parameters does not result in a large uncertainty.

The experimental results in this case fell within the uncertainty range for Wakuri's model, and were just out of the uncertainty range for Dent's model (a considerably small range). The results are reasonably out of the uncertainty bounds for the Sazhin model.

Table 6.4: Diesel spray penetration uncertainty at $P_{Inj}$ = 500 bar and $P_{ambient}$ = 17.77 bar or $\rho_{ambient}$ = 32.73 kg/m$^3$.

| Time (ms) | Measured (mm) | Dent (mm) | Uncertainty Dent (mm) | % ΔS Dent | Sazhin (mm) | Uncertainty Sazhin (mm) | % ΔS Sazhin | Wakuri (mm) | Uncertainty Wakuri (mm) | % ΔS Wakuri |
|---|---|---|---|---|---|---|---|---|---|---|
| 0.3 | 20.26 | 23.8 | 0.243 | 1.02 | 21.62 | 1.337 | 6.18 | 22.8 | 1.413 | 6.20 |
| 0.8 | 36.59 | 38.9 | 0.393 | 1.01 | 35.3 | 2.183 | 6.18 | 37.32 | 2.3 | 6.16 |
| 1.3 | 48.12 | 49.6 | 0.504 | 1.02 | 45 | 2.78 | 6.18 | 47.6 | 2.9428 | 6.18 |
| 1.8 | 57.71 | 58.4 | 0.595 | 1.02 | 52.95 | 3.275 | 6.19 | 55.99 | 3.46 | 6.18 |
| 2.3 | 66.06 | 66 | 0.6736 | 1.02 | 59.86 | 3.7 | 6.18 | 63.29 | 3.91 | 6.18 |
| 2.8 | 72.63 | 72.9 | 0.7432 | 1.02 | 66.04 | 4.08 | 6.18 | 69.83 | 4.32 | 6.19 |

# 7 Results and Discussion

An investigation was conducted on fuel spray characteristics with the emphasis being on the comparison of the spray characteristics between DME and diesel. It was first necessary to understand the spray characteristics and how they form and react to different conditions. It is then possible to analyse the DME spray characteristics with a better understanding of the consequences of the specific spray characteristics. The general parameters which were used to conduct the tests are: Injection Pressures - 200 bar to 600 bar, Ambient Pressure - atmospheric pressure to 24 bar (Nitrogen) and atmospheric pressure to 17.7 bar ($CO_2$), Frame rate -15000 to 20000fps, and $22^{o}$C ambient temperature. The injection duration was set at 3ms and the time between injections was set at 200ms. Originally the nitrogen tests were conducted up to 24 bar. It was felt however that this may have been to close to the pressure limit which the window could withstand, it was therefore decided to limit the pressure to a maximum of 18 bar in order to allow for a large safety factor.

The quantity of data gathered during the study is substantial and only the most notable results will be discussed and presented in this section in order to allow for a comprehensive analysis of the topic being studied. The remaining results will be presented in Appendix D,E,F,G as a complete set, consisting of spray images, graphs of penetration, cone angle, mean velocity, and pressure trace.

The discussion will be separated into the following sub-sections:

1. Carbon dioxide and nitrogen comparison: Results will be analysed in order to determine the effect of ambient density on the spray characteristics and to determine if $CO_2$ is a suitable ambient gas to depict real engine pressures in a safe manner.

2. Cone angle.

3. Spray penetration.

(a) Initial injection penetration analysis.

4. Spray images
5. Mean axial velocity.
6. Fuel line pressure history.

In each sub-section, the results will be analysed for diesel, DME and the theoretical predictions by the various authors are compared, with the exception of the first sub-section ($CO_2$ testing validation). DME was not tested initially for the $CO_2$ validation as DME is inherently difficult to run. Therefore it was assumed that if the results were appropriate for the diesel tests then they would be suitable for DME tests.

## 7.1 Carbon Dioxide testing

Nitrogen has been used as the ambient gas, in the past, since its properties are similar to air (78% of air is nitrogen). The molecular mass of air is 28.96 kg/kmol and that of nitrogen is 28,013 kg/kmol and the dynamic viscosity of air is approximately 18.6x$10^{-6}$Pa.s, and that nitrogen is 17.997x$10^{-6}$ Pa.s. It can be seen that the properties of these two gases differ very slightly, and thus the effects of these differences can be considered to be negligible.

Carbon dioxide gas has a higher molecular mass (44kg/kmol), which means that a higher ambient density can be achieved at a lower pressure compared to nitrogen. For the same number of particles of nitrogen and carbon dioxide in a constant volume, $CO_2$ will have the higher mass per unit volume. It is for this reason that nitrogen needs to be at a higher pressure in order to achieve the same density as $CO_2$. The dynamic viscosity of $CO_2$ is 14.94x$10^{-6}$Pa.s which is 3.1x$10^{-6}$Pa.s less than nitrogen, the effect of this small change on the spray characteristics is not certain.

During testing, the ambient temperature will be held constant (or pressure will be adjusted in order to reach the equivalent density of nitrogen tests if temperature varies). The pressure at which the $CO_2$ gas will have to be set at, is calculated by equating the density which would be obtained at nitrogen pressures of 20, 22, and 24 bar. Then using the molecular mass of $CO_2$, the pressure is determined. Since the density of the two gases are set to be equal, the only two parameters which may influence the spray characteristics are the dynamic viscosity or the ambient pressure. Any differences or deviation from the nitrogen results would be due to these parameters. The results for both gases at equal densities should be identical given the assumption that density has a greater influence on spray characteristics than chamber pressure. The injection sprays are analysed in terms of spray penetration, images, cone angle, and the mean axial velocity.

### 7.1.1 Spray penetration

Analysing the spray penetration results in Figure 7.1, it can clearly be seen that the penetration for each respective injection pressure is nearly identical for $CO_2$ and $N_2$. Generally throughout the entire injection the results for both gases are very close, with the largest difference occurring in the initial few microseconds of the spray. The difference for the 600 bar injections is noticeable between 1ms and 1.5ms, representing a deviation of approximately 10%, thereafter the deviation between $CO_2$ and nitrogen was approximately 1.8%. The percentage deviation is greater in the initial period of injection due to the fact that the spray length is small during this period, so even though the actual deviation is less than 3mm the percentage deviation is large. The 500 bar injection has a slightly lower deviation than the 600 bar injection between 1ms and 1.5ms of approximately 5%, with a maximum deviation of 3.2mm. The same can be seen for the 400 bar injection, the largest difference lies in the initial few ms, the maximum deviation being 5mm.

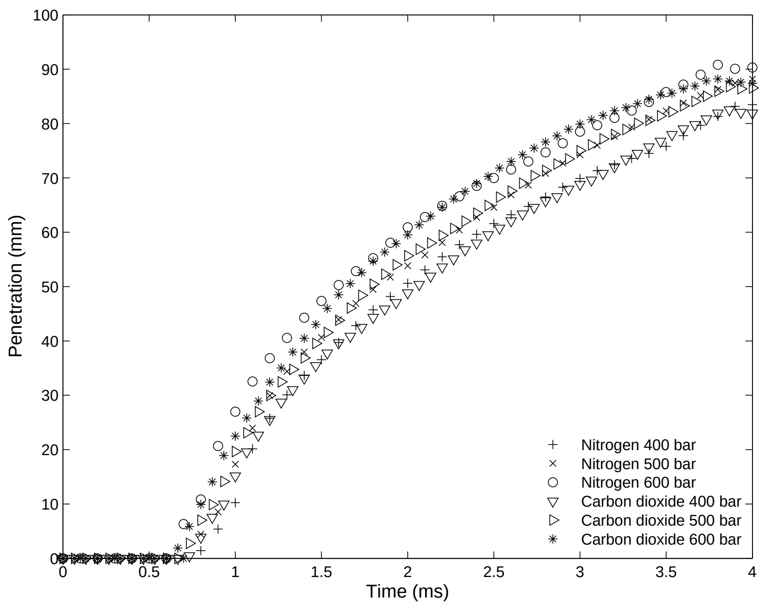


Figure 7.1: Spray penetration comparison between $CO_2$ (13 bar) and $N_2$ (20 bar) at $\rho_{ambient} = 22.955$ kg/m$^3$.

Figure 7.2 shows the results for the tests conducted at 14 bar for $CO_2$ and 22 bar for $N_2$ at 400, 500, and 600 bar injection pressures. The penetration results appear close to one another for the three injection pressures. The penetration for both ambient gases are similar throughout the injection. The maximum variation occurred during the 500 bar test where the penetration for $CO_2$ is 2-5% less than that in $N_2$ in the period between 1.5ms and 2.7ms. The 400 bar injection test for $CO_2$ follows the $N_2$ test more closely with an average deviation of about 3.5% after 2.1ms. The 600 bar test for $CO_2$ was essentially identical to the $N_2$ test, deviating on average by about 1.5%. Deviations are amplified in the first few hundred microseconds with variations of up to 15%. This seems large but the actual deviation is less than 2mm which can be accounted for in an uncertainty analysis.

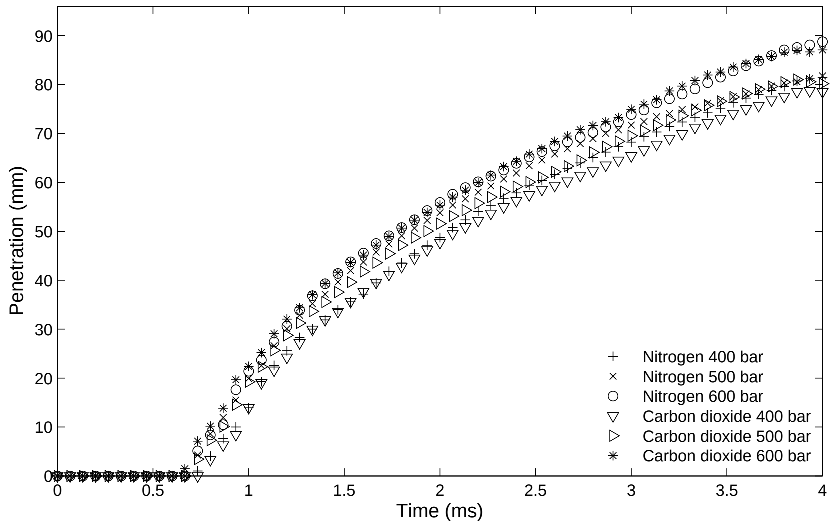


Figure 7.2: Spray penetration comparison between $CO_2$ (14 bar) and $N_2$ (22 bar) at $\rho_{ambient} = 25.5$ kg/m$^3$.

Figure 7.3 shows the injection results for $N_2$ and $CO_2$ at an equal ambient pressure of 18 bar with a resulting density for each gas as follows: $CO_2$ $\rho_{ambient} = 32.631$ kg/m$^3$ and $N_2$ $\rho_{ambient} = 20.872$ kg/m$^3$. It can clearly be seen that the penetration lengths, for the two gases at the same injection and ambient pressures, are different. The penetration lengths in $CO_2$ are consistently lower than those in $N_2$, for each injection pressure tested. The equivalent nitrogen pressure required to produce the ambient density of $CO_2$ at 18 bar would be 28.1 bar. Other tests were conducted at different ambient pressures and the results were all similar to those presented in this section.

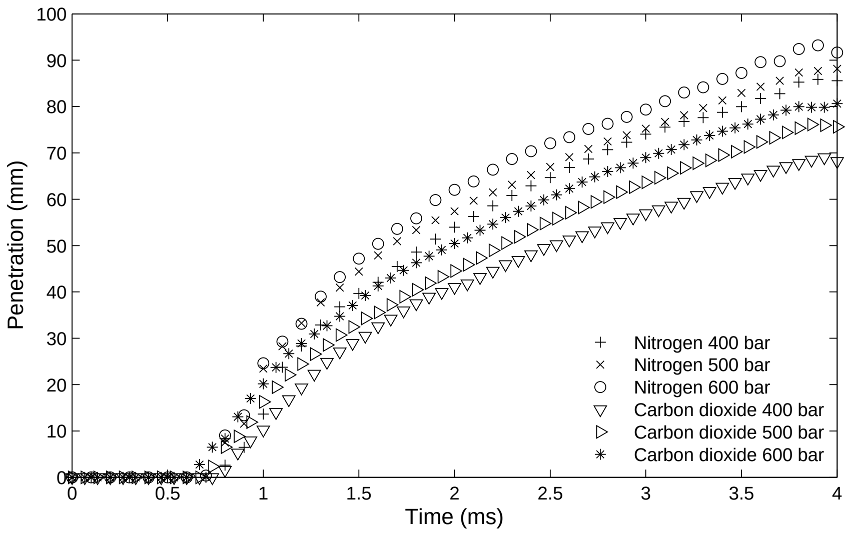


Figure 7.3: Spray penetration comparison for $CO_2$ ($\rho_{ambient}$ = 32.631 kg/m$^3$) and $N_2$ ($\rho_{ambient}$ = 20.872 kg/m$^3$) at an ambient pressure of 18 bar

### 7.1.2 Spray images

Analysing the spray images in Figure 7.4, in both gases the spray appears to be similar throughout the injection. The spray tip of the test in $CO_2$ is noted to be round throughout the injection, whereas the tip in the $N_2$ test has a small perturbation on the left side in the fifth frame. Subsequently the spray follows the same shape as the $CO_2$ test. The spray edges for the injections in $CO_2$ are slightly less well defined than $N_2$ injections. This could be due to the lower dynamic viscosity which will allow the fuel to move through the $CO_2$ slightly more easily(although not by much). The shape of the spray for both tests appears to be similar, and the manner in which the gas is entrained in the spray seems to occur in the same way for both tests. The cone angles of the spray appear to be identical in the region of 60d$_o$. The spray shape is unique to each test (even within the same ambient gas) as the vapourization may be slightly different in each test. Although the spray characteristics are largely the same for identical tests, there may be times where one spray will have a perturbation which the others do not.

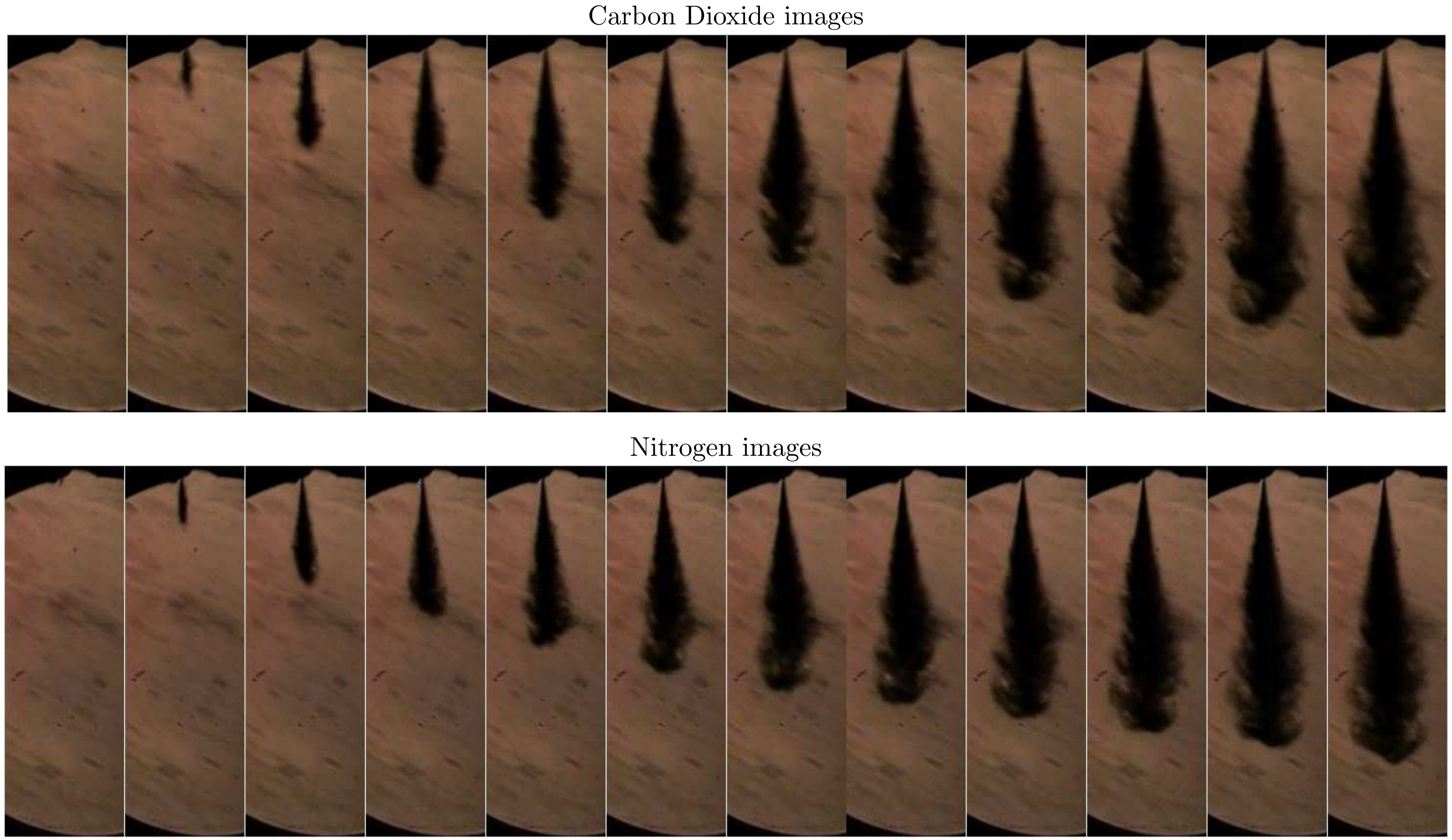


Figure 7.4: Comparison between 400 bar injections into equal density of nitrogen(22 bar ambient pressure) and CO2 (14 bar ambient)

### 7.1.3 Cone Angle

Figure 7.5 shows the comparison between the cone angle for diesel sprays in nitrogen and carbon dioxide at 500 bar injection pressure and equal density. The cone angle between 0.7 - 1 ms is extremely low but this is due to the image processing software not recognizing the cone angle properly. Once the spray has developed somewhat the imaging software measures the cone angle more accurately. The cone angles for the tests in the two ambient gases are very similar, they are within $2^o$ of each other at some of the points. Overall the cone angles are similar. The fluctuation in cone angle is as a result of the slight fluctuations of the measurement software as it sometimes over-measures the cone angle as well as the variation of the spray angle as the spray progresses. The software still gives a better overall measurement of the cone angle, than if it were to be measured by hand, as it measures consistently.

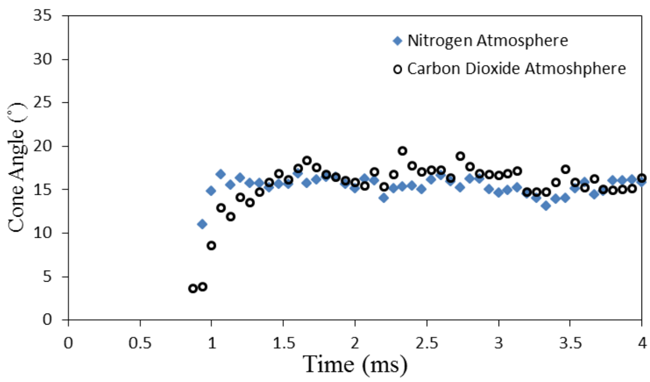


Figure 7.5: Cone Angle comparison for $CO_2$ ($P_{ambient}$ = 14 bar) and $N_2$ $P_{ambient}$ = 22 bar ($\rho_{ambient}$ = 25.5 kg/m$^3$)

### 7.1.4 Mean Spray Tip Velocity

Figure 7.6, shows the mean spray tip velocity for both gases at injection pressures of 400 and 600 bar. The velocity for both gases follows the same trend, with both reaching the same peaks with the tip velocity decreasing in the same manner.

### 7.1.5 Overall Conclusion

It is thus clear to see that there is a direct correlation between ambient density and numerous spray characteristics in the development of the spray. Delacourt et al [45] conducted diesel testing with carbon dioxide as the ambient gas and the results correlated well with predictions by the Hiroyasu and Arai model. To say that the chamber

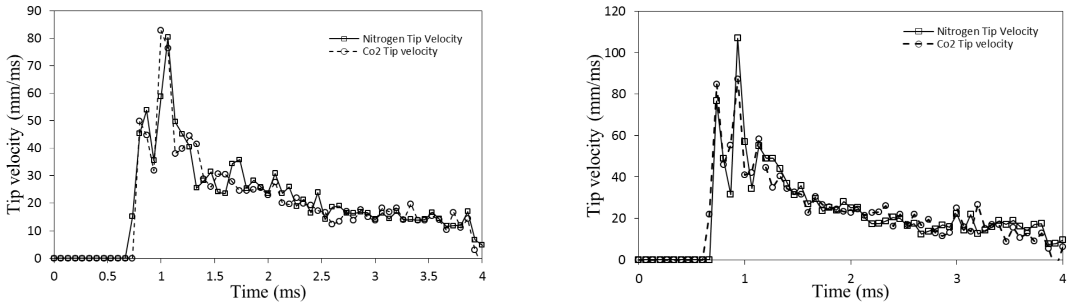


a) b)

Figure 7.6: Diesel Spray Tip Velocity comparison of $CO_2$ ($P_{ambient}$ = 14bar) and $N_2$ ($P_{ambient}$ = 22bar) a)$P_{injection}$ = 400bar b) $P_{injection}$ = 600bar

pressure does not play a significant role in the spray formation would not be valid, as the pressure, to some extent, does influence the spray characteristics. This experiment indicates that chamber density affects the spray development to a greater extent than chamber pressure, chamber pressure is mostly a means of varying density. Paryi et al[46] conducted tests using nitrogen and sulphur-hexafluoride as ambient gases. Sulphur hexafluoride has a greater molecular mass than nitrogen, and as a result similar densities to nitrogen could be achieved at much lower chamber pressures. At a chamber density of 35kg/m$^3$ the pressure difference across the injector was approximately 795 bar when sulphur-hexafluoride was used as opposed to 770 bar when nitrogen was used ($SH_6$ $P_{ambient}$ = 5 bar, $N_2$ $P_{ambient}$ = 30 bar). Paryi et al found that the spray penetration in sulphur hexafluoride was longer by, on average, 10% and had a narrower cone angle. This would suggest that chamber pressure does play a role in spray formation but not to the same extent as density. In comparison, $CO_2$ has a lower pressure difference to nitrogen (when they have the same density) and it is assumed that this is the reason that the difference in penetration is not so large. All aspects of the spray are essentially the same for both ambient gases, most subtle differences can be attributed to the slight variance of input parameters, and uncertainty. The tests conducted in an ambient gas of $CO_2$ will be adequate to perform a valid analysis of the injection spray characteristics, thus allowing higher simulated pressures (or ambient densities) to be tested, in a much safer manner.

Table 7.1 shows the carbon dioxide pressures tested and the equivalent pressure of air if the same density was to be achieved. These are absolute pressures, when testing gauge pressure is used i.e. absolute pressure = gauge pressure + atmospheric pressure.

Table 7.1: Equivalent Air to Carbon-Dioxide pressures

| Density kg/m³ | 1.2 | 6.04 | 10.88 | 15.75 | 20.59 | 25.45 | 27.89 | 30.2 | 32.7 |
|---|---|---|---|---|---|---|---|---|---|
| Carbon Dioxide Pressure (bar) | Atmosphere | 3.28 | 5.91 | 8.55 | 11.18 | 13.82 | 15.15 | 16.45 | 17.77 |
| Air Pressure (bar) | 1 | 5 | 9 | 13 | 17 | 21 | 23 | 25 | 27 |

## 7.2 Cone angle

In this study, the cone angle is defined as the angle between two divergent lines, with each line parallel to a spray edge. The point of intersection may or may not be at the orifice. This definition is thought to be more appropriate . The cone angle is measured at 60$D_o$ as done by Kim et al [34], and Yu et al [3].

Figures 7.7 and 7.8 show the full spray cone angle for Diesel and DME at 500 bar injection pressure and at 17.7 bar and atmospheric chamber pressure respectively. The theoretical model by Hiroyasu and Arai (1990) was chosen for the prediction of the cone angle, as this model predicted cone angles closest to the range of cone angles obtained in this study. The theoretical predictions for diesel and DME are also plotted in Figures 7.7 and 7.8. The cone angles for each test are averaged from three injections. The cone angle at the start of injection for most tests appears to start off higher and as the spray develops, it decreases towards a constant value. For some tests, such as the one in Figure 7.7, the processing program does not measure the angles during the first 0.3ms correctly and results in either low cone angles or extremely inflated cone angle values. This occurs as the first few hundred milliseconds of spray do not produce a clear cone, more of a mushroom type of spray is seen, but as the spray develops it takes on a more stable conical shape as seen in Figure 7.9. Figure 7.8 shows a test where the software correctly measured the cone angle for the initial 0.3ms. It can be seen that the cone angle starts at $30^o$ and gradually decreases to an approximately constant cone angle. This is true for the diesel results whereas the DME results fluctuate slightly more by about +/- $2.5^o$. The fluctuation of the DME results could be a combination of the fact that the DME at atmospheric conditions begins to change to the gaseous phase and this would increase the cone angle, and would impact the way the processing software measures the cone angle.

In both these figures, DME consistently shows a larger cone angle than diesel, by about 2 - 5 $^o$ for all the tests conducted. At the higher chamber densities, diesel was over-predicted by the theory whereas DME was predicted more accurately, but at the lowest chamber density, DME is slightly under-predicted by the theory whereas diesel appears to match the theoretical prediction. The DME spray edges tend to fluctuate more than that of diesel which gives rise to an apparent fluctuation in the cone angle. This phenomenon will be discussed in Section 7.4. The measurement of the cone angle is extremely subjective and it was for this reason that it was chosen to process the results using software as it would provide more consistent measurements.

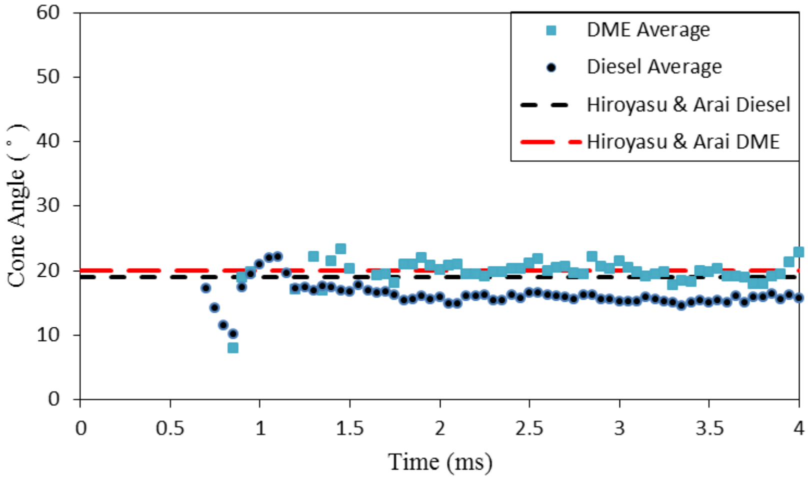


Figure 7.7: Experimental Cone angle compared to theoretical cone angle for diesel and DME at $P_{injection}$ = 500 bar and $\mathrm{P}_{ambient}$ = 17.7 bar or $\rho_{ambient}$ = 32.7 kg/m$^3$

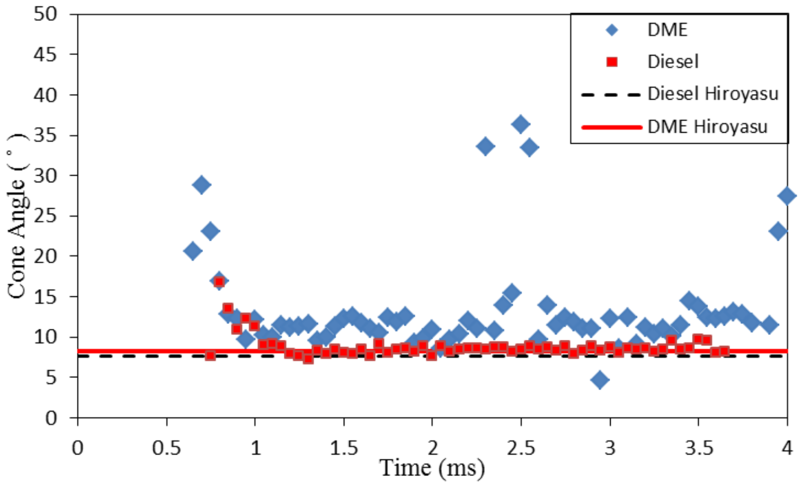


Figure 7.8: Experimental Cone angle compared to theoretical cone angle for diesel and DME at $P_{injection}$ = 500 bar and $\mathrm{P}_{ambient}$ = atmosphere or $\rho_{ambient}$ = 1.2 kg/m$^3$

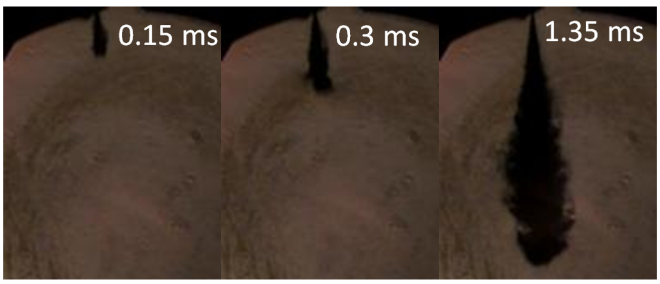


Figure 7.9: Images depicting initially large cone angle after start of injection at $P_{injection}$ = 500 bar and $\mathrm{P}_{ambient}$ = 17.7 or $\rho_{ambient}$ = 32.7 kg/m$^3$

Figure 7.10 shows the constant cone angle values for all injection and chamber pressures tested for diesel along with the theoretical cone angles calculated with the Hiroyasu and Arai (1990) model. The model over-predicts the experimental cone angles for all the tests. The cone angle at 500 bar injection pressure and atmospheric pressure is closely predicted by the model. The model does not account for injection pressure and only varies with chamber density. With the exception of the tests at atmospheric pressure, the cone angle increases as the chamber density or pressure increases. The experimental cone angle appears to increase almost linearly with an increase in chamber pressure. The predicted cone angle also increases with an increase in chamber density or pressure, however it follows more of a curve as it increases at a decreasing rate. No apparent trend is noticed with regards to injection pressure, the cone angle for all injection pressures tested at a constant chamber density are similar varying on average by $0.5^o$ to $1^o$. The cone angles at atmospheric pressure do not fit into the general trend and are larger than those of the tests conducted at the next two chamber densities. This will be analysed in Section 7.4.

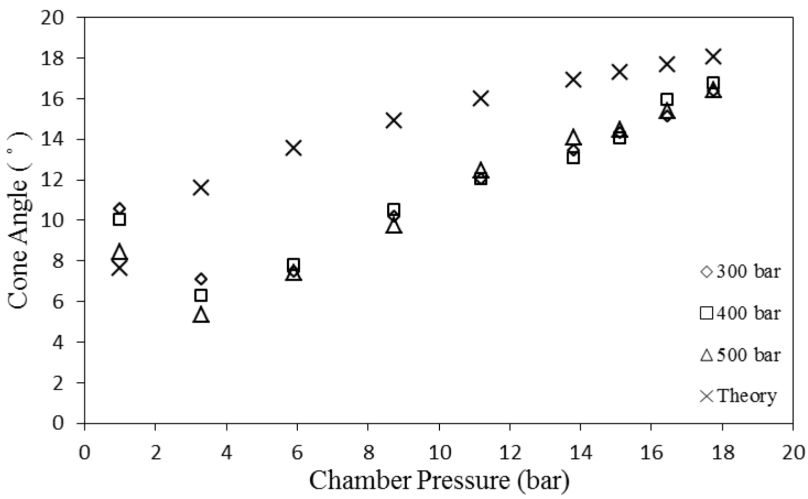


Figure 7.10: Experimental cone angles for range of diesel tests

In an attempt to see how the measured cone angle differs when measured at different points in the spray, as well as to try and see at which point the experimental cone angle would be accurately predicted by the theory, the spray images were processed again but the cone angles were measured at two different points. The cone angles were measured at 135$D_o$ and 210$D_o$ as shown in Figure 7.11, it was not possible to measure the cone angles at 30$D_o$ and 45$D_o$ as suggested by Kim[34] as the resolution was not good enough to form good spray edges at these distances. Figure 7.12,(a) and (b) show the experimental cone angle results obtained when measured at different points along the spray axis. Figure 7.12(a) shows that the cone angle is in better agreement with the theoretical predictions although it still does not follow the same trend, and at lower chamber pressures the cone angle is more accurately predicted than at higher pressures.

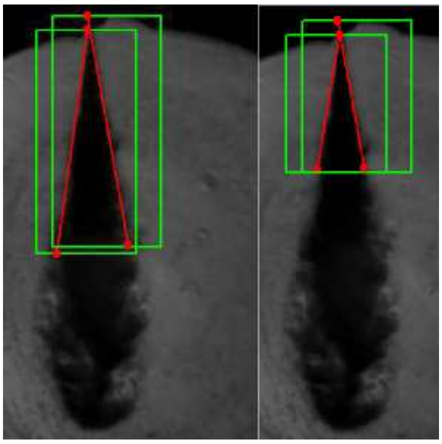

Figure 7.11: Spray images of points of Processing of Cone angles at 210D$_o$ and 135D$_o$

The higher the injection pressure the greater the cone angle (although not by much in most cases). Figure 7.12(b) also shows a slightly better agreement with the theoretical predictions, but the experimental cone angles are more accurately predicted at higher chamber pressures. Again there is no similarity between the two trends.

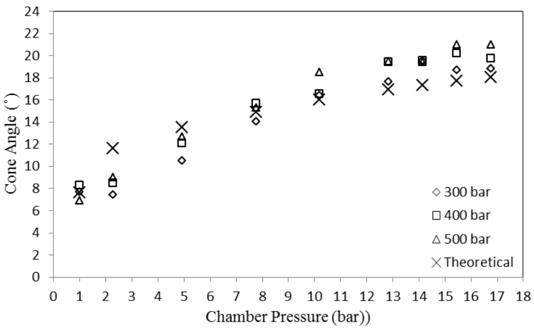


a)

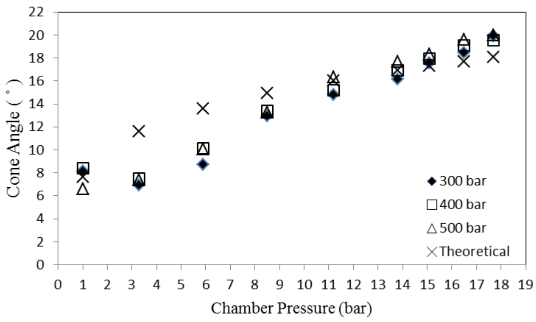


b)

Figure 7.12: Experimental cone angle for diesel at various injection and ambient pressures measured at a) 210D$_o$ and b) 135D$_o$

Figure 7.13 shows the experimental steady state cone angle values for all the tests conducted with DME, compared to the theoretical cone angle predicted using the Hiroyasu and Arai (1990) model. The DME cone angles increase with an increase in chamber pressure or density and as was found in the case of diesel, the relationship is almost linear except for the tests at atmospheric pressure. The higher chamber pressures are predicted slightly more accurately only differing by a maximum of $2^o$-$3^o$. The tests at lower chamber densities or pressures deviated the most from theory, where the experimental cone angles are $4^o$ to $5^o$ off. The higher injection pressures at 11.1, 13.8, 15.1, and 16.4 bar chamber pressures were closest to the theory. There was no particular trend with regards to the injection pressure, but a couple of the tests showed an increase in cone angle with an increase in injection pressure, but this can not be said for the tests at lower chamber pressures. The difference in cone angle with an increase in injection pressure was minimal at the higher chamber pressures, this result was also found by Yu et al[3]. The DME results were re-processed in terms of cone angle as mentioned above, but the results obtained deviated to a greater extent than those seen in Figure 7.13.

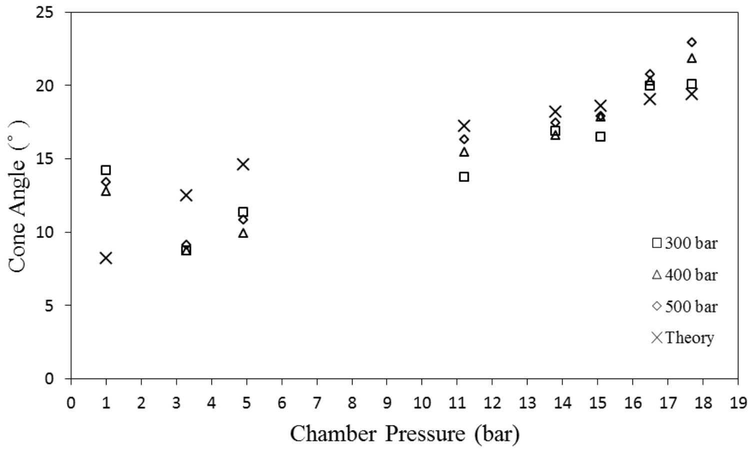


Figure 7.13: Experimental cone angles for a range of DME tests

Figure 7.14 shows a comparison between the diesel and DME cone angles at 500 bar injection pressure. DME showed a larger cone angle compared to that of diesel. Throughout the tests at each chamber pressure/density, DME consistently had a wider spray angle, correlating with the findings of Park et al [36], [37], and Youn et al [24]. With increasing chamber pressure, DME appeared to follow a similar trend to that of diesel , although at the two highest chamber pressures the DME cone angle appeared to increase at a slightly higher rate. DME tends to have a larger cone than diesel and this is most likely due to the fact that it is less dense thus the fuel droplets lose more momentum when introduced into a high density ambient. The fuel droplets struggle to proceed and as the spray develops they stagnate and instead of proceeding along the axial direction of the spray, they tend to spread outwards resulting in a larger cone [38].

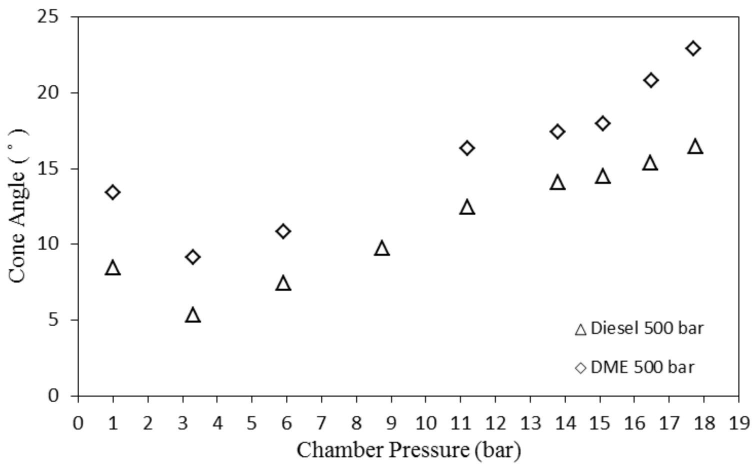


Figure 7.14: Comparison between DME and diesel cone angle at various chamber pressures and 500 bar injection pressure

## 7.3 Spray Penetration

The spray penetration results will be discussed in terms of the effects of injection and chamber pressure (or density), theoretical predictions by the models proposed by the four authors mentioned in Section 2.5, and phenomena observed in the spray images in terms of injection delay and spray hesitation.

### 7.3.1 Injection Delay, and Spray Hesitation

#### Spray Hesitation

Analysing current results and those obtained in previous years, and comparing them to theory, it was noted that the penetration length for the initial 0.5 ms was always over predicted by the theoretical considerations, shown in Figure 7.15. This figure shows how the penetration is over-predicted during this stage, but most importantly there is a trend that is evident for the first 0.2ms of spray for all the results obtained, including DME. The penetration for this first approximately 0.2ms appears to be linear and then suddenly increases and starts to follow a similar trend to that of the models. This "discontinuity" is evident in all tests and occurs at approximately the same point/time. It was for this reason that a more in depth analysis of the penetration during this stage was conducted. Tests were conducted at 100 000 fps, which gave a time resolution of 0.01 ms, a higher frame rate could not be achieved as the light source could not provide sufficient light and the resolution was insufficient resulting in poor quality images. The majority of the results were recorded at 20 000 fps as this allowed for good quality images with sufficient lighting as well as temporal resolution.

Figure 7.16 show images of injection spray at 575 bar injection pressure and 22 kg/m$^3$ chamber density. The spray progresses as one would expect, but at 0.77ms after start of energisation (indicated by the red circle) a break in the spray appears (the spray is not black from injector tip to spray edge). Thereafter a second spray can be seen coming through, the tip of which is indicated by the red arrows as the spray progresses. This can be seen much more clearly in the replay of the high speed video. The second spray can be followed through the initial spray as shown in Figure 7.16. The initial spray is moving slowly relative to the second spray due to the fact that it is only progressing due to its initial momentum provided by the pressure difference before the penetration seemed to stop. The second spray is driven by the pressure difference between rail pressure and chamber pressure. The tip of the second spray impinges on the first spray, with the result that the tip of the second spray is wider as the fuel is

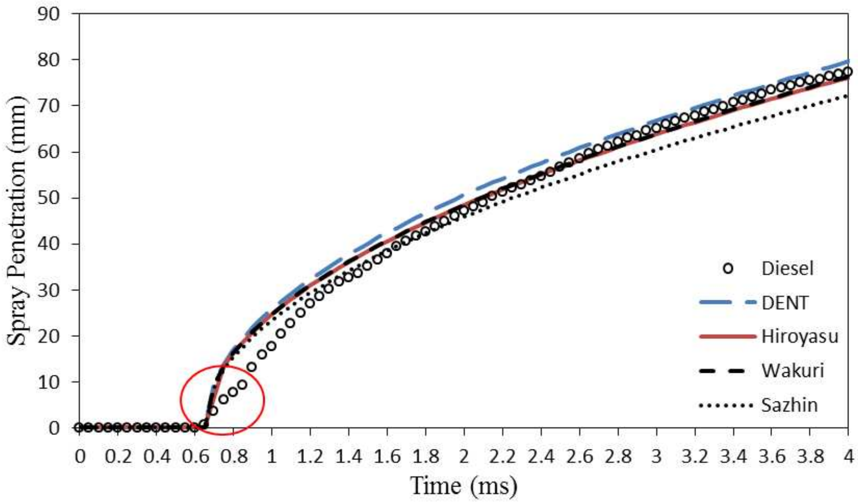


Figure 7.15: Diesel penetration compared to theoretical predictions indicating over prediction in the initial stages of penetration

being scattered slightly. This does not occur after the second spray has progressed past the fuel injected in the first part of the injection. This phenomenon was apparent in tests conducted at injection pressures of 200, 300, 400, 500, and 600 bar and at various chamber pressures, these can be found in Appendix G.

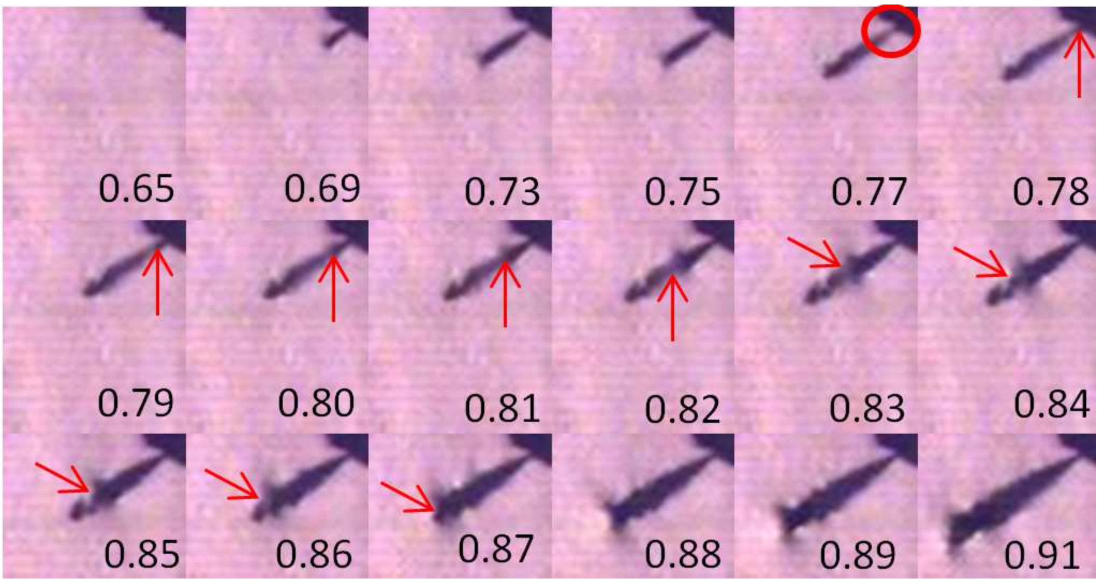


Figure 7.16: Hesitation of spray at 575 bar injection pressure

This provides a reasonable explanation as to why the penetration behaves the way it does in the circled region in Figure 7.15. The straight line section in the first 0.2 ms occurs when the software measures the tip of the initial injection even after the apparent break in spray (as the spray continues to penetrate due to the momentum in the fuel droplets) and subsequently measures the tip of the first spray until the second spray overtakes it. The discontinuity or sudden jump in penetration after the linear section is attributed to this.

Initially it was thought that the occurrence of this second spray was due to the needle lift being slow due to the current method of actuating the fuel injector using the Experiment Controller. Tests were then conducted on a separate fuel spray analysis test rig (the Innov8 test stand at the University of the Witwatersrand). This test stand allows for the analysis of fuel sprays using a mie scattering technique to capture high speed images, the injector is actuated by an ECU system providing the same voltage and current a car ECU would provide. This test stand does not allow for chamber pressures to be simulated so tests are conducted at atmospheric pressure. Figure 7.17 shows spray images obtained using the Inov8 test stand, the time steps between images was also set to 0.01 ms. Analysing these images it is noted that the exact same phenomenon can be observed, an initial spray can be seen and approximately 0.15 ms from the start of injection the second spray begins to emerge while the initial spray continues to penetrate the air. This confirmed that the method used to actuate the injector using the experiment controller was adequate to conduct proper spray analysis tests, as the results obtained were similar to those obtained by the Inov8 test stand. The two sprays observed were not related to the method of actuation of the injectors.

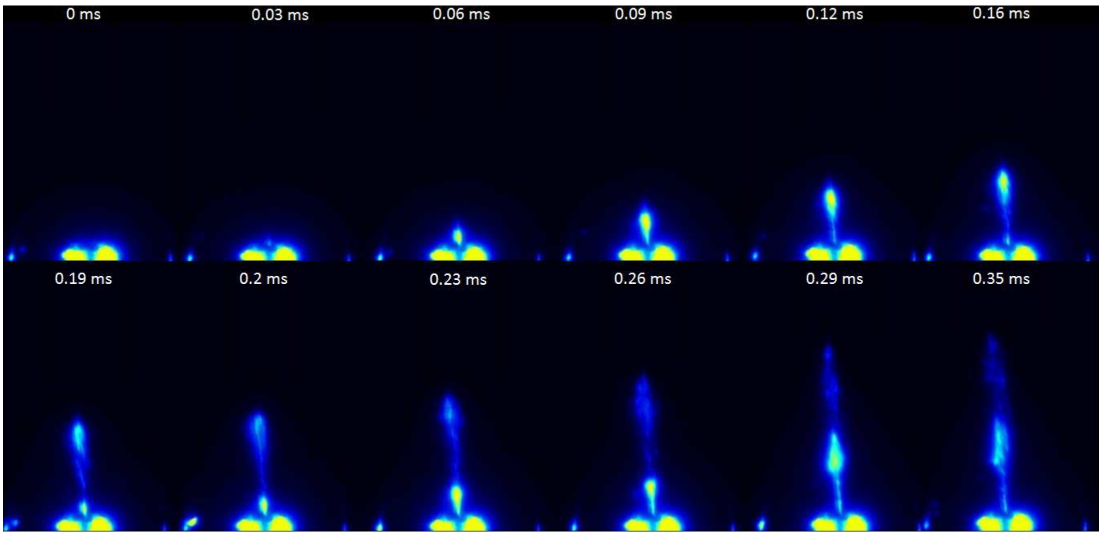


Figure 7.17: Spray images obtained using Mie scattering technique at 500 bar injection pressure and atmospheric chamber pressure

The appearance of two sprays, or "Hesitation" as it is referred to by Karimi and Kennaird [15; 47], was also found in tests they conducted with single hole Bosch VCO nozzle injectors. The occurrence of this hesitation in the spray is possibly due to the pressure distribution of the fuel around the needle. Since the nozzle being used was also a VCO nozzle and this type of nozzle, as mentioned in Section 2.1.4, is sensitive to needle misalignment, the pressure distribution will change as a result. Karimi and Kennaird suggest that since there is only one hole in the nozzle that the pressure distribution around the needle is severely affected. They suggest that as the needle is lifting, during the initial stage, the pressure on the opposing side to the hole of the needle is higher as it has nowhere to escape and the pressure on the hole side will be lower, the resultant force then would push the needle towards the hole, closing it for an instant. Once the needle has reached full lift then there is no problem in terms of the pressure distribution. There are two types of needle arrangements for VCO nozzles, single-guided and double-guided needles as shown in Figure 7.18. Karimi found that this hesitation occurred for both these needle arrangements with single hole nozzles, but the effect was less with the double-guided needle. In the current research the injector used contains a double-guided needle, which would still allow for the hesitation found in the spray images.

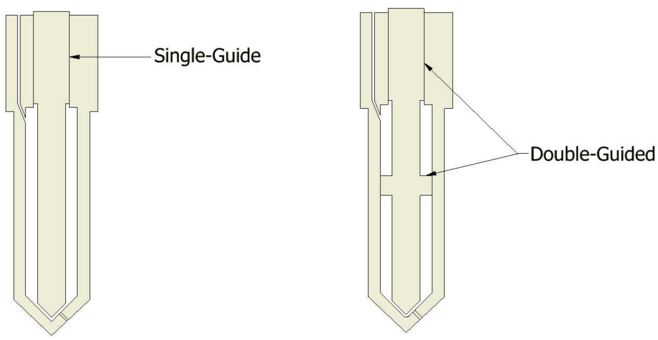


Figure 7.18: VCO Needle types a) Single Guided b) Double Guided

It was found that the time between the first spray and the appearance of the second spray is approximately equal to 0.15ms $\pm$0.01ms, which is the same time period found by Karimi [15]. The hesitation is much more noticeable at high injection pressures, the possible reason for this is that the initial spray will have a high pressure difference initially which would give the fluid a high initial velocity. The initial spray will then travel further into the ambient gas and it will be clearly visible when the initial spray stops and when the second spray appears. At 200 bar injection pressure the fuel initially has a low velocity, and if the chamber is pressurised, the initial spray will not be able to penetrate much, which would make it slightly more difficult to identify the two sprays (at atmospheric pressure this effect will be clearly seen at low injection pressures). Karimi conducted tests using a multi hole Bosch injector and no hesitation in the sprays was found, indicating that the pressure distribution around the needle was equal, implying that the pressure at each orifice would be equal. This reinforced the explanation for the hesitation found when using single hole VCO injectors, which have an offset hole.

### Injection Delay

The synchronisation of the injections with spray images and pressure traces allows for an accurate comparison of features in the results between different tests. When analysing the spray images it was noticed that the delay, from when the camera and injector receive a trigger signal to when the spray appears, varied for the range of injection pressures. The delay was much shorter at higher injector pressures, because, as mentioned in Section 2.1.3, the mechanism used to inject fuel relies on the fuel pressure. The higher the fuel pressure the greater the force acting on the annular area of the needle, thereby lifting the needle faster. Figure 7.19 shows the initial delay for varying injection pressures, the initial delay was not affected by the chamber pressure or chamber density. The initial delay between 300 - 600 bar injection pressure appears to follow a linear trend, with a decreasing delay as the injection pressure increases. The delay at 200 bar deviated slightly from this trend. The delay between the start of the first initial spray and the second spray did not seem to be affected by injection pressure, the hesitation period consistently remained approximately 0.15ms $\pm$ 0.01ms. The rate of penetration of the initial spray was affected by the chamber pressure, due to the higher resistance of the gas density.

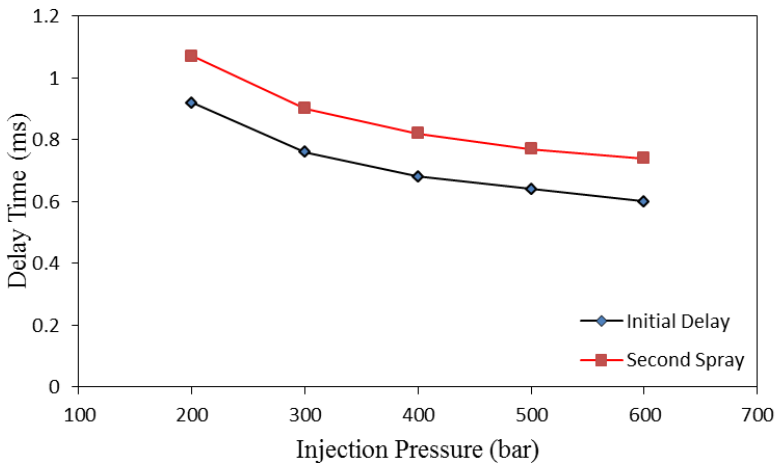


Figure 7.19: Effect of injection pressure on diesel injection delay

The DME injection delay, shown in Figure 7.20, appears to decrease as the injection pressure increases, as it did for diesel, although the gradient of the line is slightly steeper. The appearance of the second spray in the DME results was between 0.1 - 0.2 ms. The delay values for DME are more unpredictable compared to diesel, as the chamber pressure has a small impact on the delay of the DME penetration. At the lower chamber pressures the delay appears to be shorter than at higher chamber pressures as seen in Figure 7.21. This may be due to the DME initially penetrating more easily at the lower chamber pressures as there is less resistance. At the higher pressures the resistance is greatly increased and the lower density DME is not able to penetrate as easily, and the spray therefore is only seen at a later time compared to the tests at lower chamber pressures. At the lower chamber pressures (less than 5.3 bar) DME will tend to vaporise, especially as the needle is lifting only a small amount of DME will get through and the pressure drop will be extremely large causing the DME to flash. But, as the chamber pressure increases this will no longer occur as easily.

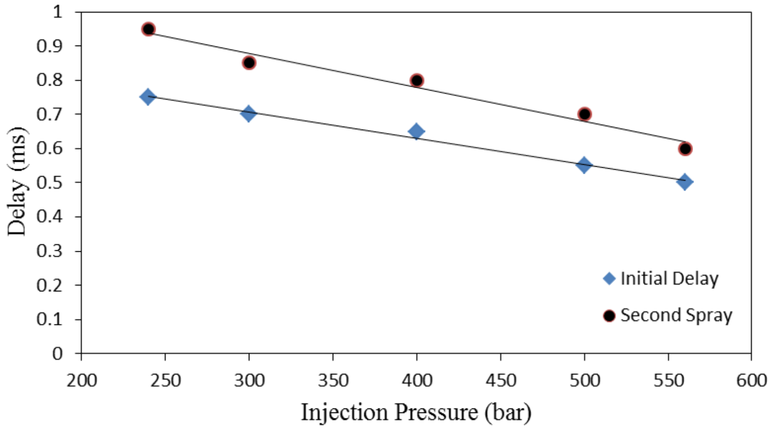


Figure 7.20: Effect of injection pressure on DME injection delay

In Figure 7.21 it can be seen that the delay does increase slightly for the higher chamber pressures, but more so for the lower injection pressures than the higher injection pressures tested. The DME injection delays are slightly more erratic when compared to the diesel delays, but generally the DME injection delays are smaller than those of diesel, although not by much.

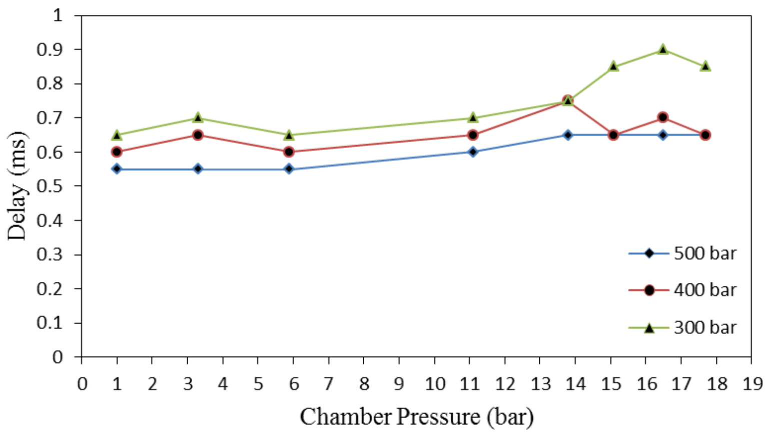


Figure 7.21: DME injection delays for complete test range

### 7.3.2 Effect of Injection Pressure

Figures 7.22 and 7.23 show the effect of injection pressure on the spray penetration for diesel and DME fuel at a chamber pressure of 17.7 bar and chamber density of 32.49kg/m$^3$. Due to the fact that injection pressure affects the injection delay, the penetration curves are adjusted so that they can be directly compared. The spray penetration increases with an increase in rail pressure. The initial 0.4 - 0.5ms of injection seems to be similar for the different rail pressures, thereafter the difference becomes evident. For DME, Figure 7.23, the difference in the initial 0.5ms is slightly greater than that between the diesel results, although not by much. The difference in penetration between the injection pressures for DME at this point is around 1-2 mm between increments in injection pressure. At a higher rail pressure the rate of penetration also increases, meaning that at a particular time the penetration for a higher injection pressure is greater. This was also the case for DME penetration. As the spray progresses the penetration increases at a decreasing rate, which gives the penetration a curve as seen in Figure 7.22.

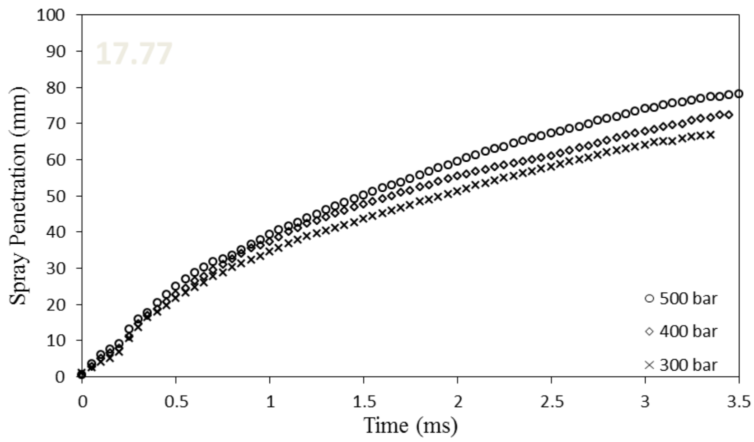


Figure 7.22: Effect of injection pressure on diesel spray penetration at P$_{ambient}$ = 17.77 bar, $\rho_{ambient}$ = 32.49 kg/m$^3$

Figures 7.25(a) and 7.25(b) shows a comparison of the spray penetration between DME and diesel. DME consistently penetrates less than diesel throughout the entire injection, it is on average 6.5 - 9 % less than diesel throughout the injection at the higher chamber pressures. This agrees with the findings of Kim et al[34], Park et al[36][37], Suh et al[38], and Youn et al[24]. The difference between DME and diesel penetration is not large, diesel as a fuel is used succesfully and its spray characteristics have been optimized to produce good combustion and low emissions, the fact that DME spray penetrates similarly to diesel means that it is possible that DME can be utilized in an engine, possibly producing better emissions. As the chamber pressure is decreased the difference between DME and diesel in the later part of the injection increases to 17 -

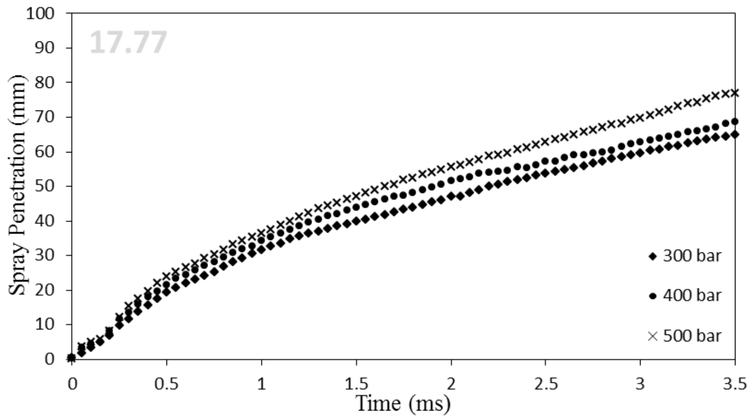


Figure 7.23: Effect of injection pressure on DME spray penetration at $P_{ambient}$ = 17.77 bar, $\rho_{ambient}$ = 32.49 kg/m$^3$

25%, as shown in Figures 7.25 (c) and 7.25 (d). Although the penetration is similar for the first 0.2ms of the second spray, the diesel penetration continues to increase at a faster rate than the DME. Unlike at higher chamber pressures, the DME and diesel do not follow a similar trend, the diesel penetration follows an almost linear path at atmospheric pressure, whereas the DME penetration increases at a decreasing rate. This is more evident at lower injection pressures but at 500 bar injection pressure the penetration still increases at a decreasing rate but it is closer to being linear. This may be due to the fact that at low injection pressures and low chamber pressures the DME begins to vaporise, as the conditions in the chamber are below the vapor pressure of DME. After a certain penetration length the DME is at a lower pressure and starts to absorb heat from the surroundings and vaporizes/flash boils at the tip of the spray as shown in Figure 7.24. DME takes longer to reach the limits of the chamber windows, at 96mm, as it loses momentum when it has vaporized and the resistance of the ambient gas has a larger effect on the less dense DME.

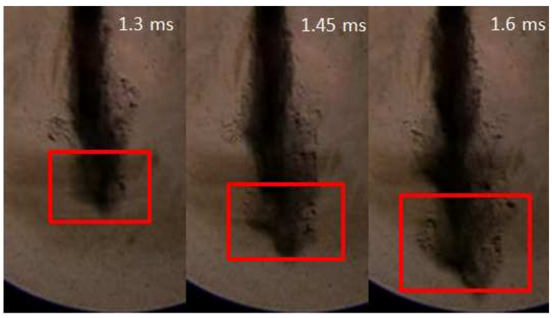


Figure 7.24: DME spray images at $P_{Injection}$ = 300 bar and $P_{Ambient}$ = atmosphere showing the vaporization of DME at the spray tip

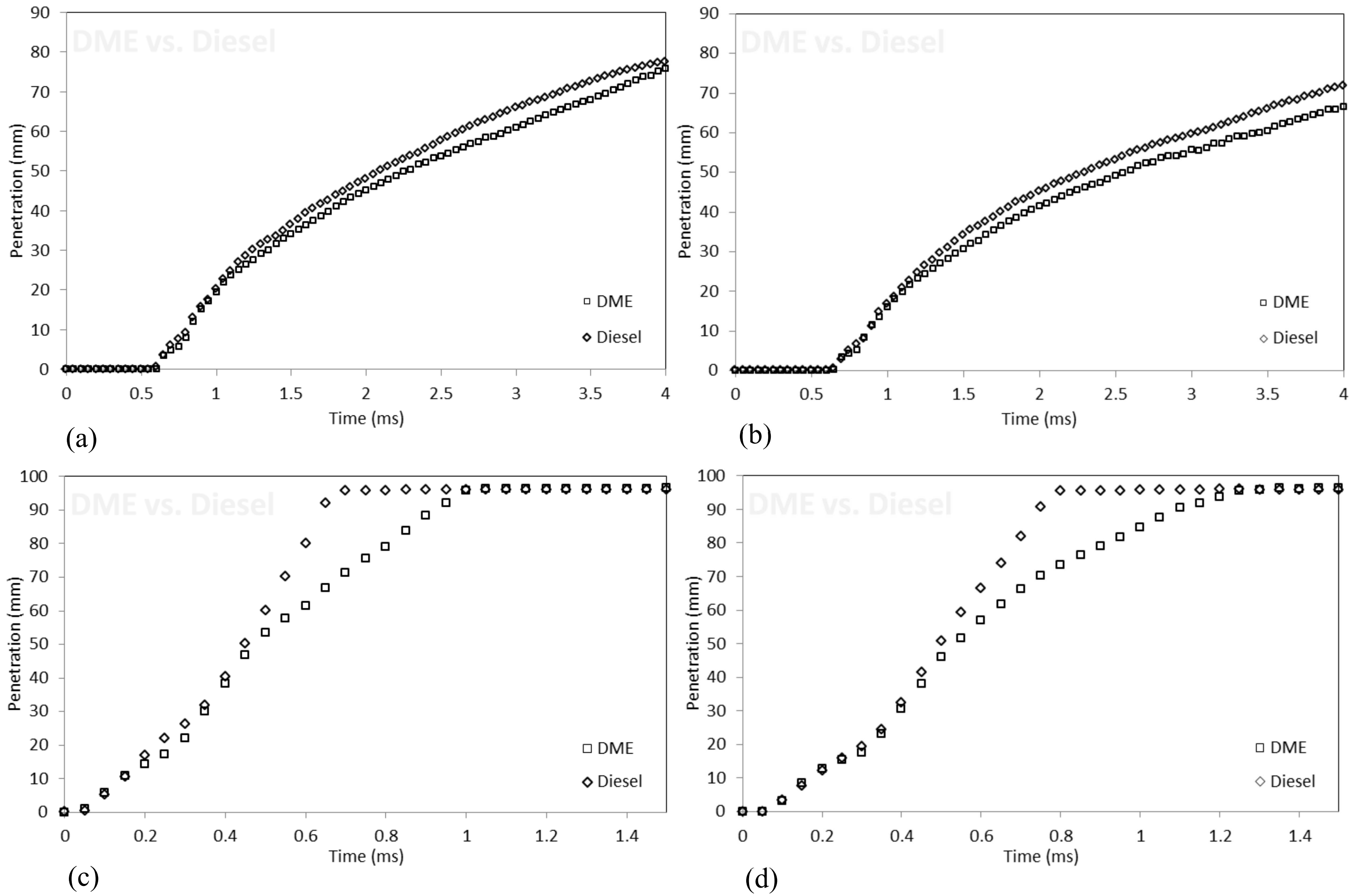


Figure 7.25: DME vs diesel penetration at $P_{ambient} = 17.7$bar, $\rho_{ambient} = 32.49$ kg/m$^3$ for (a)500 bar injection pressure (b)400 bar injection pressure, and $P_{ambient} = 1$ bar, $\rho_{ambient} = 1.2$ kg/m$^3$ and (c) 500 bar injection pressure (d) 400 bar injection pressure

### 7.3.3 Effect of Chamber Pressure and Chamber Density

Figures 7.26 and 7.27 show the effect of chamber pressure and chamber density on diesel and DME spray penetration. The penetration length for both diesel and DME decreases with an increase in chamber pressure/density. Small changes in chamber pressure do not effect the penetration greatly, only increasing or decreasing it by at most 2 mm. A 4 bar ambient pressure change produces a 5 to 6 mm change in penetration. At the higher chamber pressure range, an increase in chamber pressure does not seem to produce a large decrease in penetration for both DME and diesel. This is observed clearly with DME.

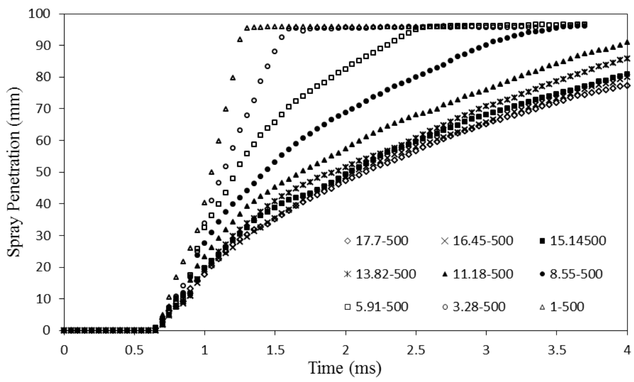


Figure 7.26: Effect of chamber pressure on diesel penetration at 500 bar injection pressure

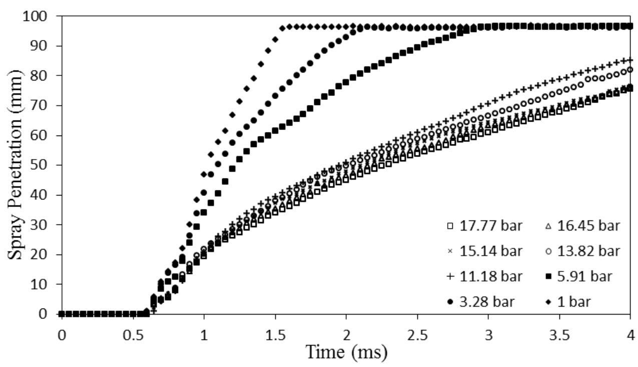


Figure 7.27: Effect of chamber pressure on DME penetration at 500 bar injection pressure

Figure 7.28 shows a comparison between DME and diesel penetration values for different sets of chamber pressures. It is interesting to note that the DME at lower chamber pressures achieves a similar, if not the same, penetration as diesel at a higher chamber pressure/density. DME is able to produce the same penetration and a larger cone angle than diesel, but at a lower cylinder pressure or with a higher injection pressure.

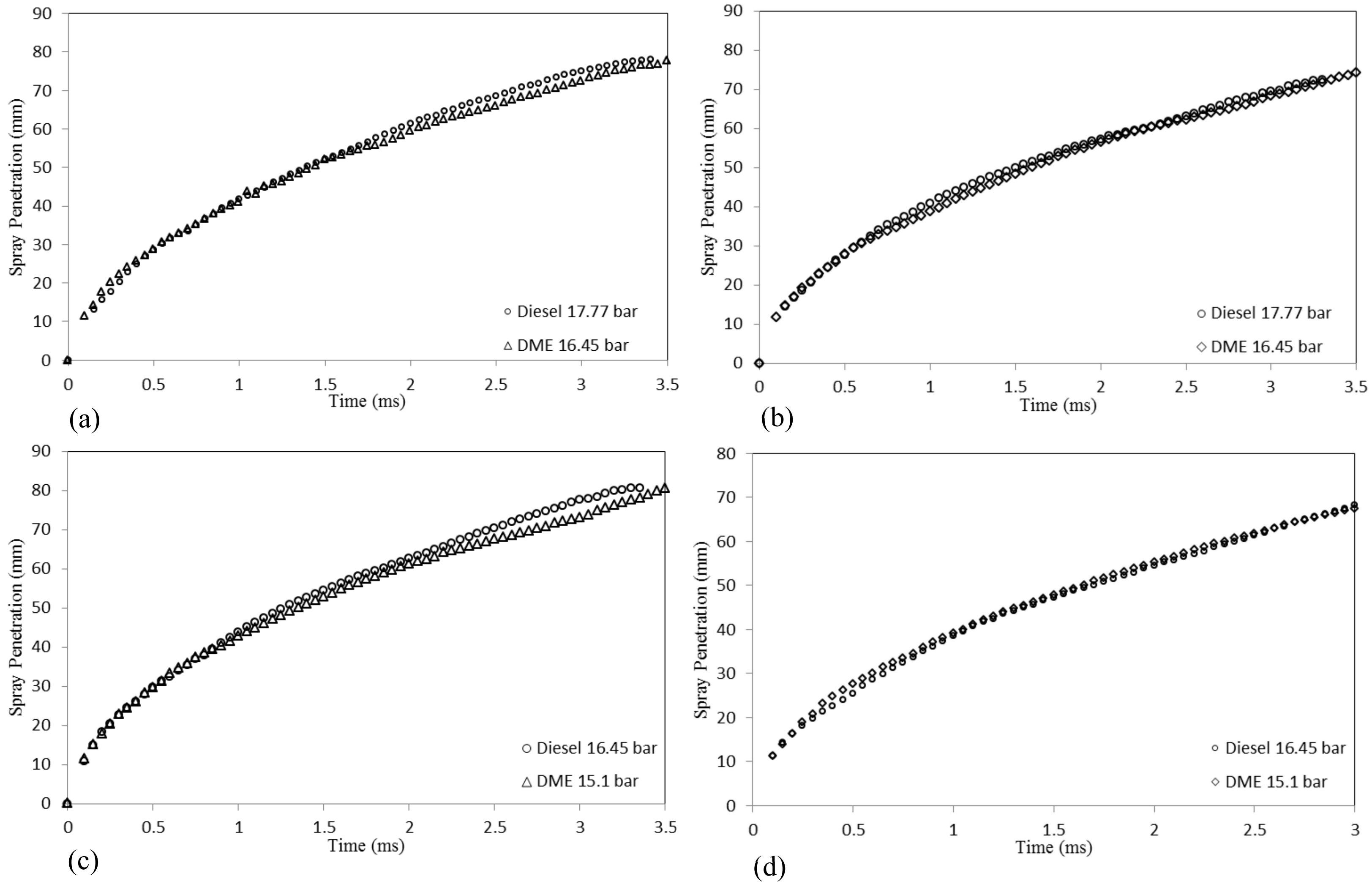


Figure 7.28: Matching diesel and DME penetration at (a) 500 bar injection pressure, (b) 400 bar injection pressure, and at (c) 500 bar injection pressure, and (d) 300 bar injection

### 7.3.4 Theoretical Predictions

Spray penetration is a large part of engine performance and engine design. It may not always be possible or may be too time consuming to perform all the tests necessary to characterize the spray from an injector using a certain fuel. It is therefore important to be able to predict, as accurately as possible, the parameters of the fuel spray.

The four models mentioned in Section 2.5, Dent, Hiroyasu et al, Sazhin et al, and Wakuri et al, are used to predict the spray penetration for both the diesel and DME tests conducted in this study. The Dent model does not take into account fuel density or any fuel specific parameters, it therefore predicts the same penetration for both fuels. The Hiroyasu model only takes into account the fuel density in the pre-break up part of the model, the post-break up equation does not take into account any fuel specific parameters. Both the Sazhin and Wakuri models take into account cone angle, which can be measured or predicted, and Kim et al [34] suggest the measured cone angle be used to predict the spray penetration. This therefore will differentiate the predictions for the two fuels.

The Sazhin and Wakuri models were calculated using the cone angles measured at the three different locations mentioned in Section 7.2, namely at $60D_o$, $135D_o$, and $210D_o$. It was found that the cone angle measured at $60D_o$ resulted in predictions by Sazhin and Wakuri that were closer (or deviated less) to the experimental results, and thus the models shown for diesel and DME from this point on are calculated using these cone angles.

In Section 7.3.1 a hesitation in the spray was observed, and it was shown to be a result of the pressure imbalance on the injector needle. Tests conducted with the multi-hole injector did not exhibit the same phenomena. Karimi [15] and Kennaird et al [47] both shifted their penetration results in order to compare the single-hole penetration results either to multi-hole results or to theoretical predictions. Since this phenomena is a characteristic of an offset single-hole injector, and in most common rail engines multi-hole injectors are used, the penetration results are shifted so that the start of the second spray coincides with the start of the theoretical curves.

Figures 7.29 to 7.33 show the experimental diesel spray penetration results plotted along with the predicted penetration from the proposed models for a selection of the test parameters. The experimental penetration is an average of three injections. The tests selected are used to discuss the main trends and findings of the study and the remainder of the results are shown in Appendix D. Figures 7.34 to 7.38 show the DME experimental penetration compared to the theoretical predictions (calculated for DME).

The graphs are displayed in this manner in order to clearly see all the results in a simple and uncluttered manner.

Figure 7.29 and 7.30 show the experimental diesel results at $P_{Ambient}$= 17.7 bar, $\rho_{Ambient} = 32.7\text{kg/m}^3$ (which is equivalent to 27 bar ambient air pressure) and $P_{Injection}$= 300 and 500 bar respectively. These two graphs look very similar except that the penetration at 300 bar injection pressure is less than at 500 bar. The models predict the experimental results in the same manner, for example, the Wakuri and Hiroyasu models predict the same penetration values while the Sazhin model, after about 1.2ms, under-predicts the experimental results and the Dent model seems to predict the experimental results quite well throughout the entire injection. This was seen at all the chamber pressures tested, the spray penetration relative to the theoretical models was the same for all the injection pressures at a specific chamber pressure. There is a minor uncertainty of 0.025ms in the x-direction, due to the difficulty of pin pointing the exact start of the second spray, which usually occurs between two frames. If one considers the uncertainty of the measurements and of the theoretical predictions it can be seen that Dent, Hiroyasu, and Wakuri predict the experimental penetration relatively well throughout the entire injection. The penetration for the 500 bar injection pressure is slightly over-predicted for the first 0.35ms, although it is only over-predicted by 5%.

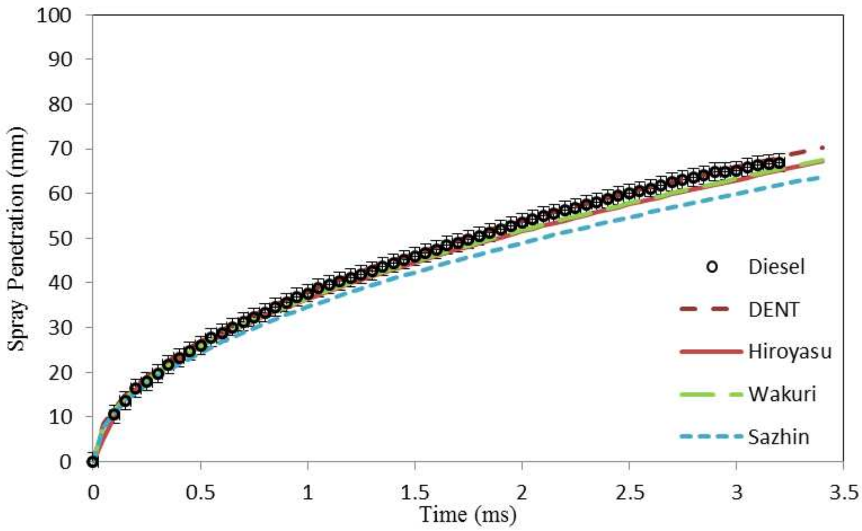


Figure 7.29: Comparison of experimental diesel results to theoretical predictions at $P_{ambient}$=17.7 bar and $P_{injection}$=300 bar

Figure 7.31 shows the experimental and theoretical penetration at $P_{Injection}$ = 500 bar and $P_{ambient}$ = 16.4 bar. Dent and Wakuri predict practically the same penetration, varying by less than 1mm throughout the entire injection. Hiroyasu and Sazhin predict similar values for the penetration and vary by a maximum of 1.6mm.
The experimental penetration follows the four models closely until about 1.2ms, but is

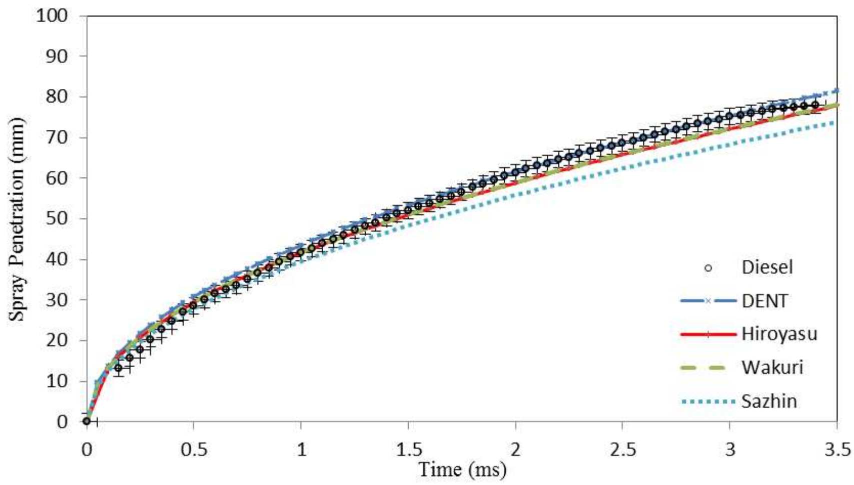


Figure 7.30: Comparison of experimental diesel results to theoretical predictions at $P_{ambient}$=17.7 bar and $P_{injection}$=500 bar

closer to Hiroyasu and Sazhin models as the percentage difference is 2% over this period. Whereas the Wakuri and Dent models over-predict the experimental penetration on average by 6%. Thereafter it continues to follow Dent and Wakuri for the remainder of the injection, the percentage difference between these models and experimental penetration being less than 1%, while Sazhin and Hiroyasu under-predict the penetration. The largest difference between the experimental results and Sazhin or Hiroyasu penetration results is 5 mm at 3.2 ms.

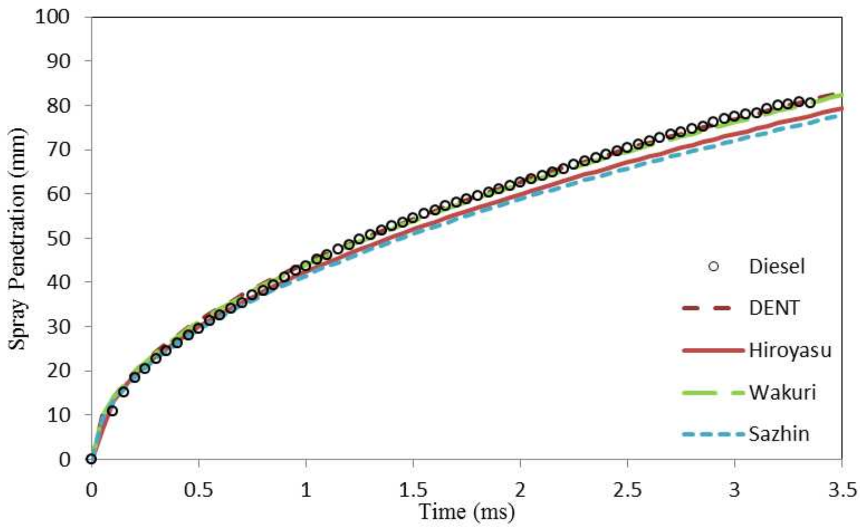


Figure 7.31: Comparison of experimental diesel results to theoretical predictions at $P_{ambient}$=16.4 bar and $P_{injection}$=500 bar

Figure 7.32 shows the experimental and theoretical penetration at $P_{Injection}$ = 500 bar and $P_{ambient}$ = 15.1 bar. At these test parameters the theoretical predictions are relatively close, the largest deviation between any theoretical model and experimental value is approximately 6mm. When compared to the previous figure, the Sazhin and Wakuri models have shifted up slightly relative to the Dent and Hiroyasu models. At these parameters the experimental penetration is reasonably predicted by all four models, although the Wakuri and Dent model predict the experimental values the best. Again during the first 0.6 - 0.7ms the penetration is predicted well by all four models: only varying by less than 3.7% for Wakuri, less than 3% for Dent, and less than 5% for Hiroyasu and Sazhin. Thereafter Dent and Wakuri models show a maximum difference of 2% for the remainder of the injection (where Dent shows the least variation at an average of 1%) and the Sazhin and Hiroyasu models have an average variation of 5%.

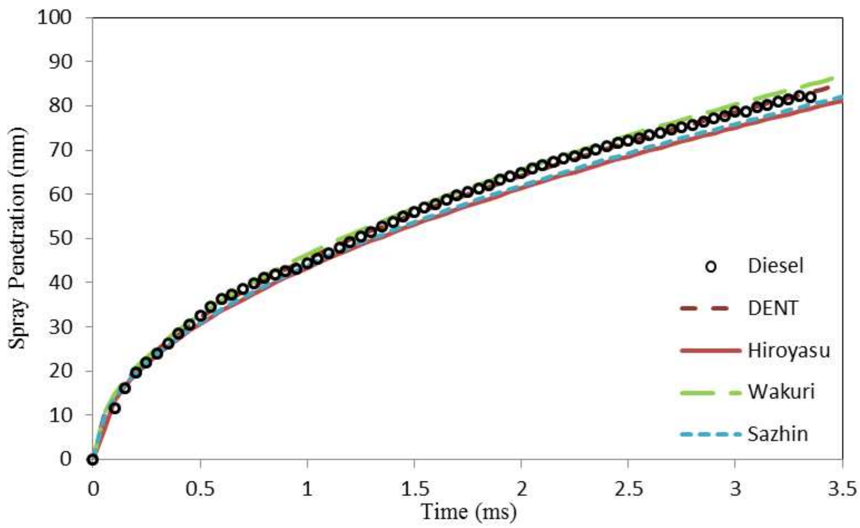


Figure 7.32: Comparison of experimental diesel results to theoretical predictions at $P_{ambient}$=15.1 bar and $P_{injection}$=500 bar

Figure 7.33 shows the penetration for a 500 bar test at atmospheric chamber pressure in the first millisecond after start of injection. At the low ambient pressures the spray reaches the window limit relatively fast and only a portion of the spray will be seen. The difference between the theoretical predictions is more pronounced under these conditions. Sazhin and Wakuri predict a similar penetration but predict a much faster rate of penetration when compared to Dent and Hiroyasu. The theoretical breakup length, as denoted by the first straight line portion, of the Hiroyasu model is substantially longer at low chamber pressures than at high chamber pressures. This would suggest that the fuel is not atomized as well as it is under higher chamber pressures. The experimental penetration for this test does not compare well to any of the theoretical predictions, the data is accurately predicted by Hiroyasu up to 0.3ms, it then continues to increase almost linearly until it reaches the limit of the chamber windows. The experimental results are consistently over-predicted by Sazhin and Wakuri, they are only over-predicted by Dent until 0.35ms thereafter they are under-predicted by both Dent and Hiroyasu.

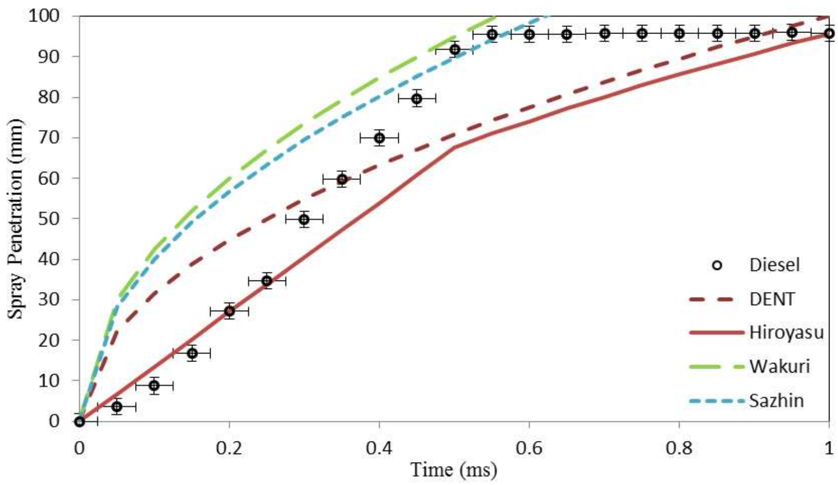


Figure 7.33: Comparison of experimental diesel results to theoretical predictions at $P_{ambient}$=1 bar and $P_{injection}$=500 bar

Analysing the trends throughout the complete set of tests it can be seen that Sazhin and Wakuri generally predict penetration lengths very similar to one another, only varying by a maximum of 5 to 10 mm at 3.5ms after start of injection depending on the chamber pressure and injection pressure. A similar trend is seen between Dent and Hiroyasu, the difference between the initial stages of these two models does, however, vary depending on the chamber pressure and injection pressure. The penetration predicted by the Sazhin and Wakuri models tend to be higher than the penetration predicted by the Dent and Hiroyasu models at lower chamber pressures. As the chamber pressure is increased all the models predict similar penetrations until the higher range of chamber pressure, where the Dent and Hiroyasu models predict higher penetration lengths.

The diesel penetration was accurately predicted by the Wakuri model in 70% of the tests conducted. If the penetration was overpredicted by the Wakuri model then it would follow the Sazhin model. The Dent model gave a reasonable prediction for the results at higher chamber pressures, where the four models were bundled closely together and the experimental penetration lengths usually agreed well with the majority of the models, (being more accurately predicted by one than the other) only varying by maximum of 7%. The Hiroyasu and Dent models decreasingly under-predicted the diesel results as the chamber pressure was increased, Suh et al [38] also found that the diesel results were underestimated by Hiroyasu's model. Throughout the chamber pressure range tested, it was found that the Sazhin and Wakuri models predicted the progression of the spray with change in chamber pressure better than Hiroyasu and Dent. The latter two predicted spray relatively well at the higher chamber pressures/densities but rather poorly at the lowest chamber pressures/densities.

Figures 7.34 and 7.35 show the experimental DME results compared to theoretical predictions at $P_{Ambient}$= 17.7 bar, $\rho_{Ambient}$ = 32.7kg/m$^3$ and $P_{Injection}$ = 300, 500 bar respectively. These two figures clearly show that an increase in injection pressure results in an increase in penetration at each time step. Analysing the predictions by the models it was noticed that with a decrease in injection pressure the Sazhin and Wakuri models increased relative to the Dent and Hiroyasu models, where the lower cone angle results in a higher penetration prediction. The other two models only change with changes in injection or chamber pressure whereas Sazhin and Wakuri additionally change with cone angle. Therefore, for most of the DME tests when the cone angle decreases slightly with decreasing injection pressure, the penetration prediction would increase relative to the other two models.

In Figure 7.34, the experimental penetration tends to follow Hiroyasu model more closely than any other model, only deviating by 3.5% for the majority of the spray. The four models generally predict the penetration well until about 0.35ms thereafter the Dent model over-predicts penetration on average by 8% and after about 0.7ms the Sazhin model completely under-predicts the penetration for the remainder of injection by about 12.5 %. The Wakuri model is able to predict the penetration reasonably well to about 2ms, thereafter it under-predicts by a greater margin on average by 7%.

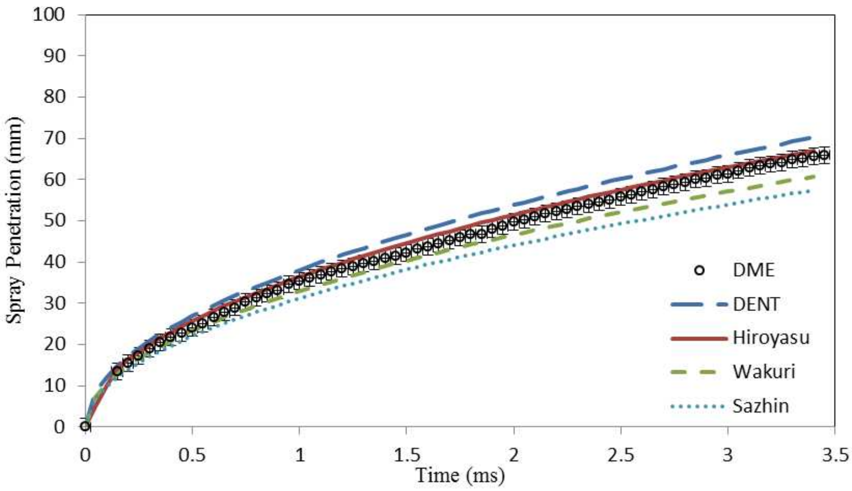


Figure 7.34: Comparison of experimental DME results to theoretical predictions at $P_{ambient}$=17.7 bar and $P_{injection}$=300 bar

In Figure 7.35 the experimental penetration follows the Hiroyasu model more closely than any other, on average it deviated by 6% until 1ms and thereafter it deviated by 2%. The Dent model over-predicted the experimental penetration throughout the injection by on average 8%, whereas both Sazhin and Wakuri under-predict the penetration by a far greater margin, on average 15% for Wakuri and 21% for Sazhin.

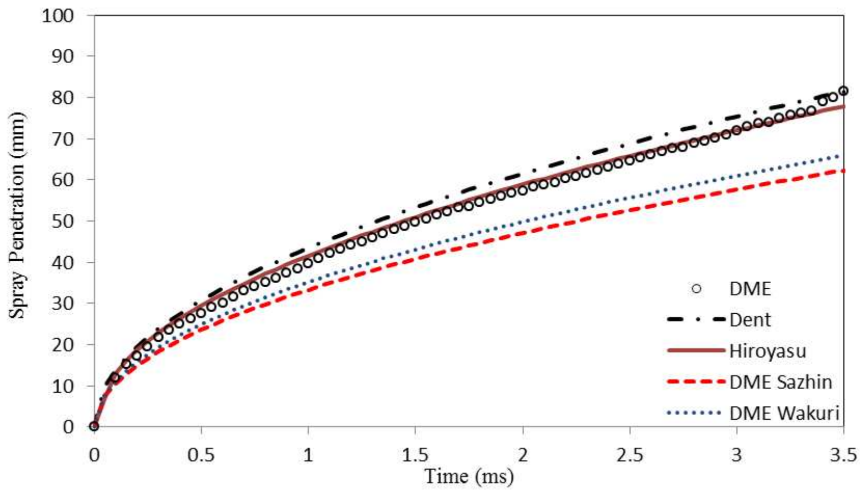


Figure 7.35: Comparison of experimental DME results to theoretical predictions at $P_{ambient}$=17.7 bar and $P_{injection}$=500 bar

Figure 7.36 shows the experimental and theoretical results for DME at $P_{Ambient}$= 16.4 bar, $\rho_{Ambient}$ = 30.2kg/m$^3$ at $P_{Injection}$ = 500 bar. Again, as in the previous figure, the experimental DME penetration is predicted accurately by Hiroyasu only deviating 5% until 0.35 ms and 0.7% thereafter. Sazhin and Wakuri under-predict the DME penetration, and Dent over-predicts the penetration throughout the entire spray development. The DME differs from the Sazhin model on average by 19%, from the Wakuri model by 12%, and from the Dent model by 4.5% throughout the spray development.

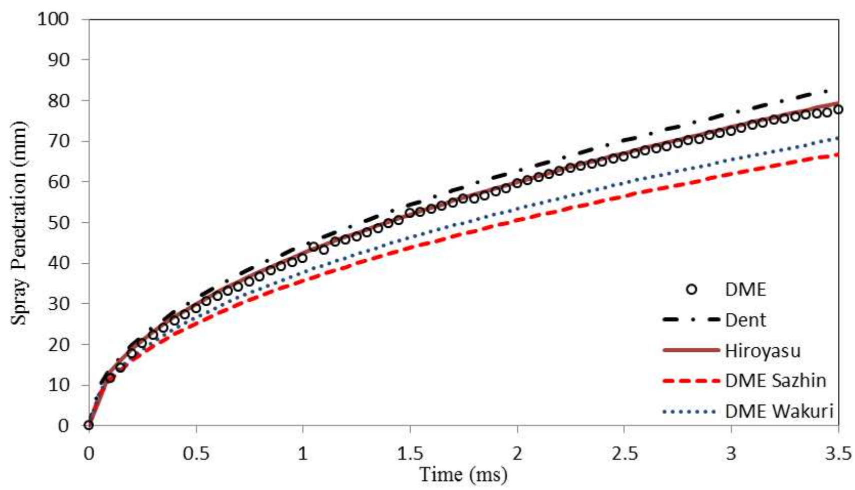


Figure 7.36: Comparison of experimental DME results to theoretical predictions at $P_{ambient}$=16.4 bar and $P_{injection}$=500 bar

Figure 7.37 shows DME penetration results at $P_{Ambient}$= 15.1 bar, $\rho_{Ambient}$ = 27.8kg/m$^3$ at $P_{Injection}$ = 500 bar. As in the 17.7 bar and, 16.4 bar tests the experimental DME penetration is accurately predicted by Hiroyasu, only differing by 5% until 0.55 ms and

1.4% thereafter. The DME penetration is also predicted well by Wakuri only deviating by on average 3% throughout the spray development. The DME is still over-predicted by Dent on average by 6.3% and under-predicted by Sazhin on average by 8%, although to lesser extent than the previous figures.

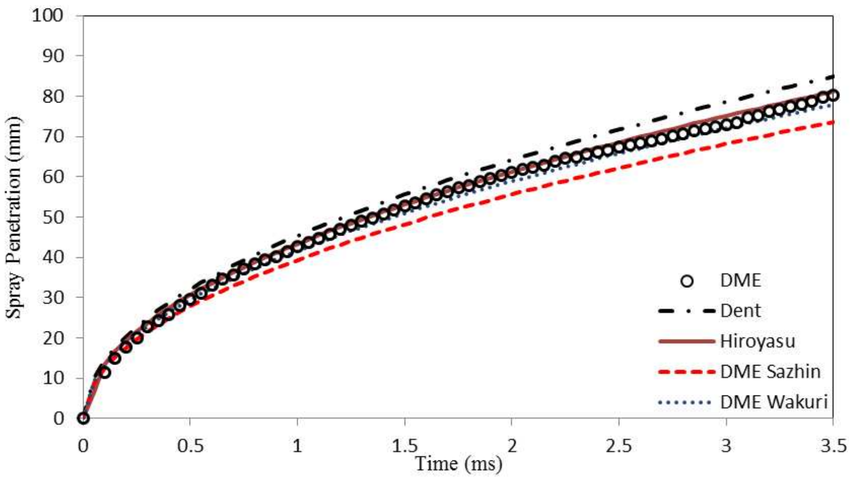


Figure 7.37: Comparison of experimental DME results to theoretical predictions at $P_{ambient}$=15.1 bar and $P_{injection}$=500 bar

Figure 7.38 shows the DME penetration at $P_{Injection}$ = 500 bar and atmospheric chamber pressure. The DME is not predicted well by any of the four models, it is over-predicted for most of the visible spray. It follows a similar trend as Hiroyasu up until 0.5ms, thereafter it approaches the Sazhin and Dent models until the spray reaches the chambers window limit.

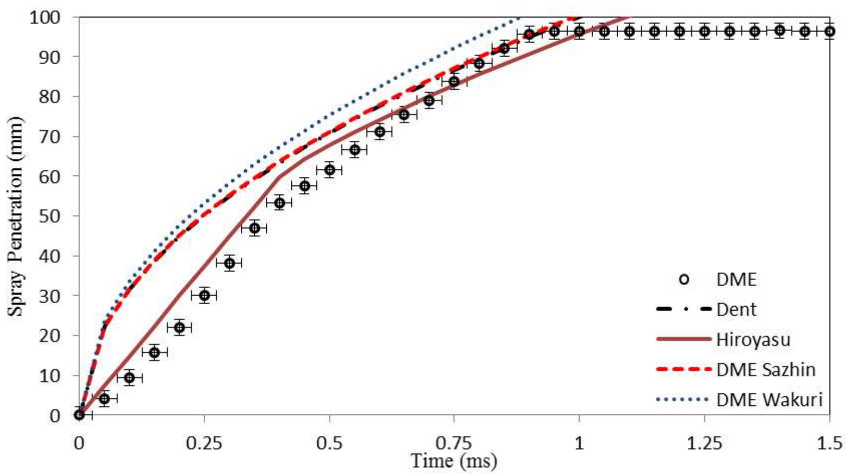


Figure 7.38: Comparison of experimental DME results to theoretical predictions at $P_{ambient}$= atmosphere and $P_{injection}$=500 bar

The trends between the four models are the same as found for the diesel results, Sazhin and Wakuri increase relative to Hiroyasu and Dent as the chamber pressure decreases and Hiroyasu and Dent predict similar penetration, only being offset by a maximum of 5mm, as did Sazhin and Wakuri. The DME penetration at all injection pressures and the five highest chamber pressures (62% of the tests conducted) were best predicted by Hiroyasu, only differing by a maximum of 5% in the worst case, this agreed with the findings of Suh et al[38]. The DME results for the mid range of the chamber pressures tested appeared to straddle the Hiroyasu and Dent model, they were reasonably well predicted by Dent in this region, which matches Yu et al's[3] findings (although Yu et al stated that all his results were best predicted by Dent). The DME penetration at the lower pressures were better predicted by either Sazhin or Wakuri, generally falling either on Sazhin or Wakuri or in between the two. At the lower pressures, the initial 0.4 ms of penetration is slightly over-predicted by Sazhin and Wakuri, and at times Dent, and it followed Hiroyasu slightly better at this time as seen in Figure 7.39. The exceptions, though, are the DME tests at atmospheric chamber pressure, where they are over-predicted by all the models, although they are reasonably close to the Hiroyasu model. This is most likely due to the phase change of the DME at atmospheric conditions. The phase change will occur much more easily as the conditions within the chamber will be above DME's boiling point.

Comparing the predictions for both DME and diesel, the Hiroyasu and Dent models do not change for the two fuels, except for Hiroyasu at lower chamber pressures as the break-up time is a large portion of the observed spray and fuel density is taken into account in the pre-breakup calculation as mentioned above. The Sazhin and Wakuri predictions for DME are generally lower than those for diesel, because of the cone angles: the DME cone angle is generally larger than that of the diesel spray, and an increase in cone angle results in a decrease in penetration in these two models.

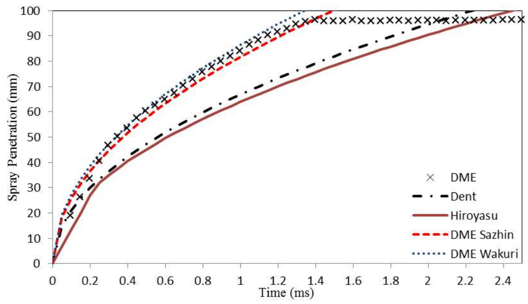


(a)

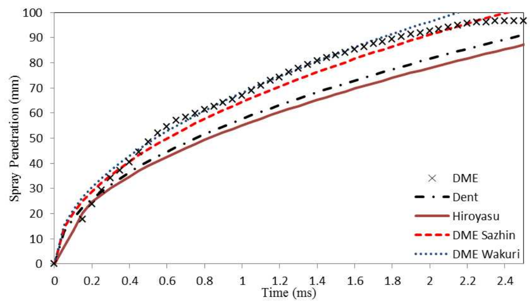


(b)

Figure 7.39: Spray penetration for DME at 500 bar injection pressure and (a)$P_{ambient}$ = 3.28 bar, and (b) $P_{ambient}$ = 5.91 bar

## 7.4 Spray Images

Figures 7.40, 7.41, and 7.42 show the spray images for diesel and DME at $P_{Injection}$ = 500 bar and $P_{Ambient}$ = atmosphere, 13.8 bar, and 17.7 bar respectively. The images for spray under atmospheric chamber pressure are given at time steps of 0.1ms from each other, and the remaining images at the two higher pressures are shown at time steps of 0.3ms.

Analysing the images at atmospheric chamber pressure, Figure 7.40, it is clear to see that the diesel spray progresses through the chamber with greater ease. The diesel spray is fine and appears to maintain a liquid core along the entire length of the spray, while the fuel at the edges of the spray appears to atomize into a fine mist. The diesel spray has a sharp tip and the spray structure in this case is not quite conical as the two spray edges bow slightly. This bow which starts close to the nozzle is what results in a larger cone angle than one would expect. The DME spray is quite different to the diesel spray, it is not as sharp and has a more rounded tip and the spray edge is gaseous. The conditions within the test chamber in which DME is being injected is conducive to a phase change, which explains why the DME, as it progresses through the chamber, starts to flash boil and vaporizes more easily. This results in a large spray when compared to diesel, and when analysing both ends of the spray this is evident. The width of the spray exiting the nozzle is about twice the size of the diesel spray at the same point. The spray does not form a cone which originates at the nozzle hole, the spray seems to expand as it comes out of the orifice and it then starts forming a cone which the rest of the spray follows. The leading tip of the DME spray is largely in the gaseous phase during the later spray development. The liquid DME tends to vaporize into gas before reaching the boundary of the chamber windows.

Figure 7.41 shows the spray images for diesel and DME at the midrange of the chamber pressures tested. It should be noted that the background of the DME images appears more noisy than the diesel images. This phenomenon is a result of DME being at an extremely low temperature; the DME cools the injector and the upper surface of the test chamber (as it is in direct contact), thus causing a temperature difference between the upper and lower parts of the chamber. The extreme cold also can cause the injector to shrink, therefore creating a leak. The higher the pressure of the gas within the chamber, the larger the pressure difference which will cause the pressure in the chamber to drop faster, resulting in a slow moving swirl producing a non-uniform background in the schlieren images. This swirl is not strong enough to affect the spray. As in the previous set of images the cone angle of DME is again larger than that of diesel, but to a lesser extent than at atmospheric pressure, and the penetration of the

DME spray is slightly slower than the diesel spray. The DME spray tip has a flatter appearance compared to that of diesel for most of the spray development. At the point around a quarter of the window length, the diesel spray edge appears to be atomizing and gas is entrained in the fuel spray. The edges of the diesel spray from this point on consist of a large part of ambient gas, and at times appear to be fish bone in nature, as referred to by Karimi [15]. The spray before this point, is solid and liquid and does not appear to have much gas mixed in. A perturbation forms on the edge of the spray and once it has fully developed it is shed, as shown in Figure 7.41. The perturbation still affects the spray but it does not seem to progress further. The shed perturbation appears to remain at the same location even when the spray has developed past it. Something similar occurs in the DME spray but in these images the perturbation are much smaller. The edges of the DME spray also show that the DME has ambient gas in the spray, perhaps a mixture of gaseous DME and $CO_2$ exists. The DME spray edge is slightly more defined than the diesel spray, where the edge most likely consists of diesel fuel droplets and gas, refracting the light less than a mixture of DME and the surrounding gas.

Figure 7.42 shows the spray images at the highest tested chamber pressure. The fish bone effect is seen again in the diesel spray edges and towards the later stages of spray development it appears that gas is entrained in the spray. Although it is difficult to see, the DME spray has gas entrained in the latter stages of the spray as well as the spray edges. The DME mixture with the chamber gas refracts the light consistently more as it is a more dense mixture than the surrounding gas (DME starts flashing and will occupy more volume), compared to the diesel-gas mixture which will consist mainly of fuel droplets and the light will be able to get through some spaces in between the fuel droplets. The DME peels off the spray edges as the spray is developing. The DME spray is not too dissimilar to the diesel spray as its penetration is only slightly less than that of diesel but its cone angle is slightly larger. This is an advantage as one is looking to increase the surface area of the fuel spray in order to produce good and efficient burning of the fuel. Again the DME spray straight after the nozzle appears to be much wider than the diesel spray at the same location. This could be due to DME having a lower density which means the high chamber density would have a larger effect on the DME as it exits the nozzle. This also explains why the DME spray is generally slower than the diesel spray, as its momentum will be affected more at the same pressure, due to lower density. The DME tends to linger slightly longer than diesel once the injection has ceased and the spray edges become extremely wavy as seen in the last frame. During the injection the diesel spray edges in the $60D_o$ region remain relatively straight and do not appear to fluctuate whereas the DME spray edges are not as straight and fluctuate slightly due to the DME peeling off on these edges.


Figure 7.40: Comparison between 500 bar Diesel and DME injections into atmosphere at time intervals of 0.1ms

Diesel Images

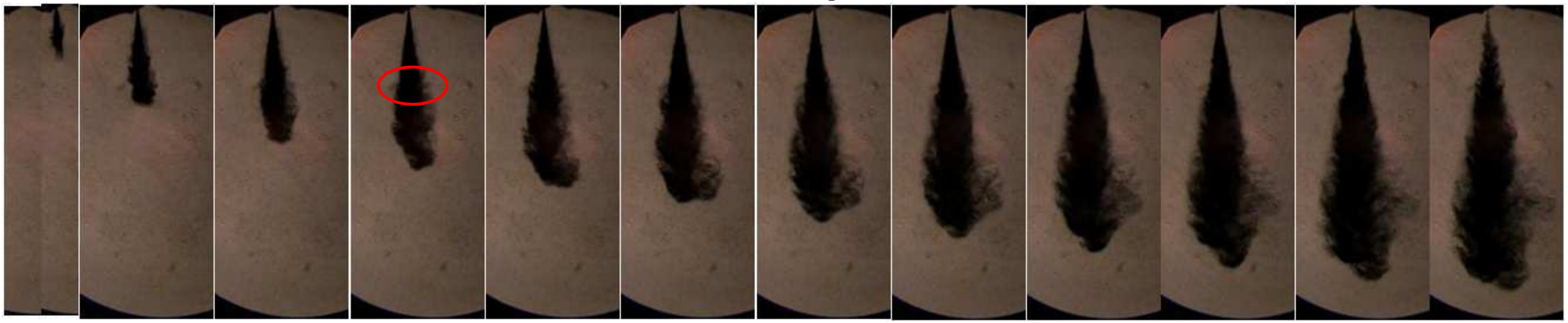

DME Images

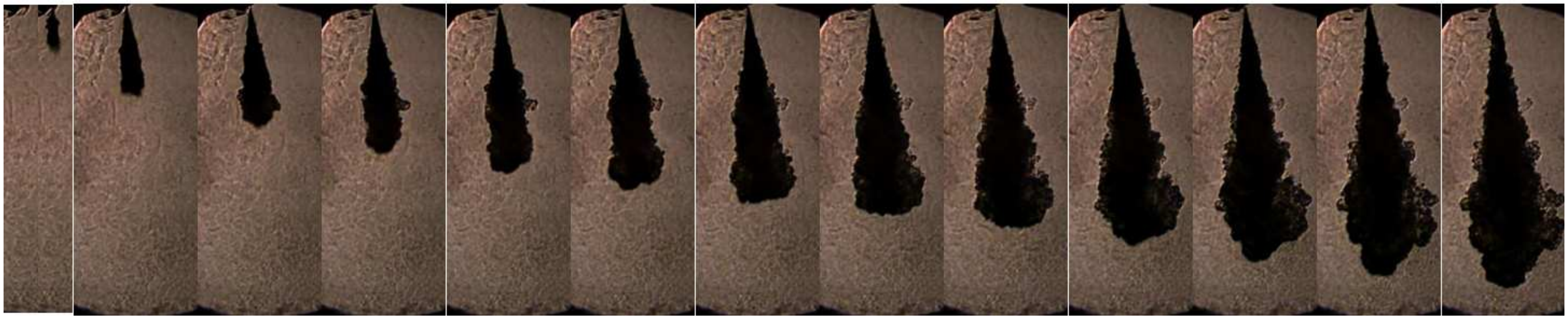

Figure 7.41: Comparison between 500 bar Diesel and DME injections into 13.8 bar $CO_2$ chamber pressure at time intervals of 0.3ms

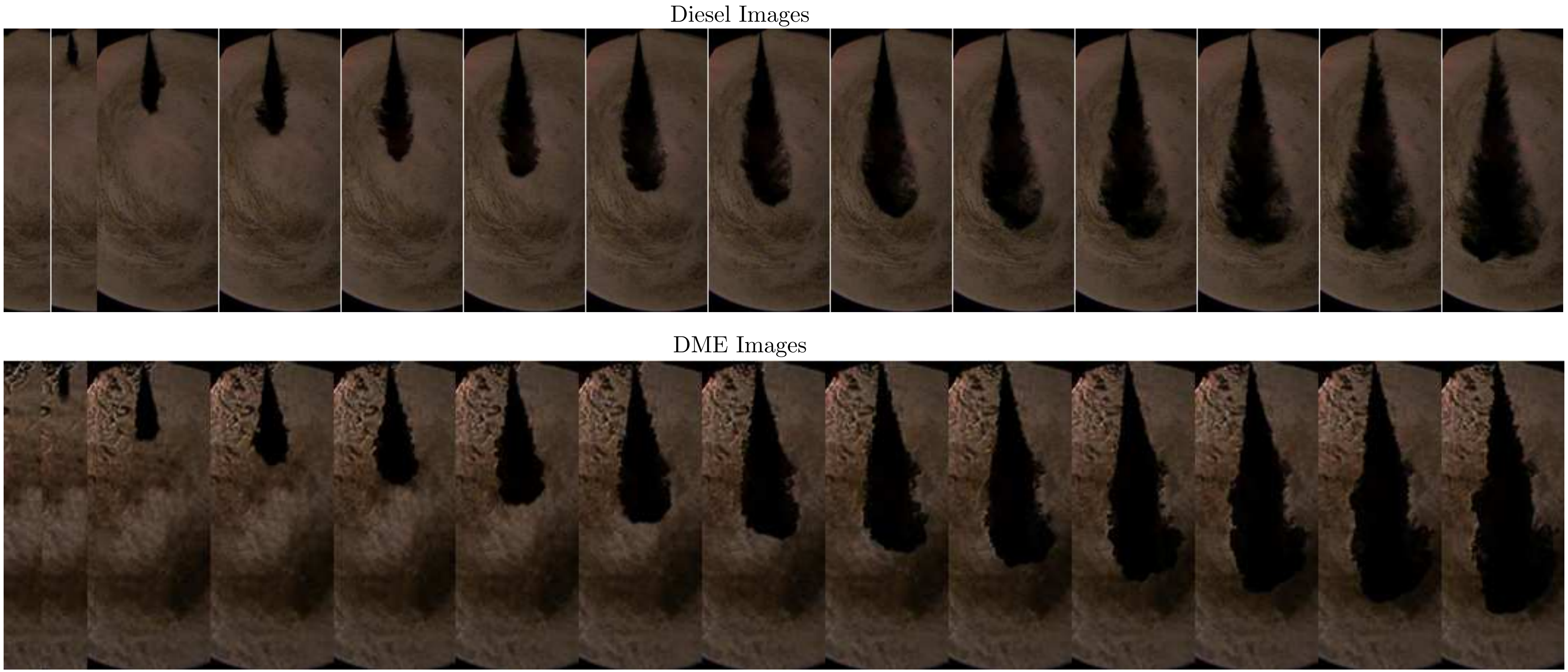


Figure 7.42: Comparison between 500 bar Diesel and DME injections into 17.7 bar $CO_2$ chamber pressure at time intervals of 0.3ms

## 7.5 Mean Tip Velocity

The mean spray tip velocity is the velocity of the spray front at each frame and is calculated by measuring the distance the spray progresses over one frame and dividing it by the period of the frame. The mean tip velocity graphs give an indication of how fast the spray tip progresses through the ambient gas and how the entrainment of gas into the fuel spray affects its velocity. Figure 7.43 shows the tip penetration for diesel and DME at atmospheric chamber pressure and 500 and 300 bar injection pressures respectively. The diesel tip velocity overall is faster than that of DME. At $P_{Injection}$=500 bar Figure 7.43(a) for the initial 0.1ms the diesel and DME tip velocities are the same (70m/s at 0.05ms and 100m/s at 0.1ms), the diesel tip velocity then continues to increase sharply whereas the DME velocity increases at a much slower rate. The tip velocity of the diesel spray is more erratic compared to that of DME, reaching a maximum of 300m/s whereas the DME slowly increases to a maximum of 160m/s, and then decreases to more or less constant velocity. Figure 7.43(b) shows a similar trend to (a), except that for the initial 0.1ms DME has a higher velocity than diesel. This could be due to the fact that DME is less dense and has a lower viscosity compared to diesel, thus when the needle is uncovering the orifice, the DME is able to get past with more ease. However, once the needle is fully open the momentum of the diesel is far greater giving it a higher velocity, particularly in the sprays at atmospheric pressure. DME begins to flash boil under atmospheric conditions and will thus tend to move slower as gas becomes entrained in the spray. It is also apparent that as the injection pressure is increased the peak tip velocity increases, as can be noted in the majority of tests conducted which are given in Appendix F.

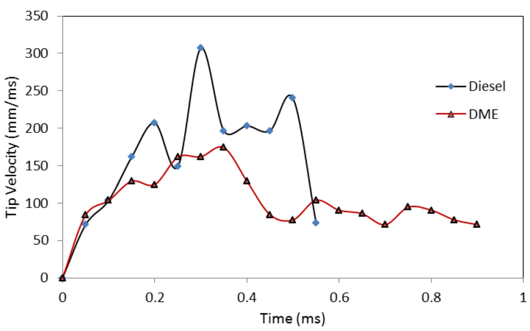


a)

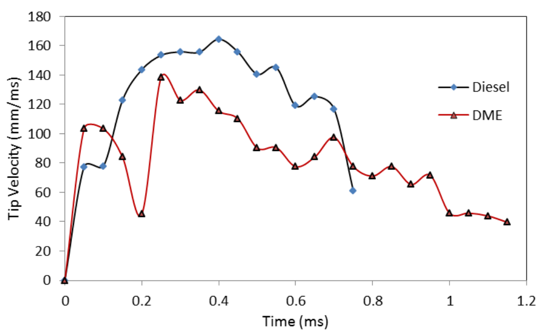


b)

Figure 7.43: Diesel Spray Tip Velocity comparison of Diesel and DME at $P_{ambient}$ = 1 bar and (a)$P_{injection}$ = 500bar (b) $P_{injection}$ = 300bar

Figures 7.44 and 7.45 show the tip velocity at the highest chamber pressure/density. The tip velocity of the diesel spray seems to be slightly higher than that of DME for both injection pressures, although not by much. Both fuels start off with a high tip velocity which then gradually decreases as the spray progresses through the dense gas. As the fuel begins to vaporise and gas becomes entrained in the spray the velocity decreases. The velocity of the liquid core might still be relatively high and this pushes the fuel forward but at the tip the velocity decreases. At this particular chamber pressure the maximum tip velocity for DME and diesel at the highest injection pressure is lower than that of the lower injection pressures, this is the only case in the set of results obtained. It should be noted that the initial velocity of the tip penetration carries some uncertainty as it is difficult to distinguish between the first and the second spray at higher chamber pressures, but after 0.2ms after start of injection the uncertainty is reduced as the spray observed in the images is conclusively the second spray. The tip velocity of the DME, although the overall trend is the same, fluctuates more along the mean compared to diesel as the spray progresses. This was seen in the majority of the tests conducted.

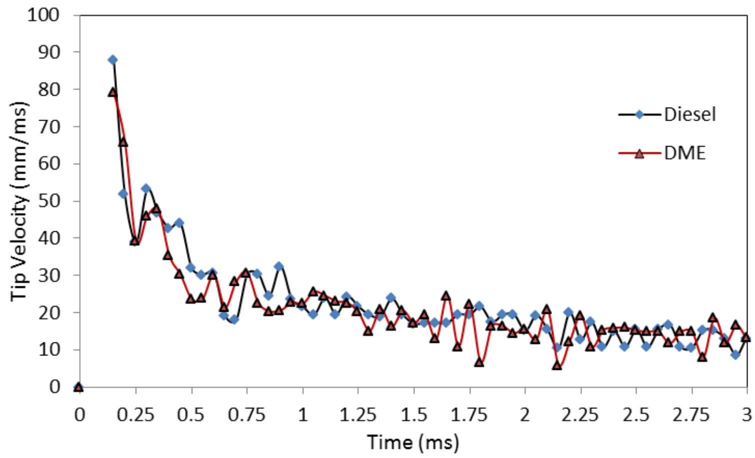


Figure 7.44: Spray Tip Velocity comparison of diesel and DME at $P_{ambient}$ = 17.7 bar and $P_{injection}$ = 500bar

In order to have an idea of the tip velocity of a predicted spray, the Wakuri model was chosen. The derivative of this model was calculated and the predicted spray tip velocity curve was obtained and is shown in Figure 7.45. The experimental data follows a similar trend to the predicted tip velocity for both diesel and DME. The only discrepancy being in the initial 0.2ms, which is known to carry a large uncertainty due to the difficulty of measuring the second spray tip at these times.

Figures 7.46 and 7.47 show the tip velocity for various chamber pressures at 500 bar injection pressure for diesel and DME. The mean tip velocity for all the higher chamber pressures seem to follow the same trend. Between 0.25ms -0.5ms it can be seen that the tip velocity for the higher pressures is slightly slower than those at the lower pressures.

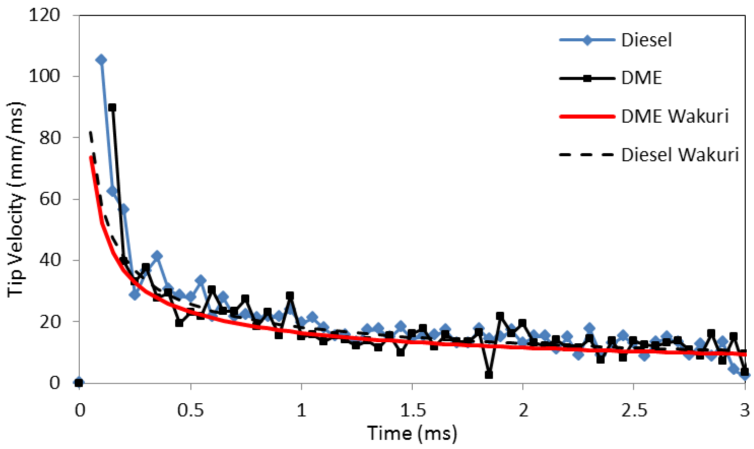


Figure 7.45: Spray Tip Velocity comparison of diesel and DME at $P_{ambient}$ = 17.7 bar and $P_{injection}$ = 300bar

As the tip velocity decreases there does not appear to be any strong trend between the tip velocities with regard to the chamber pressure. The lower chamber pressure tests do seem to have a slightly faster tip velocity compared to the higher chamber pressures but not by much. The tip velocities range over 15m/s for the diesel results and 20m/s for the DME results.

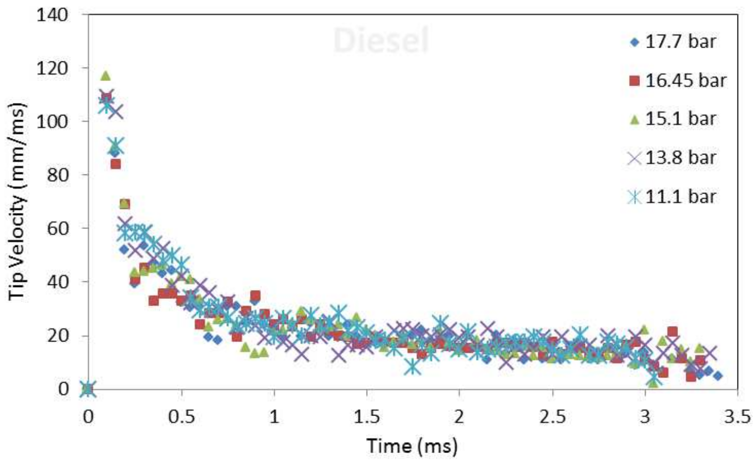


Figure 7.46: Effect of chamber pressure on diesel mean tip velocity at $P_{injection}$=500 bar

The mean tip velocity results obtained for DME correlated reasonably well with the findings of Park et al [36]. Although the conditions tested were not identical, they were reasonably close to draw a comparison between them. The values were of the same orders of magnitude although they were slightly higher in Park et al's results as his injection pressure was at 600 bar.

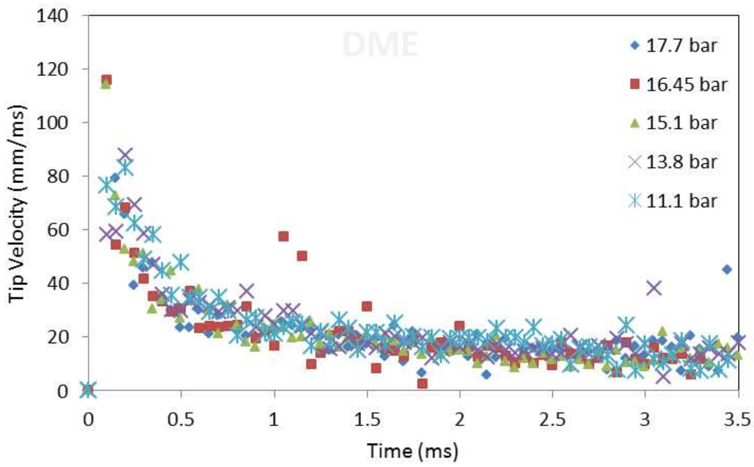


Figure 7.47: Effect of chamber pressure on DME mean tip velocity at $P_{injection}$=500 bar

## 7.6 Fuel line History

The fuel line pressure was measured between the injector and the common-rail. The pressure history gives an indication of the behaviour of the fuel pressure during injection, and during normal operation. The pressure traces show how the fuel reacts to injection events, how fast the fuel pressure recovers from injection events, as well as how the pressure is regulated within the common rail. The pressure trace measurements in this study are synchronised with the injection events, allowing the spray images and quantitative data extracted from the images to be matched to the traces. The orifice at the inlet of the high pressure pump was removed in order to prevent throttling of DME across it, which would cause vaporisation thereby making it difficult to pressurize.

### 7.6.1 Diesel Fuel Pressure History

Figure 7.48 shows the pressure trace for a diesel test at $P_{ambient}$ = 17.7 bar $CO_2$ (27 bar air pressure), and $P_{injection}$ = 500 bar. The injections are identified by the sudden pressure drops, the pressure then oscillates and after a few hundred microseconds returns to the set rail pressure before the second injection occurs. The pressure drops by approximately 30 bar as the injector needle starts opening (6% drop), once the needle opens the pressure increases and drops as the high pressure pump and pressure regulator attempt to compensate for the loss of pressure through the injector. The pressure in the rail returns consistently to the set pressure after each injection. This is shown in Figure 7.49 where after ten consecutive injections the pressure returns to its set point. The time between injections was also reduced to 50ms and the pressure recovered well after each injection and the set pressure was maintained throughout. The initial drop at the start of injection is around 15 to 20 bar for the 200 bar injections (7.5% drop) which is less than the initial drop seen in the 500 bar injections.

Figure 7.50 shows the pressure trace for a diesel test at $P_{ambient}$ = 16.4 bar $CO_2$ (25 bar air pressure), and $P_{injection}$ = 400 bar. The pressure within the rail is consistent, and the pressure recovers well after injection events and maintains the set pressure of 400 bar. The same result was found for the diesel pressure traces at 200, 300, and 600 bar. The pressure in the common rail is not affected by the chamber conditions, thus all the pressure traces for the respective injection pressures are the same. The pressure on average drops by about 6 - 7% in the very early stages of injection for all the injection pressures tested. It was noted that generally the pressure recovers to within $+/-$ 5 bar of the set pressure in roughly 30 - 50ms after the start of injection.

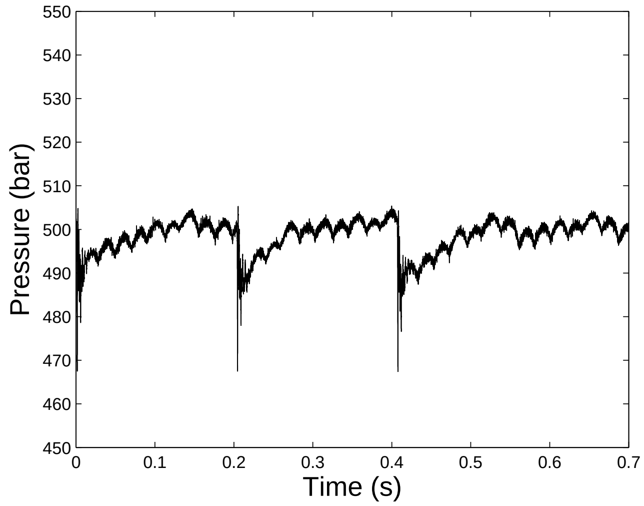


Figure 7.48: Diesel Pressure Trace at 500 bar Injection Pressure and 17.7 bar $CO_2$ Chamber Pressure (32.7kg/$m^3$)

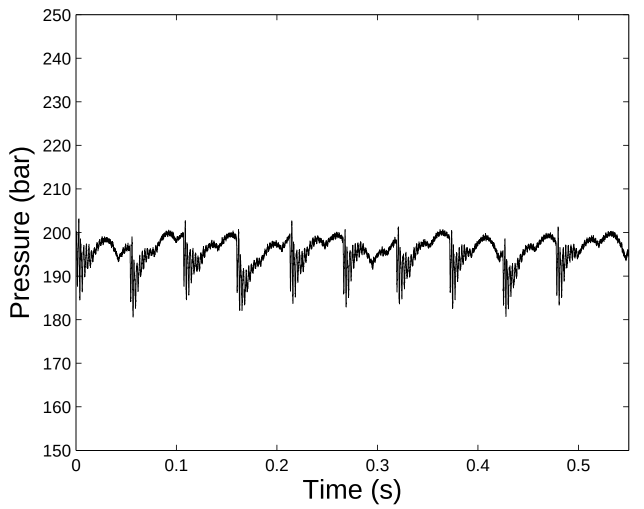


Figure 7.49: Diesel Pressure Trace at 200 bar Injection Pressure and atmospheric Chamber Pressure with 50ms injection interval

The section in between the injection events seems to follow half a sinusoidal pattern, where the humps are most likely due to the piston arrangement in the high pressure pump. The fuel pressure varies by $+/-$ 5 bar in this region. The pistons are $120^o$ out of phase causing the pressure fluctuations. The period in between the peaks is measured as approximately 20.9ms as illustrated in Figure 7.51. When considering the rotational speed of the pump (16 Hz) and the fact there are three pistons all equally offset by $120^o$, the period between the top dead centers of two consecutive pistons (which the pressure peaks should coincide with) was calculated to be 20.833ms. This indicates

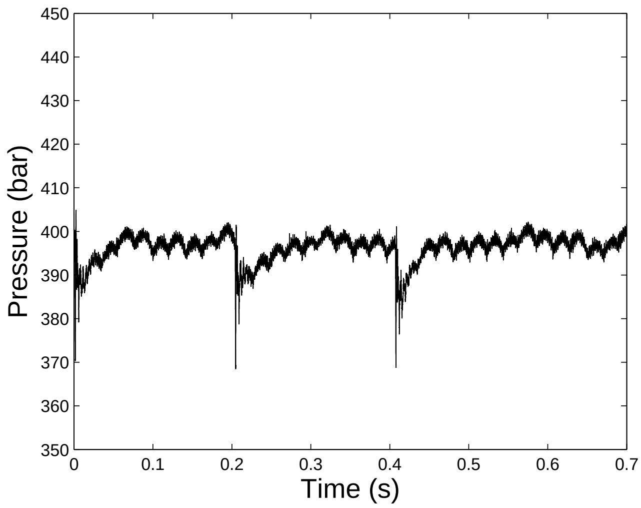


Figure 7.50: Diesel Pressure Trace at 400 bar Injection Pressure and 16.45 bar $CO_2$ chamber pressure (30.2kg/$m^3$)

that the pressure humps are most likely due to the piston arrangement of the high pressure pump.

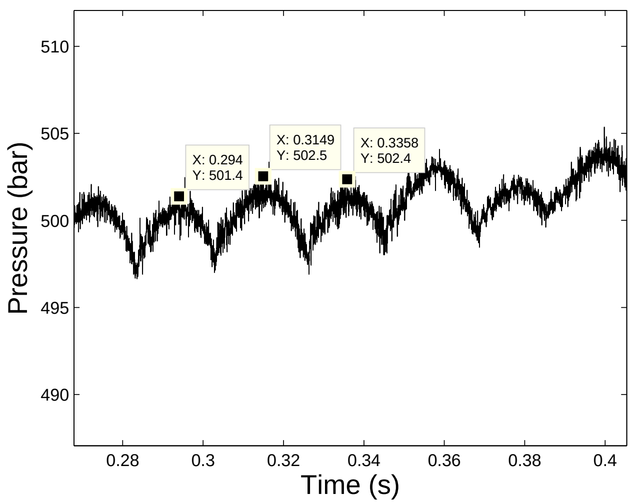


Figure 7.51: Magnified pressure trace illustrating pressure variation due to offset piston arrangement

Figure 7.52 shows how the pressure in the rail varies as the spray penetration progresses, where the pressure drops once the needle is fully lifted. The drop in pressure or fluctuation in pressure during the injection does not seem to have any effect on the actual penetration itself. After the initial drop, the pressure oscillates back to the set pressure, the amplitude of oscillations is low and oscillations caused by injection quickly dissipate.

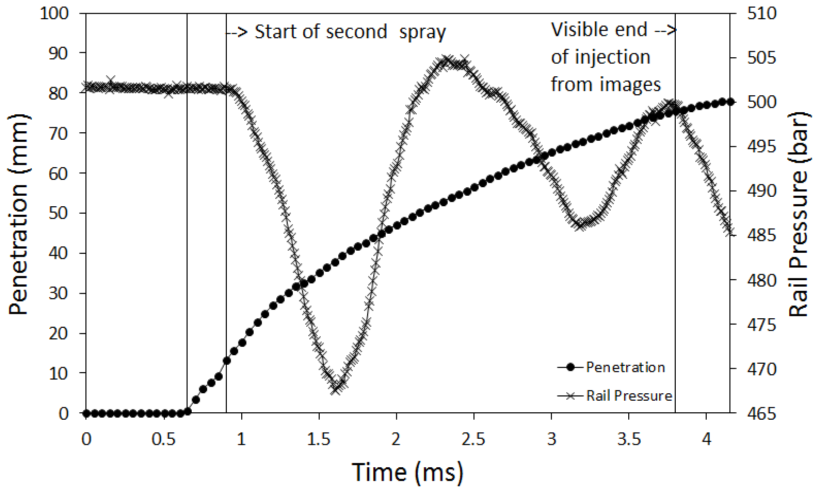


Figure 7.52: Magnified rail pressure superimposed with spray penetration at 500 bar Injection Pressure and 17.7 bar $CO_2$ Chamber Pressure (32.7kg/$m^3$)

### 7.6.2 DME Pressure Trace

The properties of DME make it substantially more difficult to achieve a consistent pressure in the common rail and the entire injection system. The largest problem with DME is the fact that it vaporises in the fuel injection system, resulting in problems with the pump and common rail regulator. When vapor bubbles are present in the rail a vapor lock forms and no flow occurs through the pressure regulator valve in the common rail. When vapor is present in the pump, the pump is attempting to compress the gas and therefore is not able to pressurise the DME to the high rail pressures required for injection. This emphasised the importance of maintaining DME in liquid form by cooling and pressurising it as well as bleeding the injection system appropriately.

Figure 7.53 shows pressure traces obtained during initial DME testing. The pressure in the rail was quite erratic but did not seem to steadily drop off by 100 bar by the end of all of the injection events, opposed to that experienced by Alimia [40]. Figure 7.53 (a) shows the first injection starting at 295 bar, the pressure then dropped by 50 bar but recovered to 310 bar where the two subsequent injections remained close to 310 bar, thereafter the pressure behaved erratically once again. The pressure in Figure 7.53 (b) behaved erratically throughout the whole test, oscillating by 60 bar at some points and the injections all occurred at different pressures (although only +/- 20 bar from each other). The erratic nature of the pressure in the rail is most likely to be attributed to the two phase DME present in the fuel injection system. If there is any vapor present in the system it could, for example, cause the pressure to drop and as soon as liquid enters the pump the pressure rises. Therefore, if the supply is not consistent the pressure will most likely be erratic as the pump attempts to pressurise the two phases of DME.

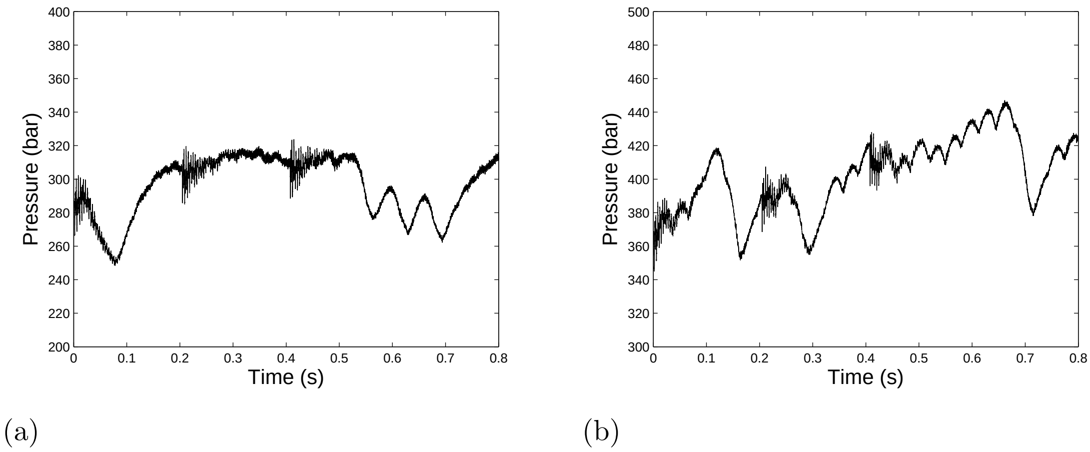


Figure 7.53: DME pressure trace at $P_{ambient}$ =5.9 bar $CO_2$ ($\rho_{ambient}$ = 10.88kg/$m^3$) (a) $P_{injection}$ = 300 bar (b) $P_{injection}$ = 400 bar

It was due to the difficulty of pressurizing DME (by following the methodology previously proposed by Mansfield, Mtshuluana and Alimia, and the results obtained in initial tests) that possibly the previous method used to bleed the fuel injection system with DME was insufficient. The current method which was used to bleed the system yielded results which were a significant improvement, and the pressure traces obtained were more consistent and behaved similarly to those of diesel as seen in Figure 7.54. Although, it should be noted that this method was difficult to perform and was only perfected at the higher chamber pressures tested. These tests showed a stable rail pressure throughout the test where the pressure was maintained even after injection events. It was also noticed that when the system was bled in the current manner, the pressure traces were consistently better and behaved in the desired manner. The common rail system ran as if diesel were being pumped through the system, no knocking or grinding noises were heard from the pump. The system ran smoothly and the pressure was easily controlled. Although some traces had some problems such as a pressure drop after the first injection or the pressure seemed to increase for each subsequent injection. This was due to the fact that the pressure regulator was being increased to the set pressure when the test was run and may have overshot the mark. The results indicate that if DME is bled correctly so that all vapor bubbles are removed, then the pressure can be regulated and maintained as desired. It was also for this reason that the proposed lubrication system was not used in the running of these tests as the pump operated as desired. Only for longer duration tests should the lubrication system be used.

Figure 7.55 shows an enlarged pressure trace of a 500 bar injection. The pressure in the rail recovered to the set pressure after each injection event and did not slowly decrease after all three injection events. The pressure dropped by 35 to 40 bar just after the start of injection (8%). The pressure appears to reach the set pressure 40 - 60ms after start of injection, which is slightly more than diesel and is possibly due to DME having a lower bulk modulus than diesel, it would thus require slightly more time for the pumping system to pressurise the DME.

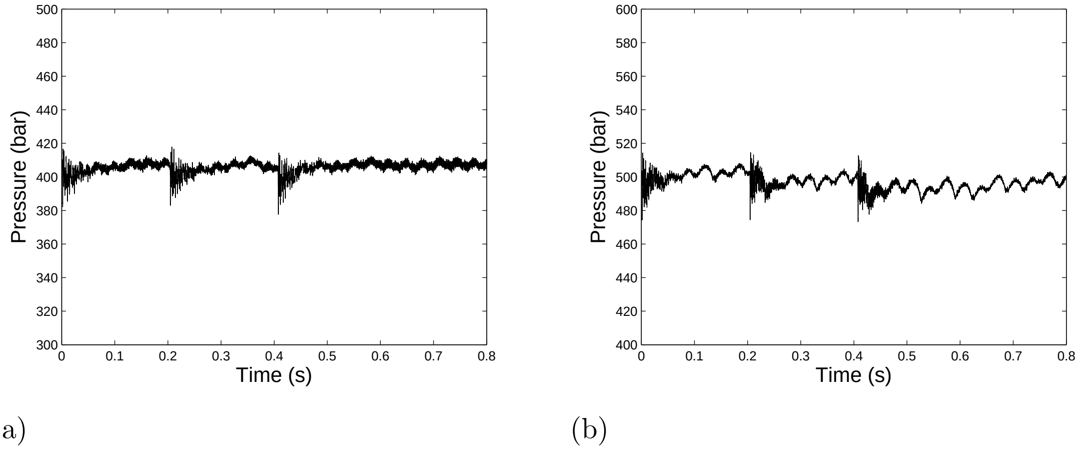


Figure 7.54: DME pressure trace at $P_{ambient}$ =17.7 bar $CO_2$ ($\rho_{ambient}$ = 32.7kg/$m^3$) (a) $P_{injection}$ = 400 bar (b) $P_{injection}$ = 500 bar

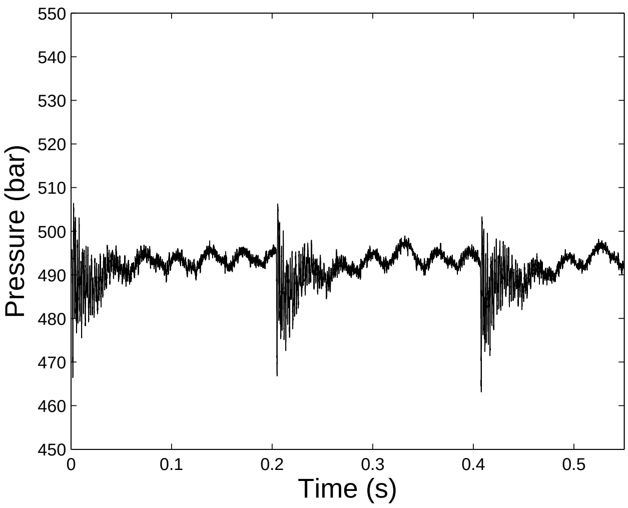


Figure 7.55: DME enlarged Pressure Trace at 500 bar injection pressure and 17.7 bar $CO_2$ chamber Pressure (32.7kg/$m^3$)

Figure 7.56 shows the DME and diesel pressure traces at 500 bar injection pressure overlapped. The initial drop in pressure after the start of injection is slightly more for diesel but only by about 5 bar. The oscillations in pressure for DME are greater than those of diesel by about +/- 20 bar versus diesel which oscillate by approximately 10 bar at most. Comparing the current results to the previous results obtained at The University of the Witwatersrand no difference was found in terms of the main aspects:

large drop initially for diesel, the larger oscillations in DME, and the longer period of oscillations for DME. The current results were analysed more closely over the actual injection period and this allowed for a good analysis of the features. The oscillations in pressure for DME last longer than those of diesel, which agrees with results obtained by Yu et al[3] although the amplitude of oscillations with DME were smaller than those of diesel in Yu's tests. The possible reason for this difference is that Yu et al used an air driven pump and different pressure regulator and this would result in a change in the way the pressure is maintained in the accumulator.

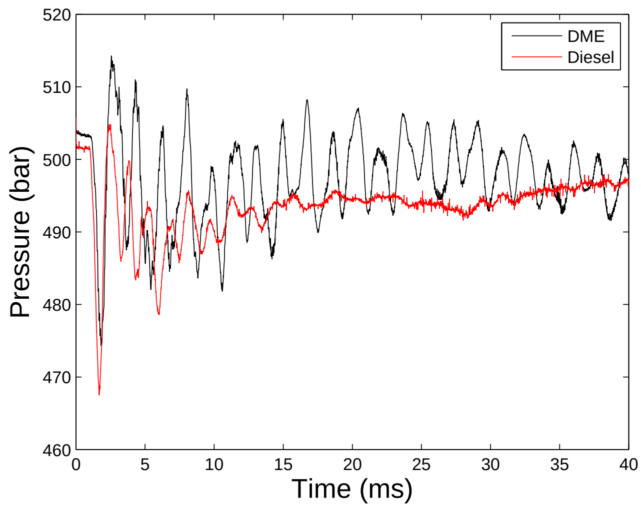


Figure 7.56: Diesel vs DME pressure trace at 500 bar injection pressure

# 8 Conclusions

Analysing the results obtained for DME and Diesel during this study the following conclusions were drawn:

- An adequate Experiment controller was developed in order to control the test process. The controller allowed synchronization of the images and pressure traces to the injection events. This aided in the comparison of injection delay times between the two fuels, the different injection parameters, and being able to match images to injection pressure values at which those images were recorded.
- The spray penetration for both fuels increased with an increase in injection pressure, on average the penetration increased by 7% per 100 bar.
- The mean spray tip velocity for both fuels seemed to increase with and increase in injection pressure for majority of the tests and the tip velocity decreased as the chamber pressure was increased. The DME tip velocity was slightly more erratic towards the later stages of spray development. DME tip velocity was slightly slower than that of diesel but more so at the lower chamber pressures.
- The chamber pressure was tested from atmospheric pressure to 17.7 bar absolute with $CO_2$, which simulated an air chamber pressure of 27 bar absolute in terms of density. The spray penetration at each time step decreased with an increase in chamber pressure/density for both diesel and DME. The change in penetration with a change in density of 2.5kg/m$^3$ was about 5 - 10 % for both fuels.
- The diesel cone angles did not have any strong correlation to a change in injection pressure. The DME cone angle appeared to have a relationship with the injection pressure, increasing with an increase in injection pressure, by about a maximum of $1^o$. The spray cone angle increased with an increase in chamber pressure/density for both fuels. The cone angle seemed to increase linearly with an increase in chamber pressure, although the predicted values using Hiroyasu and Arai model did not show the same linear relationship. The DME cone angles were consistently larger than that of diesel.

- It was found that the largest influencing factor in the spray penetration was the chamber density, where a high chamber density and low chamber pressure yielded the same penetration results as tests done at high chamber density and pressure. The high chamber pressure using nitrogen was merely a means of achieving a high ambient density, but with carbon dioxide a high chamber density was achieved at a lower chamber pressure.

- It was found that the theoretical over-prediction of the DME and diesel results in previous studies,[40][4], was due to the imbalance of pressure around the injector needle. This caused it to intermittently close the single orifice as it lifted, resulting in an initial spray and after 0.15ms the spray would hesitate or stop and the second spray would then emerge through the initial spray. The second spray took time to travel past the initial spray and this is seen by the flat part of the penetration curve for both diesel and DME until 0.3-0.4ms. Tests with a multi-hole injector did not display this hesitation. The initial spray was then factored out and the experimental spray penetration in the early stages of spray development showed a much better correlation to the theoretical predictions and thus no attempt was made to develop a correlation.

- The rail pressure for diesel was consistent with what is expected and previous results. The pressure drops by about 6-7% as the injection commences but then oscillates back to the set pressure after a few milliseconds, the oscillations have low amplitudes and are dampened quickly.

- The DME rail pressure was more unstable when compared to diesel, but when the common rail system was bled thoroughly with DME (noting that this process is difficult and did not occur with 100% of the tests conducted) the rail pressure obtained was stable and after each injection event it returned to the set pressure. If any vapour bubbles were present in the common rail system the pressure within the rail and the operation of the high pressure pump were unstable.

- Using the cone angles measured at $60D_o$ and shifting the penetration curves to factor out the initial spray, the diesel penetration results were predicted well by Wakuri for 70% of the tests conducted, these results being on the higher range of chamber pressures tested. At the higher chamber pressure tests, the penetration was also reasonably predicted by Dent (45% of the tests). Whereas Sazhin predicted the results more closely in the mid-range of the chamber pressures tested and decreasingly predicted the experimental penetration to the low-range of chamber pressures tested.

- The DME results (again shifting the penetration curve to factor out the initial spray) were best predicted by Hiroyasu for 63% of the tests conducted with DME, at the higher chamber pressures. The penetration at the lower chamber pressures was predicted well by both Sazhin and Wakuri, generally being between, or coinciding with one of the two models.

- The results for DME show promise as the penetration curves obtained for DME were not far off from the diesel curves at each respective pressure. The penetration was shorter but the cone angle was wider; the wider cone angle means the fuel has an increased surface area which should aid in the effective combustion of the fuel. DME follows the same penetration profiles as diesel, therefore in terms of spray characteristics a desired profile which is successful with diesel (for a certain engine) can be effectively achieved using DME, with either a slight increase in injection pressure or a decrease in chamber pressure.
- When DME is bled thoroughly, a stable injection pressure can be achieved. The pump can handle the DME but a better lubrication system or a pump which is designed for DME and has a stronger shaft seal, which is able to withstand the full 4 bars of pressure from the DME cylinder, would improve future tests.

# 9 Recommendations

Significant improvements to the test rig were made compared to previous projects on the apparatus in question. There are still modifications that can be made in order to progress the DME testing capabilities. Some future recommendations in order to improve or aid in improving the running or processing of data are given as follows:

- Obtain different lenses for the schlieren system in order to magnify the image to fill the CCD of the Camera in turn increasing the resolution of the images.
- Install thicker windows in the test chamber in order to be able to test higher pressures, although the test chamber should be hydraulically pressure tested by a professional before testing can be conducted.
- In order to avoid the spray hesitation, a method of capturing or diverting the spray from the other 5 holes should be developed so that one spray can be properly analysed and the others will be freely dissipated but will not be blocked or impinge on the windows.
- A different common rail pump should be fitted, an available pump with an inlet seal pressure rating of 10 bar should be tried in order to eliminate the risk of rupturing this seal, as this was a common problem with the common rail pump used in this study.
- Run the high speed camera at as high a speed as possible, closer to 50 000fps if the image quality and lighting is acceptable and the entire chamber window is visible.
- Develop PID control or some other form of feedback control for the pressure within the rail. A separate DAQ card would be required.

# References


[1] Suh, H.K., Park, S.W. and Lee, C.S.: Atomization Characteristics of Dimethyl Ether Fuel as an Alternative Fuel Injected through a Common-Rail Injection System. *Energy & Fuels*, vol. 20, no. 4, pp. 1471–1481, July 2006. ISSN 0887-0624.
Available at: `http://pubs.acs.org/doi/abs/10.1021/ef050420f`

[2] Kim, H.J., Suh, H.K., Park, S.H. and Lee, C.S.: An Experimental and Numerical Investigation of Atomization Characteristics of Biodiesel, Dimethyl Ether, and BiodieselEthanol Blended Fuel. *Energy & Fuels*, vol. 22, no. 3, pp. 2091–2098, May 2008. ISSN 0887-0624.
Available at: `http://pubs.acs.org/doi/abs/10.1021/ef700692w`

[3] Yu, J. and Bae, C.: Dimethyl ether (DME) spray characteristics in a common-rail fuel injection system. *Proceedings of the Institution of Mechanical Engineers*, vol. 217, no. August, pp. 1135–1144, 2003.
Available at: `http://pep.metapress.com/index/777K12V628328M77.pdf`

[4] Cipolat, D. and Valentim, D.: Comparison of theoretical and experimental diesel and DME injection spray characteristics. *Fuel Processing Technology*, vol. 107, pp. 36–43, March 2013. ISSN 03783820.
Available at: `http://linkinghub.elsevier.com/retrieve/pii/S0378382012002779`

[5] Burman, P.G. and DeLuca, F.: *Fuel injection and controls for internal combustion engines*. Simmons-Boardman Publishing Corporation, 1962.

[6] Judge, A.W.: *High speed Diesel engines*. Chapman and Hall Ltd, 1967.

[7] Bennett, S.: *Modern diesel Technology: Diesel Engines*. Cengage Learning,, 2009.

[8] Delphi: Delphi common Rail Systems. 2011.
Available at: `http://www.dieselaftermarket.delphi.com.`

[9] et al Sanders, F.: *Diesel Mechanics*. Global Media, 2007.

[10] Centenial College: Common rail systems. 2011.
Available at: `Commonrailsystems.transportation.centennialcollege.ca.`

[11] Heywood, J.B.: *Internal Combustion Engine Fundementals*. U.S.A.: McGraw-Hill Inc., 1988.

[12] Busch, R.: Advanced Diesel Common Rail Injection System for Future Emission Legislation. In: *10th Diesel Emission Reduction Conference*. 2004.

[13] Roth, H., Gevaises, M. and Arcoumanis, C.: Cavitation Initiation, Its Development and Link With Flow Turbulence in Diesel Injector Nozzles. *SAE 2002-01-0214*, 2002.

[14] Lindström, M.: Injector Nozzle Hole Parameters and their Influence on Real DI Diesel Performance. 2009.
Available at: `http://kth.diva-portal.org/smash/record.jsf?pid=diva2:159595`

[15] Karimi, K.: *Characterisation of multiple-injection diesel sprays at elevated pressures and temperatures*. PhD Thesis, University of Brightom, 2007.
Available at: `https://www.brighton.ac.uk/shrl/publications/Diesel/Karimi_PhD_Thesis.pdf`

[16] Kilic, A., Schultze, L. and Tschöke, H.: Influence of Nozzle Parameters on Single Jet Flow Quantities of Multi-Hole Diesel Injection Nozzles. *SAE 2006-01-1983*, 2006.

[17] Solenoids: Solenoids and Actuators. 2003.
Available at: `http://robots.freehostia.com/Solenoids/SolenoidsBody.html`

[18] Olah, G.A., Goeppert, A. and Prakash, G.K.S.: Chemical recycling of carbon dioxide to methanol and dimethyl ether: from greenhouse gas to renewable, environmentally carbon neutral fuels and synthetic hydrocarbons. *The Journal of organic chemistry*, vol. 74, no. 2, pp. 487–98, January 2009. ISSN 1520-6904.
Available at: `http://pubs.acs.org/doi/abs/10.1021/jo801260fhttp://www.ncbi.nlm.nih.gov/pubmed/19063591`

[19] saddleback educational Publishing: *Alternative Fuels*. Saddleback Educational Publishing, 2010.

[20] Hoerdeski, M.F.: *Alternative Fuels: The Future of Hydrogen*. Fairmont Press Inc., 2008. ISBN 0881735965.

[21] International DME Assosciation: About DME. 2012.
Available at: http://www.aboutdme.org/index.asp?sid=48

[22] Arcoumanis, C., Bae, C., Crookes, R. and Kinoshita, E.: The potential of di-methyl ether (DME) as an alternative fuel for compression-ignition engines: A review. *Fuel*, vol. 87, no. 7, pp. 1014–1030, June 2008. ISSN 00162361.
Available at: http://linkinghub.elsevier.com/retrieve/pii/S0016236107002955

[23] Kim, M.Y., Bang, S.H. and Lee, C.S.: Experimental Investigation of Spray and Combustion Characteristics of Dimethyl Ether in a Common-Rail Diesel Engine. *Energy & Fuels*, vol. 21, no. 2, pp. 793–800, March 2007. ISSN 0887-0624.
Available at: http://pubs.acs.org/doi/abs/10.1021/ef060310o

[24] Youn, I., Park, S., Roh, H. and Lee, C.: Investigation on the fuel spray and emission reduction characteristics for dimethyl ether (DME) fueled multi-cylinder diesel engine with common-rail injection system. *Fuel Processing Technology*, vol. 92, no. 7, pp. 1280–1287, 2011. ISSN 0378-3820.
Available at: http://dx.doi.org/10.1016/j.fuproc.2011.01.018http://www.sciencedirect.com/science/article/pii/S0378382011000361

[25] Teng, H., McCandless, J. and Schneyer, J.: Thermodynamic Properties of Dimethyl Ether - An Alternative Fuel for Compression-Ignition Engine. *SAE Technical Paper 2004-01-0093*, 2004.

[26] Teng, H. and McCandless, J.C.: Comparative Study of Characteristics of Diesel-Fuel and Dimethyl-Ether Sprays in the Engine. *SAE SP, 1978 (2005);*, pp. 77–88, 2005.

[27] Jiang, S., Hwang, J. and Jin, T.: Dehydration of methanol to dimethyl ether over ZSM-5 zeolite. *Bulletin of the Korean Chemical Society*, vol. 25, no. 2, pp. 185–189, 2004.
Available at: http://newjournal.kcsnet.or.kr/main/j_search/j_download.htm?code=B040207

[28] Martínez-Martínez, S. and Sánchez-Cruz, F.: Liquid Sprays Characteristics in Diesel Engines. *Fuel injection*, pp. 19–48.
Available at: http://cdn.intechopen.com/pdfs/11337/InTech-Liquid_sprays_characteristics_in_diesel_engines.pdf

[29] Arai, M., Tabata, M., Hiroyasu, H. and Shimizu, M.: Disintegrating Process and Spray Characterization of Fuel Jet Injected by a Diesel Nozzle. *SAE International*, , no. SAE paper 840275., 1984.

[30] Dent, J.: A Basis for the Comparison of Various Experimental Methods for Studying Spray Penetration. *SAE Technical Paper 710571*, 1971.

[31] Hiroyasu, H., Kadota, T. and Arai, M.: Supplementry Comments: Fuel spray characterization in diesel engines, in James N. Mattavi and Charles A. Amann (eds.), Combustion Modeling in Reciprocating Engines. *Plenum Press*, pp. 369–408, 1980.

[32] Ghosh, S. and Hunt, J.C.R.: Induced air velocity within droplet driven sprays. In: *Royal Society London*. 1994.

[33] Sazhin, S., Feng, G. and Heikal, M.: A model for fuel spray penetration. *Fuel*, vol. 80, pp. 2171–2180, 2001.
Available at: `http://www.sciencedirect.com/science/article/pii/S001622036101000989`

[34] Kim, S., Hwang, J., No, S. and Ha, J.: Analysis of existing spray penetration models for dimethyl ether spray. *Proceedings of the ICLASS*, 2003.
Available at: `http://www.ilasseurope.org/ICLASS/iclass2003/fullpapers/0220.pdf`

[35] Wakuri, Y., Fujii, M., Amitani, T. and Tsuneya, R.: Studies of the Penetration of a Fuel Spray in a Diesel Engine. *JSME International Journal*, vol. 3, pp. 123–130, 1960.

[36] Park, S.H., Kim, H.J. and Lee, C.S.: Macroscopic spray characteristics and breakup performance of dimethyl ether (DME) fuel at high fuel temperatures and ambient conditions. *Fuel*, vol. 89, no. 10, pp. 3001–3011, October 2010. ISSN 00162361.
Available at: `http://dx.doi.org/10.1016/j.fuel.2010.05.002http://www.sciencedirect.com/science/article/pii/S0016236110002115http://linkinghub.elsevier.com/retrieve/pii/S0016236110002115`

[37] Park, S., Kim, H. and Lee, C.: Dimethyl Ether Spray Characteristics According to the Diesel Blending Ratio and the Variations in the Ambient Pressure, Energizing Duration, and Fuel Temperature. *Energy & Fuels*, pp. 1772–1780, 2011.
Available at: `http://pubs.acs.org/doi/abs/10.1021/ef101562b`

[38] Suh, H.K. and Lee, C.S.: Experimental and analytical study on the spray characteristics of dimethyl ether (DME) and diesel fuels within a common-rail injection system in a diesel engine. *Fuel*, vol. 87, no. 6, pp. 925–932, May 2008. ISSN 00162361.
Available at: `http://www.sciencedirect.com/science/article/pii/`

S0016236107002736http://linkinghub.elsevier.com/retrieve/pii/S0016236107002736

[39] Kostas, J., Honnery, D. and Soria, J.: Time resolved measurements of the initial stages of fuel spray penetration. *Fuel*, vol. 88, no. 11, pp. 2225–2237, 2009. ISSN 0016-2361.
Available at: http://dx.doi.org/10.1016/j.fuel.2009.05.013

[40] Alimia, O.: *Analysis of Injection Spray Patterns for Common Rail Systems*. Msc Dissertation, University of the Witwatersrand, 2011.

[41] Mclean, B.: Common Rail Injection System. Tech. Rep. August, University of the Witwatersrand, Johannesburg, 2009.

[42] ice Info, D.: Dry Ice. 2013.
Available at: www.dryiceinfo.com

[43] Airliquide: Gas Encyclopedia. 2013.
Available at: http://encyclopedia.airliquide.com/encyclopedia.asp?GasID=80

[44] Stevenson, D.: *Quantitative Colour Schlieren Techniques*. MSc Dissertation, University of the Witwatersrand, Johannesburg, 2011.

[45] Delacourt, E., Desmet, B. and Besson, B.: Characterisation of very high pressure diesel sprays using digital imaging techniques. *Fuel*, vol. 84, no. 7-8, pp. 859–867, May 2005. ISSN 00162361.
Available at: http://linkinghub.elsevier.com/retrieve/pii/S0016236105000062

[46] Payri, R., Salvador, F., Gimeno, J. and Soare, V.: Determination of diesel sprays characteristics in real engine in-cylinder air density and pressure conditions. *Journal of mechanical science*, vol. 19, no. 11, pp. 2040–2052, 2005.
Available at: http://www.springerlink.com/index/T05373120K72J485.pdf

[47] Kennaird, D., Crua, C., Lacoste, J. and Heikal, M.: In-cylinder penetration and break-up of diesel sprays using a common-rail injection system. *SAE SP*, 2002.
Available at: http://www.brighton.ac.uk/shrl/publications/Diesel/SAE2002-01-1626.pdf

[48] Cardenas, N.: *Data acquisition for a common rail injection system*. Fourth year Research Project, University of the WItwatersrand, 2010.

[49] Gouws, V.: *Data Acquisition System for a Common Rail Injection Test Rig*. Fourth year Research Project, University of the Witwatersrand, 2010.

# Appendix A : DME Properties

Table A.1: DME Saturated Properties

**TABLE A: SATURATED PROPERTIES OF DME (LISTED IN TEMPERATURE)***

| Temperature (°C) | Pressure (abs) (bar) | Density ($kg/m^3$) | | Enthalpy (kJ/kg) | | Latent heat (kJ/kg) | Entropy (kJ/kg.K) | | Surface tension (N/m) |
|---|---|---|---|---|---|---|---|---|---|
| | | Liquid | Vapor | Liquid | Vapor | | Liquid | Vapor | |
| -70.0 | 0.017 | 778.06 | 0.045 | 0.000 | 515.38 | 515.38 | 0.000 | 2.539 | 0.02410 |
| -65.0 | 0.033 | 772.28 | 0.088 | 10.10 | 520.52 | 510.42 | 0.112 | 2.566 | 0.02339 |
| -60.0 | 0.062 | 766.43 | 0.161 | 20.74 | 526.12 | 505.38 | 0.220 | 2.593 | 0.02268 |
| -55.0 | 0.107 | 760.51 | 0.273 | 31.52 | 531.78 | 500.26 | 0.324 | 2.619 | 0.02197 |
| -50.0 | 0.174 | 754.53 | 0.437 | 42.45 | 537.50 | 495.05 | 0.424 | 2.644 | 0.02127 |
| -45.0 | 0.269 | 748.47 | 0.663 | 53.54 | 543.29 | 489.74 | 0.522 | 2.670 | 0.02057 |
| -40.0 | 0.396 | 742.33 | 0.960 | 64.79 | 549.13 | 484.34 | 0.616 | 2.694 | 0.01987 |
| -35.0 | 0.559 | 736.11 | 1.334 | 76.19 | 555.04 | 478.84 | 0.707 | 2.719 | 0.01917 |
| -30.0 | 0.762 | 729.81 | 1.790 | 87.36 | 560.60 | 473.24 | 0.795 | 2.742 | 0.01848 |
| -25.0 | 1.005 | 723.42 | 2.327 | 98.51 | 566.03 | 467.52 | 0.881 | 2.766 | 0.01778 |
| -24.8 | 1.013 | 723.22 | 2.346 | 98.96 | 566.25 | 467.29 | 0.884 | 2.767 | 0.01776 |
| -20.0 | 1.290 | 716.94 | 2.947 | 109.93 | 571.61 | 461.68 | 0.964 | 2.789 | 0.01709 |
| -15.0 | 1.616 | 710.35 | 3.647 | 121.57 | 577.29 | 455.72 | 1.045 | 2.812 | 0.01641 |
| -10.0 | 1.985 | 703.66 | 4.427 | 133.38 | 583.01 | 449.63 | 1.125 | 2.834 | 0.01572 |
| -5.0 | 2.398 | 696.86 | 5.291 | 145.31 | 588.70 | 443.40 | 1.202 | 2.857 | 0.01505 |
| 0.0 | 2.857 | 689.94 | 6.242 | 157.30 | 594.32 | 437.01 | 1.278 | 2.878 | 0.01437 |
| 5.0 | 3.367 | 682.90 | 7.292 | 169.32 | 599.80 | 430.48 | 1.352 | 2.900 | 0.01370 |
| 10.0 | 3.934 | 675.72 | 8.456 | 181.32 | 605.09 | 423.77 | 1.424 | 2.921 | 0.01304 |
| 15.0 | 4.570 | 668.40 | 9.757 | 193.25 | 610.13 | 416.88 | 1.495 | 2.942 | 0.01238 |
| 20.0 | 5.287 | 660.92 | 11.23 | 205.06 | 614.87 | 409.80 | 1.564 | 2.963 | 0.01172 |
| 25.0 | 6.107 | 653.28 | 12.91 | 216.72 | 619.24 | 402.52 | 1.632 | 2.983 | 0.01106 |
| 30.0 | 7.055 | 645.46 | 14.87 | 229.51 | 624.51 | 395.00 | 1.699 | 3.002 | 0.01040 |
| 35.0 | 8.108 | 637.44 | 17.06 | 242.37 | 629.61 | 387.24 | 1.764 | 3.021 | 0.00974 |
| 40.0 | 9.273 | 629.22 | 19.49 | 255.20 | 634.42 | 379.22 | 1.828 | 3.040 | 0.00909 |
| 45.0 | 10.56 | 620.75 | 22.21 | 268.03 | 638.93 | 370.90 | 1.892 | 3.058 | 0.00844 |
| 50.0 | 11.96 | 612.04 | 25.23 | 280.88 | 643.14 | 362.27 | 1.954 | 3.075 | 0.00780 |
| 55.0 | 13.50 | 603.04 | 28.58 | 293.79 | 647.06 | 353.27 | 2.015 | 3.092 | 0.00716 |
| 60.0 | 15.18 | 593.73 | 32.30 | 306.80 | 650.68 | 343.88 | 2.075 | 3.108 | 0.00653 |
| 65.0 | 17.00 | 584.06 | 36.43 | 319.96 | 654.01 | 334.05 | 2.134 | 3.122 | 0.00592 |
| 70.0 | 18.97 | 573.99 | 41.01 | 333.33 | 657.04 | 323.71 | 2.192 | 3.136 | 0.00531 |
| 75.0 | 21.09 | 563.45 | 46.10 | 346.98 | 659.77 | 312.78 | 2.250 | 3.149 | 0.00471 |
| 80.0 | 23.38 | 552.38 | 51.77 | 361.01 | 662.20 | 301.18 | 2.307 | 3.160 | 0.00413 |
| 85.0 | 25.83 | 540.68 | 58.08 | 375.54 | 664.33 | 288.79 | 2.364 | 3.171 | 0.00357 |
| 90.0 | 28.46 | 525.78 | 65.13 | 390.72 | 666.17 | 275.44 | 2.424 | 3.183 | 0.00296 |
| 95.0 | 31.26 | 511.01 | 73.02 | 406.79 | 667.70 | 260.92 | 2.483 | 3.192 | 0.00242 |
| 100.0 | 34.24 | 495.32 | 81.88 | 424.04 | 668.94 | 244.90 | 2.542 | 3.199 | 0.00192 |
| 105.0 | 37.41 | 477.48 | 91.88 | 440.45 | 667.36 | 226.91 | 2.604 | 3.205 | 0.00145 |
| 110.0 | 40.78 | 457.21 | 106.23 | 460.98 | 667.13 | 206.14 | 2.669 | 3.207 | 0.00100 |
| 115.0 | 44.34 | 433.34 | 122.79 | 484.23 | 665.33 | 181.10 | 2.737 | 3.204 | 0.00061 |
| 120.0 | 48.10 | 401.58 | 148.49 | 504.82 | 653.08 | 148.27 | 2.810 | 3.187 | 0.00027 |
| 122.0 | 49.66 | 384.33 | 165.32 | 512.38 | 643.27 | 130.89 | 2.844 | 3.175 | 0.00015 |
| 124.0 | 51.25 | 361.91 | 189.94 | 521.44 | 629.79 | 108.35 | 2.886 | 3.159 | 0.00006 |
| 126.0 | 52.88 | 327.46 | 229.04 | 539.83 | 612.08 | 72.25 | 2.956 | 3.138 | 0.00001 |
| 126.5 | 53.29 | 312.81 | 242.61 | 550.93 | 606.93 | 55.99 | 2.991 | 3.131 | 0.000002 |
| 127.0 | 53.70 | 258.51 | 258.51 | 601.46 | 601.46 | 0.000 | 3.125 | 3.125 | 0.00000 |

*: *Developed by AVL Powertrain Technologies, Inc.*

# Appendix B : Test Rig Automation and Control

## B.1 Experiment Controller

### B.1.1 Injector Control

In order to control an injector two separate systems need to be considered, one which controls the injection parameters such as injection duration as well as injection frequency. This system generates pulses. Secondly, a separate circuit is required, to handle the high currents which are necessary to actuate the injector solenoid. The signal generation system does not have the capability of delivering the appropriate currents and it is therefore necessary to incorporate an amplification circuit.

#### Previous Student Designs

Brendan Mclean[41] developed an analogue circuit, as stated in Section 4.1.3, which made use of two 555 timing chips as well as a mosfet transistor and a mosfet driver. The 555 chips are used to generate the required injection pulses. One of the chips controls the frequency of the pulses and the second controls the pulse width. The mosfet is used to switch the power to the injector on and off. Mosfets are essentially switches which can be switched at high frequencies, and are normally open, and close when a voltage on its gate pin is recieved. In order to ensure that the mosfet opens and closes rapidly, a mosfet driver is used, which amplifies the signal to the mosfet which ensures that it is actuated accordingly. Mclean's injector bot (injection triggering circuit) only provided the injector with one current of 20A, which if applied constantly to the injector would burn the solenoid. When considering the period in which injections occur and the duration of the injections, the solenoid will not be actuated long enough for damage to occur. Brendan Mclean's circuit is shown in Figure B.1 and B.2.

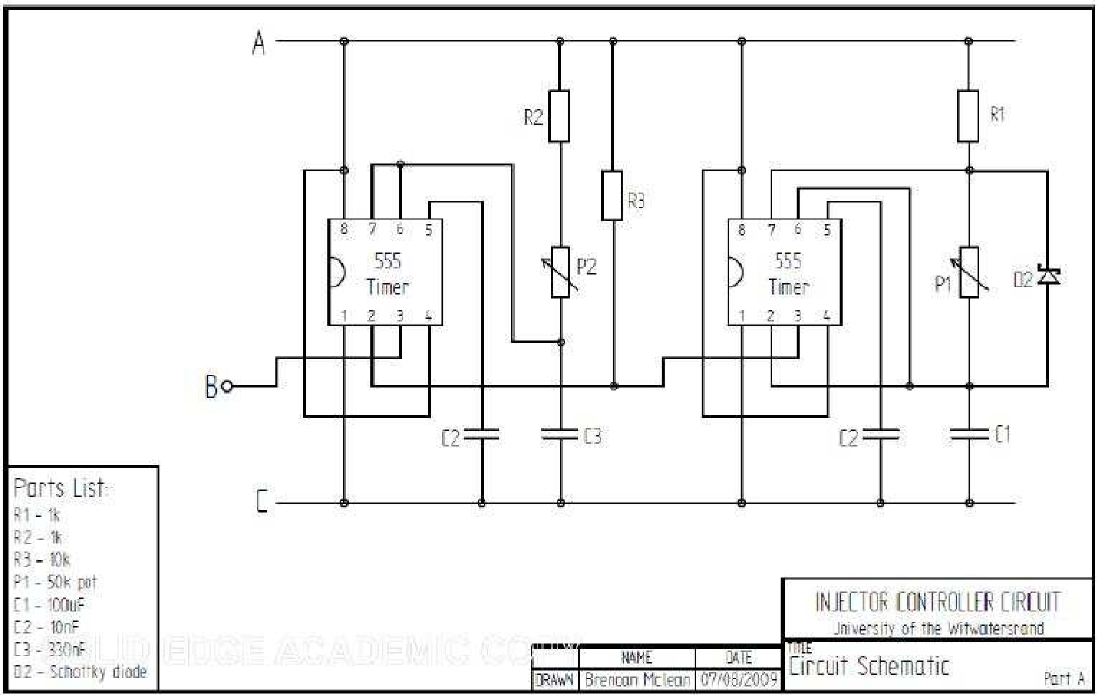


Figure B.1: Brendan Mclean circuit diagram: Part 1

An injector solenoid is essentially an inductor and one of the major effects which needs to be controlled, and which the circuit needs to be guarded against, is the voltage spike produced when the coil is rapidly turned off. This voltage spike can be three to six times that of the source voltage. This voltage spike occurs because, as the inductor is turned off rapidly, it has a tendency to resist the change in current in the coil, thereby creating a large voltage spike. This voltage spike, once both mosfets are open, has no path to travel through, but it is large enough that when it is applied across the mosfet switches, it may damage them (Mosfets are not able to tolerate voltages of the opposite polarity [17]. This voltage spike can damage the other components such as the mosfet and mosfet driver if not guarded against. Mclean used a 600V 3A diode across the injector to protect the circuitry from such voltage spikes. Although, an identical circuit constructed by T Mansfield stopped working, and when trouble shooting, it was found that the mosfet driver had been damaged, which leads to the possibility that after a number of injections the voltage spike may have damaged the driver.

In 2010 two projects by Cardenas[48] and, Gouws [49] were based on the development of an injector firing system which would be digital, as opposed to the analogue solution developed by Mclean. N Cardenas undertook this project in the first quarter and Victor Gouws in the second quarter. Gouws made improvements on the Cardenas project and therefore the focus will be on Gouws's project. Gouws developed a circuit which controlled the inrush current time and the holding current times, as shown in Figure B.3. This circuit consists of two branches in the power circuit, both these branches

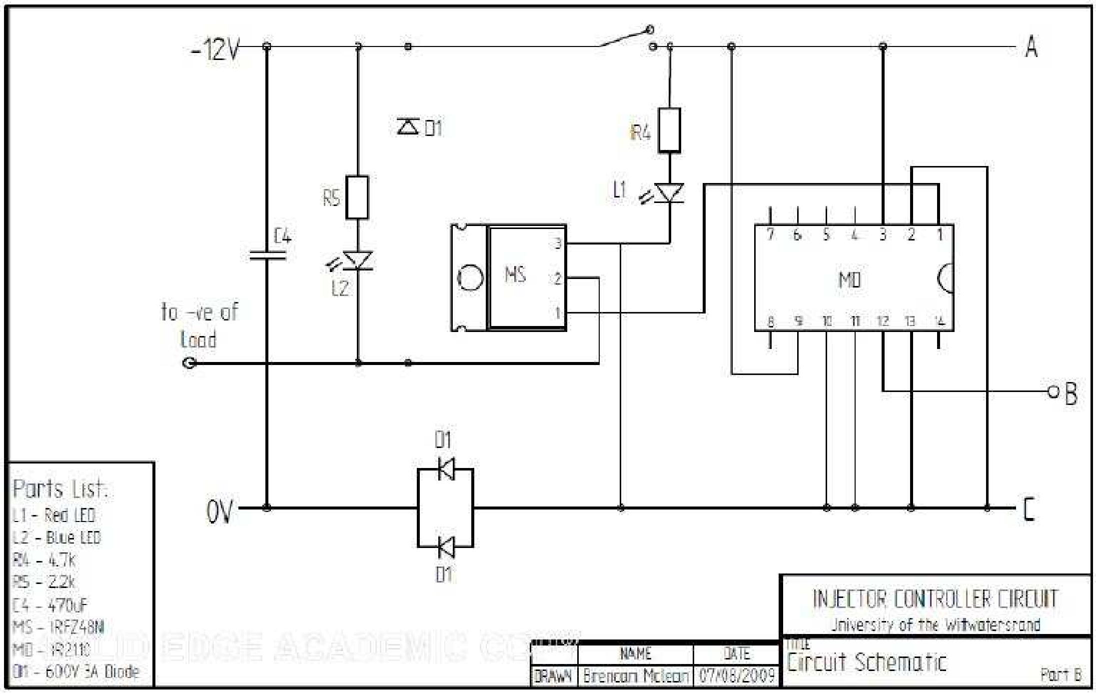


Figure B.2: Brendan Mclean circuit diagram: Part 2

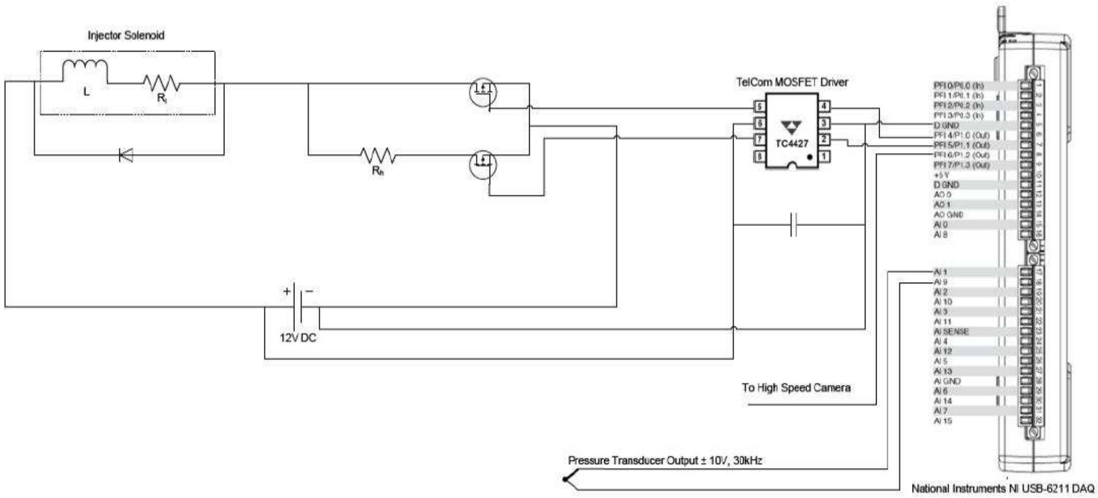


Figure B.3: Injector control circuit developed by Victor Gouws

can be open or closed by the mosfet switches. One branch, the upper branch in Figure B.3, has no resistance, only relying on the resistance of the injector solenoid to regulate the current in the injector. This current with a 12V source is then calculated to be approximately 20A, and is the inrush current. The second branch contains a 0.33 Ohm resistor, and in conjunction with the solenoids resistance, Gouws calculated the current in this branch with a 12V source to be 14A, which is the holding current. In order to actuate the injector appropriately, Gouws initially activated the first mosfet for the inrush current for 100$\mu$s, while the second mosfet remained open. After the inrush time has elapsed the first mosfet is opened and the second mosfet is now activated, thereby reducing the current to the injector. In order to actuate the mosfets they require an input voltage on their gate pin. This voltage is generated by a Data Acquisition Card from National Instruments. The DAQ card is a hardware interface between the computer software and external circuitry. The DAQ card is accompanied by a graphical programming language called Labview. Gouws used Labview to generate a program which controlled the mosfets, as well as log data from the pressure transducer. A small diode was inserted across the injector in order to protect the circuitry from any voltage spikes.

### Injector Solenoid Control Development

In order to develop the "injector controller" it was required to consider the available resources. The most complex or expensive part of the development was the signal or pulse generator, which would be required to be some sort of hardware which could be programmed or be able to communicate (at high speed) with a computer. For the Cardenas and Gouws' projects a NI USB-6211 DAQ card was purchased. The acquisition of another superior DAQ card was an option but only if there was no possibility of adapting the existing DAQ card to meet the project requirements.

Gouws's report concluded that his injector control circuit performed as required, it was thus taken as working, and the circuit was duplicated and the injector was tested and seemed to be functioning as required. After testing the circuit a second time it was found that the circuit was malfunctioning and the mosfet switches were held in the closed position and not anticipating this, the injector solenoid burnt out due to the extended period connected to the 12V battery. After trouble shooting it was found that the mosfet driver had been damaged and was continuously actuating one of the mosfet switches. This was found to be the cause of one of two things: either the voltage spike was larger than the diode could handle and the surge damaged the driver or the injection events were placed too close to one another essentially providing the solenoid with a continuous current and so burning the solenoid. A solution to ensure that this voltage spike was guarded against was to place a zener diode between the negative side of the injector and ground. A zener diode does not allow current to flow through it as long as the voltage is under a certain threshold, once the voltage exceeds this threshold then current is able to pass through the diode. This diode then gives the current a path so that it does not go through the mosfets and damage the mosfets, the voltage will be dissipated and then the diode will return to disallowing current flow. Mcleans circuit used a large diode and this diode was used across the injector as a safety precaution. Gouws used the digital outputs of the DAQ card, these outputs were not able to provide the resolution required, in terms of time. If an inrush current in the order of hundreds of microseconds is required, the digital outputs are not able to produce the requested signal. An inrush time of 100 - 200 $\mu$s was set and the output was observed on an oscilloscope and it was seen that the signal did not behave as desired. It was then thought that the DAQ in hand was inadequate, but the DAQ had two counter outputs which are normally used for accurate counting and pulse generation, it was then thought that these two counter outputs could be used to control the injector. Signals of 100$\mu$s were accurately generated and observed on an oscilloscope. The one issue with the DAQ card is that there are limitations, while trying to get the circuit developed by Gouws to work it was found that when using the two counter outputs it was not possible to trigger the injection events in sync with the pressure measurement and camera, this could only be achieved when one counter output was used. It was also difficult to change injection parameters in the user interface, the user would have to go through a lengthy procedure to change the inrush and holding times. It was because of this that other options were analysed.

One of the options considered for actuating the injector was the use of an LM1949 injector controller integrated circuit. This circuit layout can be seen in Figure B.4. All that is required is a pulse to be sent to the V$_{in}$ pin which will dictate the length of the injection event. This integrated circuit (IC) is able to control the inrush current and

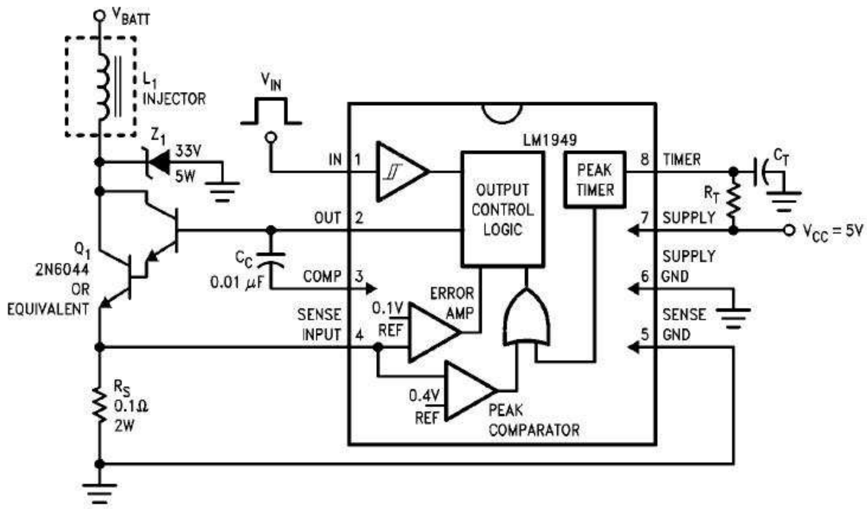


Figure B.4: LM1494 Injector control circuit Schematic

the holding current which the injector solenoid receives. The chip allows full current to the injector for a certain period (or in other words allows the current in the circuit to reach a pre-set value of inrush current), once it has reached this value it is regulated down to the holding current for the remainder of the input pulse, where the holding current is four times less than the peak current. The values of the currents are set by the value of the sense resistor RS, because of a comparator in the IC, which measures the voltage across this resistor. When the voltage drop across the resistor is 0.385V, the peak current has been reached, after which it will drop to a holding current. The holding current is again determined by the resistance in the holding phase, the IC circuit regulates the current in order to achieve a voltage drop of 0.094V across the resistor. The resistance for RS as shown in Figure B.4 results in a peak current of 4A and a holding current of 1A. The peak and holding currents for the injector being used in this project is known, 20A inrush current and 11A holding current, from this the required resistance can be calculated. It was calculated that with a sense resistance of 0.02Ω, the inrush current would be 19.25A and the holding current would be 4.7A.

This circuit was then tested and found that it did not provide enough current to open the solenoid, the precise reason for this was not found. One of the possibilities was that the holding current was to low for the solenoid to be kept open, this was assumed as a feint clicking was heard in the injector solenoid. The sense resistance was dropped in the hopes that a higher holding current would result in the injector making the loud clicking sound that would indicate the injector is opening and closing appropriately. This too did not work. The circuit may only be suitable for a high resistance solenoid unlike the low resistance injector that is being used.

The Labview + DAQ combination allows for various signals to be generated. It was thought that, since the previous projects conducted using Mclean's Injectorbot were performed well and the injectorbot triggered the injectors adequately, the same principle could be applied in the current design. The generation of signals was much simpler using the DAQ card and all that would be required would be one mosfet switch which would allow current to flow to the injector. Although the current is high and would burn the solenoid, the length of the injections are too short to allow the solenoid to burn out. Also considering the timing of fuel injections in a common rail engine:

engine speed = 6000rpm
number of strokes = 4
Therefore an injector will be fired every second revolution of the crank shaft.

The period between the injections is then:

$$\frac{1}{\left(\frac{6000}{60}\right) \times \left(\frac{1}{2}\right)} = 20ms \tag{B.1}$$

This time is long enough to allow the current to dissipate from the injector before the next injection, and in this way the solenoid will not stay on and burn out.

The circuit was then designed to operate the injector as mentioned above. A zener diode was used to protect against any reverse voltage spikes, and a diode was placed across the injector as an extra safety measure. This circuit diagram can be seen in Figure 4.8 and Figure B.6.

### B.1.2 Rail Pressure Control

The pressure within the accumulator is regulated by a pressure control valve solenoid, this valve allows the pressure in the rail to be increased or decreased depending on the state of the solenoid. When the solenoid is de-energised, the pressure in the rail is at its minimum (about 80 to 100 bar) as fuel overflows back to the fuel tank. When the solenoid is energised, the flow of fuel through the overflow is restricted and the pressure within the common rail increases.

In order to be able to control the pressure within the common rail, it is necessary to control the solenoid valve. This valve is simply controlled using pulse width modulation. The solenoid valve requires 12V as it would receive from a car battery and the frequency of the PWM must be approximately 1000Hz [10]. The positioning of the valve is controlled with PWM, and depending on the duty cycle of this PWM signal, the pressure maintained in the common rail will vary, e.g. 50% duty cycle will result in 50% of the input voltage (0.5*12V)and this allows for a certain pressure in the common rail and 70% duty cycle will create a larger pressure as the valve will be in a slightly more closed position. This solenoid valve does not require as much current as the injector solenoid valve, it draws approximately 1A, but an amplification circuit will still be required to transfer the commands from the operation software and hardware to the pressure regulator.

It has been shown that Mosfet switches are a reliable and effective manner to switch high currents at high speeds, and since we will need to essentially switch power "on" and "off" to the pressure regulator (according to the PWM) at 1kHz, the mosfet switch will be suitable. The PWM signal will be generated by the National Instruments USB 6211 DAQ card (from analogue output 1). This signal is amplified by the mosfet driver in order to ensure that the mosfet switch opens and closes effectively and with the required speed.

The pressure control solenoid valve will behave in the same manner as the injector solenoid, this means that as the mosfet is turned off and the solenoid tries to reach its original position a voltage spike will occur, and it is for this reason that a diode is placed across the pressure regulator solenoid valve. A zener diode is placed between the negative side of the valve and ground as a safety precaution. The power for the regulator is supplied by an alimented 13V DC power supply. The circuit for the pressure regulator is shown in Figure B.7.

### B.1.3 Total Circuit Design

Figure B.5 shows the actual circuit developed to control the experimental facility.

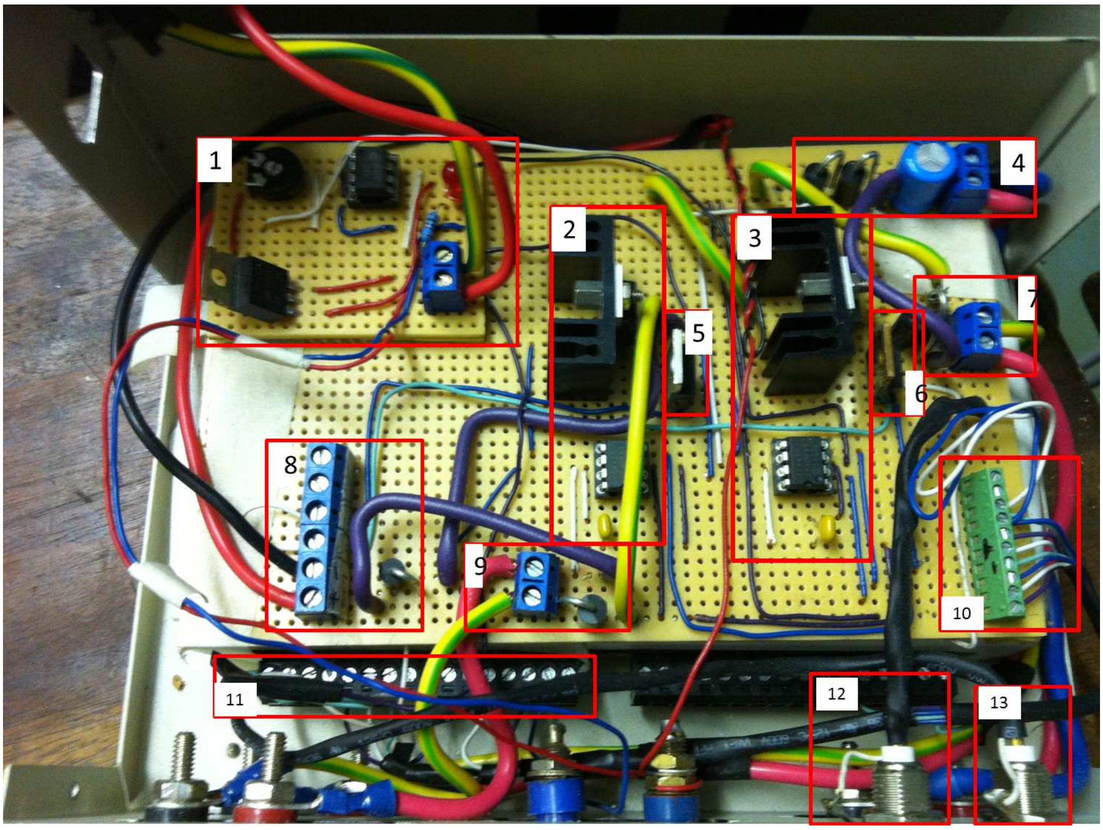


Figure B.5: Final built circuit

The different parts of the circuit are described as follows:

1. Voltage regulator - This circuit is used as the safety feature for the common rail pressure regulator. It consists of a voltage comparator, a mosfet switch, a resistor and a variable resistor. The circuit compares the voltage from the pressure transducer on the rail to the voltage set on the variable resistor (a percentage of the 5V input). If the voltage is below the set value the mosfet switch remains closed, if it is above, the mosfet switch opens cutting the current to the pressure regulator. This is in case the controlling software runs into an error and sends random signals to the pressure regulator.

2. Pressure regulator circuit - This includes the mosfet switch with heatsink and the mosfet driver. The mosfet switch creates a break in the regulator circuit and only when an input into the driver is produced does the switch close allowing current to the solenoid.

3. Injector circuit - this includes the mosfet switch and the mosfet driver used to rapidly activate the injector. The mosfet opens and closes rapidly with the pulse generated by the DAQ card, it then allows high current to flow to the injector. The mosfet driver is also used to activate a trigger signal to the camera, the mosfet driver activates a separate mosfet switch which then allows a voltage to trigger the acquisition of images. The mosfet driver ensures the opening and closing of the mosfet switches is done with high speed.

4. Battery power - The power from the battery comes in to these terminals, a capacitor is used to smooth the input voltage and the two large diodes are placed in order to protect against the incorrect connection of the battery.

5. Camera trigger - This mosfet is the second mosfet in the camera trigger circuit, it is controlled by the mosfet driver mentioned in point 3, high speed actuation of this mosfet is essential, when this switch closes the camera will be triggered. It is activated by the same pulse which triggers the injector and the pressure trace readings (PFI7).

6. Camera on/off - This mosfet is the first mosfet in the camera trigger circuit. It is activated by a check box in the software, it is not linked to a mosfet driver as speed is not important in its activation. It is turned on or off long before the tests are to commence, it therefore is already closed when the time comes to activate the camera.

7. Injector leads - The injector is connected to the circuit board via these terminals. The zener diode and the diode are connected just after the two terminals. These two wires come from banana terminals on the front of the case (the injector is simply plugged in on the front of the case).

8. Pressure regulator terminal - The pressure regulator is connected to these terminals, a zener diode is placed to avoid the voltage spike as mentioned previously.

9. Pressure regulator power supply - The 13V power supply is connected to the circuit via these terminals, a diode is placed in order to prevent reverse current from flowing (if connected incorrectly).

10. Signal terminals - All the signals received by the circuit from the DAQ card enter the circuit via this row of terminals. The camera trigger signal, injector pulse,

and the pressure regulator PWM all come in at this point and are then connected to all the appropriate circuits.

11. DAQ terminal block - The signals generated by the computer and output by the DAQ card are output by each respective terminal.
12. Camera BNC - The BNC cable from the delay unit is connected to the circuit via this BNC connector.
13. Pressure measurement - The input from the charge amplifier is connected to this BNC connector and then it is connected to the DAQ card in order to record the data.

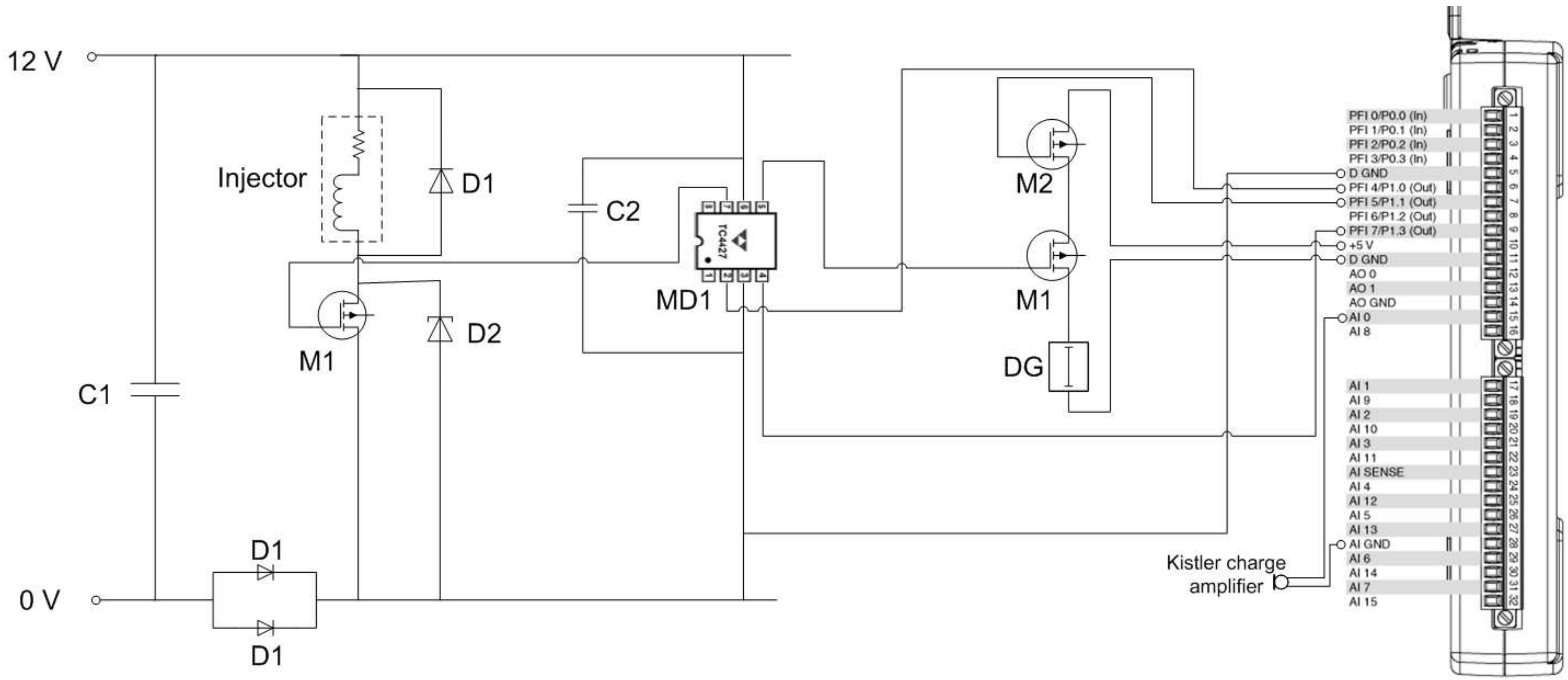


Figure B.6: Injector control circuit diagram

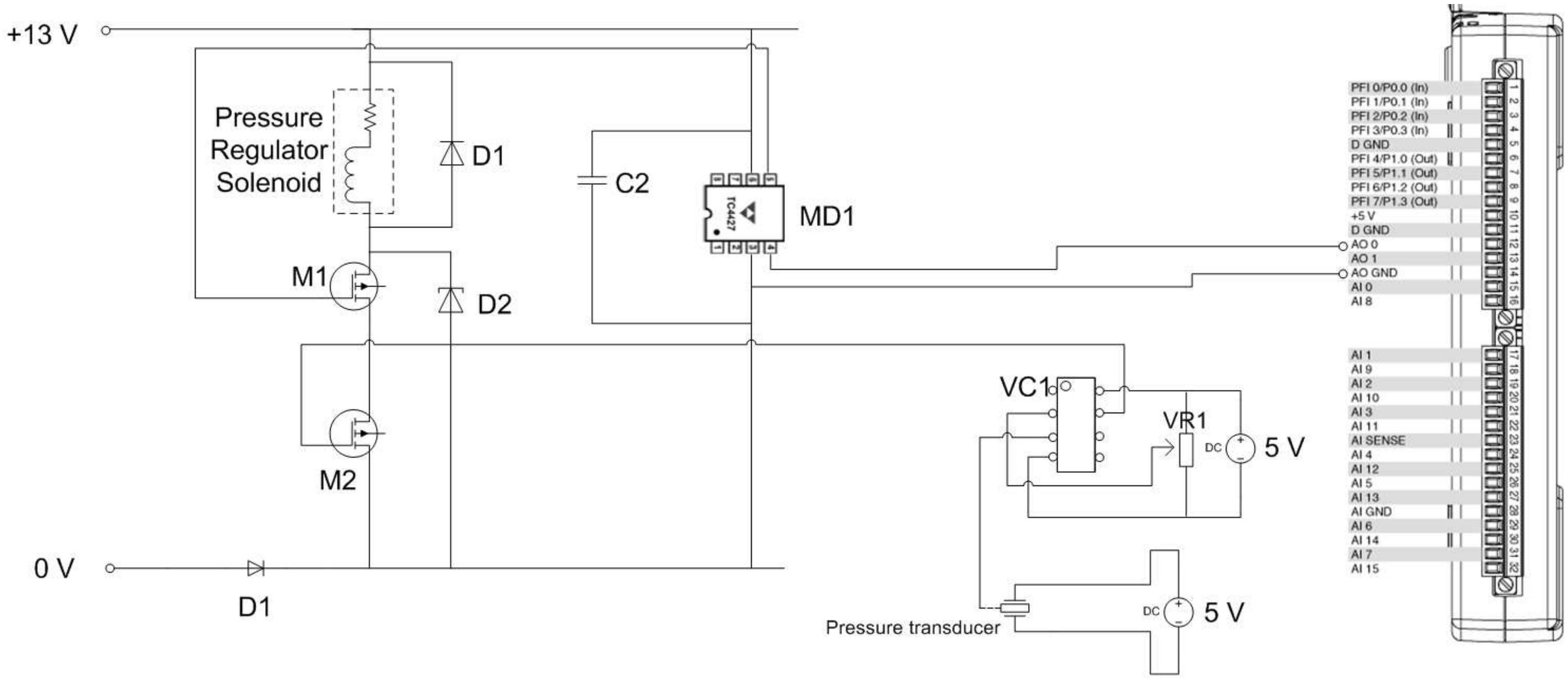


Figure B.7: Rail pressure control circuit diagram

Table B.1 lists the components used in the injector and pressure regulator circuits.

Table B.1: Circuit Components

| Code | Description | Code | Description |
|---|---|---|---|
| D1 | Diode - 600V 3A | D2 | Zener diode - 33V |
| C1 | Capacitor - 470$\mu$F 25V | C2 | ceramic capacitor - 0.1$\mu$F |
| M1 | Mosfet switch - IRF3808 140A | MD1 | Mosfet driver - TC4427 |
| M2 | Mosfet switch - IRF 710 | DG | Delay generator/Camera trigger |
| VC1 | Voltage comparator - LM311 | VR1 | Variable resistor - |

## B.2 Experimental Controller Software

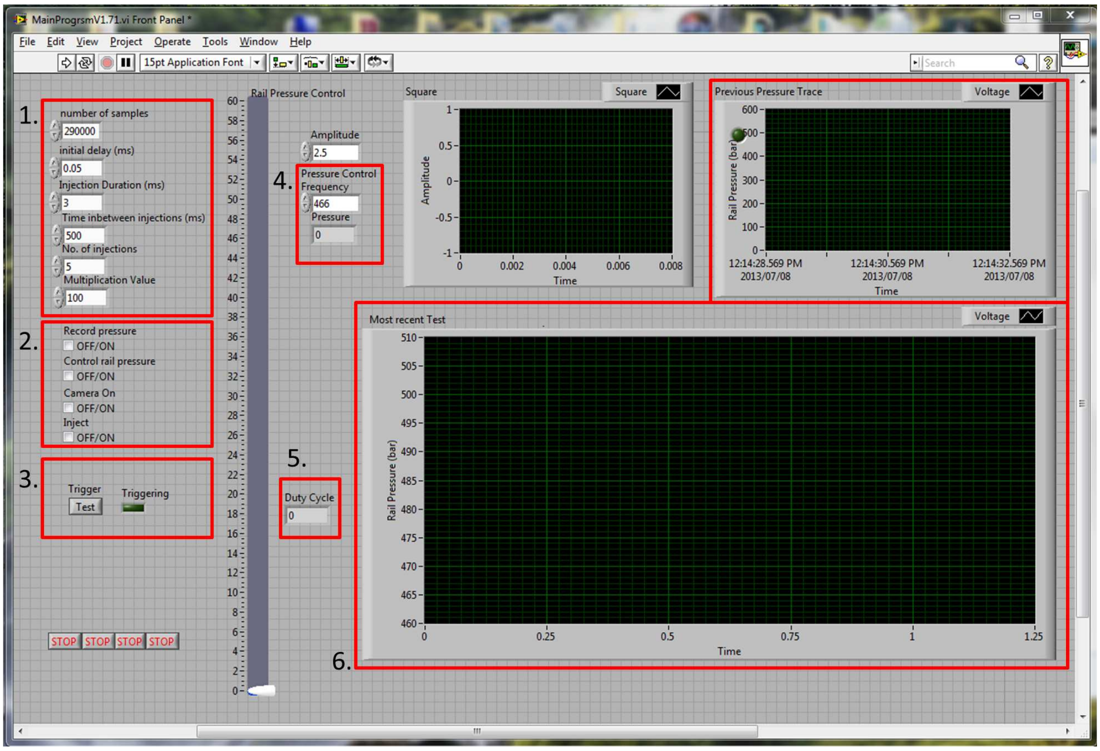


Figure B.8: Main program window or user interface

Figure B.8 shows the main user interface for the experiment controller software, also known as the front panel in labview.

1. Injection Parameters - All the relevant injection parameters are set in these boxes such as: injection Duration, injection spacing, number of injections, and the delay box delay is offset here.

2. Function selection - These check boxes allow the user to record images and pressure traces together or they can be done separately if the function needs to be tested.

3. Trigger - This button is clicked once all the appropriate settings have been set and a test is to be conducted.

4. Common-rail pressure regulator frequency - The frequency of the square wave is set in this box.

5. Rail Pressure Adjust - The duty cycle is varied by adjusting the slider, which then in turn controls the rail pressure.

6. Pressure Trace Display - The graph will indicate the pressure trace of the test most recently conducted, after the pressure trace data is saved first, a separate graph also shows the pressure trace for the second last test conducted.

Figure B.9 shows the main block diagram for the experiment controller program, the numbered descriptions that follow relate to this figure.

### 1. Square wave generator

This block of code generates a square wave, attributes of the square wave are adjusted using the inputs shown. The frequency of the wave, the amplitude (or voltage output), and the duty cycle can be varied. In order to control the mosfet transistor which switches the power on and off to the pressure regulator, the voltage amplitude is set to 2.5 V and the curve is offset by 2.5 V and in doing this the voltage oscillates between 0V and 5V. This square wave is then passed to the DAQ assistant.

### 2. DAQ Assistant for rail pressure control

The DAQ Assistant receives the output from the digital signal generator and outputs it to an analogue voltage output on the DAQ card. The mosfet gate pin is then connected to this voltage output and is controlled by the signal generated. The DAQ Assistant is placed in a case statement such that the control of the pressure in the rail can be turned on or off by simply checking or un-checking the check box "Control Rail Pressure".

### 3. Event trigger

This piece of code is used to trigger all the events that need to be synchronised. The trigger button is simply a push button which does not latch i.e. it is on while it is being pushed but once released it goes off. This enables a "true" signal to be generated when it is on and it goes to "false" right after it is pushed and let go. The DAQ Assistant allows a signal to be created from the program to the physical output. The DAQ Assistant sets a 5V voltage to PFI7 (pin 9) or P1.3, the voltage is only applied when the signal from the push button received by the DAQ Assistant is true. The PFI7 port is used as a trigger for the separate tasks that are to be performed. The voltage sent to the delay generator originates from this port. The voltage generated by this port triggers the mosfet driver which in turn closes one of the mosfet switches in the camera trigger loop. This switch is continuously activated every time the trigger button is pressed.

The trigger code is placed in a while loop, this ensures that the system is ready to trigger at any time as the code is always running unless the stop button is pressed.

### 4. Camera control

The camera on check box allows the user to turn off the camera and exclude it for testing, this is mainly done in case the user simply wants to test the pressure history in the common rail system or if the injector needs to be bled for DME tests. This code controls the second of the two switches in the camera loop. This switch is the slower switch but when the camera on check box is checked it is continuously closed and awaits the trigger button to be pressed in order to complete the circuit.

### 5. Injection parameters

The injector parameters are set in these control blocks, each one feeds to the correct place in the injector SubVI. The injector subVI controls the input parameters and outputs them appropriately.

### 6. Injector pulse sub VI

The injector pulse sub VI is used to reduce clutter and as it performs its own function it is used in a single block.

This function takes the input parameters and controls the injector accordingly, it outputs signals which correspond to the injector on and off time as well as the amount of injections. The contents of this VI is shown in Figure B.10. The injection events (i.e. number of injections, injection length, and injection timing) occur once the trigger push button is pressed, even though the push button is pushed on for only a few microseconds, the injection event follows through until it is complete (the injection code only requires the trigger signal to initiate its process) and then waits until the trigger button is pressed again.

### 7. DAQ assistant to read in pressure traces

The Pressure trace code is also surrounded by a case statement, this allows the user to record or disable the pressure recording function.

The DAQ Assistant in this case is used to receive the analogue voltage and display it in the software. The number of samples and the sampling rate is set in this DAQ Assistant.

### 8. Write to measurement file

This function allows the voltage read in to be written to a measurement file. A boolean constant is used to reset the write to file function so that a new file is created each time the trigger is pressed. The format of the files is set to TDMS, it can be set to .txt but the writing occurs faster in the TDMS format. A plugin can be installed in excel in order to read these files, or a matlab code can be used to extract the information.

Before the value of the pressure is saved into a file, it is multiplied by the calibration value which is given on the Kistler charge amplifier in order to save the data in bars which is the value required.

The file which is generated by the function prompts the user to input a file name as soon as all the data has been written to the file, once the data is saved then it is displayed on a graph on the user interface (front panel). The block which has an arrow to the right and a star beneath it is a feedback node, this is used to store the location of the previous pressure trace saved and when prompted to input the name for a new pressure trace, the folder opened will be that of the previous file. (It links the filename out to the filename in) This is purely to make the program more efficient and user friendly.

### 9. Read from measurement file

This function simply reads the data from the previous test and displays it on the graph. This function is slightly redundant as the pressure of the current test is most important at the time of testing.

Error out blocks are place on all of the functions, these are important when debugging as they will show the error which has occurred. The most important function of this block is that if some simple error occurs in one of the write or read measurement functions, then the whole program will not crash and cause havoc with the outputs to the injector or pressure regulator.

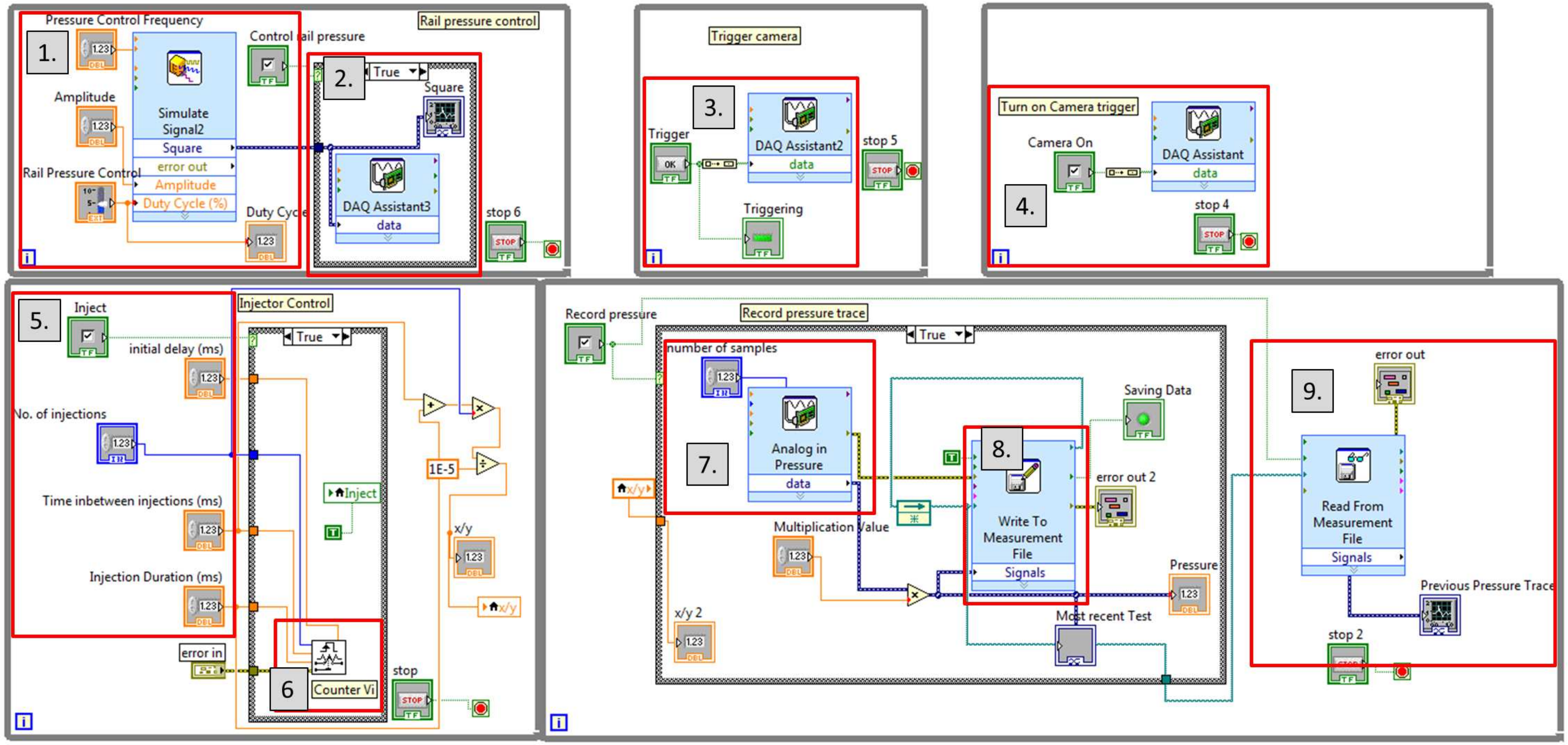


Figure B.9: Main program Visual Instrument Block diagram

Figure B.10 shows the block diagram for the injector pulse Sub VI. The numbered description that follows relates to this figure.

### 1. Create a task

### 2. Create channel

This block creates channels to generate digital pulses. The high time (injection duration) and low time (time in between injections) is set here (this is linked to the control boxes shown in figure B.9 point 5. The pulse time is in seconds therefore the duration values are multiplied by 0.001 in order to use millisecond values.

The channel which the output is to occur is set here, as well as the idle state which in this case is low as we want the injector to be off unless commanded to be on.

### 3. Samples

This function is related to the number of injections desired (number of samples). It is set so a finite number of samples will be generated and the number of samples to be generated is set.

### 4. Triggering

This function allows the injector to be triggered when the signal to PFI7 goes high. It is triggered off a rising edge.

### 5. DAQmx task functions

DAQmx start task, DAQmx wait until done, and the DAQmx clear task. These functions start the signal generation then wait until the signal or task is complete and then clears the task and releases any resources used. The timeout needs to be set to -1, this tells the task to wait indefinitely for a command or signal, otherwise it will timeout and the program will stop while waiting for the trigger.

The function of this VI is available in a DAQ Assistant VI, but it does not allow the user to simply change the high and low times in the Main user interface, one would have to stop the program, open the Assistant and change these values every time. The DAQ Assistant was used to create a channel to the correct port, it was then converted to a block diagram as seen in figure B.10 and all the appropriate parameters were changed and added to the code. One draw back with this setup is that the injection parameters can be changed while the program is running but will only take effect after one test has been completed. otherwise the program will need to be stopped and the parameters changed and then the software can be run again.

Figure B.11 shows the settings for the DAQ Assistant used to record the pressure traces. In the configuration tab the channel to record from is shown, it is can be changed by removing channels (button on the top of the window) and then adding the desired channel. The input range is left at the default 10V to -10V. The "Terminal Configuration" should be set to reference single ended (RSE). The timing settings can be set here or on the main user interface, but in this case only the number of samples will be set in the user interface and the sampling rate is set here. A sampling rate of 100kHz was found to measure the pressure trace with great detail. The acquisition mode of N Samples was chosen as we only required the data for while the injection events were occurring.

The synchronisation of the pressure trace measurement and injection events is set in the triggering tab. The trigger type is a digital edge from channel PFI7. It is set to trigger on a rising edge i.e. 0 to 5V jump.

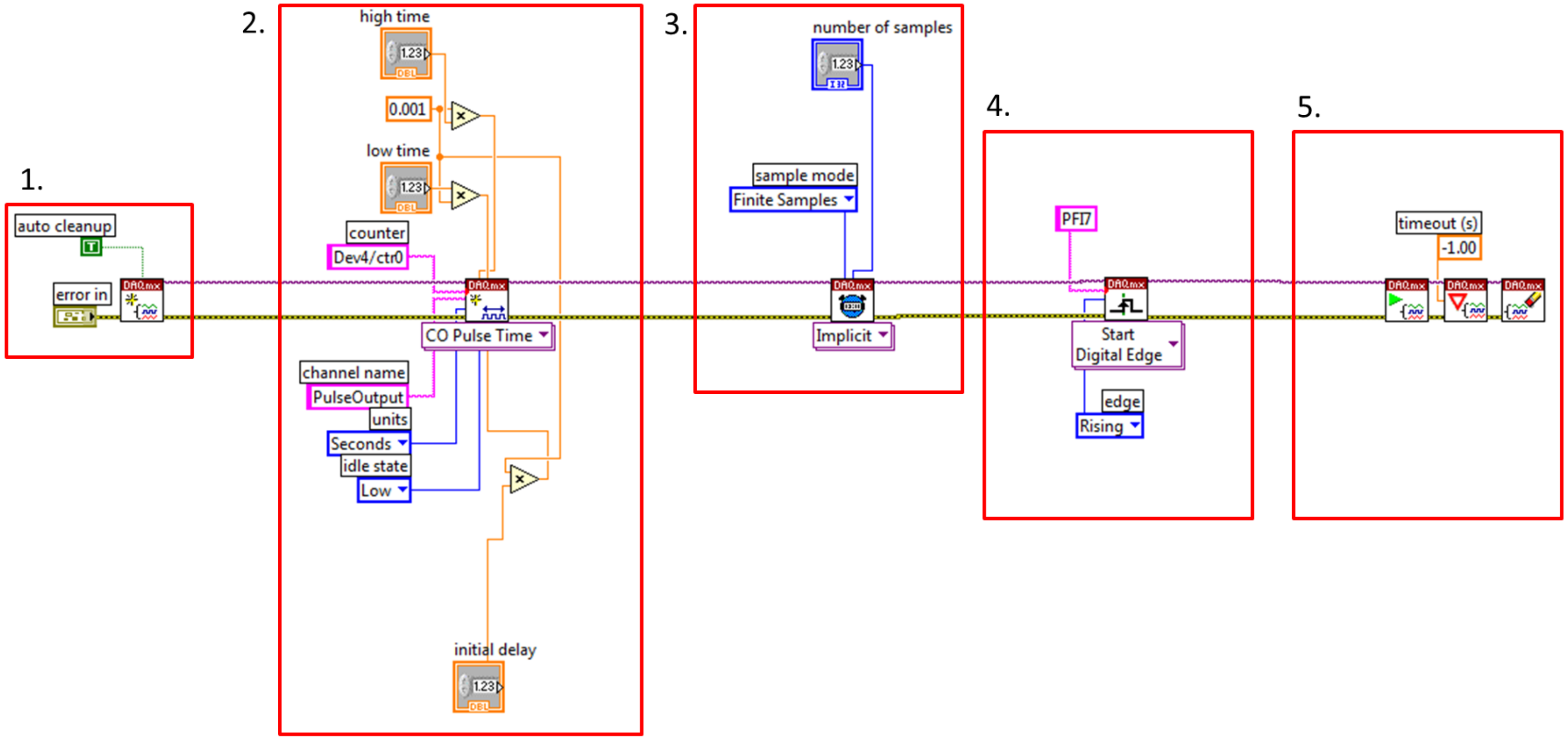


Figure B.10: SubVI for injector timing control

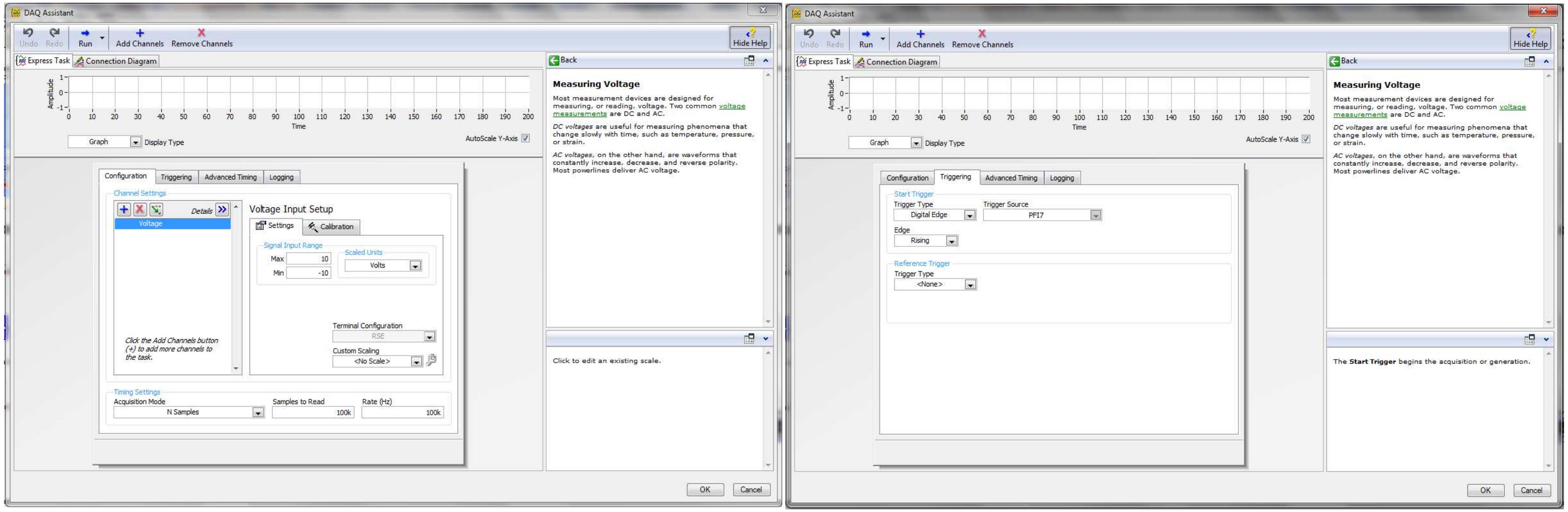


Figure B.11: VI assistant for pressure trace measurement

## B.3 Image Processing Software

In order to attempt to consistently process all the spray images, a program was constructed in order to process the images and extract the spray penetration and cone angle. The outline of how the image processing software works is given in this section.

Figure B.12 show the main interface for the image processing software. An attempt was made to mass process all the images at once, but the program did not function 100% and it was also decided to process each test separately in order to ensure that the program was measuring the relevant parameters correctly. The user must set the folder path for the images to be processed (only one test at a time, so the folder of a specific test), the file name (excluding the "C001H001S0001"), and then set the folder to which the excel spreadsheets are to be saved. The user can process either the spray cone angle or spray penetration or both together, this is achieved by checking the appropriate check boxes. The number of images to process must be set as well, this will vary according to the frame rate and the injection duration.

In order to process the images for spray penetration a background image has to be created first, this is done by clicking the button for "Make background images". once this is done the "Process" button can be pressed and the results for the Cone angle and penetration will be shown in the appropriate windows, all the images processed for each set are shown in these windows and can be seen by clicking on the up or down arrows on the top left corner of the image window. The results should be checked to ensure that they were processed properly otherwise settings should be adjusted in order to produce useful results.

Figure B.13 shows the block diagram for the main processing program.

1. The block diagram in this section gathers and generates the file paths to the spray images and the background images in order to process them. The different folder paths are concatenated and then input into the rest of the program. Only the file path of the first image in the test set is required, the software then will process the specified number of subsequent images.

2. The code in this section generates the name of the spreadsheets which are generated with the cone angle and penetration results.

3. This section of code generates the background image. It takes the first image of every test (in order to remove any dirt or common occurrences from the parameter processing) and converts it to greyscale in the Vision Assistant, it then uses a template

with the correct threshold settings to create an image, this image is then saved in the same folder as the test images.

4. This section of code is what processes the images for the penetration and cone angle. The two subVI's, "PEN" and "CA" are used to process the images. They are activated or deactivated by the two check boxes.

Figure B.14 shows the two Sub VI's with the code used to extract the penetration and cone angle results. In both these VI's the image path is inputted into the vision acquisition function, the images are then passed on to the Vision Assistant where the processing is done, the results are then written to a spreadsheet by the write to file function. The difference lies in the settings of the vision assistant which are shown in figure B.15 and B.16.

Figure B.15 shows the settings for the vision assistant used for processing the penetration. The Raw original image is input to the Vision assistant, the image is then calibrated. This is done by measuring the pixels along the diameter of the chamber window and relating it to a physical dimension (mm), this is done when the "Image Calibration" block function is run. The image is then converted to gray scale using the "Colour Plane Extraction" function. The next step is background subtraction, this is performed by the "Golden Template Comparison" function. In this function the background image is used and a threshold value of between 30 to 40 is used to differentiate the spray from the background. The resulting spray is then shown in red, it is sometimes necessary to raise or lower the threshold and see when the red spray (detected spray) matches the spray in the image. The image is then rotated so that it is in the vertical direction using the "Geometry" function. A "Clamp" is used to detect the penetration length. The region from the tip of the injector to the limits of the chamber window is selected, and the clamp only looks for the two extreme points of spray within this region. A "Caliper" is then used to measure the distance between the two points found by the clamp. The calibration performed earlier is then used to convert the pixel distance into millimeters.

This process is performed for every image input into the program, and the results are then shown in a spreadsheet.

Figure B.16 shows the settings from the cone angle processing visual assistant. The process for the cone angle is slightly shorter than that for the penetration. The raw image is input into the vision assistant, it is also converted to gray scale. The spray is then rotated to the vertical position. A "Find Straight Edge" function is then used to find the spray edge, one is used to detect the left edge and the other is used to detect the right edge. The region in which these functions look for the spray edge is set from the injector tip to 60 nozzle diameters length away from the injector tip. The threshold value is set in these functions and may need to be adjusted. It is also important to note that this region may change if the camera is moved, it will result in the position of the window in the cameras view to change and therefore the image will change. A" Caliper" is then used to measure the angle between the two detected spray edges, and the results are then written to a spreadsheet file.

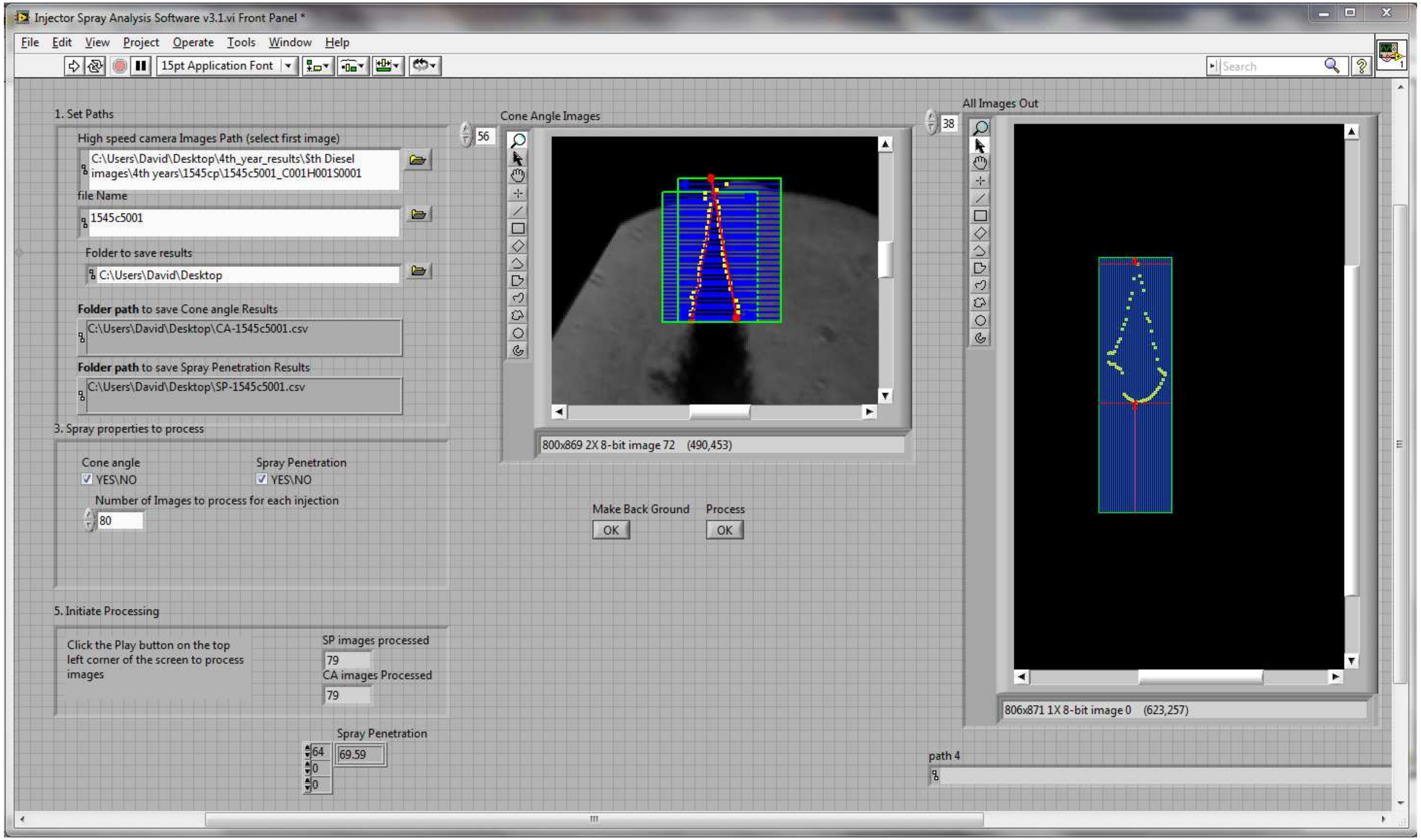


Figure B.12: Image processing main interface

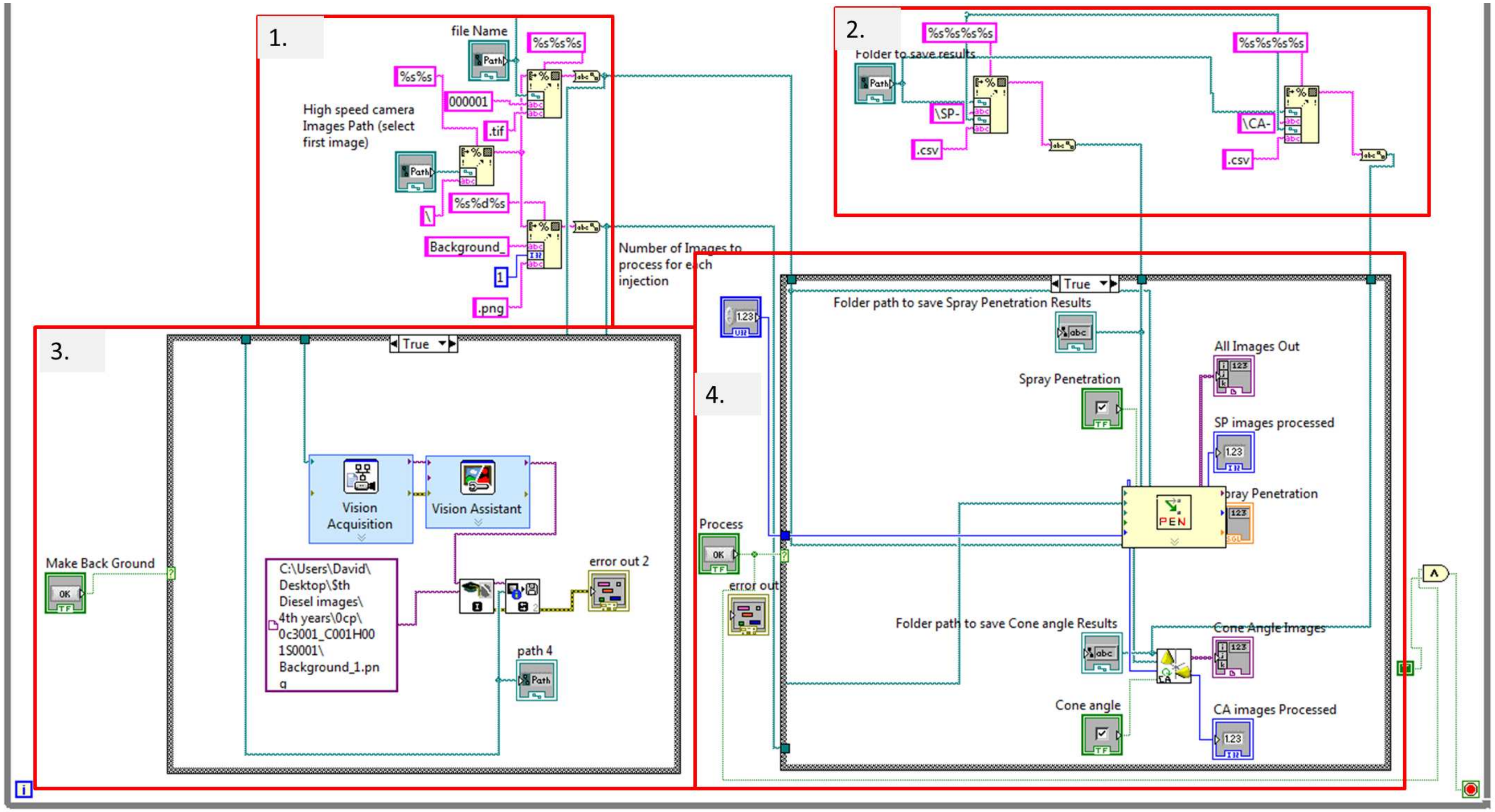


Figure B.13: Block diagram for main program

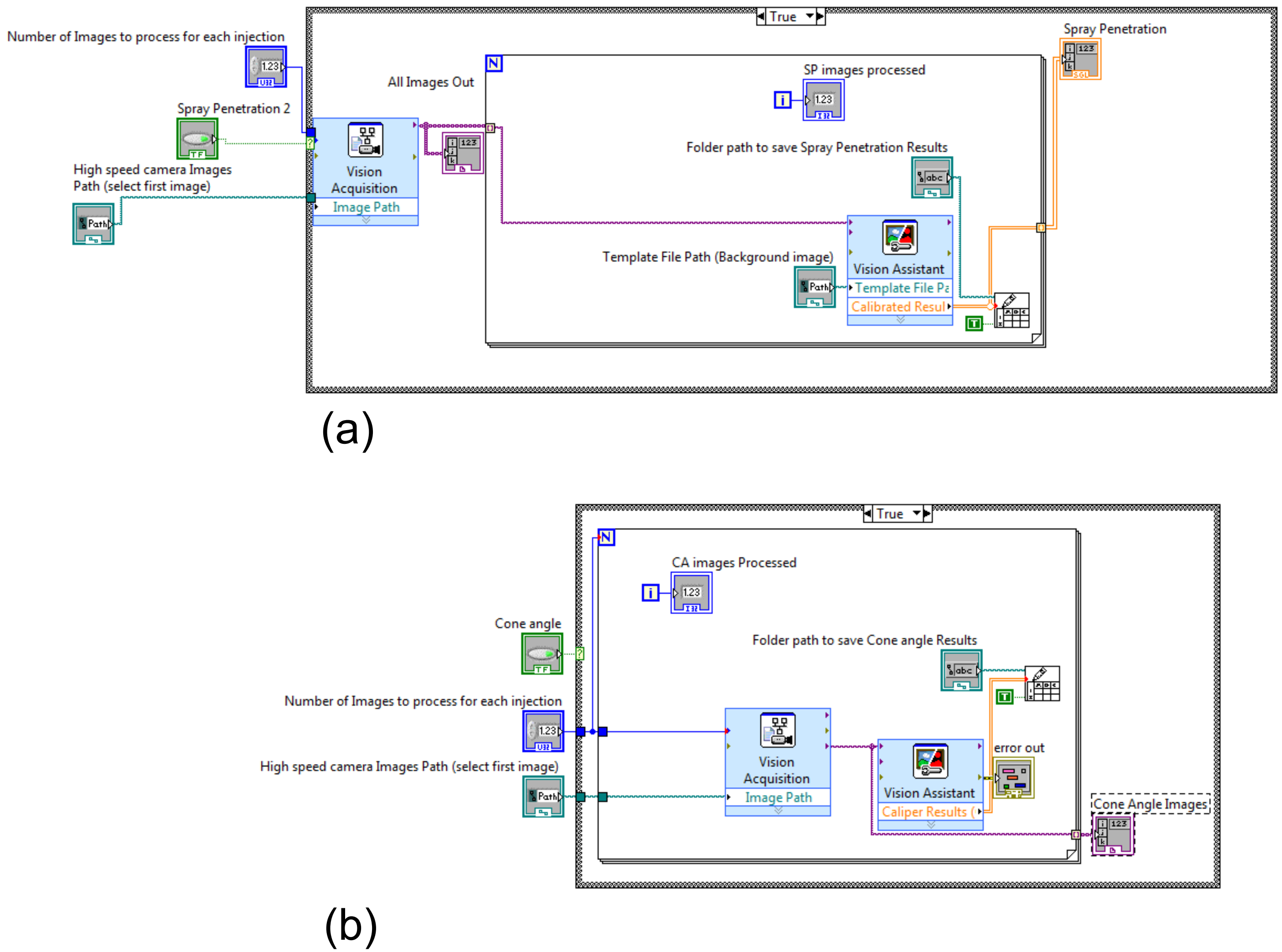


Figure B.14: (a) Penetration Sub VI block diagram, (b) Cone Angle SubVI block diagram

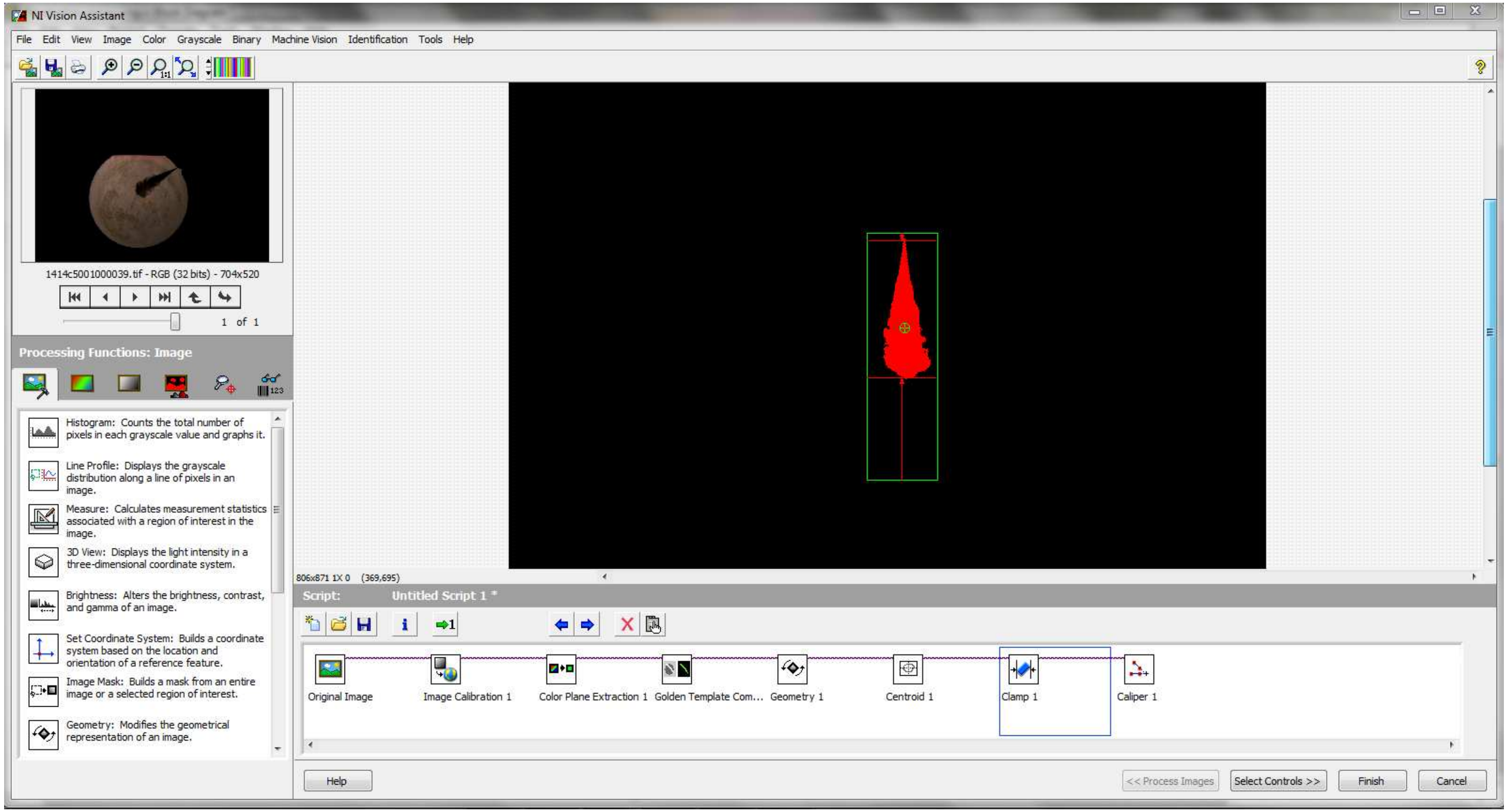


Figure B.15: Vision Assistant settings for penetration measurement

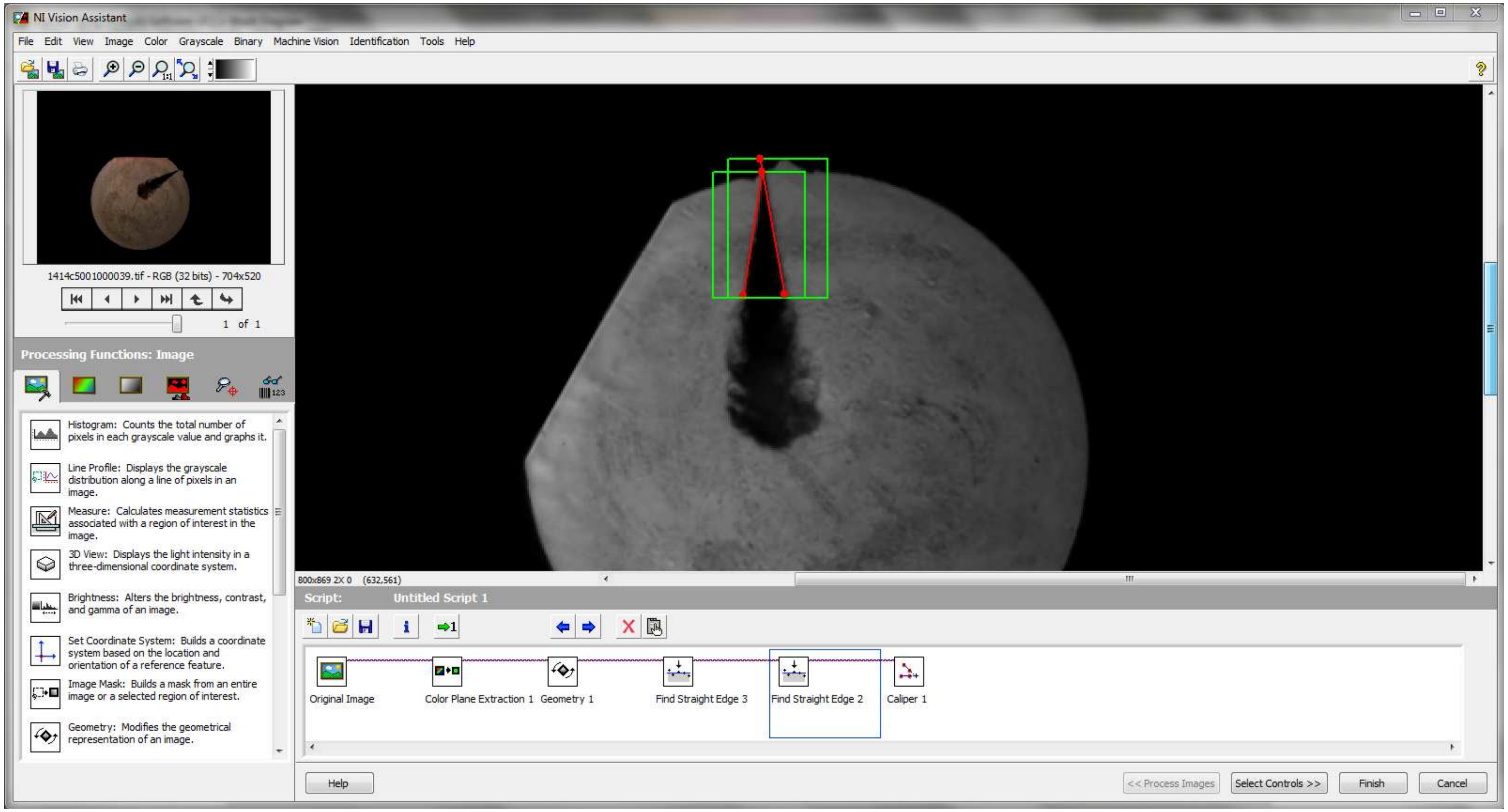


Figure B.16: Vission Assistant settings for Cone Angle measurement

# Appendix C : Uncertainty Analysis Calculations

Chamber density uncertainty:

$$\frac{\delta \rho_g}{\delta P_{amb}} = \frac{1}{R \times T_g}$$
$$\frac{\delta \rho_g}{\delta T_g} = \frac{P_{amb}}{R \times T_g^2}$$

$$\Delta \rho_g = \sqrt{\left(\frac{\delta \rho_g}{\delta P_{amb}} \times \delta P_{amb}\right)^2 + \left(\frac{\delta \rho_g}{\delta T_g} \times \delta T_g\right)^2}$$

Uncertainty for Dent

$$\Delta S = \sqrt{\left(\frac{\delta S}{\delta(\Delta P)} \times \delta(\Delta P)\right)^2 + \left(\frac{\delta S}{\delta T_g} \times \delta T_g\right)^2 + \left(\frac{\delta S}{\delta \rho_g} \times \delta \rho_g\right)^2}$$

Where:

$$\frac{\delta S}{\delta(\Delta P)} = 3.07 \times (td_n)^{0.5} \times \left(\frac{294}{T_g}\right)^{0.25} \times 0.25 * \left(\frac{1}{\rho_g}\right)^{0.25} \times \left(\frac{1}{\Delta P}\right)^{0.75}$$
$$\frac{\delta S}{\delta T_g} = 3.07 \times (td_n)^{0.5} \times \left(\frac{294 \times \Delta P}{\rho_g}\right)^{0.25} \times 0.25 \times \left(\frac{1}{T_g}\right)^{1.25}$$
$$\frac{\delta S}{\delta \rho_g} = 3.07 \times (td_n)^{0.5} \times \left(\frac{294 \times \Delta P}{T_g}\right)^{0.25} \times 0.25 \times \left(\frac{1}{\rho_g}\right)^{1.25}$$

Uncertainty for Sazhin.

Note: the angle must be in radians for the uncertainty analysis. Therefore $\pm\ 1^o = \pm$ 0.01745 Radians.

$$\Delta S = \sqrt{\left(\frac{\delta S}{\delta \theta}\delta\theta\right)^2 + \left(\frac{\delta S}{\delta C_d}\delta C_d\right)^2 + \left(\frac{\delta S}{\delta(\Delta P)}\delta(\Delta P)\right)^2 + \left(\frac{\delta S}{\delta \rho_g}\delta \rho_g\right)^2}$$

Where:

$$A = 1.189\left(\frac{1}{(1-\alpha_d)^{0.5}}\right)^{0.5}(d_o t)^{0.5}$$

$$\frac{\delta S}{\delta\theta} = A\left(\frac{\Delta P}{\rho_g}\right)^{0.25}(C_d)^{0.5}\left(-0.25\frac{1}{cos^{0.5}(\frac{\theta}{2})sin^{1.5}(\frac{\theta}{2})}\right)$$

$$\frac{\delta S}{\delta C_d} = A\left(\frac{\Delta P}{\rho_g}\right)^{0.25}\left(\frac{1}{tan(\frac{\theta}{2})}\right)^{0.5}0.5\left(\frac{1}{C_d}\right)^{0.5}$$

$$\frac{\delta S}{\delta(\Delta P)} = A\left(\frac{1}{\rho_g}\right)^{0.25}\left(\frac{C_d}{tan(\frac{\theta}{2})}\right)^{0.5}0.25\left(\frac{1}{\Delta P^3}\right)^{0.25}$$

$$\frac{\delta S}{\delta\rho_g} = -A\left(\frac{C_d}{tan(\frac{\theta}{2})}\right)^{0.5}(\Delta P)^{0.25}0.25\left(\frac{1}{\rho_g^5}\right)^{0.25}$$

Uncertainty for Wakuri

$$\Delta S = \sqrt{\left(\frac{\delta S}{\delta\theta}\delta\theta\right)^2 + \left(\frac{\delta S}{\delta C_d}\delta C_d\right)^2 + \left(\frac{\delta S}{\delta(\Delta P)}\delta(\Delta P)\right)^2 + \left(\frac{\delta S}{\delta\rho_g}\delta\rho_g\right)^2}$$

Where :

$$\frac{\delta S}{\delta\theta} = 1.189(d_o t)^{0.5}\left(\frac{\Delta P}{\rho_g}\right)^{0.25}(C_d)^{0.25}\left(-0.25\frac{1}{cos^{0.5}(\frac{\theta}{2})sin^{1.5}(\frac{\theta}{2})}\right)$$

$$\frac{\delta S}{\delta C_d} = 1.189(d_o t)^{0.5}\left(\frac{\Delta P}{\rho_g}\right)^{0.25}\left(\frac{1}{tan(\frac{\theta}{2})}\right)^{0.5}0.25\left(\frac{1}{C_d}\right)^{0.75}$$

$$\frac{\delta S}{\delta(\Delta P)} = 1.189(d_o t)^{0.5}\left(\frac{C_d}{\rho_g}\right)^{0.25}\left(\frac{1}{tan(\frac{\theta}{2})}\right)^{0.5}0.25\left(\frac{1}{\Delta P^3}\right)^{0.25}$$

$$\frac{\delta S}{\delta\rho_g} = -1.189(d_o t)^{0.5}\left(\frac{1}{tan(\frac{\theta}{2})}\right)^{0.5}(\Delta P C_d)^{0.25}0.25\left(\frac{1}{\rho_g^5}\right)^{0.25}$$

# Appendix D : Spray Penetration Results

A catalogue of the spray penetration graphs for both diesel and DME are given in this section. The spray penetration for each test is shown along with the theoretical predictions by all four models shown in section 2.5.

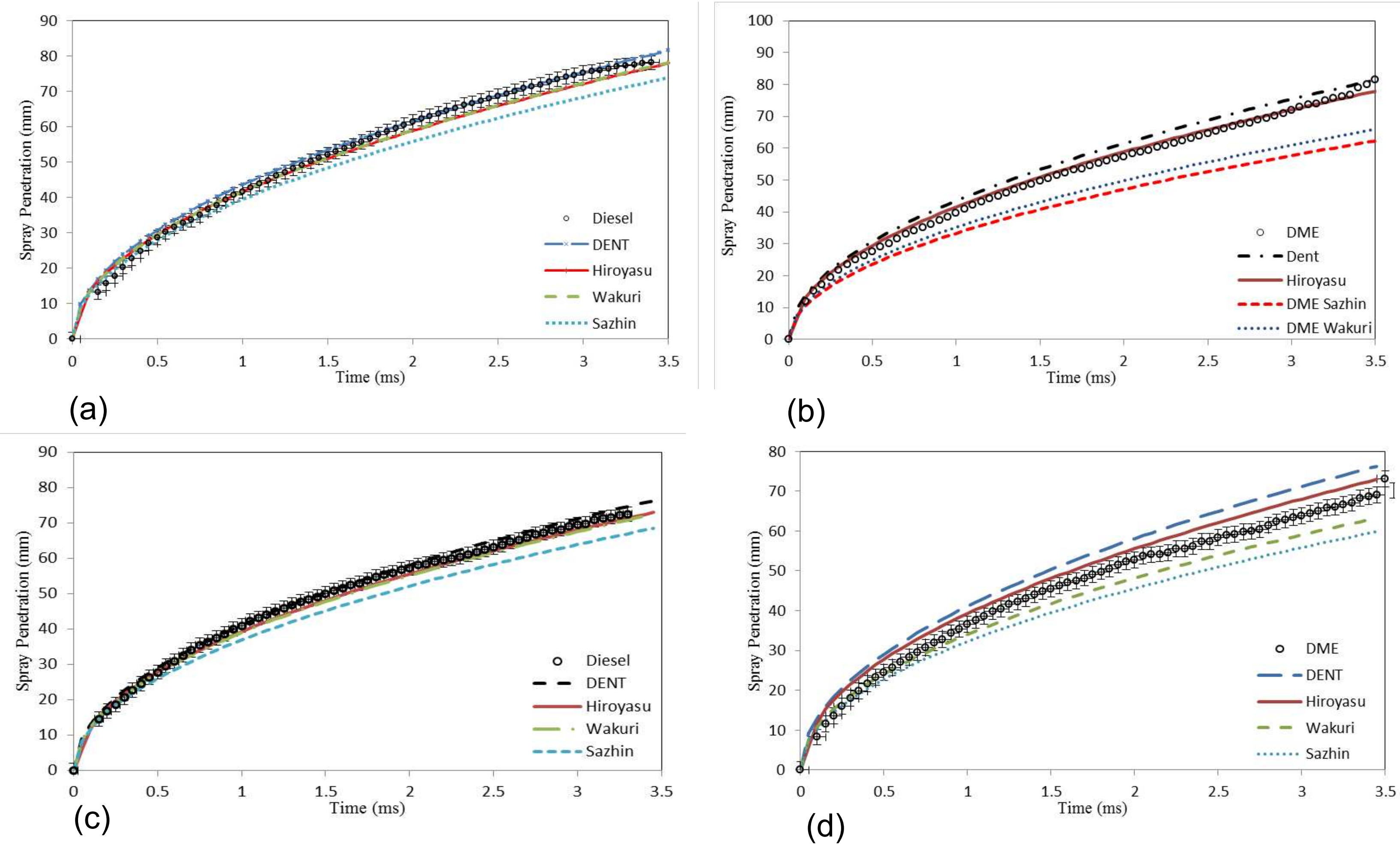


Figure D.1: Experimental spray penetration compared to Theoretical penetration for Diesel and DME at $P_{amb} = 17.7$ bar or $\rho_{amb} = 32.7$ kg/m$^3$ and (a) Diesel $P_{inj} = 500$ bar, (b) DME $P_{inj} = 500$ bar (c) Diesel $P_{inj} = 400$ bar, and (d) DME $P_{inj} = 400$ bar

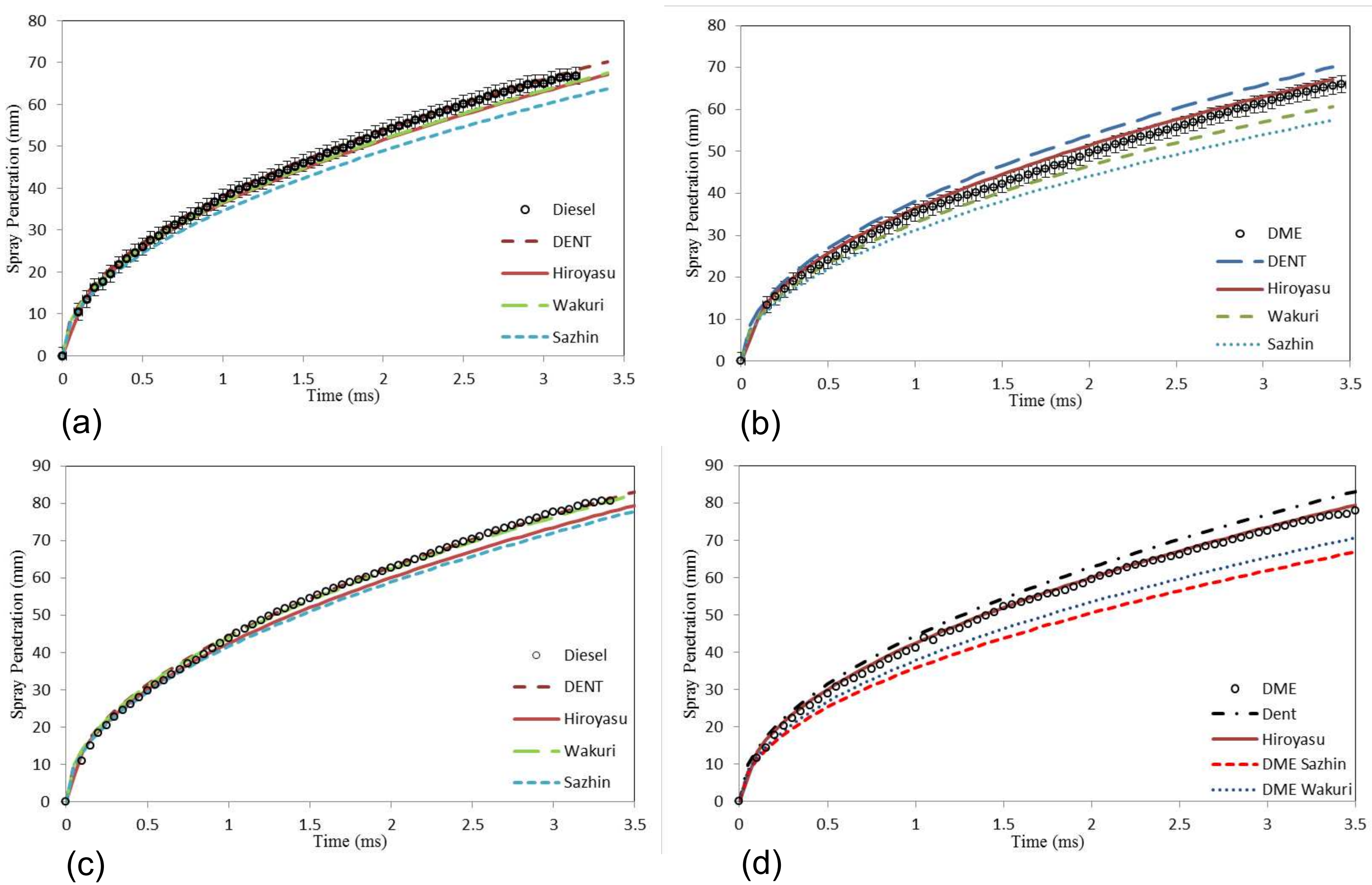


Figure D.2: Experimental spray penetration compared to Theoretical penetration for Diesel and DME at $P_{amb} = 17.7$ bar or $\rho_{amb} = 32.7$ kg/m$^3$ and (a) Diesel $P_{inj} = 300$ bar, (b) DME $P_{inj} = 300$ bar, and then $P_{amb} = 16.5$ bar or $\rho_{amb} = 30.2$ kg/m$^3$ at $P_{inj} = 500$ bar for (c) Diesel , and (d) DME

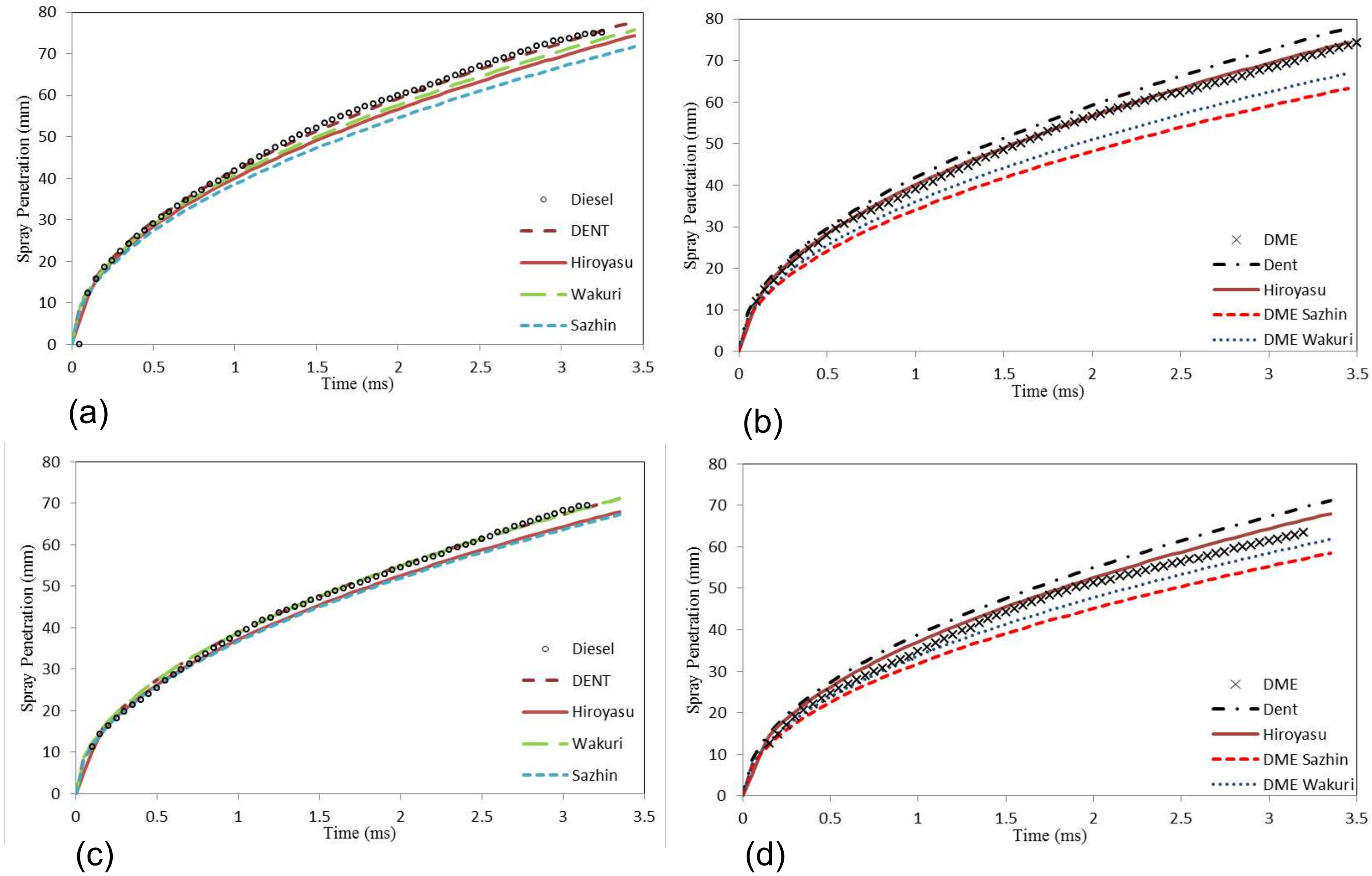


Figure D.3: Experimental spray penetration compared to Theoretical penetration for Diesel and DME at $P_{amb} = 16.5$ bar or $\rho_{amb} = 30.2$ kg/m$^3$ and $P_{inj} = 400$ bar for(a) Diesel, and (b) DME, and at $P_{inj} = 300$ bar for (c) Diesel , and (d) DME

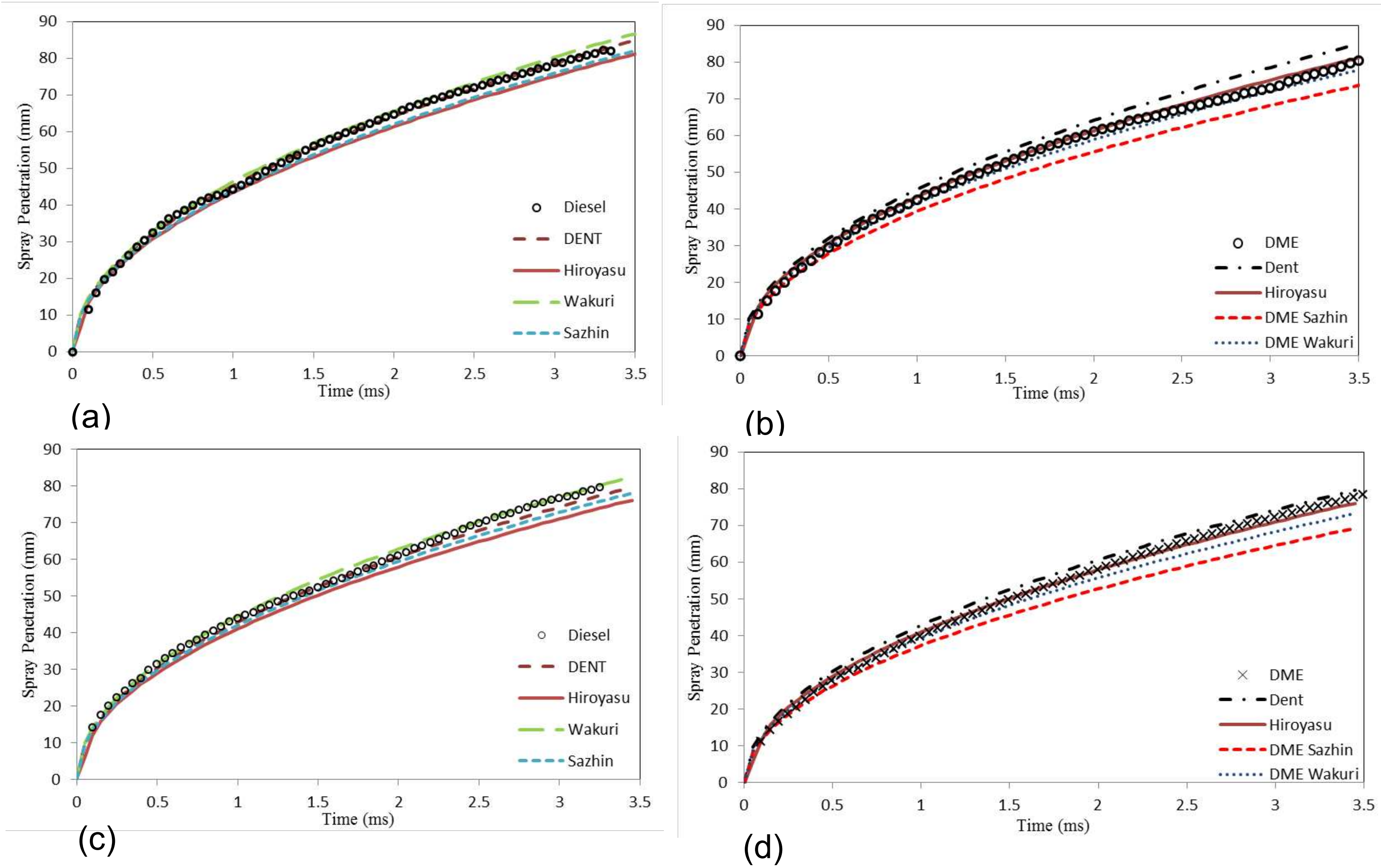


Figure D.4: Experimental spray penetration compared to Theoretical penetration for Diesel and DME at $P_{amb}$ = 15.1 bar or $\rho_{amb}$ = 27.9 kg/m$^3$ and $P_{inj}$ = 500 bar for(a) Diesel, and (b) DME, and at $P_{inj}$ = 400 bar for (c) Diesel , and (d) DME

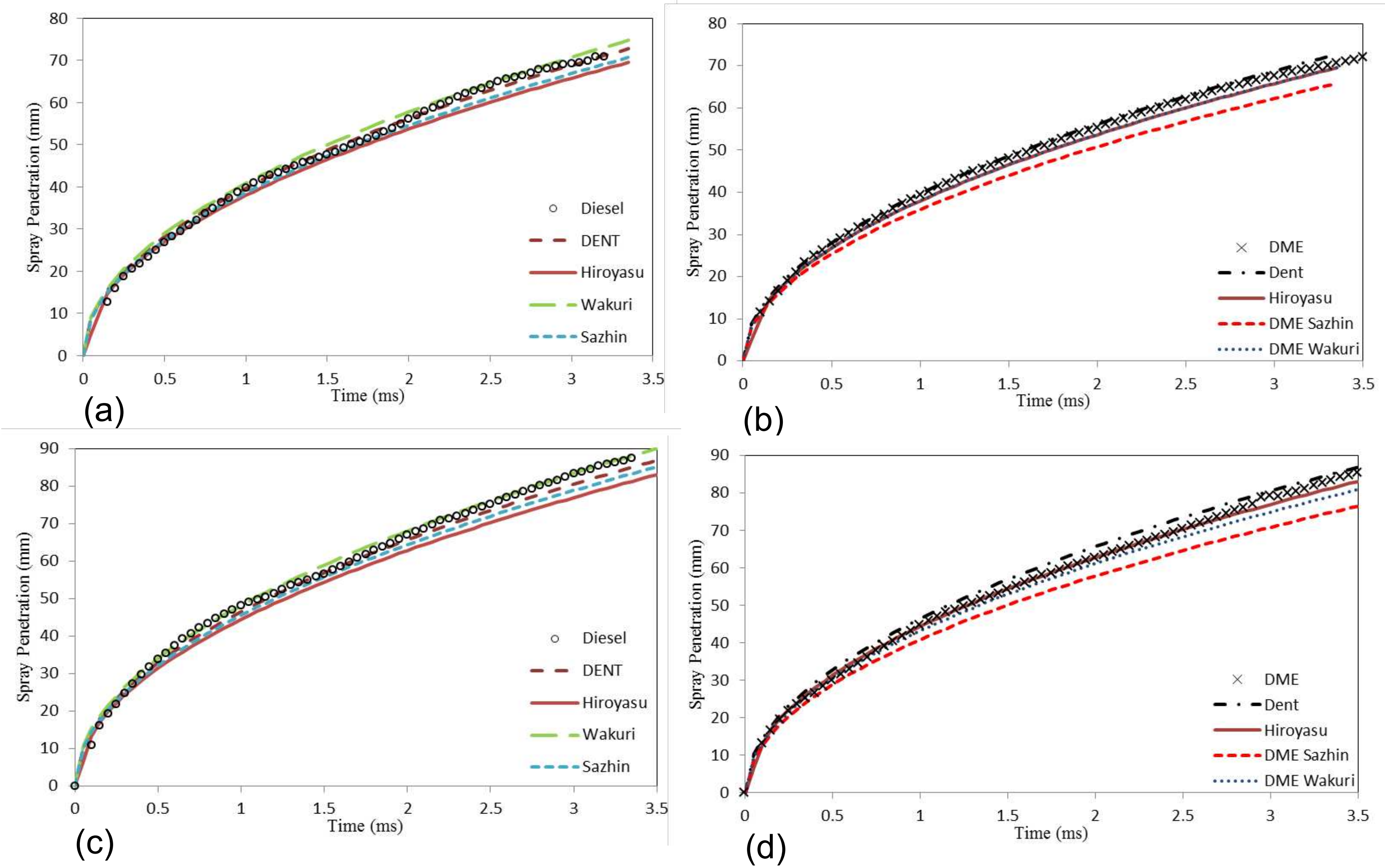


Figure D.5: Experimental spray penetration compared to Theoretical penetration for Diesel and DME at $P_{amb}$ = 15.1 bar or $\rho_{amb} = 27.9$ kg/m$^3$ and $P_{inj}$ = 300 bar, and (a) Diesel (b) DME, and then $P_{amb}$ = 13.8 bar or $\rho_{amb} = 25.45$ kg/m$^3$ at $P_{inj}$ = 500 bar for (c) Diesel , and (d) DME

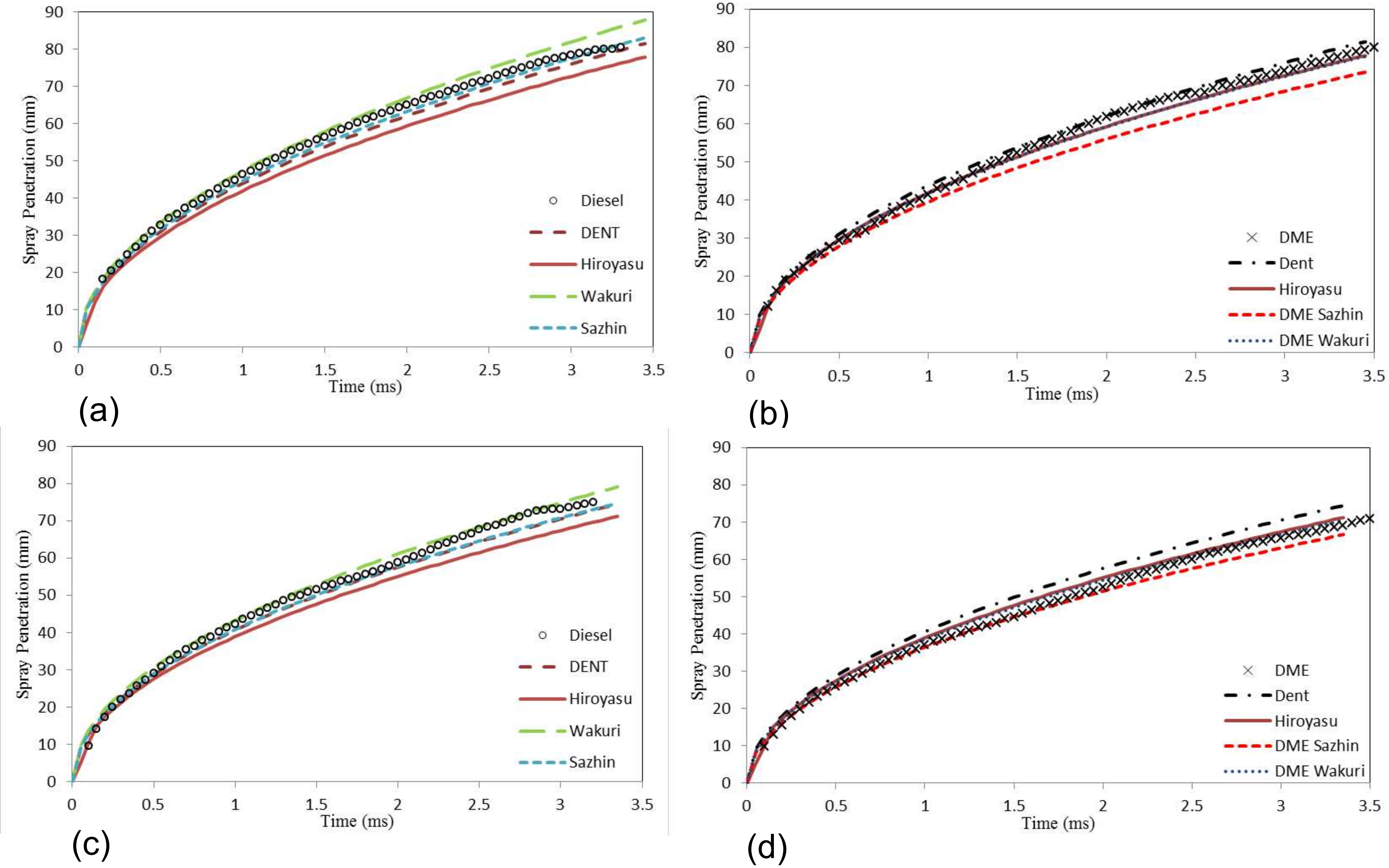


Figure D.6: Experimental spray penetration compared to Theoretical penetration for Diesel and DME at $P_{amb} = 13.8$ bar or $\rho_{amb} = 25.45$ kg/m$^3$ and $P_{inj} = 400$ bar for(a) Diesel, and (b) DME, and at $P_{inj} = 300$ bar for (c) Diesel , and (d) DME

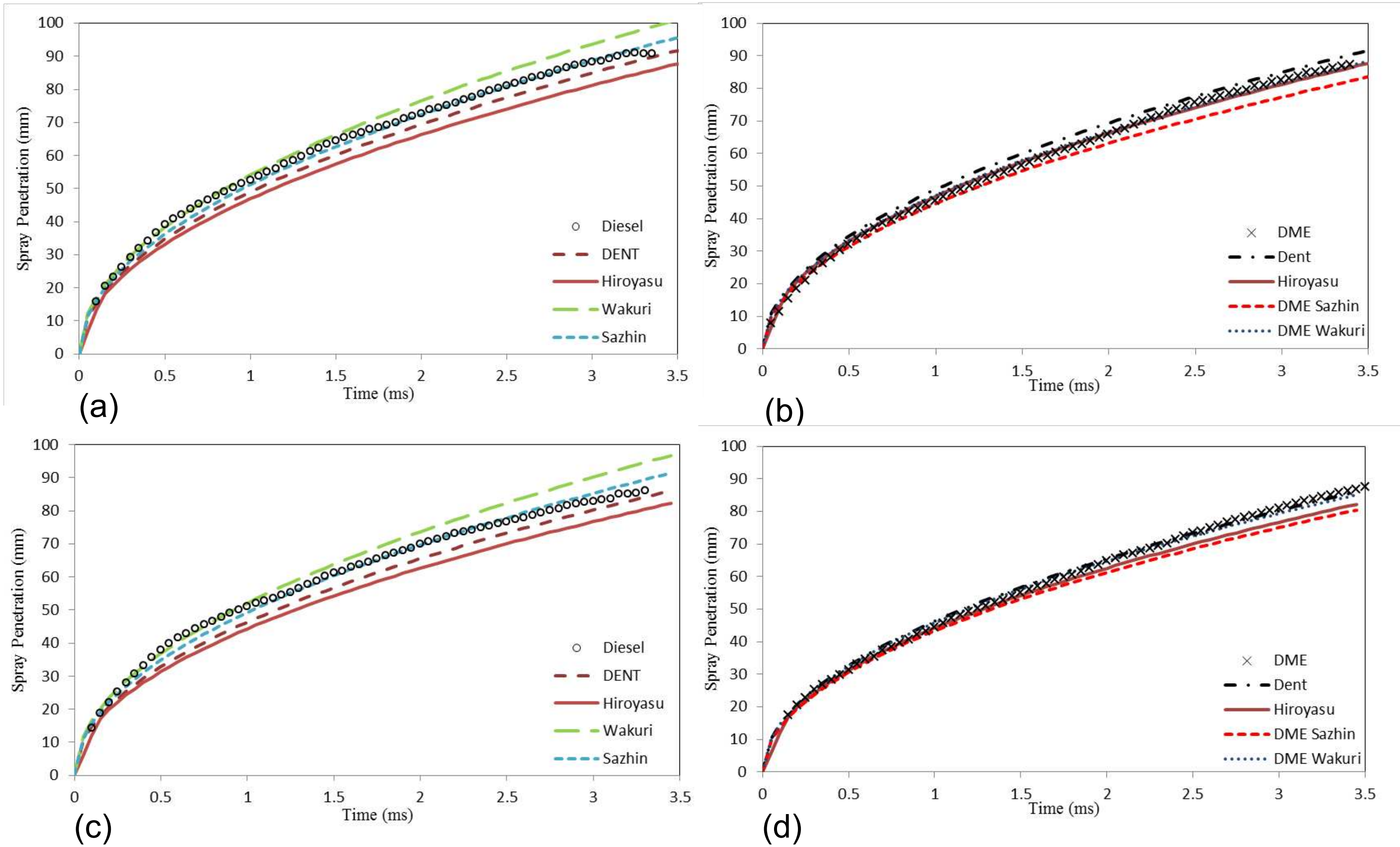


Figure D.7: Experimental spray penetration compared to Theoretical penetration for Diesel and DME at $P_{amb} = 11.2$ bar or $\rho_{amb} = 20.59$ kg/m$^3$ and $P_{inj} = 500$ bar for(a) Diesel, and (b) DME, and at $P_{inj} = 400$ bar for (c) Diesel , and (d) DME

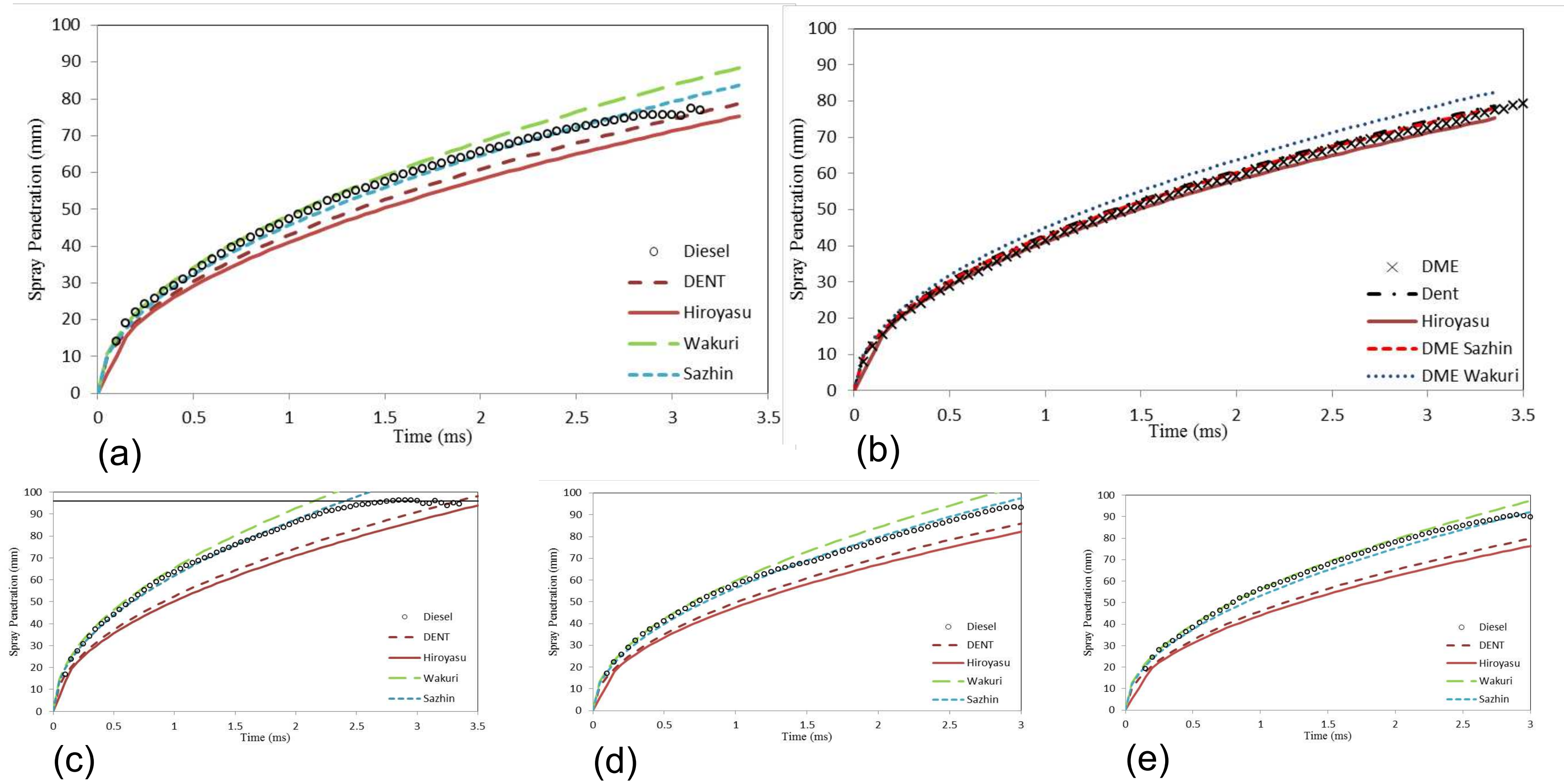


Figure D.8: Experimental spray penetration compared to Theoretical penetration for Diesel and DME at P$_{amb}$ = 11.2.1 bar or $\rho_{amb}$ = 20.59 kg/m$^3$ and $P_{inj}$ = 300 bar, and (a) Diesel (b) DME, and then P$_{amb}$ = 8.55 bar or $\rho_{amb}$ = 15.75 kg/m$^3$ for diesel at (c) $P_{inj}$ = 500 bar, (d) $P_{inj}$ = 400 bar, and (d) $P_{inj}$ = 300 bar,

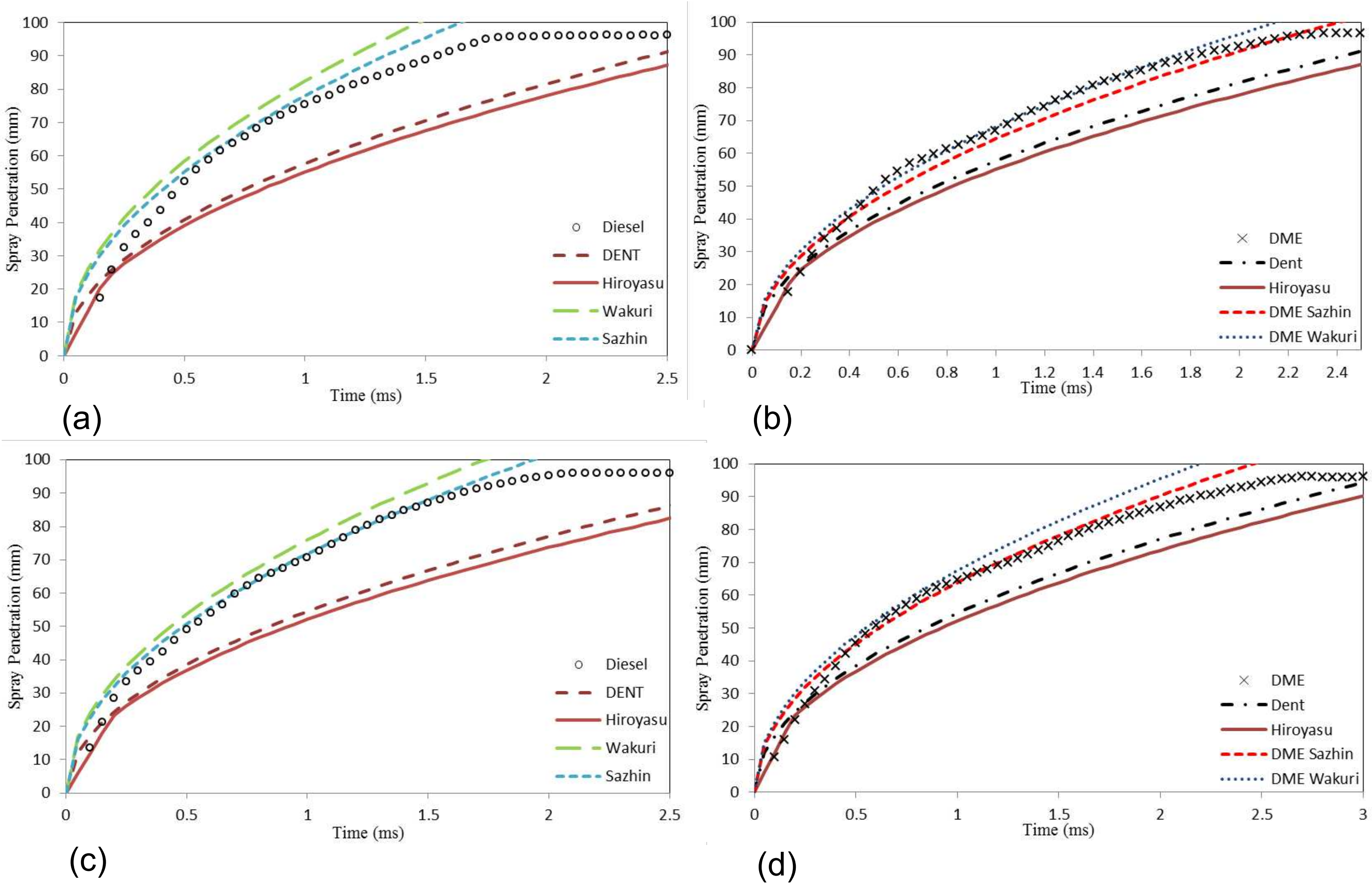


Figure D.9: Experimental spray penetration compared to Theoretical penetration for Diesel and DME at $P_{amb} = 5.91$ bar or $\rho_{amb} = 10.88$ kg/m$^3$ and $P_{inj} = 500$ bar for(a) Diesel, and (b) DME, and at $P_{inj} = 400$ bar for (c) Diesel , and (d) DME

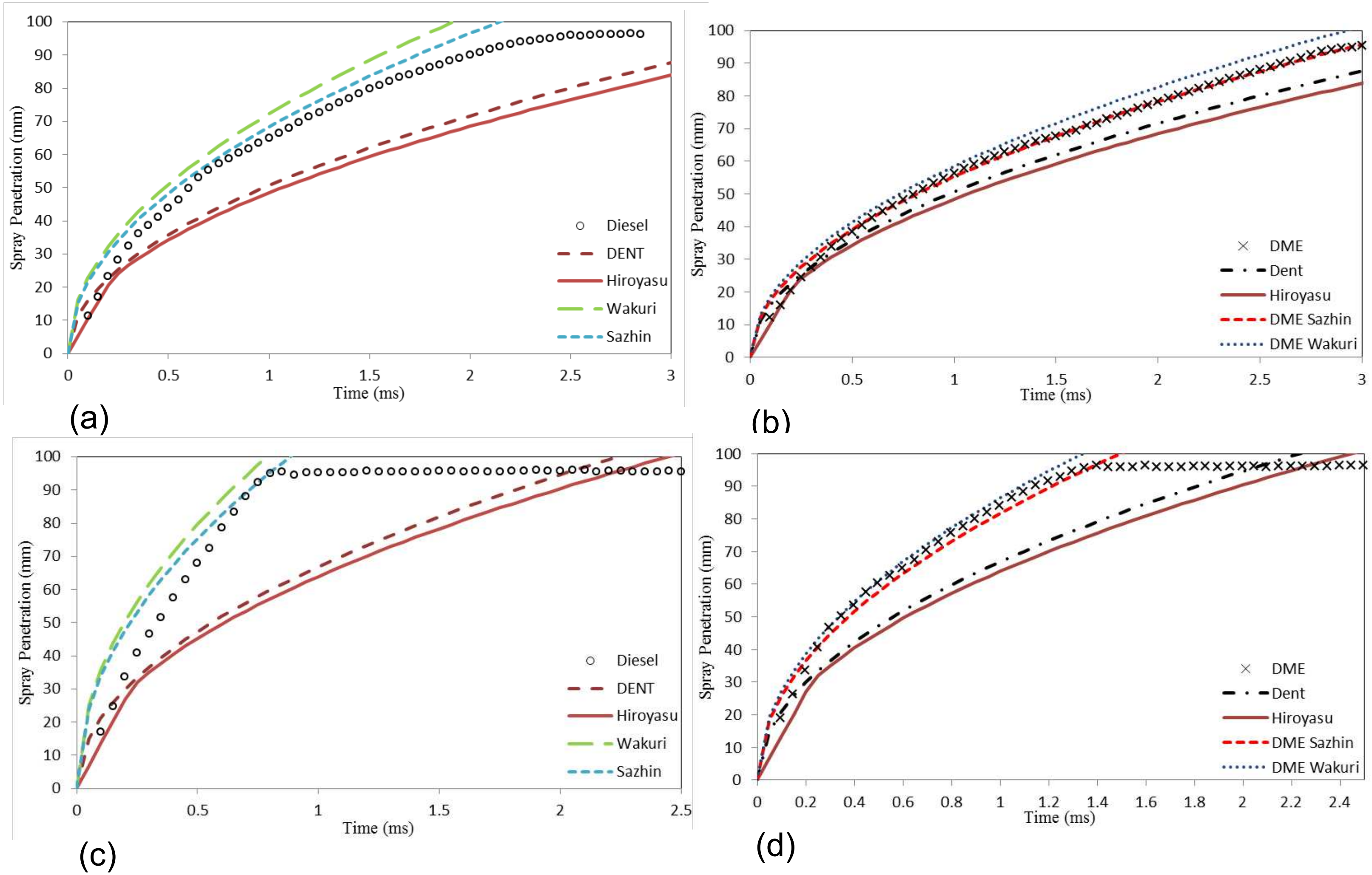


Figure D.10: Experimental spray penetration compared to Theoretical penetration for Diesel and DME at $P_{amb}$ = 5.91 bar or $\rho_{amb}$ = 10.88 kg/m$^3$ and $P_{inj}$ = 300 bar, and (a) Diesel (b) DME, and then $P_{amb}$ = 3.28 bar or $\rho_{amb}$ = 6.04 kg/m$^3$ at $P_{inj}$ = 500 bar for (c) Diesel , and (d) DME

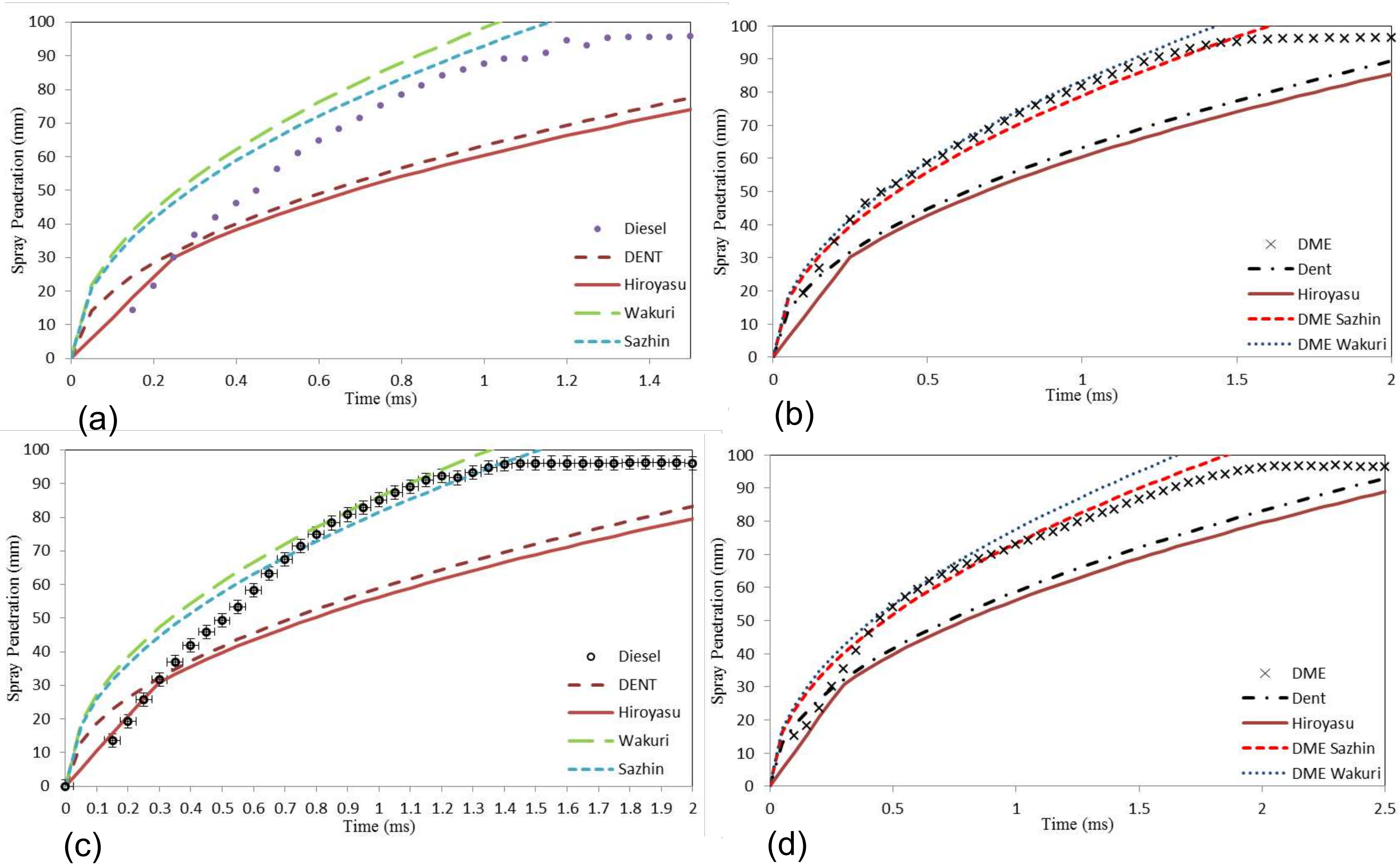


Figure D.11: Experimental spray penetration compared to Theoretical penetration for Diesel and DME at $\mathrm{P}_{amb} = 3.28$ bar or $\rho_{amb} = 6.04$ kg/m$^3$ and $P_{inj} = 400$ bar for(a) Diesel, and (b) DME, and at $P_{inj} = 300$ bar for (c) Diesel , and (d) DME

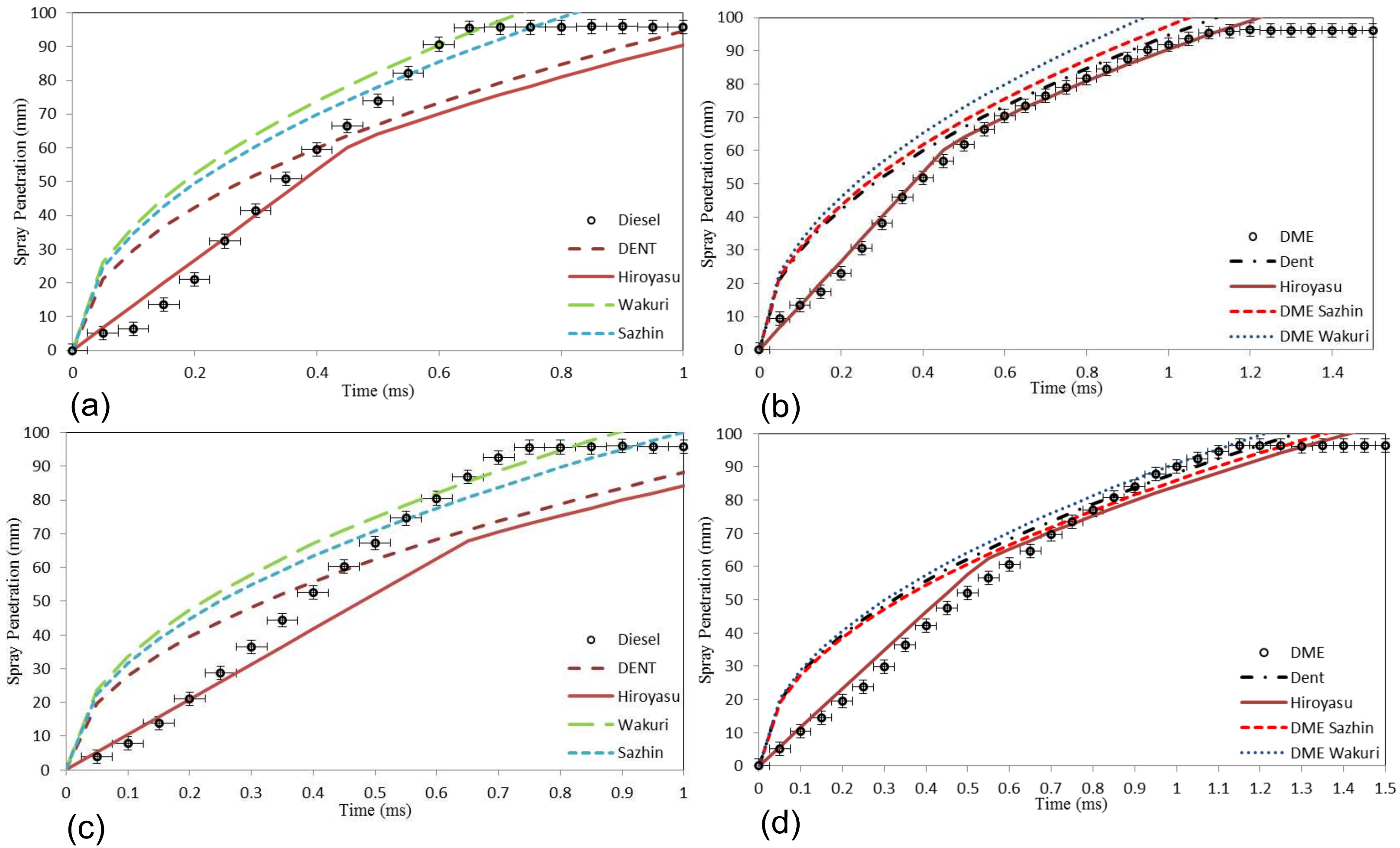


Figure D.12: Experimental spray penetration compared to Theoretical penetration for Diesel and DME at $P_{amb}$ = atmospheric pressure or $\rho_{amb}$ = 1.2 kg/m$^3$ and $P_{inj}$ = 400 bar for(a) Diesel, and (b) DME, and at $P_{inj}$ = 300 bar for (c) Diesel , and (d) DME

# Appendix E : Pressure Traces

The DME and diesel pressure traces are shown in this section. The pressure traces are essentially identical for each injection for all the chamber pressures.

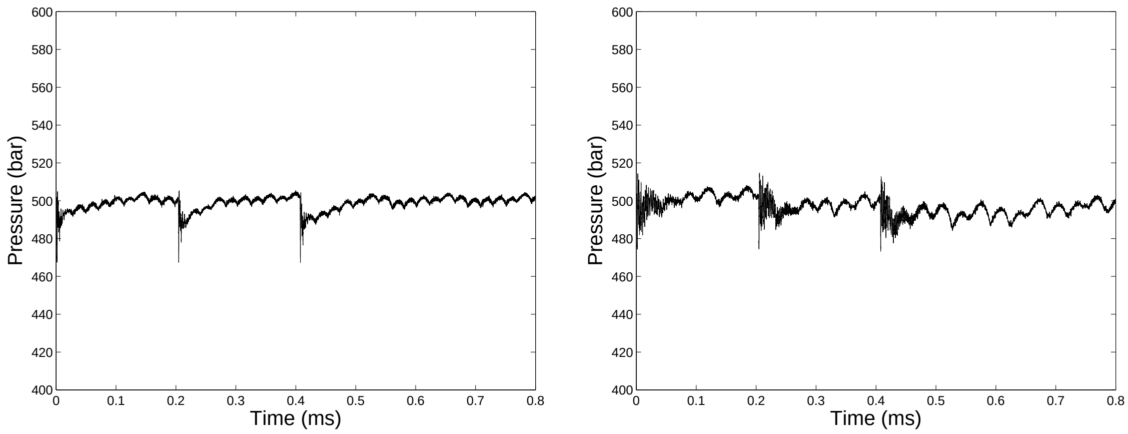


a) b)

Figure E.1: Pressure trace at $P_{amb}$ = 17.7 bar and $P_{inj}$ = 500bar a)Diesel, and b) DME

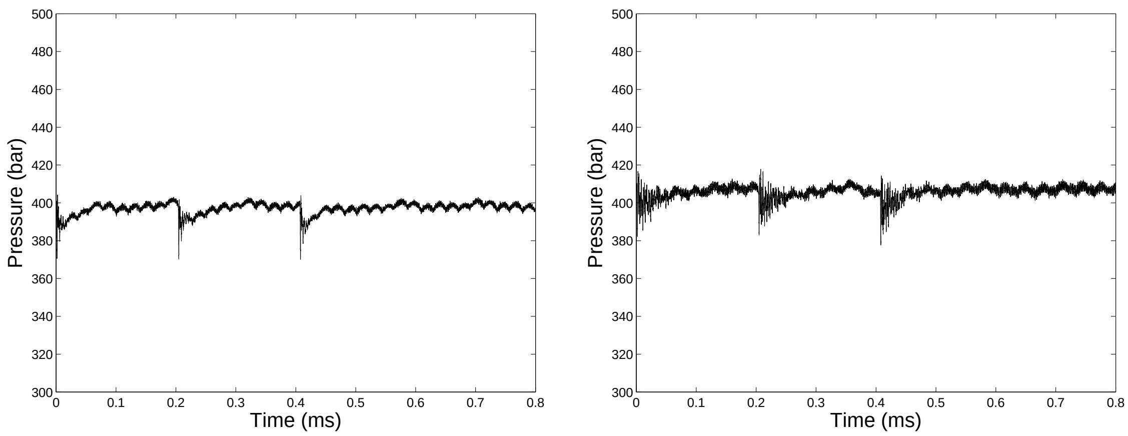


a) b)

Figure E.2: Pressure trace at $P_{amb}$ = 17.7 bar and $P_{inj}$ = 400bar a)Diesel, and b) DME

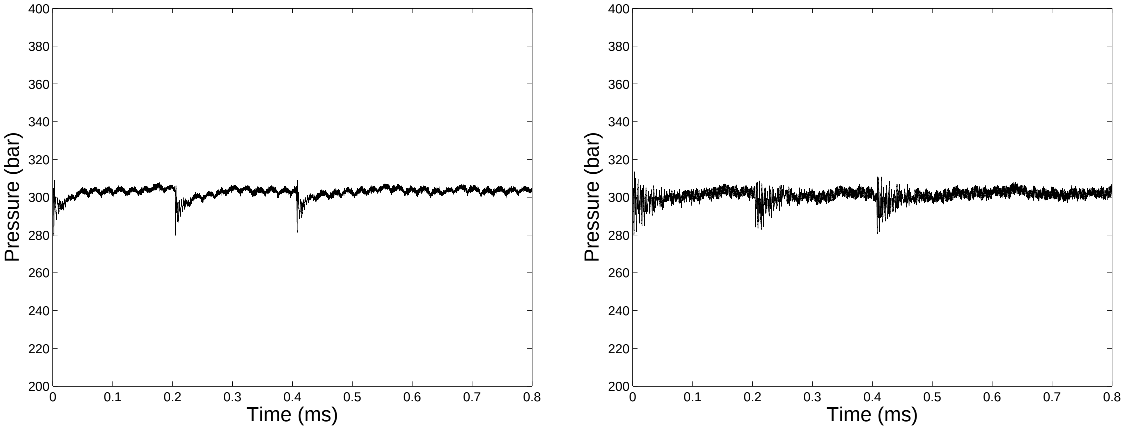


a) b)

Figure E.3: Pressure trace at $P_{amb}$ = 17.7 bar and $P_{inj}$ = 300bar a)Diesel, and b) DME

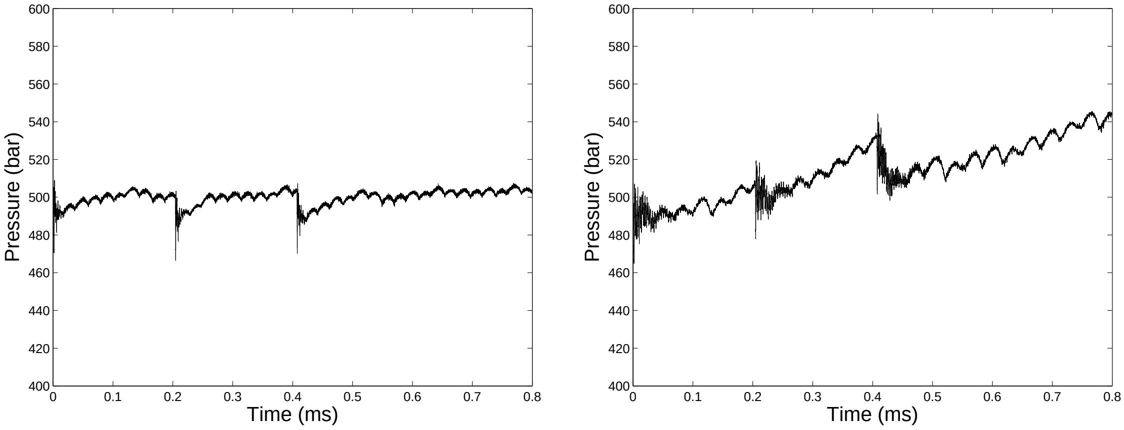


a) b)

Figure E.4: Pressure trace at $P_{amb}$ = 16.45 bar and $P_{inj}$ = 500bar a)Diesel, and b) DME

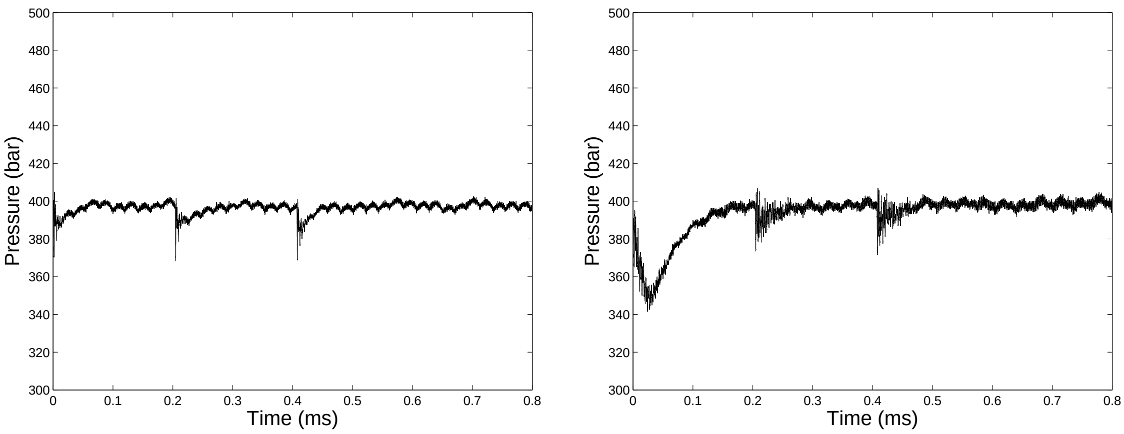


a) b)

Figure E.5: Pressure trace at $P_{amb}$ = 16.45 bar and $P_{inj}$ = 400bar a)Diesel, and b) DME

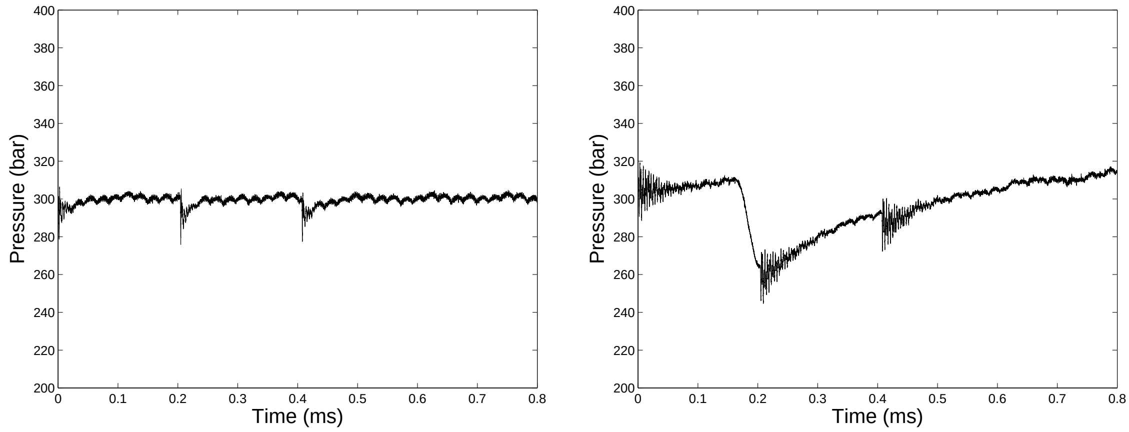


a) b)

Figure E.6: Pressure trace at $P_{amb}$ = 16.45 bar and $P_{inj}$ = 300bar a)Diesel, and b) DME

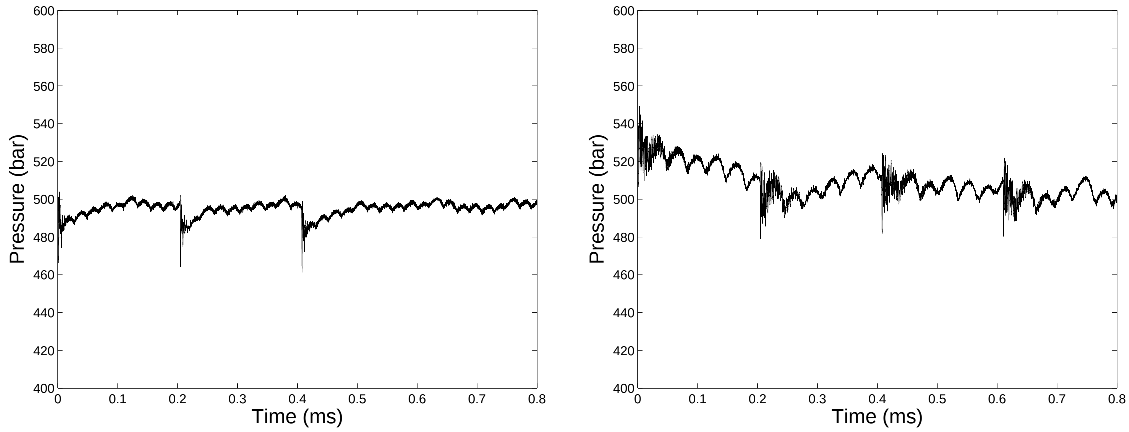


a) b)

Figure E.7: Pressure trace at $P_{amb}$ = 15.1 bar and $P_{inj}$ = 500bar a)Diesel, and b) DME

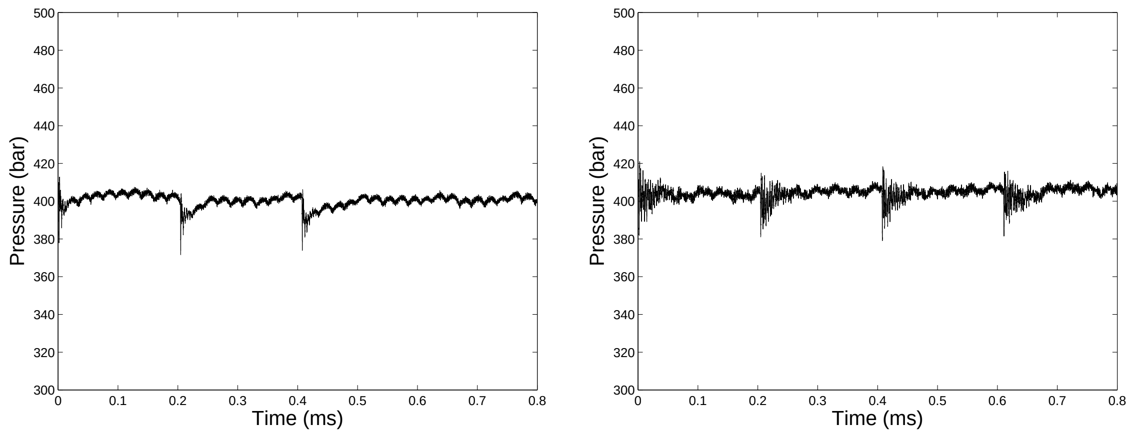


a) b)

Figure E.8: Pressure trace at $P_{amb}$ = 15.1 bar and $P_{inj}$ = 400bar a)Diesel, and b) DME

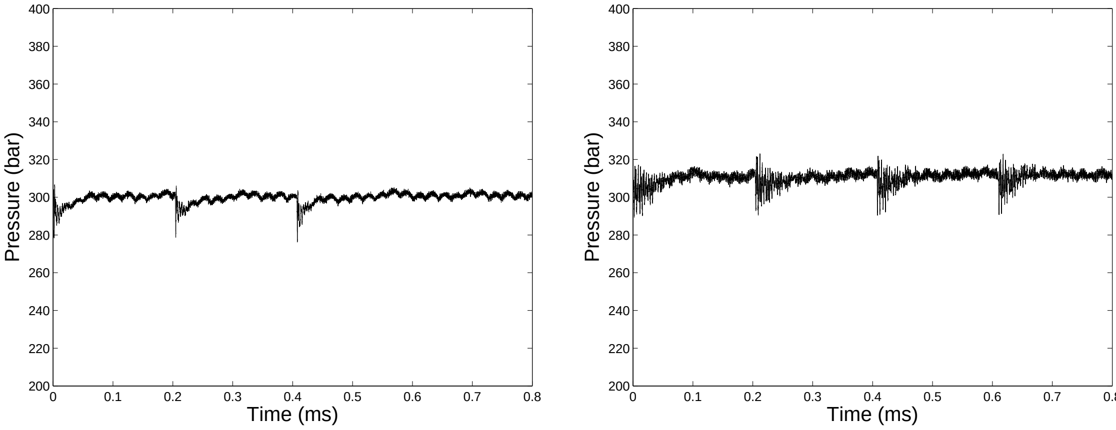


a) b)

Figure E.9: Pressure trace at $P_{amb}$ = 15.1 bar and $P_{inj}$ = 300bar a)Diesel, and b) DME

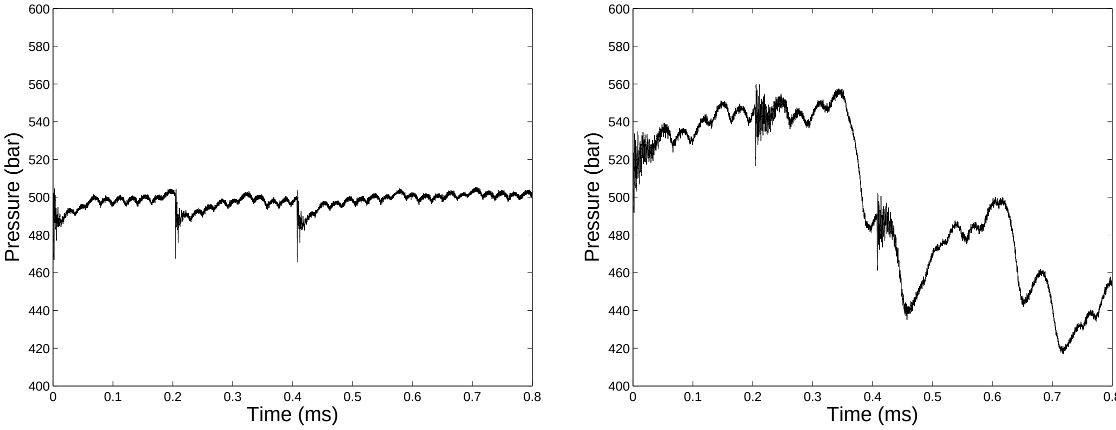


a) b)

Figure E.10: Pressure trace at $P_{amb}$ = 13.8 bar and $P_{inj}$ = 500bar a)Diesel, and b) DME

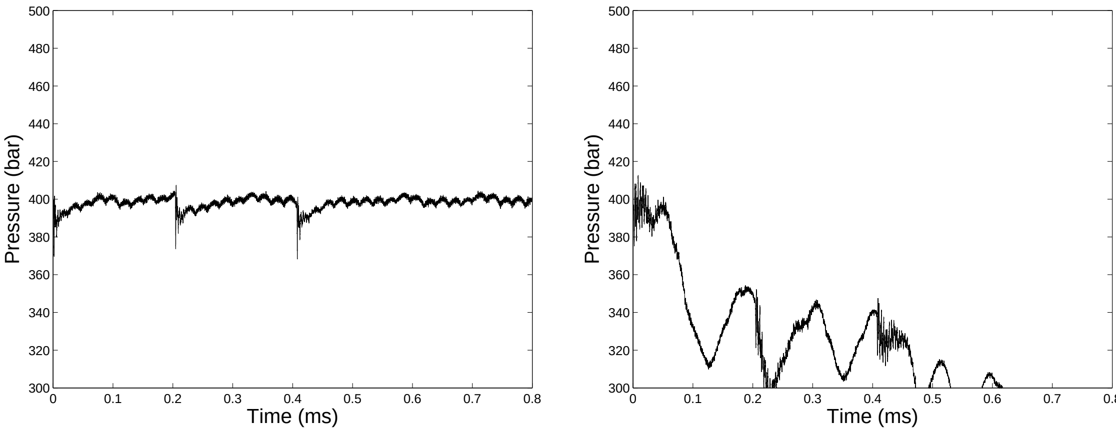


a) b)

Figure E.11: Pressure trace at $P_{amb}$ = 13.8 bar and $P_{inj}$ = 400bar a)Diesel, and b) DME

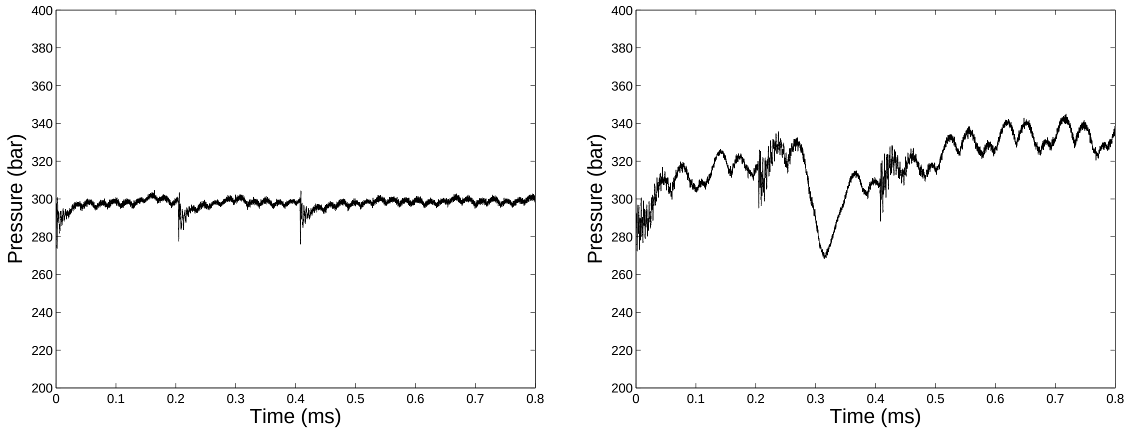


a) b)

Figure E.12: Pressure trace at $P_{amb}$ = 13.8 bar and $P_{inj}$ = 300bar a)Diesel, and b) DME

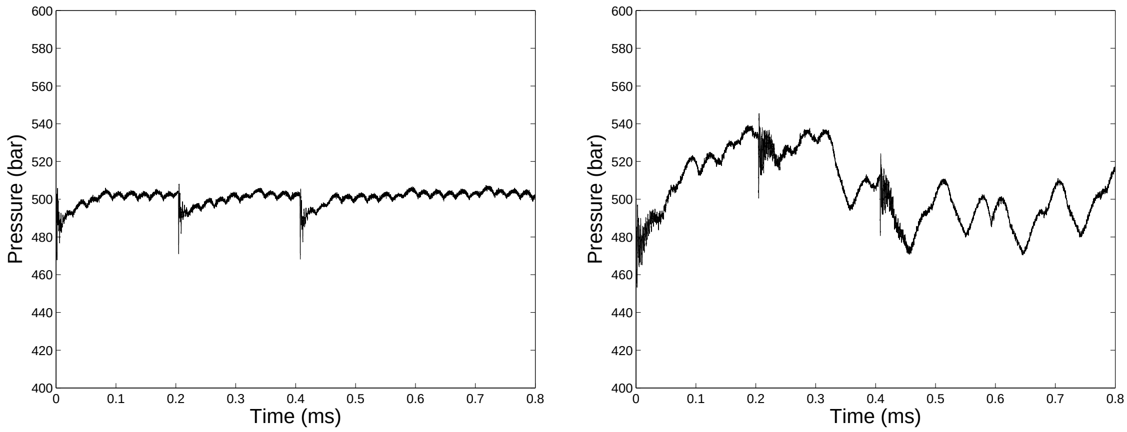


a) b)

Figure E.13: Pressure trace at $P_{amb}$ = 11.2 bar and $P_{inj}$ = 500bar a)Diesel, and b) DME

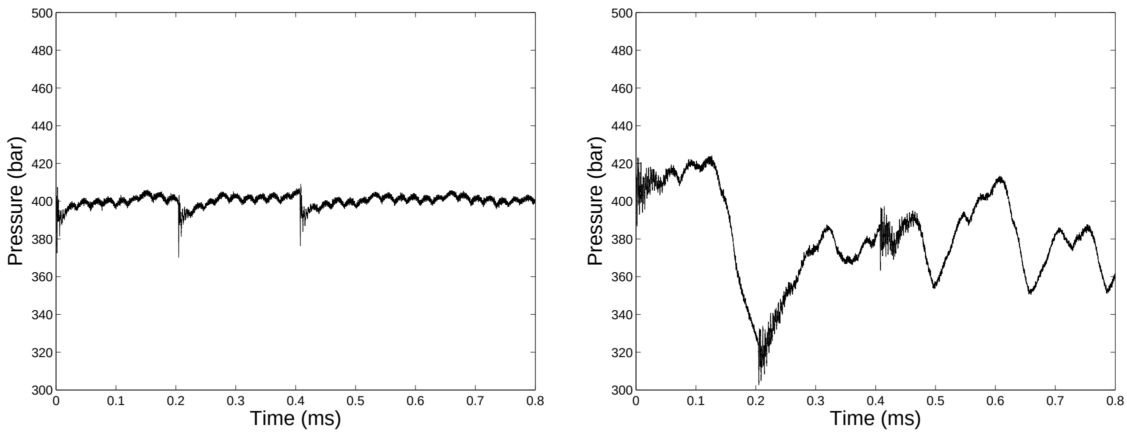


a) b)

Figure E.14: Pressure trace at $P_{amb}$ = 11.2 bar and $P_{inj}$ = 400bar a)Diesel, and b) DME

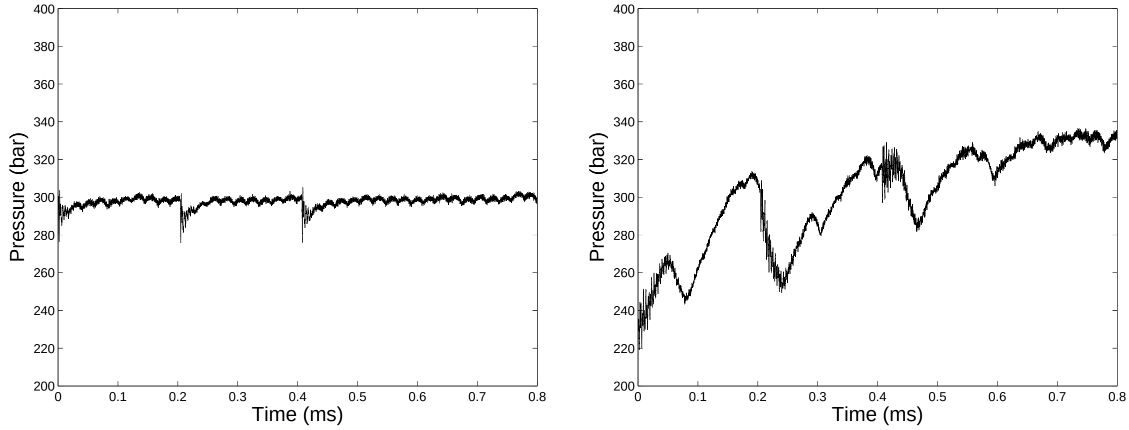


a) b)

Figure E.15: Pressure trace at $P_{amb}$ = 11.2 bar and $P_{inj}$ = 300bar a)Diesel, and b) DME

# Appendix F : Mean Tip Velocity

The mean tip velocity for both diesel and DME fuels at the various injection and chamber pressures tested are given in graphical format in this section. It should be noted that there is a large uncertainty on the first point of each graph, as this was the first point in which the second spray was visible and due to the frame rate it was difficult in identifying this point accurately, thereafter the tip velocity can be taken in confidence.

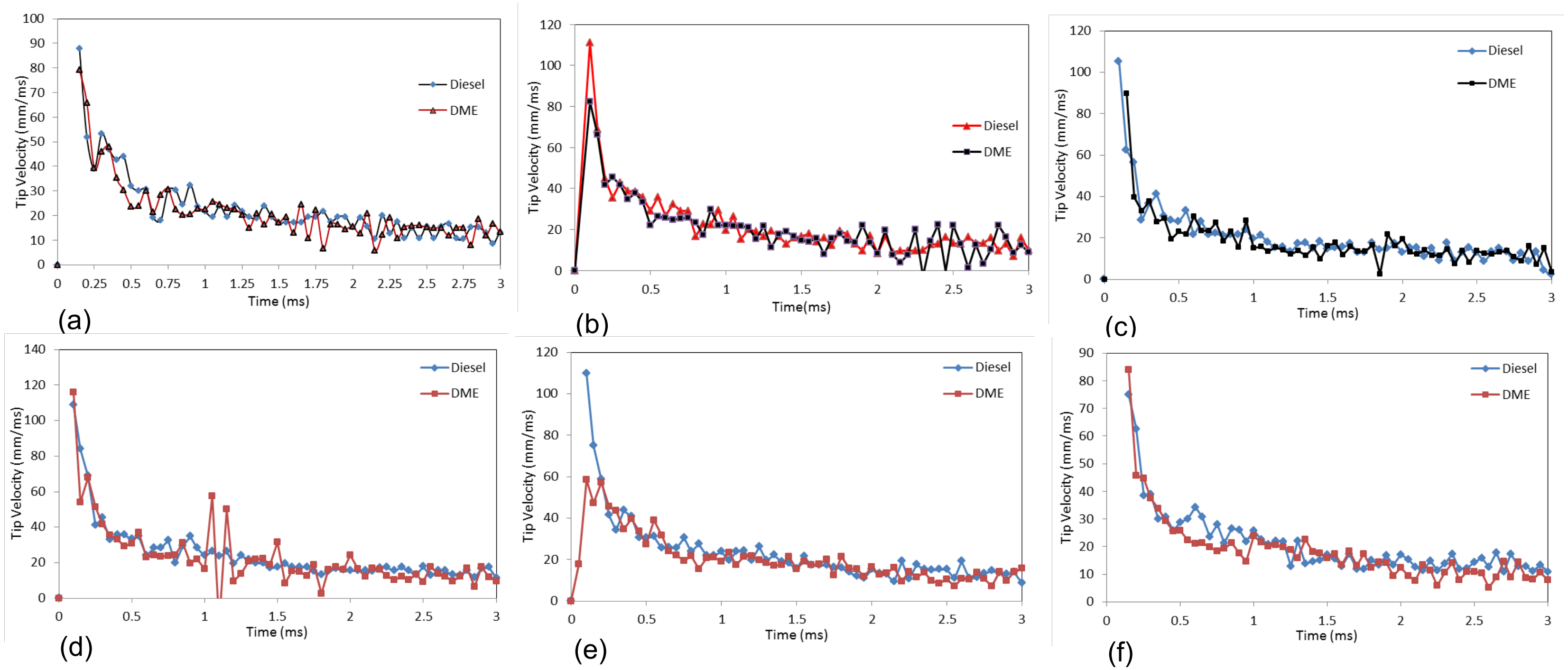


Figure F.1: Experimental Mean Tip Velocity for Diesel and DME at P$_{amb}$ = 17.7 bar or $\rho_{amb}$ = 32.7 kg/m$^3$ and (a) $P_{inj}$ = 500 bar, (b) $P_{inj}$ = 400 bar, and (c) $P_{inj}$ = 300 bar, as well as P$_{amb}$ = 16.45 bar or $\rho_{amb}$ = 30.2 kg/m$^3$ at (d) $P_{inj}$ = 500 bar, (e) $P_{inj}$ = 400 bar, and (f) $P_{inj}$ = 300 bar

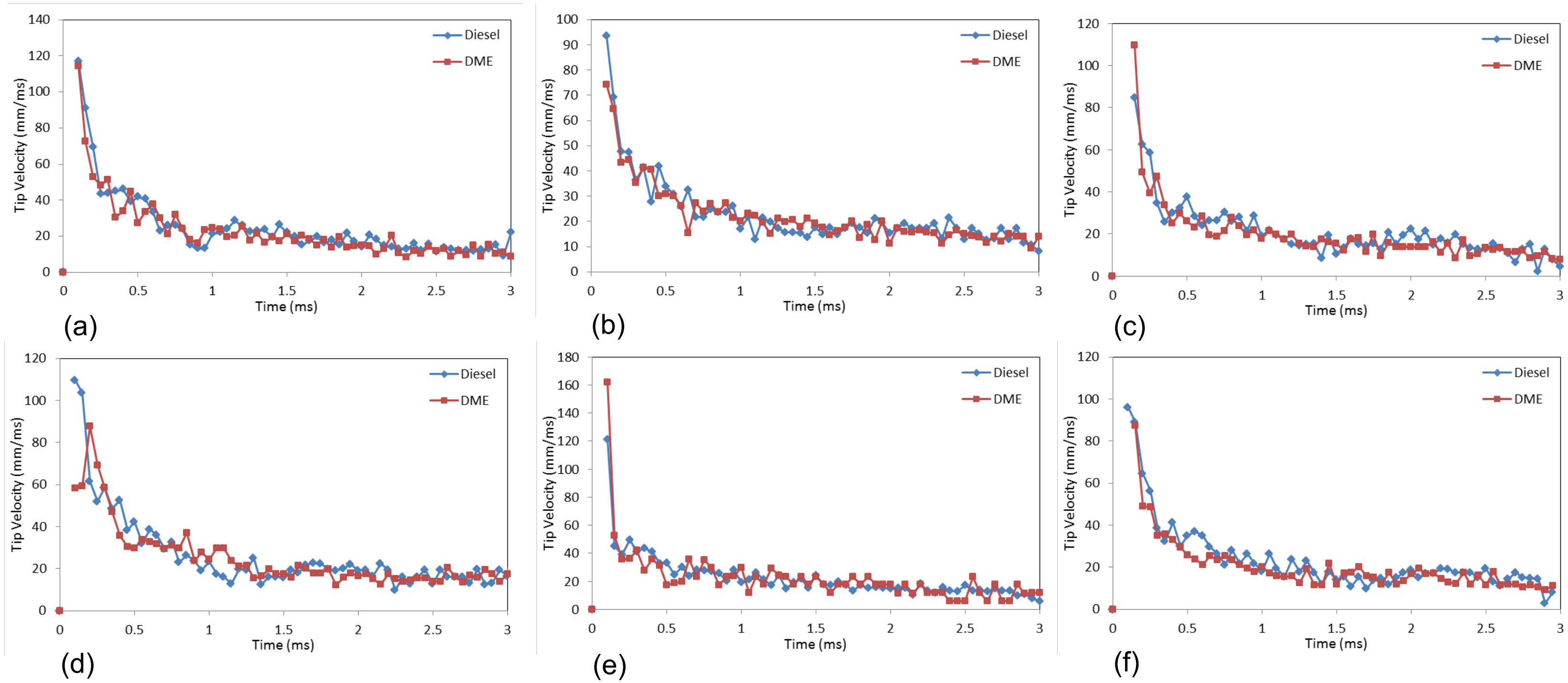


Figure F.2: Experimental Mean Tip Velocity for Diesel and DME at $P_{amb}$ = 15.1 bar or $\rho_{amb}$ = 27.9 kg/m$^3$ and (a) $P_{inj}$ = 500 bar, (b) $P_{inj}$ = 400 bar, and (c) $P_{inj}$ = 300 bar, as well as $P_{amb}$ = 13.82 bar or $\rho_{amb}$ = 25.45 kg/m$^3$ at (d) $P_{inj}$ = 500 bar, (e) $P_{inj}$ = 400 bar, and (f) $P_{inj}$ = 300 bar

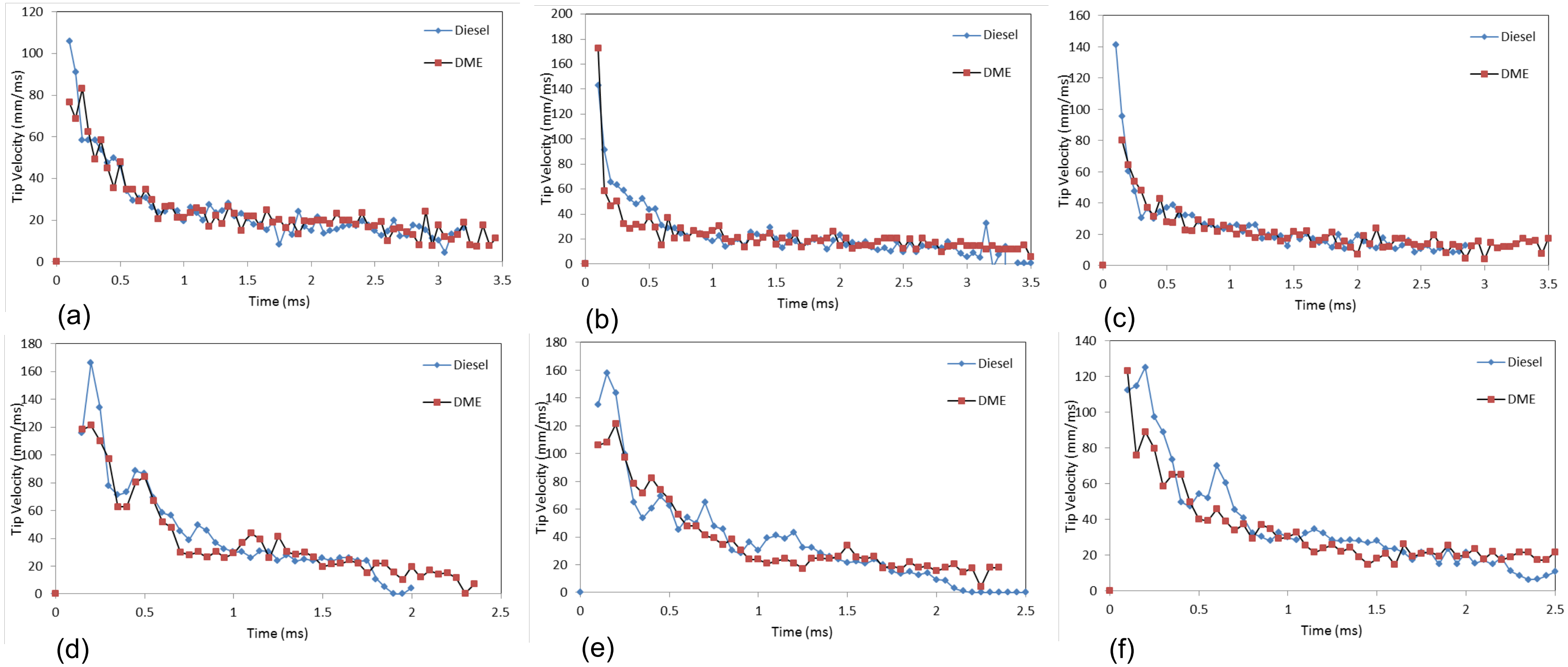


Figure F.3: Experimental Mean Tip Velocity for Diesel and DME at $P_{amb}$ = 11.2 bar or $\rho_{amb}$ = 20.59 kg/m$^3$ and (a) $P_{inj}$ = 500 bar, (b) $P_{inj}$ = 400 bar, and (c) $P_{inj}$ = 300 bar, as well as $P_{amb}$ = 5.91 bar or $\rho_{amb}$ = 10.88 kg/m$^3$ at (d) $P_{inj}$ = 500 bar, (e) $P_{inj}$ = 400 bar, and (f) $P_{inj}$ = 300 bar

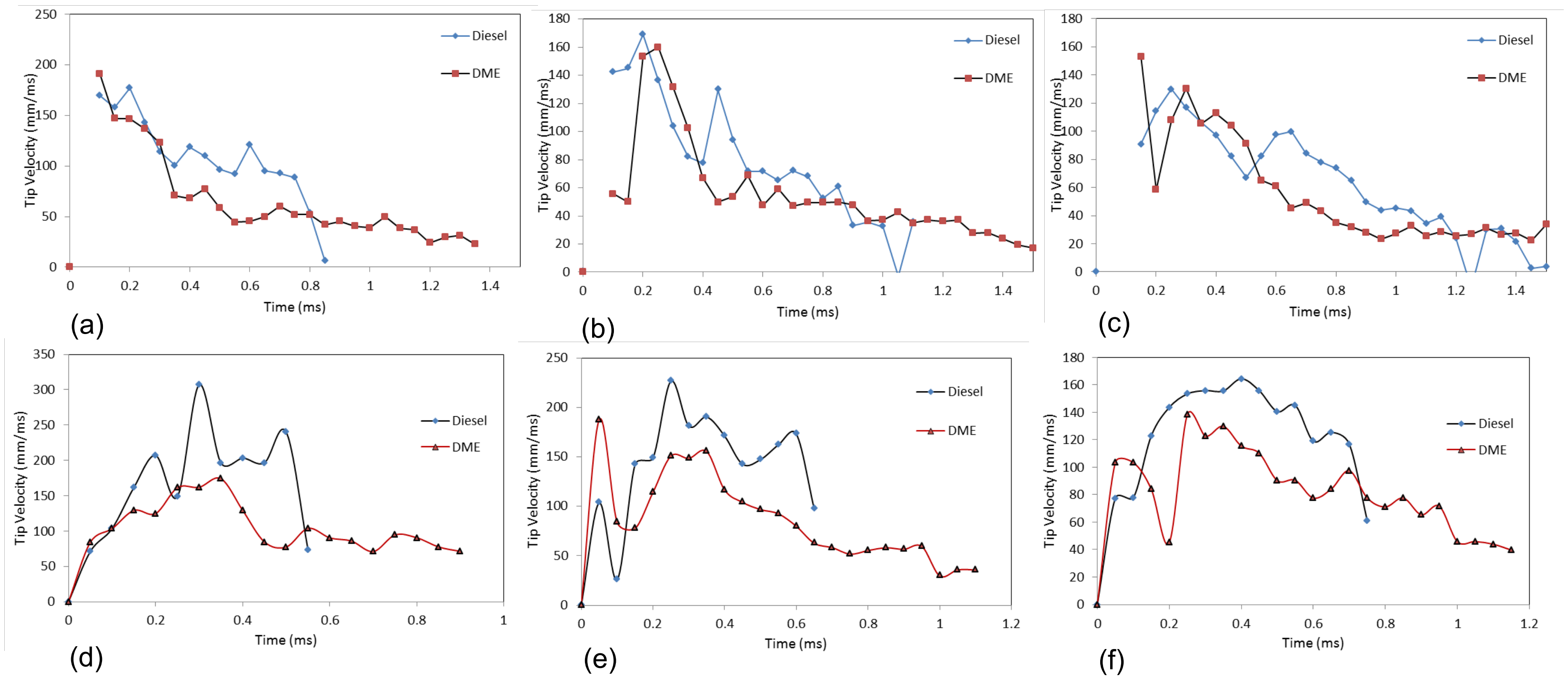


Figure F.4: Experimental Mean Tip Velocity for Diesel and DME at $P_{amb} = 3.28$ bar or $\rho_{amb} = 6.08$ kg/m$^3$ and (a) $P_{inj} = 500$ bar, (b) $P_{inj} = 400$ bar, and (c) $P_{inj} = 300$ bar, as well as $P_{amb} = 1$ bar or $\rho_{amb} = 1.2$ kg/m$^3$ at (d) $P_{inj} = 500$ bar, (e) $P_{inj} = 400$ bar, and (f) $P_{inj} = 300$ bar

# Appendix G : Data Drive

This Appendix consists of information to large and tedious to place in the report. The Contents of this data drive are as follows:

- Matlab code
- Labview Programs
  - Image Processing
  - Experiment Controller Software
- High Speed Images
  - High Speed Images
  - $CO_2$ images
  - DME Images
  - Diesel Images
- Spreadsheets
  - Total Penetration Results
  - Diesel Cone angle
  - DME Cone angle

# Appendix H : Equipment Specification

| **Equipment/Instrument** | **Type** | **Serial No.** |
|---|---|---|
| Kistler Charge Meter | 501541000 | SN1413654 |
| DC Power Supply | Topward6306A | 744795 |
| AC Motor (three phase) | GEC Machines | PD5756/07 |
| Solenoid Fuel Injector | Bosch | A612 070 0095 |
| Radial High pressure pump | Bosch | A611 070 05 01 |
| AC motor Controller | FRN37G11S-4 | 8X2736R0006 |
| DAQ Card | National Instruments | NI USB6211 |
| Fluke Thermometer | Digital Thermometer 52-2 | |
| Condor Valve | 1/2” 3 way | 33-10-L |
| Kistler Pressure Transducer | 6229A | 1714181 |
| Thermocouple probe | K type | |